Foundation experiments in quantum atom optics with ultracold metastable helium

Andrew Geoffrey Manning

A thesis submitted for the degree of Doctor of Philosophy
at the Australian National University

October, 2014

Foundation experiments in quantum atom optics with ultracold metastable helium

Andrew G. Manning

Atomic & Molecular Physics Laboratories,
Research School of Physics & Engineering,
College of Physical & Mathematical Sciences,
Australian National University, Canberra, Australia.

Supervisory committee: Dr. Andrew G. Truscott
Dr. Robert G. Dall
Prof. Kenneth G. H. Baldwin

Abstract

The field of atom optics has progressed rapidly over the past 20 years since the realisation of Bose-Einstein condensation, such that the wave behaviour of atomic gases is now routinely demonstrated. Furthermore, the study of quantum atom optics, which goes beyond a 'mean-field' description of quantum systems to consider the behaviour of single particles, has demonstrated both the similarities between photons and massive species, and their differences as a result of the internal structure and external interactions of atoms. An important class of observable quantities which allow such effects to be measured are nth order correlation functions, which can be interpreted as a result of either particle or wave behaviour. These functions provide a statistical description of fluctuations in n-tuples of particles in a source, which rigorously defines concepts such as coherence. The quantum statistics of a Bose-Einstein condensate should be the same as that for an optical laser, while an ideal thermal Bose gas matches the behaviour of incoherent light. However, correlation measurements can also be used to quantify the influence of interactions, dimensionality, confining potentials and waveguides, and the difference in quantum statistics between fermions and bosons, which illustrates the rich range of behaviour exhibited by atomic gases.

In this thesis, several aspects of quantum atom optics are explored with experiments using ultracold metastable helium, a species with the unique advantage of facilitating simple single-atom detection with high resolution, while still allowing Bose-Einstein condensates to be formed. The coherence of atomic systems is shown to be maintained when outcoupled as pulsed atom lasers, and the long-range order characteristic of Bose-

Einstein condensates is demonstrated to third order for the first time. Conversely, thermal bunching is observed for a variety of atomic systems, including the measurement of correlation functions up to sixth order with near-ideal interference contrast. These results clearly demonstrate the correspondence between the quantum statistics of photons and atoms as was formalised by Glauber, as well as confirming the validity of applying Wick's theorem to simplify the statistics of atomic gases. Correlation functions are also shown to be an ideal tool to probe the quantum state of an ultracold gas, and were used to observe the phenomenon of transverse condensation in an elongated Bose gas, as well as characterise the mode occupancy of matter waves guided by an optical potential.

Ultracold metastable helium is also suitable for exploring other fundamental topics in quantum optics such particle/wave duality. The notion of complementarity stimulated long running philosophical discussions about how apparently mutually exclusive behaviours can coexist, which culminated in Wheeler devising his famous 'delayed choice' *gedankenexperiment*. A proposed experimental method to realise Wheeler's experiment with ultracold atoms is discussed, and preliminary measurements presented which indicate that the completion of this experiment could be achieved in the near future. Not only is this of interest in its own right, but the implementation of this experiment has also developed techniques which may enable further studies in quantum atom optics such as investigations of the Hong-Ou-Mandel effect and quantum entanglement with massive particles.

Declaration

Except where acknowledged in the customary manner, the material presented in this thesis is, to the best of my knowledge, original and has not been submitted in whole or part for a degree in any university.

Andrew G. Manning _____

Date _____

Acknowledgements

I am indebted to many people who helped me through the challenges and triumphs of my PhD. It has been a privilege working with the friendly and talented people in the helium BEC group at ANU, and I have learned a lot about science as well as life in general from doing so. My supervisor Andrew Truscott has created a great environment to do cutting-edge research in, and has lead the group purposefully towards exciting new territory. His breadth of knowledge and insight into how complicated physics works has taught me a lot about how to tackle difficult problems while keeping in mind the importance of the 'big picture'. I am deeply grateful for the guidance provided by my other supervisor Robert Dall, who shared his prodigious knowledge of both the conceptual and technical aspects of our experiment with me, while tolerating periods of frustration with admirable patience and good humour. I could not have asked for a better role model to learn the craft of scientific research from.

I also learned a great deal from fellow PhD student Sean Hodgman, who is a master of the underappreciated art of 'getting the job done' by quickly identifying the key components of complicated problems. Sean was also a great friend to have in the lab, and I thank him for dragging me to Raiders and Brumbies games in the freezing Canberra winter, and for the insanely complicated board game battles. I also benefited from sharing the lab with RuGway 'Ruggers' Wu, who should be acknowledged for his hard work and dedication to the project, while I now look forward to following the progress of the experiment under new PhD student Roman Khakimov. I would also like to thank Ken Baldwin for his support, in particular for providing the opportunity to attend eye-opening conferences and workshops.

Our department is fortunate to have access to several highly skilled technicians, who are critical to the success of our research. Colin Dedman's wizardry with electronics is largely responsible for the finesse with which we can control our experiment, in particular with the pursuit of the fabled 'Dedman limit' of noise suppression. Steve Battisson and Ross Tranter in the mechanical workshop were also pivotal with their expertise in the design and engineering aspects of the experiment, providing everything from CAD diagrams to precisely machined custom metalwork. I would also like to acknowledge the valuable collaborations with several theorists, such as Mattias Johnsson at ANU and the groups of Karén Kheruntsyan and Matt Davis at the University of Queensland.

I have been lucky enough to spend my time in Canberra with a variety of friendly and interesting individuals, especially the gallery of rogues at University House. Having a fantastic group of people to shoot the breeze or hit a tennis ball with has made this time far more enjoyable. Special mention among that lot must go to Alison for enduring the 'paved' bushwalks, and to George for all the fascinating conversations.

The support from my family, friends and mentors has also been immensely valuable over the years. In particular, I should thank Jason Dicker and Julian Robinson for encouraging me to pursue my interest in science beyond the confines of Tasmania. I will

always be grateful to my mother Frances who has supported and encouraged me every step of the way, and certainly none of this would have been possible without her. Finally, I would like to thank Tamara for the games of chess, the bus rides, and for always being there for me. *Esto es para la bestia del infierno.*

Contents

Chapter 1

Introduction

In the beginning of the history of experimental observation, or any other kind of observation on scientific things, it is intuition, which is really based on simple experience with everyday objects, that suggests reasonable explanations for things. But as we try to widen and make more consistent our description of what we see, as it gets wider and wider and we see a great range of phenomena, the explanations become what we call laws instead of simple explanations. One odd characteristic is that they often seem to become more and more unreasonable and more and more intuitively far from obvious.

— Richard Feynman [1]

Quantum mechanics is arguably the most powerful yet perplexing physical theory in existence. Despite the remarkable accuracy to which it has been tested, and its widespread application to modern science and technology, some consequences of quantum theory remain poorly understood to the point where consensus among physicists has not yet been reached on a variety of fundamental ideas [2–4]. While this may appear disconcerting, it continues to stimulate the development of new ideas to this day which contribute to a deeper understanding of physical behaviour. Many of the misconceptions about quantum mechanics are the result of a desire to reconcile this abstract theory with the more intuitively familiar concepts of classical physics, however it is this process which also helped uncover many of the revolutionary aspects of quantum mechanics.

Accordingly, the development of humankind's understanding of light has taken a long and winding path, with a history of conflicting theories being proposed to describe its behaviour[1]. After several centuries of rudimentary use of optics to provide basic technologies, the seventeenth century gave rise to the first detailed studies which provided insight into the true nature of light [5]. Central to this was the question of whether light behaved as a wave, which would be compatible with measurements such as those of interference patterns by Robert Hooke and the subsequent wave theory of light by Christiaan Huygens; or that light was corpuscular, which for example Isaac Newton used to explain the colour of light. Despite the considerable sway of Newton's convictions, the case for a wave description of light was strengthened by Thomas Young's study of interference, particularly after his famous double slit experiment. This was followed by a thorough mathematical theory of interference by Augustin-Jean Fresnel,

[1] A detailed history of which is presented in books such as Ref. [5].

and the work of James Clerk Maxwell and Heinrich Hertz among others which firmly established light as an electromagnetic wave [6].

At the beginning of the 20th century, during the early development of quantum theory, Max Planck assumed that light was to be treated as particles to explain the spectrum of black body radiation [7]. Albert Einstein also invoked this assumption to explain the photoelectric effect [8], and as did Arthur Compton to explain the wavelength change for scattered x-rays [9], and these early results of quantum mechanics confirmed that light did indeed behave as a particle. Eventually, it was accepted that the concepts of both particles and waves were both equally applicable for understanding light. Louis de Broglie then extended this to include the notion that massive bodies normally thought of as particles could also display wave behaviour [10], and an experimental measurement of electron diffraction in the famous Davisson-Germer experiment [11] confirmed that de Broglie's hypothesis was correct (as did a later famous experiment which showed that interference can even be observed with much larger C_{60} 'bucky-balls' [12]).

Classical descriptions of radiation are still used to understand not only familiar phenomena such as diffraction and image formation, but also in some cases non-linear optical effects [13]. However, development of theory for the particle nature of light and its interaction with quantum atoms with discrete energy levels was one of the key achievements of quantum mechanics. Among the most fundamental concepts was that light of frequency f could be absorbed and subsequently emitted by atoms as photons with energy $E = hf$, where $h = 2\pi\hbar$ is Planck's constant. Equations to describe the evolution of quantum systems were developed in the context of particles with the matrix mechanics of Werner Heisenberg, while Erwin Schrödinger's equation captured the wave nature of quantum systems [5]. Later, a more thorough treatment for this was provided by Paul Dirac [14], which accounted for both interference and interactions with matter and thus provided a unified theory of wave and particle behaviour [15].

As these abstract mathematical theories were being produced, the views of the scientists who formulated them on how to reconcile these theories with experimental observations, not to mention intuition, began to diverge. Many people such as Heisenberg were unconcerned with the failure of classical ideas, and were content to 'trust the mathematics', while others such as Niels Bohr wanted to explore the significance of the act of measurement, and the interface between a microscopic quantum system to be measured and a classical macroscopic measurement device [5]. While Bohr's so-called *correspondence principle* does reconcile quantum theory with classical physics in the limiting case of large systems (or more specifically, large quantum numbers), it certainly does not imply that classical analogies can be extended to microscopic systems.

While providing a theory which accurately describes the behaviour of light and atoms, quantum mechanics also has many counter-intuitive consequences which have challenged long-held ideas about the physical world, to the point where a variety of interpretations have been invoked to reconcile quantum theory with our understanding of nature. In particular, the discontinuity that occurs upon the interaction of quantum system with measurement device was problematic for Bohr, as it implied a lack of determinism. It therefore became important to define the act of measurement carefully, and to consider how to separate the microscopic from the macroscopic. Another key highly non-classical consequence of this new quantum theory was Heisenberg's uncertainty principle, which mathematically dictates that a pair of conjugate observables such as position and momentum, or time and energy, cannot both be known simultaneously with arbitrary precision. Bohr saw this as an example of a deeper-lying *complementarity*

in quantum theory, where the application of a classical concept to understand a particular aspect of a system prevents a different and complementary aspect from being described with reference to classical concepts within the same picture. This was largely inspired by the distinction between the experimental apparatus used to measure pairs of complementary behaviours, which inevitably precludes the measurement of the two behaviours simultaneously, as is illustrated by the Heisenberg microscope *gedankenexperiment*. Bohr used this idea to address the issue of why light and matter could sometimes be observed to act as particles, and sometimes as waves [16]. With his complementarity principle, Bohr claimed that whether particle or wave behaviour of light or matter is measured is determined by the nature of the experiment being performed, a concept which Richard Feynman later identified as the 'only mystery' in quantum mechanics [1]. For example, Bohr claimed that for an electron incident on a pair of holes [1],

> it is impossible to design any apparatus whatsoever to determine through which hole the electron passes that will not at the same time disturb the electron enough to destroy the interference pattern.

The concept for complementarity, along with the classical concept of determinism being replaced with a probabilistic view of nature, formed the centrepiece of the *Copenhagen interpretation* of quantum mechanics championed by Bohr, which eventually became a widely but not universally accepted way of understanding the indisputably accurate mathematics of quantum theory. However, there were some notable dissidents of Bohr's position, including Einstein and his colleagues Boris Podolsky and Nathan Rosen, who were uncomfortable with the abandonment of determinism and were motivated to identify a perceived problem with the Copenhagen interpretation by outlining the famous Einstein-Podolsky-Rosen (EPR) paradox [17]. The purpose of this paper was to advocate the idea that the quantum theory developed to that point was incomplete, as it was unable to account for correlations between causally separated pairs of particles which were supposed to not be in a specific state before measurement. Through the discussions following this paper, concepts such as *entanglement* were introduced to account for the apparent non-local link between the pair of particles (famously coined 'spooky action at a distance'), while *hidden variables* were required to 'complete' quantum theory. This fuelled a long-running debate between Bohr and Einstein which is covered in detail in Ref. [5], and remained in the realm of philosophical discussion until an experiment could be devised to determine if either view was correct.

A resolution for the EPR paradox was finally found several decades later by David Bell, who mathematically defined an inequality which unambiguously distinguishes between quantum physics and a classical picture where hidden variables and local realism both hold (a complete history of which can be found in Ref. [18]). When it was shown experimentally by Alain Aspect that Bell's inequality was indeed violated by entangled pairs of photons [19, 20], it seemed like Einstein's idea of a realist world where properties exist independent of observation was discredited and that the Copenhagen interpretation had been proven to be correct. However, a variety of other interpretations have emerged in the following years, some of which such as the Bohm pilot-wave theory are able to circumvent problems associated with complementarity by allowing particle and wave behaviours to coexist, while others have revived some of Einstein's arguments, such that the issue is still yet to be settled conclusively[5].

While progress continued to be made which refined the quantitative accuracy of quantum theory, an interest in exploring the philosophical aspects of quantum mechan-

ics remained. Bohr's concept of complementarity was readdressed by John Wheeler, who wished to isolate the role that the experimenter plays in choosing whether particle or wave behaviour is observed in a twin slit-style experiment. In his famous delayed-choice *gedankenexperiment*, the choice of experimental configuration is made after the particle to be measured has exited the slits, however the fact that the experiment does not have a definite configuration at that point does not prevent the expected result according to the principle of complementarity from being found. Although it took some time for an experiment to be performed which matched Wheeler's idea sufficiently closely, upon its successful completion [21] the conclusions drawn by Wheeler and Bohr were vindicated. However, this again shows the fallacy of thinking in terms of classical concepts, as this result does not imply that the choice of experimental configuration influenced the past behaviour of the particle, but instead emphasises that nothing can be concluded about the behaviour of the particle until a measurement is made.

A further twist to the concept of complementarity is the idea that a continuum of intermediate behaviours exist between the two limits of particle and wave, as opposed to the naïve view of the two being mutually exclusive [22]. This is quantified by the Englert–Greenberger duality relation [23], which defines the limit of the which-way information characteristic of particles is available depending on the wave interference visibility observed, without making reference to Heisenberg's uncertainty relation. Furthermore, the choice of the experimental configuration in Wheeler's experiment can be switched with a quantum state in any arbitrary superposition of the two options [24], which not only demonstrates a mixture of particle and wave behaviours, but also shows that the behaviour observed depends on whether the result of the quantum 'switch' state is known or not [25–27]. This is an example of quantum erasure of information.

Other concepts from classical physics required less confronting revisions as quantum theory was developed, such as statistical distributions of particles, and the concept of coherence. While the Maxwell-Boltzmann distribution remains appropriate at high temperatures, as a collection of particles is cooled, the discrete nature of the energy levels that the particles can occupy becomes important, as does the parity of the particle wavefunctions which determine how many particles can occupy the same level according to the Pauli exclusion principle [28]. A particular feature of the statistics of bosons in the phenomenon of Bose-Einstein condensation [29, 30], in which a macroscopically large portion of particles occupy the exact same quantum state. This is in stark contrast to a thermal distribution, in which the properties of the system are strongly dependent on temperature, as the particles in a Bose-Einstein condensate (BEC) can all be represented by the 'same wavefunction' and have properties which are not associated with a temperature.

While there intuitively appears to be an unmistakable contrast in coherence between a BEC and a thermal distribution, in the sense of how 'alike' the particles are to one another, the classical definition of coherence is not necessarily able to distinguish the two. The invention of the laser, which produces a source of photons with identical quantum behaviour, not only gave rise to the field of quantum optics where the behaviour of individual photons is significant, but also provided an experimental way to evaluate a more rigorous definition of coherence, which is discussed at length later in this thesis. Essentially, quantum coherence is determined by correlation functions which consider the interference between individual particles. It is important to note that such correlations are not the result of entanglement or interactions in this case, but are rather dependent only on quantum statistical distributions. In this context, coherent states such as lasers

and BECs can be identified as those with the lowest uncertainty allowable by the Heisenberg uncertainty principle in their properties, and are consequently the states which in some sense most closely mimic the behaviour of classical states.

Robert Hanbury Brown and Richard Twiss devised an experiment to measure the size of distant stars with quantum correlation functions [31], by replacing standard single-body Michelson interferometry with two-particle interference which demonstrates an effect which bears their name. While this was a controversial proposal at the time, the experiment was placed on a solid theoretical basis by a new theory of quantum coherence by Roy Glauber [32], who later won a Nobel Prize for this work which laid the theoretical foundation for modern quantum optics. In doing so, a truly quantum-mechanical definition of coherence was established, which addresses the failings of the classical notion of coherence by unambiguously showing the contrast between coherent and incoherent sources, and clarified both the particle and wave-like aspects of interference. Furthermore, it provided a framework to understand the quantum statistics of systems at a single particle level, and lead to further novel phenomena to test indistinguishability such as the Hong-Ou-Mandel effect [33], where pairs of particles that interfere at a beamsplitter always exit via the same port.

Clearly, our understanding of quantum physics is yet to be completed or at the very least agreed upon, which continues to stimulate study in fields such as quantum optics. As technology improves, it provides the opportunity to not only test established theory in novel ways, but to also learn about more complicated systems. A prominent example of this is the field of quantum atom optics, which explores effects normally associated with photons in the context of atomic systems. This will indeed be the main objective of this thesis: to develop experimental techniques to observe novel quantum statistical and matter wave interference effects in ultracold metastable helium.

Fundamental tests of quantum mechanics with ultracold atoms

A large portion of the research exploring the fundamental tenets of quantum theory has been performed with photons. As sources of light with unique quantum properties such as lasers became readily available, and given that the resultant photons are relatively easily manipulated with experimental setups of modest size and complexity, light provides a natural testing ground for novel quantum phenomena. However, a fundamental result of quantum mechanics is that massive particles such as atoms should show much of the same behaviour as light, as the de Broglie hypothesis indicates that atoms should be subject to the same particle/wave duality as photons, in addition to the fact that bosonic atoms obey the same quantum statistical distribution as light. Glauber's theory of quantum coherence is therefore also appropriate for describing quantum gases [34], where interference is characterised by the overlapping of de Broglie wave packets, which for dilute gases occurs largely in the absence of electromagnetic interactions between the atoms.

While it is relatively easy to observe the interference of light macroscopically, the de Broglie wavelength for atomic systems is proportional to $T^{-1/2}$ and is typically far too small for interference effects for gases at room temperature (~ 300 K) to be measured, which corresponds to the familiar view of atoms as being 'billiard ball' particles. However, the development of the optical laser inspired significant advances in the precise manipulation of atomic species, such that gases could be cooled to temperatures of microkelvin or below, at which point interference occurs over length scales which can be

resolved on modern detectors. Success with this objective gave rise to the field of *atom optics*, in which the roles of matter and light are essentially interchanged such that light is used in addition to the application of external magnetostatic fields to cool, trap and manipulate matter waves [35].

As was mentioned earlier, a characteristic feature of the Bose-Einstein distribution is the condensation of a macroscopic portion of particles into the ground energy state of a system. For this to occur, a bosonic gas must be cooled so that the de Broglie wavelength of atoms approaches the mean inter-particle spacing such that there is significant overlap between the wave packets [36]. Condensation in dense and strongly interacting systems such as superfluid helium was identified as early as 1938 [37–39], and theory was developed to demonstrate that such a system possessed long-range order [40–43], which is a characteristic of coherence. However, while superfluids can display some interesting phenomena such as quantised vortices, condensed dilute atomic gases in which interparticle interactions are typically very small were seen as the ideal way to test the principles of quantum mechanics with massive particles. Initial work in the 1970s attempted to condense hydrogen, however it was realised that alkali metals were a better candidate for laser cooling due to their favourable electronic structure. Condensation of a dilute quantum gas this was achieved in 1995 for ^{87}Rb [44], ^{23}Na [45] and most probably ^{7}Li [46] after several decades of effort, while condensation of a variety of alkali, alkaline earth and lanthanide metals, as well as metastable helium [47, 48], soon followed. Condensation is currently a topic of much interest in other systems, such as exciton-polaritons [49] which uniquely can undergo this transition at room temperature [50], and curiously, with photons[2] [51].

It was soon demonstrated that BECs of ultracold atoms were able to exhibit the same mean-field optical effects as conventional lasers, including a high interference fringe visibility characteristic of classical coherence. Many of the standard operations of linear optics were also realised for condensed or ultracold but incoherent atomic sources via atom-light interactions, such as diffraction, reflection, beamsplitting, focusing, waveguiding and interferometry. This enables a wide range of experiments in atom optics which emulate classical optics with intense and coherent sources of light to be performed. In addition, non-linear effects such as four-wave mixing [52, 53] can be realised, which may be facilitated by the production of atomic analogues of laser beams by controllably releasing trapped atoms from a BEC.

However, the fundamental behaviour of quantum gases on a single particle level is also of interest, just as it is in the study of quantum optics for sources of light. The relatively new field of *quantum atom optics* is concerned with nonlinear and quantum statistical effects in ultracold gases, which allows effects beyond the more classically oriented mean-field behaviour to be observed. Indeed, there is a close correspondence between processes such as parametric downconversion in optics with molecular dissociation or collisions in atomic systems. While it is typically more difficult to measure single atoms with high temporal and spatial resolution than it is for photons, noble gases in a metastable excited state contain enough internal energy to be easily detected with standard micro-channel plates. Of these gases, it is only helium which can be cooled to the temperatures required for Bose-Einstein condensation, however metastable helium has proven to be an ideal atomic species for exploring quantum atom optics, as its

[2]This process requires that the system is able to rethermalise a thermal distribution of photons while conserving photon number, which does not occur for blackbody radiation or an optical laser.

small atomic mass results in a large de Broglie wavelength and thus a more pronounced wavelike behaviour.

Despite the considerable experimental difficulty in creating ultracold gases, research in quantum atom optics has progressed rapidly since the realisation of Bose Einstein condensation in dilute gases. Hanbury Brown-Twiss bunching has been observed in atomic systems [54], and Glauber's quantum definition of coherence was shown to be satisfied for BECs to second order [55], while the uniquely quantum-mechanical phenomenon of anti-bunching due to the Pauli exclusion principle was observed for a fermionic isotope of helium [56]. The latter of those results highlights the richness of quantum atom optics compared to its photonic counterpart, where the mass and internal structure of atoms add to the complexity of possible phenomena, such that atomic experiments extend beyond demonstrations of optical concepts carrying over from photonics verbatim. A variety of other phenomena such as the Mott insulator to superfluid transition [57] or the demonstration of atomic systems characterised by negative temperatures [58] are further examples of the appeal of exploring quantum mechanics with ultracold gases. Currently, atomic systems are proving to be crucial for advances in fields such as quantum computing and precision measurement, which suggests that the study of quantum atom optics will remain of interest for some time in the future.

The objective of this thesis is to develop and utilise novel techniques for observing matter-wave interference and quantum statistical effects in ultracold gases of metastable helium. The unique advantages of our experimental setup, such as the exceptionally stable magnetic and optical traps, and high-resolution single atom detector located deep in the far field to accentuate matter-wave interference, are favourable for achieving significant improvements in a variety of quantum atom optics experiments. Despite the success of previous work to demonstrate phenomena such as the Hanbury Brown-Twiss effect in atomic clouds, the experimental effort required to do so rendered such experiments inappropriate in many cases for using quantum statistical measurements as a probe to learn novel information about the quantum state of ultracold atomic systems. Several of the experiments described in this thesis describe how the signal-to-noise ratio of atomic bunching experiments can be improved concurrently with a considerable reduction in the time required to acquire experimental data. Such improvements allowed bunching measurements to break new ground for probing quantum gases in several different experiments, such as the evaluation of higher-order correlation functions, the modal structure of waveguides, and the onset of transverse condensation in an elongated trapped cloud. Several other investigations of matter-wave interference were also undertaken, which take advantage of the unique advantages of our apparatus, while additional work extended towards realising Wheeler's delayed choice experiment with massive particles for the first time.

1.1 Thesis structure

An overview of the concepts central to this thesis, including the quantum-mechanical effects to be explored in the subsequent chapters, as well as the cooling and trapping procedures used to prepare ultracold atomic samples, is provided in Chapter 2. The chapter concludes with a brief discussion of the properties of metastable helium, the species of choice for the experiments performed, which articulates the unique advantages of its use in quantum atom optical experiments. This is followed by a description

of the experimental setup in Chapter 3, which covers the implementation of the cooling and trapping techniques introduced in the previous chapter, and the generation of atom lasers from magnetic and optical traps, which plays a key role in several experimental results. Of particular importance is our detection systems for measuring individual atoms with high resolution in up to three dimensions, such that statistical measurements requiring single atom counting can be performed.

Chapter 4 describes the development of several methods for measuring Hanbury Brown-Twiss quantum correlations. The experimental results presented in this chapter range from a demonstration of the contrast between the quantum statistics of a thermal source and a pulsed atom laser, to the first measurement of long-range three-body correlation functions and the confirmation that BECs are coherent to at least third order. Following this are experiments which greatly improve both the signal-to-noise and data acquisition rates of quantum correlation measurements, such that higher-order correlation functions can easily be measured for clouds in a variety of trapping configurations. This culminates in the observation of thermal bunching up to sixth-order in the ideal limit which is no longer hampered by statistical errors or imperfect detector resolution. These new experimental techniques are then utilised in Chapter 5 to enable a subsequent experiment where correlation measurements revealed unique information about quantum systems, such as the observation of transverse condensation as an elongated Bose gas is cooled.

A variety of investigations of macroscopic matter-wave interference are detailed in Chapter 6. The production of a far-field diffraction pattern by imaging an atom laser on a microscopy diffraction mask appears to be a promising method for calculating the Wigner function of a coherent quantum gas. The modal profile of ultracold gases guided with an optical potential was also explored by either decomposing the transverse density profile of a matter wave which is predominantly loaded into a single higher-order mode of the confining potential, or with correlation measurements which illustrate the contrast between guided atom laser and thermal gases which may otherwise be indistinguishable.

Finally, a new method which aims to realise Wheeler's delayed-choice *gedankenexperiment* is presented in Chapter 7, which includes the development of an interferometer for single ultracold atoms, and preliminary results which suggest the potential success of this approach are discussed. While this experiment is yet to be completed due to painstaking stability demands[3], it not only represents an opportunity to test fundamental quantum-mechanical concepts such as complementarity, but also leads to further similar experiments which could investigate topics such as the Hong-Ou-Mandel effect and Bell's test of quantum entanglement with massive particles.

1.2 List of publications

The work described in this thesis resulted in the following publications:

- A. G. Manning, S. S. Hodgman, R. G. Dall, M. T. Johnsson, and A. G. Truscott, "The Hanbury Brown-Twiss effect in a pulsed atom laser," *Optics Express* **18**, 18712 (2010) [59].

[3] After the submission of this thesis, further work by the ANU group has brought this experiment to completion.

- S. S. Hodgman, R. G. Dall, A. G. Manning, K. G. H. Baldwin, and A. G. Truscott, "Direct measurement of long-range third-order coherence in Bose-Einstein condensates," *Science* **331**, 1046 (2011) [60].
- R. G. Dall, S. S. Hodgman, A. G. Manning, and A. G. Truscott, "Observation of the first excited transverse mode in guided matter waves," *Optics Letters* **36**, 1131 (2011) [61].
- R. G. Dall, S. S. Hodgman, A. G. Manning, M. T. Johnsson, K. G. H. Baldwin, and A. G. Truscott, "Observation of atomic speckle and Hanbury Brown-Twiss correlations in guided matter waves," *Nature Communications* **2**, 291 (2011) [62].
- A. G. Manning, W. RuGway, S. S. Hodgman, R. G. Dall, K. G. H. Baldwin, and A. G. Truscott, "Third-order spatial correlations for ultracold atoms," *New Journal of Physics* **15**, 013042 (2013) [63].
- R. G. Dall, A. G. Manning, S. S. Hodgman, Wu RuGway, K. V. Kheruntsyan, and A. G. Truscott, "Ideal n-body correlations with massive particles," *Nature Physics* **9**, 341 (2013) [64].
- Wu RuGway, A. G. Manning, S. S. Hodgman, R. G. Dall, A. G. Truscott, T. Lamberton, and K. V. Kheruntsyan, "Observation of Transverse Bose-Einstein Condensation via Hanbury Brown-Twiss Correlations," *Physical Review Letters* **111**, 093601 (2013) [65].
- A. G. Manning, R. Khakimov, R. G. Dall, and A. G. Truscott, "A Source of Single Metastable Atoms in the Nanokelvin Regime," *Physical Review Letters* **113**, 130403 (2014) [66].
- A. G. Manning, R. Khakimov, R. G. Dall, and A. G. Truscott, "Wheeler's Delayed Choice *Gedankenexperiment* with a Single Atom," under review (2014).

Chapter 2

Background theory

The central theme of this thesis will be the study of quantum atom optics, where effects typically associated with light are observed with massive particles. This essentially exchanges the roles of matter and light with regards to standard quantum optics experiments, where light is now used to manipulate matter waves such that phenomena including interference can be measured. Not only does this provide the opportunity to test fundamental quantum mechanics with massive bodies containing internal structure, but also allows a range of novel effects not possible for photons to be investigated. As the field of ultracold atomic physics has matured and expanded significantly over the last few decades, the cooling and trapping of quantum gases has become relatively routine, and consequently will not be covered comprehensively here due to the range of review publications available which are cited as appropriate throughout this chapter. This chapter will therefore only provide a brief overview of the processes required to produce quantum gases which are sufficiently coherent for wave-like properties of matter to be apparent, including the phenomenon of Bose-Einstein condensation, which is the atomic analogue of an optical laser. However, the unique quantum-mechanical effects which will be the focus of the results presented in this thesis are explored in more detail.

2.1 The quantum nature of light and atoms

The development of quantum physics has required the revision of many classical theories. In some cases, this seems to occur as an extension of existing ideas, however at their heart quantum effects cannot generally be reconciled with our intuitive understanding of nature. In particular, while coherence can be understood in a classical sense, a fully quantum-mechanical treatment leads to not only fundamental change in the definition of coherence, but also the possibility of observing many highly non-classical effects. Furthermore, due to a perceived need to associate interpretations with quantum theory, analysis of the role of measurement of a quantum system has uncovered many apparent paradoxes, the discussion of which has lead to improvements in our understanding of quantum processes.

This chapter begins with a discussion of the two driving themes of this thesis: quantum correlation functions, which can be used to quantify the coherence of ultracold atomic gases; and Wheeler's delayed choice *gedankenexperiment*, which highlights the importance of complementarity in the understanding of quantum behaviour. Although theoretical discussions of such topics could constitute theses in their own right, an emphasis will be placed on experimental considerations, and this section serves as a primer

for the chapters that follow which describe experiments aiming to measure these phenomena.

2.1.1 Development of quantum optics – the Hanbury Brown-Twiss effect and correlation functions

Interferometry is a widely used technique for making accurate measurements on microscopic scales, with applications ranging from the famous Michelson-Morley experiment which disproved the existence of luminiferous ether [67], to modern studies of metrology, surface testing, and the search for gravity waves. After the invention of the optical laser in the 1950s, techniques of laser cooling (discussed in §2.2) were developed to slow atoms such that their de Broglie wavelengths become significant, and matter-wave interference can be observed. Interferometry of ultracold neutral atoms is currently an active area of research, where for example the precision of atomic clocks and gravitation sensors are improving in a remarkable manner.

Interferometry is usually thought of as the consequence of wave superposition, the most obvious example of which being Young's double-slit experiment, which allows the interference of sub-millimetre wavelength light to be observed on a macroscopic scale. A key characteristic of the stationary interference pattern seen for an interferometer is its fringe visibility

$$V = \frac{I_{\max} - I_{\min}}{I_{\max} + I_{\min}}, \tag{2.1}$$

which compares the highest intensity $I_{\max}$ and lowest intensity $I_{\min}$ of the interference pattern. In the classical theory of wave interference, the visibility reveals the coherence of the wave source, where a completely coherent source has a perfectly resolved wave interference pattern and $V = 1$, while a completely incoherent source does not show any interference whatsoever and $V = 0$. Essentially, this depends on the spectral linewidth of the source, where monochromatic light results an a high-visibility pattern, while interference washes out for broadband light.

Classical fringe (first-order) correlation functions

The use of fringe visibility to determine classical wave coherence can be extended to the notion of correlation functions, which measure how well a source of waves retains its state over distance or time. Light is treated classically as a continuous wave, where the wave amplitudes for two or more nearby points in time or space are linked by having the same phase and fluctuations. On the other hand, the correlation between these points decreases at larger temporal or spatial separations for incoherent light, until different locations in the wave become independent and show no interference [13]. Before the invention of the laser, any source of light had a spectral shape with a finite width, and the Fourier transform of this sets the separations over which correlations can occur.

A monochromatic plane wave of light with wavevector $\mathbf{k} = 2\pi\hat{\mathbf{k}}/\lambda$ for wavelength λ is considered to be a continuous, oscillating electric field $\mathbf{E}(\mathbf{r}, t) = \mathbf{E}_0 \cos(\mathbf{k} \cdot \mathbf{r} - \omega t)$, while any arbitrary waveform can be composed from a linear superposition of plane waves. If we take the amplitude of any such arbitrary electric field to be $E(\mathbf{r}, t)$, with an intensity $I(\mathbf{r}, t) = E^*(\mathbf{r}, t)E(\mathbf{r}, t)$, we can define the first-order correlation function which

compares the wave between spatial positions $\mathbf{r}_1$ and $\mathbf{r}_2$ and times t_1 and t_2 as [13]

$$G^{(1)}(\mathbf{r}_1, t_1; \mathbf{r}_2, t_2) = \langle E^*(\mathbf{r}_1, t_1) E(\mathbf{r}_2, t_2) \rangle \,, \tag{2.2}$$

where the angular brackets signify an average over time and space. Furthermore, this function can be normalised to remove the dependence on the bulk intensity, to

$$g^{(1)}(\mathbf{r}_1, t_1; \mathbf{r}_2, t_2) = \frac{G^{(1)}(\mathbf{r}_1, t_1; \mathbf{r}_2, t_2)}{\langle E^*(\mathbf{r}_1, t_1) \rangle \langle E(\mathbf{r}_2, t_2) \rangle}. \tag{2.3}$$

For situations such as the commonly used Michelson interferometer, where the average light intensity is constant in time and we want to compare the relative behaviour between positions $\mathbf{r}$ and $\mathbf{r} + \Delta\mathbf{r}$, Eq. 2.3 simplifies to

$$g^{(1)}(\Delta\mathbf{r}) = \frac{\langle E^*(\mathbf{r}) E(\mathbf{r} + \Delta\mathbf{r}) \rangle}{\langle E^*(\mathbf{r}) \rangle \langle E(\mathbf{r} + \Delta\mathbf{r}) \rangle}. \tag{2.4}$$

If the average intensity of the light is spatially uniform, then $V = \max\{|g^{(1)}(\Delta\mathbf{r})|\}$. Similarly, measuring correlations in photocurrent between times t and $t + \tau$ can be written $g^{(1)}(\tau) = \langle E^*(t) E(t + \tau) \rangle / \left[\langle E^*(t) \rangle \langle E(t + \tau) \rangle \right]$, where in this case spatial information is not considered.

Initial attempts to measure the angular size of distant stars made use of Michelson-type interferometers, where this angle results in a phase shift between light travelling along different paths from the star to the interferometer. For time-independent illumination, the angle ϕ between two wavevectors $\mathbf{k}_1 = k\hat{\mathbf{k}}_1$ and $\mathbf{k}_2 = k\hat{\mathbf{k}}_2$ for plane waves $E_{\mathbf{k}_j}$ ($j = 1, 2$) with $\langle E_{\mathbf{k}_j} \rangle = 0$ and $\langle E_{\mathbf{k}_j} E_{\mathbf{k}_n} \rangle = \delta_{jn} I_0$ emanating from the star can be determined from [68]

$$\begin{aligned} G^{(1)}(\Delta\mathbf{r}) &\propto I_0 \left\{ 1 + \frac{1}{4} \cos\left[(\mathbf{k}_1 + \mathbf{k}_2) \cdot \Delta\mathbf{r} \right] \cos\left[(\mathbf{k}_1 - \mathbf{k}_2) \cdot \Delta\mathbf{r} \right] \right\}, \\ &\approx I_0 \left\{ 1 + \frac{1}{4} \cos\left[(\mathbf{k}_1 + \mathbf{k}_2) \cdot \Delta\mathbf{r} \right] \cos\left[\frac{\pi \left| \Delta\mathbf{r} \right| \phi}{\lambda} \right] \right\}. \end{aligned} \tag{2.5}$$

However, the term proportional to $(\mathbf{k}_1 + \mathbf{k}_2) \cdot \Delta\mathbf{r}$ in Eq. 2.5 is highly susceptible to mechanical and atmospheric instabilities, which compromises the usefulness of this approach.

Intensity (second-order) correlations

To circumvent the limitations of first-order interferometry encountered as a result of Eq. 2.5, Robert Hanbury Brown and Richard Twiss borrowed the idea of intensity interferometry from radio astronomy, and applied it to optical measurements. Instead of interfering light on the wavelength scale, as occurs for a Michelson-type interferometer, correlations are computed between the photocurrents measured on two individual detectors. Although the amplitude and phase of photons incident on the two detectors will vary considerably, within the coherence length of the source the intensity fluctuations will be correlated in the same way as for first-order correlations.

Analogously to Eqs. 2.2 and 2.3, we can define unnormalised and normalised

second-order correlation functions

$$G^{(2)}(\mathbf{r}_1,t_1;\mathbf{r}_2,t_2) = \langle E^*(\mathbf{r}_1,t_1)E^*(\mathbf{r}_2,t_2)E(\mathbf{r}_2,t_2)E(\mathbf{r}_1,t_1)\rangle$$
$$= \langle I(\mathbf{r}_1,t_1)I(\mathbf{r}_2,t_2)\rangle\,, \tag{2.6}$$
$$g^{(2)}(\mathbf{r}_1,t_1;\mathbf{r}_2,t_2) = \frac{\langle I(\mathbf{r}_1,t_1)I(\mathbf{r}_2,t_2)\rangle}{\langle I(\mathbf{r}_1,t_1)\rangle\,\langle I(\mathbf{r}_2,t_2)\rangle}, \tag{2.7}$$

while simplified forms which consider correlations in separations of one variable can be made in a similar fashion to that of Eq. 2.4. As can be seen in Eq. 2.6, the relative phase between the arms of the interferometer for the fields E_1 and E_2 determines the value of the second-order correlation function, even though the absolute phase of the light is not measured directly. This means that measurements of the second-order correlation function are far less sensitive to the instabilities than Michelson-type interferometers. Indeed, if we replicate the reasoning for a plane wave source in Eq. 2.5 for second-order correlations, we arrive at [68]

$$G^{(2)}(\Delta\mathbf{r}) \propto I_0^2\left\{1+\frac{1}{2}\cos\left[(\mathbf{k}_1-\mathbf{k}_2)\cdot\Delta\mathbf{r}\right]\right\}, \tag{2.8}$$

where the term proportional to $(\mathbf{k}_1+\mathbf{k}_2)\cdot\Delta\mathbf{r}$ has now been eliminated. If instabilities do occur, their effect on the measurement will be minimised by the common mode between $\mathbf{k}_1$ and $\mathbf{k}_2$.

Incoherent sources of bosons such as light from a star will exhibit a phenomenon referred to as bunching, which results in enhanced intensity fluctuations in coincidence measurements for separations within the correlation time or length. This effect can be understood in a classical sense by analysing the light intensity measured on the two detectors $I(t_j)$ $(j=1,2)$, where a path length difference[1] induces a time lag $t_1-t_2=\tau$ between the two arms. The measured intensity $I(t)=\langle I\rangle+\delta I(t)$ can be decomposed into an average intensity $\langle I\rangle$ and a term containing fluctuations $\delta I(t)$. These fluctuations average in time to zero $\langle\delta I(t)\rangle=0$, and correlations are seen between the two arms for values of τ smaller than the correlation time t_c such that $\langle\delta I(t)\delta I(t+\tau)\rangle\neq 0$ due to the local coherence of the wave, while for $\tau\gg t_c$ the correlation disappears and $\langle\delta I(t)\delta I(t+\tau)\rangle=0$. Thus, the behaviour of the classical second-order correlation function can be characterised by

$$g^{(2)}(\tau) = \frac{\langle I(t)I(t+\tau)\rangle}{\langle I(t)\rangle^2},$$
$$\approx \begin{cases} \frac{\langle I^2+\delta I(t)^2\rangle}{\langle I\rangle^2} > 1 & \tau \lesssim t_c, \\ 1 & \tau \gg t_c, \end{cases} \tag{2.9}$$

where bunching is signified by $g^{(2)}(\tau)>1$. A basic property of this second-order correlation function is its symmetry where $g^{(2)}(\tau)=g^{(2)}(-\tau)$, while the Cauchy–Schwarz inequality bounds the function such that $g^{(2)}(0)\geq g^{(2)}(\tau)\geq 1$.

Intensity interferometry for classical radio waves was a well established method prior to the work of Hanbury Brown and Twiss, who believed that a similar technique would

[1] Since the two photocurrents are not necessarily mixed before being recorded, any arbitrary time difference can be achieved in post-processing of the data.

apply for optical interferometry. Indeed, they succeeded in demonstrating this bunching effect which later bore their name in a proof of principle table-top experiment using a mercury arc lamp [69], before applying it in a measurement of the angular size of Sirius [31]. However, it was not long before serious doubt was cast over the validity of this result[2], which is often attributed to being the consequence of a quote from Dirac [71] stating that

> each photon ... interferes only with itself. Interference between two different photons never occurs.

In particular, Brannen and Ferguson [72] among others claimed that bunching was not observable in their experiments which also attempted to measure Hanbury Brown-Twiss bunching. A resolution to this was provided by Purcell [73], who concluded that the bandwidth of Brannen and Ferguson's light source, which determines its correlation length, resulted in a bunching signal which was too small to be observed given their experimental parameters, but was nevertheless present. Even Dirac's famous quote, which is appropriate for describing average interference, was shown to be misleading by Mandel [74, 75] in experiments which clearly demonstrated that instantaneous interference between two independent beams could occur.

Quantum correlation functions

The invention of the optical laser in the 1950s provided a new source of light with coherence properties which far surpassed any other available sources. It was realised that a full quantum-mechanical treatment of coherence was required to understand this, where light must be considered as individual photons as opposed to continuous classical waves. A description of the Hanbury Brown-Twiss effect for particles was provided by Fano [76], which considered the measurement of two particles described by the states $|a\rangle$ and $|b\rangle$ on a pair of detectors $\langle 1|$ and $\langle 2|$. Assuming the two detectors have the same behaviour, the probability amplitude of measuring particle $|a\rangle$ is $\langle 1\,|a\rangle = \langle 2\,|a\rangle = A$, and similarly $\langle 1\,|b\rangle = \langle 2\,|b\rangle = B$. If we attempt to measure two distinguishable particles, such as those separated by a large enough time or distance that they do not interfere, then the probability of measuring a single particle on each detector is

$$P_{\text{dist}} = |\langle 1|a\rangle\,\langle 2|b\rangle|^2 + |\langle 2|a\rangle\,\langle 1|b\rangle|^2 = 2\,|A|^2\,|B|^2\,. \tag{2.10}$$

However, when the pair of detectors are within the correlation length of the particles such that interference does occur, bosons become indistinguishable, and due to the symmetry of their overall wavefunction we find that

$$P_{\text{bosons}} = |\langle a|1\rangle\,\langle b|2\rangle + \langle a|2\rangle\,\langle b|1\rangle|^2 = |2AB|^2 = 2P_{\text{dist}}. \tag{2.11}$$

On the other hand, the parity of fermion wavefunctions leads to the famous Pauli exclusion principle, giving the highly non-classical result of

$$P_{\text{fermions}} = |\langle a|1\rangle\,\langle b|2\rangle - \langle a|2\rangle\,\langle b|1\rangle|^2 = 0, \tag{2.12}$$

[2] A history of the development of the now-famous Hanbury Brown-Twiss effect was written by Robert Hanbury Brown [70].

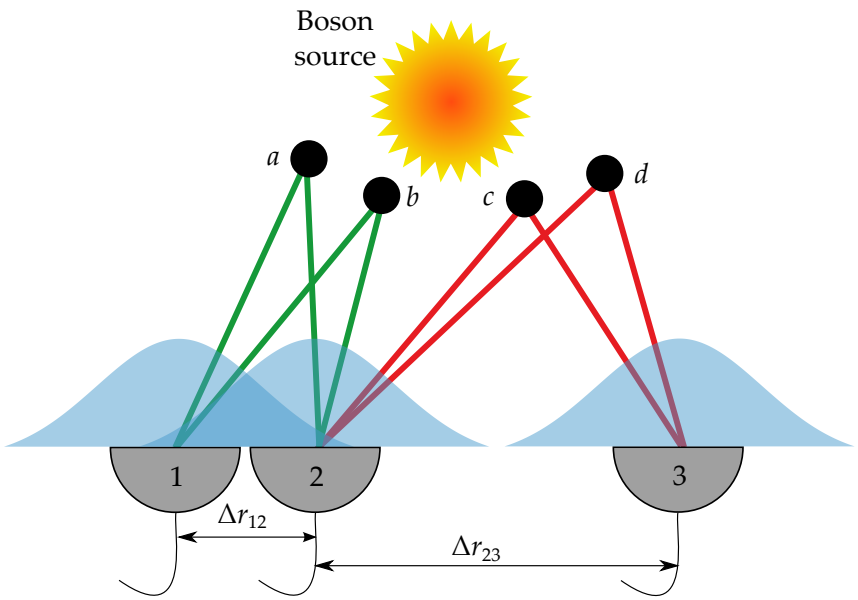

Figure 2.1: If a pair of photons (a and b) from a source such as a star are measured such that one falls on each of two detectors (1 and 2), and these detectors are separated by less than the correlation length of the source (r_{12} is less than the size of the wave packets shown in blue), then bunching will be observed due to the interference of the two particles as they are recorded. However, if another two photons (c and d) arrive on two detectors (2 and 3) which are separated by a distance r_{23} larger than the correlation length, the particles remain distinguishable and no bunching will be seen.

which is in clear violation of the Cauchy-Schwartz inequality. It is important to note that only the behaviour of the two particles at the detector influences whether interference occurs, irrespective of the separation at the source, which for example allows the size of an extended source such as a distant star to be measured. This is shown in Fig. 2.1.

However, a theory was needed to distinguish between monochromatic light which could be produced by a lamp, and the truly coherent output of a laser. Glauber, in his landmark theory of quantum statistics [32], addressed this by defining nth order correlation functions for quantum fields, which described the probability of coincidence measurements of n particles separated in time or space. In doing so, a true definition of coherence requiring coherence to all orders $n \in \mathbb{N}$ was established, which distinguished laser light from thermal light which can only possibly be coherent to first order. This definition, which formally eliminated the condition for monochromaticity, also had the important consequence that it did not require stationary states and allows for any arbitrary time dependence for the fields. Therefore, coherence can occur for sources with non-uniform and time-dependent density profiles, which will be of particular importance for the atomic measurements described in this thesis.

The results derived from Glauber's theory had two main consequences, which were to provide a solid quantum-mechanical framework to support the conclusions of the semi-classical treatment of the Hanbury Brown-Twiss effect, while providing an explanation of effects which cannot be understood in the context of classical theory. A synopsis of this theory will be presented here, which was originally developed to describe light, but will prove equally applicable to quantum gases.

As was the case for the classical treatment, correlations in the electric field of light

$\mathbf{E}(\mathbf{r},t)$ will be calculated. This field can be split into positive $\mathbf{E}^{(+)}(\mathbf{r},t)$ and negative $\mathbf{E}^{(-)}(\mathbf{r},t)$ frequency components such that $\mathbf{E}(\mathbf{r},t)=\mathbf{E}^{(+)}(\mathbf{r},t)+\mathbf{E}^{(-)}(\mathbf{r},t)$, where the two frequency components are the adjoint of one another and represent the annihilation and creation of a single photon respectively. The transition rate between an initial state $|i\rangle$ and a final state $|f\rangle$ is proportional to the matrix element $\langle f|\mathbf{E}^{(+)}(\mathbf{r},t)|i\rangle$ by Fermi's golden rule, where

$$\begin{aligned}\sum_f \left|\left\langle f\left|\mathbf{E}^{(+)}(\mathbf{r},t)\right|i\right\rangle\right|^2 &= \sum_f \left\langle i\left|\mathbf{E}^{(-)}(\mathbf{r},t)\right|f\right\rangle\left\langle f\left|\mathbf{E}^{(+)}(\mathbf{r},t)\right|i\right\rangle, \\ &= \left\langle i\left|\mathbf{E}^{(-)}(\mathbf{r},t)\mathbf{E}^{(+)}(\mathbf{r},t)\right|i\right\rangle. \end{aligned} \tag{2.13}$$

It is important to note that the average of $\mathbf{E}^{(-)}(\mathbf{r},t)\mathbf{E}^{(+)}(\mathbf{r},t)$ is the 'intensity' quantity measured by a detector, rather than $\mathbf{E}(\mathbf{r},t)^2$ which fails to account for vacuum states.

This can be extended to a measurement of the correlation of the field on several detectors at different points $\mathbf{r}_1$ and $\mathbf{r}_2$ and times t_1 and t_2. Such a measurement is proportional to the matrix elements $\langle f|\mathbf{E}^{(+)}(\mathbf{r}_2,t_2)\mathbf{E}^{(+)}(\mathbf{r}_1,t_1)|i\rangle$, giving a transition rate proportional to

$$\sum_f \left|\left\langle f\left|\mathbf{E}^{(+)}(\mathbf{r}_2,t_2)\mathbf{E}^{(+)}(\mathbf{r}_1,t_1)\right|i\right\rangle\right|^2 = \left\langle i\left|\mathbf{E}^{(-)}(\mathbf{r}_1,t_1)\mathbf{E}^{(-)}(\mathbf{r}_2,t_2)\mathbf{E}^{(+)}(\mathbf{r}_2,t_2)\mathbf{E}^{(+)}(\mathbf{r}_1,t_1)\right|i\right\rangle. \tag{2.14}$$

This is the basis of understanding the Hanbury Brown-Twiss effect, which measures a pair of particles at position and time coordinates $(\mathbf{r}_1,t_1)$ and $(\mathbf{r}_2,t_2)$ with the application of the annihilation operator $\mathbf{E}^{(+)}$. Furthermore, this can be generalised to n-fold coincidence count rates for $n\in\mathbb{N}$ as

$$\left\langle i\left|\mathbf{E}^{(-)}(\mathbf{r}_1,t_1)\mathbf{E}^{(-)}(\mathbf{r}_2,t_2)\ldots\mathbf{E}^{(-)}(\mathbf{r}_n,t_n)\mathbf{E}^{(+)}(\mathbf{r}_n,t_n)\ldots\mathbf{E}^{(+)}(\mathbf{r}_2,t_2)\mathbf{E}^{(+)}(\mathbf{r}_1,t_1)\right|i\right\rangle. \tag{2.15}$$

While this reasoning has so far only considered pure states, determining the statistical distribution of a source means that the exact field is not well known, but is characterised by a density matrix $\hat{\rho}$. This represents the average over the unknown parameters of a distribution of pure states $|\psi\rangle$ such that $\hat{\rho}=\{|\psi\rangle\langle\psi|\}_{\text{av}}$, and is appropriate for describing thermal sources of light such as stars or lamps. Given that the expectation value of any operator $\hat{O}$ is $\langle\hat{O}\rangle=\text{tr}\{\hat{\rho}\hat{O}\}$, where $\text{Tr}\{\hat{O}\}$ denotes the trace of $\hat{O}$, we can generalise Eq. 2.14 to

$$G^{(1)}(\mathbf{r}_1,t_1;\mathbf{r}_2,t_2)=\text{tr}\left\{\hat{\rho}\mathbf{E}^{(-)}(\mathbf{r}_1,t_1)\mathbf{E}^{(+)}(\mathbf{r}_2,t_2)\right\}. \tag{2.16}$$

This is the (unnormalised) first-order correlation function, and the quantum counterpart of the classical correlation function Eq. 2.2. Extending this to higher orders $n\in\mathbb{N}$ gives

$$\begin{aligned}G^{(n)}(\mathbf{r}_1,t_1;\ldots;\mathbf{r}_n,t_n;\mathbf{r}_{n+1},t_{n+1};\ldots\mathbf{r}_{2n},t_{2n}) = \\ \text{Tr}\left\{\hat{\rho}\mathbf{E}^{(-)}(\mathbf{r}_1,t_1)\ldots\mathbf{E}^{(-)}(\mathbf{r}_n,t_n)\mathbf{E}^{(+)}(\mathbf{r}_{n+1},t_{n+1})\ldots\mathbf{E}^{(+)}(\mathbf{r}_{2n},t_{2n})\right\}.\end{aligned} \tag{2.17}$$

Normalising these functions to

$$g^{(n)}(\mathbf{r}_1,t_1;\ldots;\mathbf{r}_n,t_n;\mathbf{r}_{n+1},t_{n+1};\ldots;\mathbf{r}_{2n},t_{2n}) = \frac{G^{(n)}(\mathbf{r}_1,t_1;\ldots;\mathbf{r}_n,t_n;\mathbf{r}_{n+1},t_{n+1};\ldots\mathbf{r}_{2n},t_{2n})}{\prod_{j=1}^{2n}\left[G^{(1)}(\mathbf{r}_j,t_j;\mathbf{r}_j,t_j)\right]^{1/2}}, \tag{2.18}$$

gives the normalised probability of measuring n particles at positions and times $(\mathbf{r}_1,t_1)$, $(\mathbf{r}_2,t_2)$, …, $(\mathbf{r}_n,t_n)$ respectively, such that a measurement of $g^{(n)}(0,\ldots,0)=1$ means that the ensemble follows an uncorrelated Poissonian distribution, while $g^{(n)}(0,\ldots,0)>1$ implies that particles prefer to 'bunch' together.

While the property that $0 \leq |g^{(1)}(\mathbf{r}_1,t_1;\mathbf{r}_2,t_2)| \leq 1$ carries over from the classical case, higher-order correlation functions have the property of $g^{(n)}(\mathbf{r}_1,t_1;\ldots;\mathbf{r}_n,t_n;\mathbf{r}_{n+1},t_{n+1};\ldots\mathbf{r}_{2n},t_{2n}) \geq 1$ for statistical distributions of bosons under most circumstances. This serves as the basis of the definition of a fully coherent field, which requires that for all $n\in\mathbb{N}$,

$$\left|g^{(n)}(\mathbf{r}_1,t_1;\ldots;\mathbf{r}_n,t_n;\mathbf{r}_{n+1},t_{n+1};\ldots\mathbf{r}_{2n},t_{2n})\right| = 1. \tag{2.19}$$

It is immediately obvious that plane waves, which are the archetype of a classically coherent source, satisfy this condition, while other sources are not excluded from also doing so.

This definition of coherence is also capable of differentiating between incoherent sources, such as monochromatic thermal light which is capable of forming interference patterns in the manner of Young's experiment, and fully coherent sources such as lasers which satisfy the requirements of Eq. 2.19. In particular, classically coherent sources will only satisfy this condition for $n=1$, and are thus considered to be coherent to first order, but not fully coherent. A consequence of Eq. 2.19 is that the numerator and denominator of Eq. 2.18 must be equal for a coherent state, which means that the count rate measured on the individual detectors are statistically independent for coherent states. Therefore, fields which are eigenstates of the annihilation operator $\mathbf{E}^{(+)}$ (which is indeed a well-known characteristic of coherent states in the sense of minimising Heisenberg uncertainty) imply coherence automatically. Conversely, incoherent sources of bosons such as those used by Hanbury Brown and Twiss to demonstrate bunching result in a positive correlation for small separations, such that interference occurs and $g^{(2)}(\mathbf{r},t;\mathbf{r},t+\tau)>1$ for small τ within the correlation time of the source.

Hanbury Brown-Twiss bunching can be examined by simplifying the second-order correlation function to consider temporal measurements of stationary pure boson modes represented by the annihilation operator $\hat{a}$ and creation operator $\hat{a}^\dagger$. The probability of detecting a second particle a time delay τ after a previous one is

$$g^{(2)}(\tau) = \frac{\left\langle \hat{a}^\dagger(0)\hat{a}^\dagger(\tau)\hat{a}(\tau)\hat{a}(0)\right\rangle}{\left\langle \hat{a}^\dagger(0)\hat{a}(0)\right\rangle^2}. \tag{2.20}$$

By taking $\tau=0$, and recalling the commutator relation for bosons $\left[\hat{a},\hat{a}^\dagger\right]=1$, this can be

further simplified to

$$\begin{aligned} g^{(2)}(0) &= \frac{\left\langle \hat{a}^\dagger(\hat{a}\hat{a}^\dagger - 1)\hat{a} \right\rangle}{\left\langle \hat{a}^\dagger\hat{a} \right\rangle^2}, \\ &= \frac{\left\langle \hat{a}^\dagger\hat{a} \right\rangle^2 + \left\langle \left(\hat{a}^\dagger\hat{a}\right)^2 \right\rangle - \left\langle \hat{a}^\dagger\hat{a} \right\rangle^2 - \left\langle \hat{a}^\dagger\hat{a} \right\rangle}{\left\langle \hat{a}^\dagger\hat{a} \right\rangle^2}, \\ &= 1 + \frac{\sigma_{\bar{N}}^2 - \bar{N}}{\bar{N}^2}, \end{aligned} \tag{2.21}$$

where the expectation number of bosons is $\bar{N} = \langle \hat{a}^\dagger\hat{a} \rangle$, and the variance in number is $\sigma_{\bar{N}}^2 = \langle (\hat{a}^\dagger\hat{a})^2 \rangle - \langle \hat{a}^\dagger\hat{a} \rangle^2$.

The correlation function of different sources can therefore be determined from the statistical distribution of particle number. For example, a chaotic black-body light source has $\sigma_{\bar{N}}^2 = \bar{N}^2 - \bar{N}$, which leads to the bunching seen according to the Hanbury Brown-Twiss effect where $g^{(2)}(0) = 2$. On the other hand, coherent sources such as lasers have $\sigma_{\bar{N}}^2 = \bar{N}$ and thus $g^{(2)}(0) = 1$ as expected. Non-classical states can have correlation functions which deviate from the predictions of classical wave theory, where for example number (Fock) states have $\sigma_{\bar{N}}^2 = 0$ and their correlation function shows the unique property of 'anti-bunching' where $g^{(2)}(0) = 1 - 1/\bar{N} < 1$. Similarly, fermions have $0 \leq g^{(2)}(0) \leq 1$ due to the substitution of the bosonic commutator for a fermionic anticommutator.

Higher-order correlation functions for thermal sources

Correlation functions rapidly become cumbersome at higher orders, however Wick's theorem [77] allows functions for $n \geq 2$ to be simplified to products of first-order correlation functions for thermal distributions. First, we recall that the first-order correlation function for pure stationary modes $\hat{a}$ are $G^{(1)}(\mathbf{r}_1, t_1; \mathbf{r}_2, t_2) = \langle \hat{a}^\dagger(\mathbf{r}_1, t_1)\hat{a}(\mathbf{r}_2, t_2) \rangle$, where the particle density is $\rho(\mathbf{r}_i, t_i) = \left\langle \hat{a}^\dagger(\mathbf{r}_i, t_i)\hat{a}(\mathbf{r}_i, t_i) \right\rangle$. To apply Wick's theorem, it is important to recognise the distinction between the second-order correlation function, which is

$$\begin{aligned} \left\langle \hat{a}^\dagger(\mathbf{r}_1, t_1)\hat{a}^\dagger(\mathbf{r}_2, t_2)\hat{a}(\mathbf{r}_2, t_2)\hat{a}(\mathbf{r}_1, t_1) \right\rangle &= \left\langle \hat{a}^\dagger(\mathbf{r}_1, t_1)\hat{a}(\mathbf{r}_1, t_1)\hat{a}^\dagger(\mathbf{r}_2, t_2)\hat{a}(\mathbf{r}_2, t_2) \right\rangle \\ &\quad - \left\langle \hat{a}^\dagger(\mathbf{r}_1, t_1)\hat{a}(\mathbf{r}_1, t_1) \right\rangle \delta(\mathbf{r}_1 - \mathbf{r}_2)\delta(t_1 - t_2), \end{aligned} \tag{2.22}$$

and density-density correlations, which are described by the $\langle \hat{a}^\dagger(\mathbf{r}_1, t_1)\hat{a}(\mathbf{r}_1, t_1)\hat{a}^\dagger(\mathbf{r}_2, t_2)\hat{a}(\mathbf{r}_2, t_2) \rangle$ term in Eq. 2.22. However, the second term in Eq. 2.22, which represents density autocorrelations, is generally negligible and can be ignored in the high temperature limit. Therefore, the theoretical second-order correlation function is essentially equivalent to density-density correlations, which is what is measured experimentally.

Following on from this (the detail of this derivation have been relegated to the Appendix §A.2), the application of Wick's theorem to the second order correlation function simplifies it to

$$g^{(2)}(\mathbf{r}_1, t_1; \mathbf{r}_2, t_2) = 1 + \frac{\left| G^{(1)}(\mathbf{r}_1, t_1; \mathbf{r}_2, t_2) \right|^2}{\rho(\mathbf{r}_1, t_1)\rho(\mathbf{r}_2, t_2)}. \tag{2.23}$$

This can be extended further to the third-order correlation function, which is

$$g^{(3)}(\mathbf{r}_1,t_1;\mathbf{r}_2,t_2;\mathbf{r}_3,t_3) = 1 + \frac{\left|G^{(1)}(\mathbf{r}_1,t_1;\mathbf{r}_2,t_2)\right|^2}{\rho(\mathbf{r}_1,t_1)\rho(\mathbf{r}_2,t_2)} + \frac{\left|G^{(1)}(\mathbf{r}_2,t_2;\mathbf{r}_3,t_3)\right|^2}{\rho(\mathbf{r}_2,t_2)\rho(\mathbf{r}_3,t_3)} + \frac{\left|G^{(1)}(\mathbf{r}_3,t_3;\mathbf{r}_1,t_1)\right|^2}{\rho(\mathbf{r}_3,t_3)\rho(\mathbf{r}_1,t_1)} + 2\Re\left\{\frac{G^{(1)}(\mathbf{r}_1,t_1;\mathbf{r}_2,t_2)G^{(1)}(\mathbf{r}_2,t_2;\mathbf{r}_3,t_3)G^{(1)}(\mathbf{r}_3,t_3;\mathbf{r}_1,t_1)}{\rho(\mathbf{r}_1,t_1)\rho(\mathbf{r}_2,t_2)\rho(\mathbf{r}_3,t_3)}\right\}, \tag{2.24}$$

several measurements of which will be presented in Chapter 4. Decompositions of correlation functions up to any arbitrary order of n follow in a similar way (functions up to $n = 4$ are derived in §A.2), however a pattern emerges as a consequence of Wick's theorem, such that the maximum bunching amplitude is $g^{(n)}(0,\ldots,0) = n!$ for the nth order correlation function of an incoherent source. A key result of this thesis is the measurement of correlation functions up to order $n = 6$ (described in §4.5) for an incoherent gas of bosons, the results of which illustrate this relationship.

Correlation measurements with matter

Matter is composed of massive particles, which can interfere as waves according to the de Broglie hypothesis. Therefore, the concepts of coherence and the computation of correlation functions for light carry over directly to describe quantum systems of massive particles. Dilute ultracold quantum gases are particularly conducive to correlation measurements, as cold temperatures lead to substantial de Broglie wavelengths of atoms, and incoherent thermal gases can be compared to Bose-Einstein condensates (BEC), which are considered to be the matter wave analogue of optical lasers.

Naraschewski and Glauber extended the latter's original theory of optical coherence to describe trapped Bose gases [34], where the atomic field annihilation operators $\hat{\Psi}(\mathbf{r},t)$ replace those of the electric field $E^{(+)}(\mathbf{r},t)$ (or pure bosonic modes $\hat{a}(\mathbf{r},t)$), and similarly for the respective creation operators. With this substitution, the general results of the optical case are replicated for atoms, where thermal gases exhibit bunching, while BECs are fully coherent. The theory of Bose-Einstein condensation, which will be covered in §2.3.1, describes the condensate mode with an order parameter which is the classical limit of a quantum wavefunction. As coherent states can be thought of as being states with interference properties which most closely match that of a precisely defined classical field [34], perfect coherence naturally follows from having all atoms in the same single-particle state, which is the phenomenon of condensation. Although imaging individual atomic clouds will only allow density to be measured, off-diagonal terms of the density matrix corresponding to first-order correlations can be revealed via interferometry. As for incoherent sources of light, thermal clouds will display visible fringes which quickly decay on a lengths scale of order λ_{dB}, while the correlation length of BECs extend over the entire condensed portion of the cloud.

One of the principal differences between light and atoms is the existence of interactions for the latter, where interactions of sufficient strength can alter the form of correlation functions, especially over the short spatial separations between particles. However, as the densities and interaction strengths of atoms in the quantum gases produced by our experiment are quite low, these effects will not be significant for most of the results presented in this thesis, most notably for those in Chapter 4. This is especially true

considering that we measure correlation functions in the 'far field' where the gas has expanded considerably during its time of flight from the trap to the detector. More specific details on this topic relevant to the experiments presented in this thesis can be found in §4.1.1. On the other hand, weak interparticle interactions are seen to play an important role in understanding the observation of transverse condensation in an elongated ultracold gas, as is discussed in Chapter 5.

Novel and non-classical correlation effects

For bosonic sources, we expect to measure $g^{(n)}(\mathbf{r}_1, t_1; \ldots; \mathbf{r}_n, t_n) \geq 1$ for $n \geq 2$ under most circumstances, a concept which is adequately predicted by a classical treatment of correlation functions. However, the quantum-mechanical theory of correlation functions (§2.1.1) has introduced the possibility of $g^{(n)}(\mathbf{r}_1, t_1; \ldots; \mathbf{r}_n, t_n) \leq 1$ for particular statistical distributions, which cannot be explained classically. A key result which confirmed the validity of Glauber's theory was the prediction by Carmichael and Walls of sub-Poissonian, 'anti-bunched' light from resonance fluorescence of a two-level atom [78], and the successful measurement of this effect [79] was pivotal in the establishment of the field of quantum optics. Sources dependent on the statistical behaviour of small numbers of photons, such as heralded single photons [80] and parametric down-conversion sources [81] can also be investigated with correlation measurements. Indeed, a strongly sub-Poissonian single-atom state will be investigated in §7.2 of this thesis.

Another unique correlation phenomenon is the Hong-Ou-Mandel effect [33, 82], where the interference of two indistinguishable photons incident on a 50:50 beamsplitter causes the pair of photons to always exit on the same port of the beamsplitter. If the path length travelled by the two photons is the same, which is equivalent to the measurement of the photons being within their correlation time, then the non-classical result of $g^{(n)}(\mathbf{r}_1, t_1; \ldots; \mathbf{r}_n, t_n) \leq 1$ will again be found. Correlation measurements can also be used to identify exotic quantum states such as entangled states which violate Bell's inequalities, for example by the Rarity and Tapster scheme [83], or to enhance ghost imaging [84, 85].

As has been alluded to, correlation effects should also be measurable in systems of massive particles, and indeed have been observed for nuclear collisions [86], free electrons [87], and neutrons [88]. Of particular importance to this thesis was the successful measurement of correlations in atomic gases, which was first achieved in a beam of thermal bosonic neon [54], and the difference in coherence between chaotic and condensed Bose gases [55] confirmed the correspondence between statistical distributions of atoms and photons. Furthermore, observations of anti-bunching in thermal fermionic systems [56, 89] provided a clear illustration of the Pauli exclusion principle.

Correlation measurements for atomic systems can also be used to probe processes such as molecular dissociation [90] and four-wave mixing in the spontaneous [91] and stimulated [53] regimes. As four-wave mixing produces pairs of atoms scattering back-to-back in the centre of mass frame, violation of the Cauchy-Schwarz inequality can be observed directly for atom number correlations for modes with opposite momenta [92]. Studies of exotic states in quantum gases such as those exhibiting spin-squeezing entanglement [93, 94], spin interactions in optical lattices [95], and spin polarisation spectroscopy [96, 97] are also fruitful applications of correlation measurements.

When measuring quantum correlations in ultracold gases, it is quite often the second-order correlation function that is measured. While first-order correlation mea-

surements typically require the quantum gas to undergo an explicit interferometry operation, second-order functions can be measured directly from a statistical analysis of the cloud's density distribution. However, it is not generally the case that correlation functions for orders above $n = 2$ are measured, due to not only the experimental difficulty encountered in such an undertaking, but also that the behaviour of the third-order function can be extrapolated from density correlations by Wick's theorem. Although Glauber's theory requires coherence to exist for all orders of n for a state to be fully coherent, limitations are set by the physical size or number of particles in a source, and thus satisfying correlations to the first few orders is usually considered sufficient to establish full coherence. Correlation functions up to $n = 3$ have been measured for exciton-polaritons [98], while fourth-order thermal bunching has been measured for light from a microcavity [99] and compared to laser light of that order [100]. To the best of the author's knowledge, the highest-order correlation function ever measured was one which confirmed that laser light is coherent to $n = 8$, while demonstrating pseudo-thermal bunching up to $n = 6$ [101].

However, it is only with the experiments described in Chapter 4 that this has been confirmed for atomic systems above $n = 2$. In particular, the measurement of true thermal bunching up to $n = 6$ (§4.5), as opposed to inducing noise on a coherent source, makes this result the most thorough test yet of the applicability of Wick's theorem to quantum statistical systems. In addition to verifying that the predicted $g^{(n)}(0, \ldots, 0) = n!$ relationship holds for a thermal distribution, higher-order correlation functions in quantum gases may deviate from this idealised form due to pair production processes, three-body losses, the formation of Efimov states [102], or other effects specific to a certain number of particles. Such measurements could also provide information beyond that of $g^{(2)}$ when probing processes such as the thermalisation of isolated quantum systems [103], or could aid with determining the tomography of quantum states [104].

2.1.2 Wheeler's delayed choice *gedankenexperiment*

Importance of measurement

Of the many significant departures from classical mechanics which are required to understand quantum theory, one of the most discussed is the effect that the act of measurement has on a physical system. Despite overwhelming experimental evidence which supports predictions derived from the mathematical framework of quantum mechanics, the implications of many quantum phenomena do not correspond to intuitive classical behaviour, which has resulted in a variety of interpretations which aim to account for these discrepancies. This has remained a topic of debate to the present day, where a consensus is still yet to be reached on how to understand many foundational ideas of quantum mechanics [2].

Perhaps the most widely known of the many debates resulting from different interpretations of quantum behaviour was the apparent paradox presented by Einstein, Podolsky and Rosen [17] (commonly referred to as EPR). The basic premise of the EPR argument was that if strong correlations occur between a pair of particles which have interacted and subsequently separated by a space-like distance, the measurement of one of the pair could result in 'spooky action at a distance' and thus knowledge of the behaviour of the other particle without directly performing a measurement on it. Furthermore, if a different observable is measured for each particle, and those observables

are incompatible (such as position and momentum), it was claimed that this would allow measurements violating the Heisenberg uncertainty principle to be achieved. The result of this argument was to question the completeness of quantum theory, and to advocate the existence of 'hidden variables' which would account for such correlations which are referred to as being the result of entanglement, without invoking the notion of non-local action.

A response to counter the conclusions drawn by Einstein, Podolsky and Rosen was proposed by Bohr [105] which appealed to his previous idea of complementarity [16], a cornerstone of the widely used Copenhagen interpretation of quantum mechanics. Essentially, Bohr highlighted the inapplicability of classical ideas to explain quantum behaviour, and argued that the measurement of one observable would inevitably preclude the measurement of the other. While it is generally considered that Bohr's exposition of this argument is particularly unclear [106], his views were nevertheless widely accepted, if not fully understood. However, the possibility of a local hidden-variable theory was not conclusively dismissed until Bell mathematically derived an inequality which results in a contradiction between theories containing local hidden-variables and the predictions of quantum mechanics [18]. Experiments which demonstrate a violation of Bell's inequality have been performed [20], and have thus ruled out local hidden-variable theories and settled this particular argument in favour of Bohr.

Complementarity and particle-wave duality

In the years after his exchange with Einstein, Bohr sought to clarify the importance of complementarity, which lead to an emphasis being placed upon the act of measurement to determine what brings about 'reality'. A particularly striking example of this is particle-wave duality, where photons or atoms can behave as either waves or discrete particles depending on the type of experiment performed. A basic example of this is shown in Fig. 2.2, where the presence or absence of a double slit at the intersection of two beams of light gives either a wave-like interference pattern or particle-like directional information respectively. While Einstein would have argued that it should in principle be possible to observe an interference pattern while simultaneously knowing which path each photon took, this example provides a simple illustration of Bohr's view that the two properties are mutually exclusive [107].

Wheeler decided to test the idea of complementarity further with his famous 'delayed-choice' *gedankenexperiment*[3] [108], and in particular investigate whether photons or matter could have particle and wave properties simultaneously. Bohr's statement that [109]

> it can make no difference, as regards observable effects obtainable by a definite experimental arrangement, whether our plans for constructing or handling the instruments are fixed beforehand or whether we prefer to postpone the completion of our planning until a later moment when the particle is already on its way from one instrument to another

spurred Wheeler to devise a scheme which conclusively rules out Einstein's argument

[3]The word '*gedankenexperiment*' is German for 'thought experiment', and is used as a nod to the vast contribution of German speakers to modern physics in general, and in particular the discussion of apparent paradoxes like EPR or Schrödinger's cat.

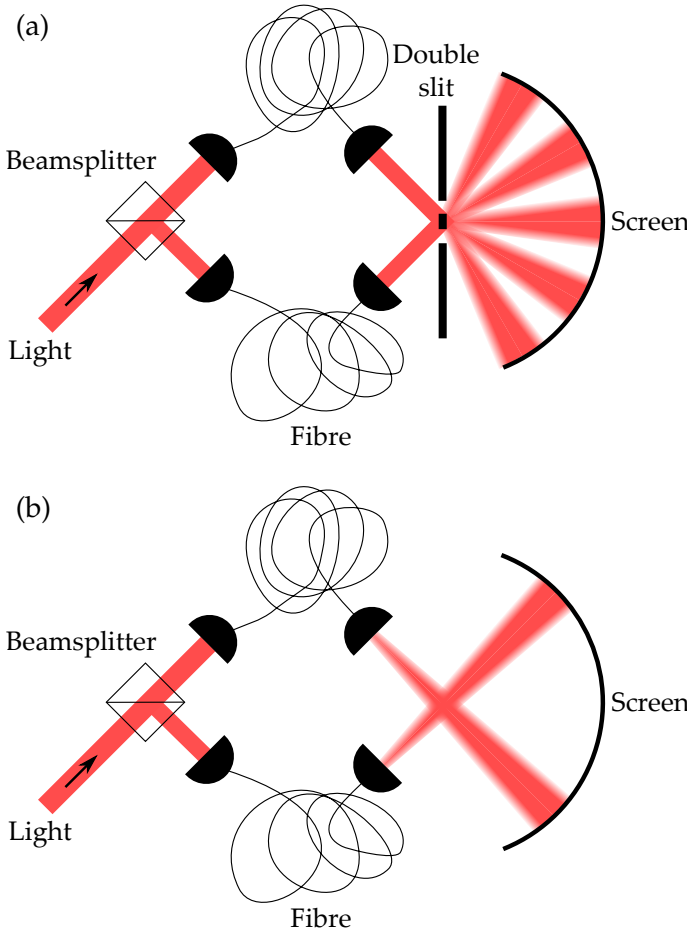

Figure 2.2: An experiment in the style of an interferometer which demonstrates complementarity. Light incident on a beamsplitter then passes through a pair of fibres (or through free space), and is either recombined with a double slit aperture (a) or passes directly to a screen (b), where in either case it creates a distinctive intensity distribution. If the double slit aperture is present, information about the path taken by photons from the fibres to the screen is lost, but instead a pattern of wave interference can be observed. Conversely, if the slits are removed, no interference is seen, but the positions of photons in the light beam are well defined. The design of the interferometer, such as the length or layout of the fibres, can have implications for the relativistic separation of the choice of interferometer orientation from the entry of the photon to the interferometer.

for local reality. Wheeler's reasoning can be paraphrased[4] by an extension to the experiment described in Fig. 2.2, where a single photon traverses the beamsplitter and enters the fibres. If the fibres are long enough, a decision about whether the slits should be present or not can be made, and its result implemented, before the photon exits the fibre. In particular, the layout of the fibre and the timing of the choice must be such that there is no inertial frame in which information about the slit configuration can reach the photon before it enters the interferometer, to exclude explanations of local reality which support Einstein's argument.

To create a wave interference pattern, it could be said that the single photon must have passed through both fibres, while information about the location of the particle is possible if the photon only travelled down one of the fibres. It would therefore appear that the delayed choice could influence the past dynamics of the photons, as producing a result to match the configuration of the slits requires the photon to have 'known' which of the fibres to enter. Wheeler argues against the violation of causality, however, by stating that [108]

> ... the past has no existence except for that which is recorded in the present. No phenomenon is a phenomenon until it is an observed phenomenon.

This builds upon Bohr's view that [110]

> it is wrong to speak of the 'route' of the photon in the experiment of the beamsplitter. It is wrong to attribute tangibility to the photon in all its travel from the point of entry to its last instant of flight.

Instead, Wheeler proposes that no paradox exists as we are only influencing what we know about the past, where the past is undefinable without observation. It is indeed the measurements that are made which shape the reality that is observed, rather than reality having to exist before a measurement is made. According to Bohr, it is the 'irreversible act of amplification' resulting in measurement, rather than the presence of 'conscience', which constitutes an 'observation' [110].

Experimental realisations of complementarity and Wheeler's experiment

It is relatively easy to perform experiments which confirm that the basic behaviour of the experiment described in Fig. 2.2 is as expected, in that the addition or removal of a 'mixing' operation (such as a double slit or a second beamsplitter and waveplate) to a bimodal source in a static configuration lacking a 'delayed choice' results in complementary observations [111]. A multitude of experimental schemes have added the delayed choice element for investigations with photons [112–114], while other approaches include the application of Stern-Gerlach interferometry to a beam of metastable hydrogen [115] or spin interferometry for cold neutrons [116] to test complementarity. While these experiments did essentially support the arguments put forth by Wheeler, each of them were not able to avoid violating the strict conditions required to conclusively deny Einstein's local hidden variables view. These conditions, which include the requirement for true single particle sources, and that the delayed choice is performed in a truly (quantum) random way while relativistically separated from the entry of the photon to the

[4] Wheeler's original proposal included seven different experimental setups which essentially measure the same effect, and the one chosen here is another equivalent modification based on the Mach-Zehnder configuration suggested by Stapp [108].

interferometer, can be seen somewhat analogously with loopholes in entanglement measurements. A recent landmark experiment was able to satisfy each of these criteria [21], and thus by realising the idealised version of Wheeler's experiment it was conclusively demonstrated that Bohr's concept of complementarity was correct.

Delayed choices have also been used in conjunction with quantum erasers [117, 118] to show that acquiring or subsequently 'erasing' knowledge about the path taken by one of an entangled pair of photons can influence whether an interference pattern can be produced by the other photon. In this case, the delayed choice is achieved by deciding whether 'which way' information is recorded after having recorded the photon which reveals whether wave-like behaviour is present. Further extensions to this have been explored, including experiments which probe the particle and wave behaviours of photons simultaneously, and actually show that a continuum of behaviours exist rather than the simplistic view of wave and particle properties being absolute and mutually exclusive [24–27]. However, experiments with atoms have not reached the same level of sophistication as those using photons, and are yet to realise the idealised version of Wheeler's experiment. An experiment which has made progress towards this aim is discussed in Chapter 7.

2.2 Atom cooling and trapping

To obtain a sample of atoms suitable for measuring quantum behaviour, dilute clouds of weakly-interacting bosons must be cooled to temperatures at which their wave nature becomes apparent. This requires multiple stages of cooling and trapping, each of which rely on the interaction of atoms with electromagnetic radiation. An overview of the concepts required to understand the experimental apparatus described in Chapter 3 is given here, and more detail can be found in textbooks such as Refs. [119, 120] or review papers such as [121].

2.2.1 Atom-light interactions

In the context of laser cooling and trapping, atoms can be thought of as quantum systems containing many energy levels which can be coupled with electromagnetic radiation. The energy levels in helium are the result of fine structure due to spin-orbit coupling, where atoms with total electronic angular momentum $|\mathbf{J}| = |\mathbf{L} + \mathbf{S}|$ for spin $\mathbf{S}$ and orbital angular momentum $\mathbf{L}$ are often labelled by the angular momentum quantum number J, which takes integer values between $|L - S|$ and $|L + S|$. The projection of the angular momentum on the direction of an externally-applied magnetic field m_J, which ranges from $-J$ to J in integer steps, gives the atom a magnetic dipole moment which can interact with the applied magnetic field. It is generally instructive, and in many cases sufficient, to simplify this by considering atoms to be two-level systems, where transitions between the ground and excited states can be induced by laser light. The transfer of momentum occurring as an atom absorbs and emits a photon applies either a coherent dipole force or a spontaneous scattering force, depending on the detuning $\delta = \omega_{\text{laser}} - \omega_{\text{atom}}$ of the laser light angular frequency ω_{laser} from the energy difference $\hbar\omega_{\text{atom}}$ between the two levels in the atom.

Scattering force

Incoherent scattering of photons is the primary method used for the initial stages of the cooling process. In the low detuning limit, the absorption of a photon with wavevector $\mathbf{k}$ transfers an impulse of $\Delta\mathbf{p} = \hbar\mathbf{k}$ to the atom. After an average decay time $\tau = \Gamma^{-1}$, where Γ is the natural transition linewidth, the atom of mass m will emit the photon in a random direction, resulting in a change in energy of $E_{\text{rec}} = \hbar^2 k^2/2m$ due to the recoil experienced by scattering the photon. While the incoming direction of the photons is collimated, the emission will by symmetrically distributed and thus averages to a net momentum transfer of zero after many absorption and emission cycles, which results in an overall force which acts in the direction of the laser beam. The average force in one dimension applied over many scattering events to atoms with a velocity $\mathbf{v}$ interacting with such a laser field of intensity I will be

$$\mathbf{F}(\mathbf{v}) = \hbar\mathbf{k}\frac{\Gamma}{2}\left[\frac{I/I_{\text{sat}}}{1 + I/I_{\text{sat}} + 2(\delta - \mathbf{k}\cdot\mathbf{v})/\Gamma}\right], \tag{2.25}$$

where $I_{\text{sat}} = \Gamma hck^3/24\pi^2$ is the saturation intensity of the transition, such that the scattering rate does not increase for $I > I_{\text{sat}}$.

Zeeman slower

A beam of atoms emanating from a source will have an average velocity which is far too high to be successfully captured in a magneto-optical trap. Therefore, a red-detuned $(\delta < 0)$ beam of near-resonant laser light can be used to apply a scattering force to oppose the motion of the atoms. Although it is possible to apply the maximal scattering force of $\hbar\mathbf{k}\Gamma/2$ for a detuning that matches the Doppler shift $\mathbf{k}\cdot\mathbf{v}$, the scattering rate will decrease as the atom slows and shifts the incident laser light off resonance. In particular, the linewidth of the transition must be much greater than the frequency shift $\hbar k^2/m$ induced by a single scattering event, otherwise the scattering process will fall off resonance too quickly for the scattering force to effectively cool the atom[5].

However, after absorbing and emitting many photons, the atoms will eventually slow such that the laser is too far away from resonance to apply a significant scattering force. This can be compensated by a spatially-varying magnetic field. A Zeeman slower utilises a tapered solenoid which produces a magnetic field $\mathbf{B}$ such that the energy levels are shifted by $U_{\text{Zeeman}} = -\boldsymbol{\mu}\cdot\mathbf{B}$, where $\boldsymbol{\mu}$ is the magnetic moment of a particular atomic state [122]. This Zeeman shift is tuned to match the Doppler shift experienced by the atoms as they decelerate during their passage through the centre of the solenoid, such that the laser remains on resonance along the entire length of the solenoid.

Magneto-optical trap

Once the atoms are slowed to a velocity such that $\mathbf{k}\cdot\mathbf{v} \lesssim \Gamma$, they can be further cooled by applying the scattering force with two counterpropagating red-detuned laser beams, so that the Doppler shift brings atoms moving in the opposite direction of the beam closer to resonance, while moving the copropagating beam away from resonance. This means that the atom scatters more photons from the beam which opposes its motion, which

[5]For the 1083 nm transition for metastable helium, the frequency shift of 260 kHz is much smaller than $\Gamma = 2\pi \times 1.6$ MHz, while alkali atoms have an even smaller shift due to their large mass.

slows it down. From Eq. 2.25, we see that such a laser setup with $I \gg I_{\text{sat}}$ applies a velocity-dependent damping force to the atoms

$$F_{\text{tot}} = |\mathbf{F}(\mathbf{v}) + \mathbf{F}(-\mathbf{v})| \simeq \left\{ 4\hbar k^2 \frac{I}{I_{\text{sat}}} \frac{2\delta/\Gamma}{[1+(2\delta/\Gamma)^2]^2} \right\} v, \tag{2.26}$$

which is strongest for $\delta \simeq -\Gamma/2$. Atoms can thus be cooled by applying light in this manner along all three Cartesian directions to form an optical molasses.

However, atoms cannot typically be trapped solely by radiation pressure, as atoms eventually diffuse out of the molasses. A quadrupole magnetic field produced by a pair of anti-Helmholtz coils, which gives a field linear in all directions with a zero at the centre, can be applied to form a magneto-static trap, which will be discussed further in the following section. However, this field is typically not used in this manner, but instead to add a position and polarisation dependence to the scattering force applied by a 3D optical molasses to form a magneto-optical trap (MOT) [123]. In a similar way to the Zeeman slower, the field lifts the degeneracy of different magnetic substates such that the $(\delta - \mathbf{k}\cdot\mathbf{v})$ term in Eq. 2.25 is modified to $(\delta - \mathbf{k}\cdot\mathbf{v} + \beta(r))$, for Zeeman shift $\beta(r) = g_J \mu_B m_J B(r)/h$ at position r in each Cartesian direction, where μ_B is the Bohr magneton and g_J is the Landé g-factor.

If we consider for example transitions from the $J=0$ singlet to the $J=1, m_J = 0, \pm 1$ triplet of states, red-detuned light will be closer to resonance for the transition to the $m_J = -1$ state for spatial locations where the field is positive, and similarly for transitions to $m_J = 1$ for areas of negative field. To conserve angular momentum, these transitions must be driven with light of the correct polarisation, in this case σ^- and σ^+ which carry -1 and 1 unit of angular momentum respectively. By choosing beam polarisations for the counterpropagating pairs such that scattering pushes atoms towards the trap centre, Eq. 2.26 can be modified from the form $F_{\text{tot}} = -\alpha v$ to $F_{\text{tot}} = -\alpha v - (\alpha\beta/k)z$. Therefore, the motion of atoms in a MOT is that of an overdamped harmonic oscillator, which is now dependent on both position and velocity, and provides a combination of trapping and cooling.

In principle, the cooling achievable will be bounded by the recoil limit $T_{\text{recoil}} = (\hbar k)^2/2m$, at which point the scattering of a single photon adds energy to the system. However, in practice the natural atomic transition linewidth will determine the rate at which atoms go on a random walk due to spontaneous scattering of individual photons, which results in Doppler temperature limit $T_{\text{Doppler}} = \hbar\Gamma/2k_B$ for a two-level system. Although the Doppler limit is usually at a considerably higher temperature than the recoil limit, sub-Doppler cooling techniques are available for atomic species with degenerate energy levels. However, a lack of nuclear spin $\mathbf{I} = \mathbf{0}$ results in the absence of hyperfine splitting for helium and consequently the total atomic angular momentum $\mathbf{F} = \mathbf{I} + \mathbf{J} = \mathbf{J}$, which prevents this from being used in our experiment.

2.2.2 Magnetic and dipole trapping

The temperatures and phase-space densities possible for atoms in a MOT are generally not sufficient for achieving Bose-Einstein condensation or the observation of atom-optical effects. Neutral atoms can be confined by external fields, and while these static traps do not inherently cool the atoms further, they allow other mechanisms for cooling below the Doppler limit towards quantum degeneracy while in principle not providing

any heating mechanisms. Such traps are typically either magnetic fields, which interact with the permanent dipole moment of the atoms, or optical traps which apply a force by inducing an electric dipole in the atom. Our experiment utilises both of these types of trap, to take advantage of the contrasting advantages that they offer.

Magnetostatic traps

Magnetostatic traps apply a force $\mathbf{F} = \nabla(\boldsymbol{\mu} \cdot \mathbf{B})$ due to an inhomogeneous magnetic potential $U = -\boldsymbol{\mu} \cdot \mathbf{B}$ by the Zeeman effect [124]. As a well-known consequence of Maxwell's equations of electrodynamics is that local field maxima are forbidden, these traps will capture low-field seeking atoms in the $m_J = 1$ state, while being insensitive to $m_J = 0$ atoms and repulsive to $m_J = -1$ atoms. Atoms are typically pre-cooled in a MOT before transferring to a purely magnetic trap, as the depth of the latter is usually limited to temperatures only possible after laser cooling is applied to the atomic cloud. Although it would seem obvious to use the quadrupole field produced by the MOT as the magnetostatic confinement, the point of $\mathbf{B} = \mathbf{0}$ at the trap centre allows atoms to undergo Majorana transitions, which spin-flip the atoms into magnetic substates not trapped by the field ($m_J = 0$ or -1) and therefore forms a significant loss channel as the cloud cools.

The trap must ideally provide sufficiently strong confinement to facilitate a reasonable collision rate, which ensures that the atoms rethermalise during cooling, while simultaneously lacking a zero in the magnetic field. A variety of coil designs have been implemented to achieve this, each of these resulting in a potential which is essentially harmonic at the trap centre, and most commonly produces a 'cigar' shaped cloud with two tightly confined axes and a weak direction along which the cloud extends while trapped. The geometry of these traps is generally fixed, and although the strength of the trap can be altered by changing the current passing through the trap coils, substantial changes to the trap aspect ratio, and therefore dimensionality of the trapped cloud, often cannot be achieved.

Cooling to temperatures far below the Doppler limit can occur with atoms held in a magnetic trap by the process of radio-frequency (RF) evaporative cooling. As magnetic potentials are conservative, atoms can only reach spatial locations further away from the trap centre by having a relatively large amount of kinetic energy. Thermal equilibrium occurs through elastic collisions which redistribute energy between atoms in the cloud, such that the temperature of the cloud depends on the most probable kinetic energy of the atoms. By selectively removing the most energetic atoms, the cloud will eventually rethermalise to a lower temperature after each atom undergoes several collisions. This can be achieved by outcoupling atoms from a specific spatial location, or equivalently magnetic field strength, by applying RF radiation of the correct energy to spin-flip atoms from the field sensitive, trapped $m_J = 1$ state to the untrapped $m_J = 0$ state which can escape from the cloud. By slowly sweeping the energy of the RF radiation applied from high to low, at a rate slow enough to allow the cloud to remain in equilibrium at all times, yet fast enough to not allow other loss mechanisms such as inelastic collisions to become dominant, the temperature will drop while the peak atomic density remains high. In particular, if a high enough phase-space density is achieved, a Bose-Einstein condensate can be formed.

Optical dipole traps

In contrast to the spontaneous scattering force applied to atoms by laser light with a small detuning from an atomic transition, light with a large detuning can apply a stimulated dipole force to trap atoms [125]. This force is the result of coherent scattering of light, where the electric field $\mathbf{E}$ of the radiation induces an electric dipole moment in the atom $-e\mathbf{r}$. The interaction energy between the two is $U = e\mathbf{r}\cdot\mathbf{E}/2 \approx \hbar\Gamma^2 I/8\delta I_{\text{sat}}$, which is analogous to the Zeeman shift for magnetic fields. The force applied can be likened to a classical harmonic oscillator driven below resonance for red-detuned light, where the electric dipole is driven by an oscillating electric field and undergoes an a.c. Stark shift dependent on laser intensity, while the spontaneous scattering rate is negligible in the limit of a large detuning. As is always the case, the force applied is proportional to the spatial derivative of the potential, which will in turn depend on the intensity gradient of the light field. While the scattering rate of the radiation pressure force is proportional to $1/\delta^2$, the dipole force goes as $1/\delta$ and thus large detunings are favourable to avoid spontaneous scattering which results in loss of atoms from the trap.

A trapping potential can be formed by a gradient in the intensity of a focused red-detuned laser beam, where different trap geometries can be realised in accordance with beam parameters calculated with classical Gaussian optics. Optical traps allow for greater control over trapping geometries than is generally possible for magnetic traps, where regimes of lowered dimensionality can be reached, in addition to the formation of lattice potentials. The use of crossed-beam traps can allow for precise control over the trap aspect ratio, while altering the laser beam intensity tunes the harmonic trapping frequencies and trap depth. In addition, waveguides can be formed which confine the atoms in two Cartesian dimensions, without sufficient trap depth to hold them in a third direction.

This forms a conservative potential in a similar manner to a magnetic trap, although cooling can be achieved by lowering the trap depth to allow more energetic particles to escape. Although dipole traps with a large enough trap depth and volume can in principle capture atoms directly from a MOT, in our experiment atoms are evaporatively cooled to near the critical temperature for BEC formation in a magnetic trap before being transferred to the optical trap. A unique feature of dipole traps is their ability to hold atoms of any magnetic substate m_J, which will be exploited for our single atom source described in §7.2.

2.3 Bose-Einstein condensation

Bose-Einstein condensates serve as a testbed for a wide array of quantum-mechanical phenomena, as they are relatively easy to manipulate with external electromagnetic fields, and are often quite isolated from environmental perturbations. In many of the quantum statistical experiments undertaken in this thesis, the coherence of a condensed gas will be contrasted with the chaotic nature of a thermal cloud, which exemplifies the correspondence of a BEC with an optical laser and highlights the importance of Glauber's theory of coherence for understanding quantum systems. While several sources such as Refs. [36, 126, 127] provide detailed information about theoretical and experimental aspects of Bose-Einstein condensation, a brief review of concepts relevant to our experiment is presented here.

2.3.1 Requirements for condensation in three-dimensional gases

The cooling and trapping techniques described in the previous section are typically able to cool quantum gases from room temperature, where either a bosonic or fermionic gas will behave as an ideal gas described by a Maxwell-Boltzmann energy distribution, to ultracold temperatures where the quantisation of energy levels becomes important. With Einstein's extension [30] to Bose's theory of photon statistics [29], it was realised that low temperatures and high densities would result in macroscopic occupation of the ground state of a bosonic system, which occurs even in the absence of interactions which are required for familiar phase transitions such as the freezing of a liquid. The average occupation $\langle n_i \rangle$ of the ith energy level with energy ϵ_i for a system of N indistinguishable bosons at a temperature T is given by the Bose-Einstein distribution

$$\langle n_i \rangle = \frac{1}{\mathrm{e}^{(\epsilon_i - \mu)/k_B T} - 1}, \tag{2.27}$$

where k_B is the Boltzmann constant. The chemical potential μ is the energy required to add one particle to the system, and is set by the requirement that $N = \sum_i \langle n_i \rangle$. In the limiting case of high temperatures and low densities, the Maxwell-Boltzmann distribution is recovered from Eq. 2.27.

However, at low temperatures, high energy states become inaccessible, while the populations of the lower energy states increase until a critical temperature T_c is reached, where the lowest energy state becomes macroscopically occupied. This signals the onset of Bose-Einstein condensation, which occurs when there is significant overlap of the wave packets of the atoms in the gas, which are characterised by the de Broglie wavelength

$$\lambda_{\mathrm{dB}} = \sqrt{\frac{2\pi\hbar^2}{m k_B T}}, \tag{2.28}$$

for Planck's reduced constant $\hbar$ and mass m. At room temperatures, λ_{dB} is very small, and the atoms act classically. However, when the phase-space density of the gas is sufficiently high such that the λ_{dB} approaches mean particle spacing $\rho^{-1/3}$ for particle density ρ, which is quantified as

$$\rho \lambda_{\mathrm{dB}} = \zeta(3/2) \approx 2.612, \tag{2.29}$$

where $\zeta(x) = \sum_{j=1}^{\infty} j^{-x}$ is the Riemann zeta function, the wave packets of individual atoms become indistinguishable in the ground state. This signifies that T_c has been reached.

The temperature at which condensation occurs depends on the trapping potential $V(\mathbf{r})$ holding the atoms. Magnetic and optical dipole traps will generally be harmonic at their centre, taking the form

$$V(\mathbf{r}) = \frac{1}{2} m \left(\omega_x^2 x^2 + \omega_y^2 y^2 + \omega_z^2 z^2 \right), \tag{2.30}$$

where ω_i is angular harmonic trap frequency from each Cartesian direction. Then, the temperature at which Eq. 2.29 is satisfied for three-dimensional systems will be

$$T_c = \frac{\hbar \bar{\omega}}{k_B} \left[\frac{N}{\zeta(3)} \right]^{1/3} \approx \frac{0.94 \hbar \bar{\omega} N^{1/3}}{k_B}, \tag{2.31}$$

where the geometric mean of trap frequencies is $\bar{\omega} = \left(\omega_x \omega_y \omega_z\right)^{1/3}$. For temperatures lower than T_c, the occupation of the ground state N_0 is

$$\frac{N_0}{N} = 1 - \left(\frac{T}{T_c}\right)^3, \tag{2.32}$$

while a thermal component will remain for a gas at temperatures above absolute zero.

While interactions are negligible for a high-temperature gas, and remain relatively weak at quantum degeneracy compared to other systems such as liquid helium superfluids, they are still important for condensed gases. For clouds with a macroscopic occupation of the ground state, mean field repulsive interactions due to a two-body contact potential of the form $V_{\text{int}}(\mathbf{r}, \mathbf{r}') = g\delta(\mathbf{r} - \mathbf{r}')$, where δ is the Dirac delta function and g is the two-body interaction energy, can be used to alter the familiar linear Schrödinger equation to the non-linear Gross-Pitaevskii equation for the expectation value of the bosonic field order parameter $\Psi(\mathbf{r}, t)$ [126]

$$\mathrm{i}\hbar \frac{\partial \Psi(\mathbf{r}, t)}{\partial t} = \left(-\frac{\hbar^2}{2m}\nabla^2 + V(\mathbf{r}) + U_0 \left|\Psi(\mathbf{r}, t)\right|^2\right) \Psi(\mathbf{r}, t). \tag{2.33}$$

The interaction energy is approximated by the $U_0 \left|\Psi(\mathbf{r}, t)\right|^2$ term proportional to local density $\left|\Psi(\mathbf{r}, t)\right|^2$, where $U_0 = 4\pi\hbar^2 a/m$ for s-wave scattering length a. The order parameter can be interpreted as the classical limit of a de Broglie wave, where quantisation is no longer important and $\Psi(\mathbf{r}, t)$ acts as the wavefunction of the BEC with density $\rho(\mathbf{r}) = \left|\Psi(\mathbf{r}, t)\right|^2$ [36]. For dilute gases where the mean particle spacing is much larger than the s-wave scattering length, the order parameter is useful for computing the behaviour of macroscopically occupied condensates on length scales which exceed a.

This is particularly useful for calculating condensate dynamics, where in the Thomas-Fermi approximation the kinetic energy term $-\frac{\hbar^2}{2m}\nabla^2$ is negligible and can be discarded, allowing the density profile to be easily computed for a harmonic potential as

$$\rho(\mathbf{r}) = \max\left(\frac{\mu - V(\mathbf{r})}{U_0}, 0\right) = \frac{\mu}{U_0}\left(1 - \sum_i \frac{x_i^2}{R_i^2}\right). \tag{2.34}$$

Normalisation of the wavefunction allows the chemical potential to be determined from N_0 as

$$\mu = \frac{1}{2}\hbar\bar{\omega}\left(\frac{15 N_0 a}{l}\right)^{2/5}, \tag{2.35}$$

where the ground state harmonic oscillator length is $l = \sqrt{\hbar/m\bar{\omega}}$. The size of the trapped condensate is given by the Thomas Fermi radii

$$R_{\text{TF},i} = \sqrt{\frac{2\mu}{m\omega_i^2}}. \tag{2.36}$$

In contrast, the size of a trapped thermal gas is

$$R_i = \sqrt{\frac{2k_B T}{m\omega_i^2}}, \tag{2.37}$$

which allows the condensed portion of the cloud to be identified from the bimodal spatial density distribution of the trapped cloud.

2.3.2 Ballistic expansion of ultracold clouds

A feature unique to our experimental setup is the ∼850 mm distance between the trap and the delay-line detector used to acquire most of our experimental data, which will be discussed in detail in the following chapter. A cloud released from the trap will evolve as it falls under gravity such that the position distribution at the detector will essentially depend on the in-trap momentum. Taking the trapped size $R(0)$ of a BEC from Eq. 2.36, for the tight trapping axes $R_\perp$ of the trap [128] after an expansion time t_{exp},

$$R_\perp(t_{\text{exp}}) = R_\perp(0)\sqrt{1+(\omega_\perp t_{\text{exp}})^2} \approx R_\perp(0)\omega_\perp t_{\text{exp}}, \tag{2.38}$$

while in the weak, axial direction $R_\parallel$ we have

$$R_\parallel(t_{\text{exp}}) = R_\parallel(0)\left\{1+\left(\frac{\omega_\parallel}{\omega_\perp}\right)\left[\omega_\perp t_{\text{exp}}\arctan\left(\omega_\perp t_{\text{exp}}\right) - \ln\sqrt{1+(\omega_\perp t_{\text{exp}})^2}\right]\right\}. \tag{2.39}$$

In contrast, the expansion of the thermal cloud will be dependent on thermal energy rather than the trapping potential, such that 2.37 is modified to

$$R_i(t_{\text{exp}}) = \sqrt{R_i(0)^2 + t_{\text{exp}}^2\frac{2k_BT}{m}} \approx t_{\text{exp}}\sqrt{\frac{2k_BT}{m}}. \tag{2.40}$$

In the far field, the thermal cloud will be spherical and symmetric, while the density distribution of the condensate will retain its asymmetry which again allows the condensate to be resolved from the thermal background.

2.4 The effect of dimensionality on Bose gases

The phenomenon of Bose-Einstein condensation occurs purely as a result of quantum statistics, where the chemical potential μ of the Bose gas becomes close to zero and the ground state of the system becomes macroscopically occupied [129]. Identifying the onset of condensation amounts to determining a value for μ which normalises the number of atoms N in the Bose-Einstein distribution, which we recall from Eq. 2.27 is

$$N = \sum_i \frac{1}{\mathrm{e}^{(\epsilon_i-\mu)/k_BT}-1} \approx \int_0^\infty g(\epsilon)\frac{1}{\mathrm{e}^{(\epsilon-\mu)/k_BT}-1}\,\mathrm{d}\epsilon, \tag{2.41}$$

where converting the sum to an integral is valid when the discretisation of the states becomes insignificant for $k_BT \gg \epsilon_0$. The density of states $g(\epsilon)$ represents the number of single-particle states available as a function of energy, which will be dependent on the confining potential of the system, and in particular the dimensionality of the gas. For high temperatures, $\mu \ll \epsilon_0$ and the occupation of each state is very small, according to Eq. 2.27, and the gas essentially follows the Boltzmann distribution.

As the temperature decreases and the average occupation of each low-energy state grows, the chemical potential increases but is bounded by the requirement that $\mu < \epsilon_0$, as violation of this would result in $\langle n_0\rangle < 0$. Therefore, the mean occupation of each

state is restricted to

$$\langle n_i \rangle_{i>0} < \sum_i \frac{1}{\mathrm{e}^{(\epsilon_i - \epsilon_0)/k_B T} - 1}. \tag{2.42}$$

In this case, it is possible for $n_{\text{excited}} = \sum_i \langle n_i \rangle_{i>0} < N$, in which case the remaining particles must accumulate in the ground state, with a population $n_0 = N - n_{\text{excited}}$ [127].

Whether condensation can occur in a given system will clearly depend on the density of states at small energies, which takes the general form $g(\epsilon) \propto \epsilon^{(d/2-1)}$ for an untrapped d-dimensional gas [127]. However, for a harmonic oscillator potential,

$$g(\epsilon) = \frac{\epsilon^{d-1}}{(d-1)! \prod_{i=1}^{d} \hbar\omega_i} = C_d \epsilon^{d-1}. \tag{2.43}$$

The condensation temperature T_c will thus be T for which Eq. 2.41 is satisfied for $\mu = 0$, as this is the condition for which the integral approximation due to $k_B T \gg \epsilon_0$ results in the largest value of N. For $T > T_c$, $\mu < 0$ and no one particular state is macroscopically occupied, whereas for $T < T_c$, Eq. 2.41 only accounts for particles in excited states and n_0 is no longer negligible, at which point a Bose-Einstein condensate forms. We can explicitly calculate this for a harmonic potential by inserting Eq. 2.43 into Eq. 2.41, which results in

$$T_c = \frac{N^{1/d}}{k_B \left[C_d \Gamma(d) \zeta(d) \right]^{1/d}}, \tag{2.44}$$

where $\zeta(d)$ is again the Riemann zeta function, and $\Gamma(d) = \int_0^\infty x^{d-1} \mathrm{e}^{-x} \, \mathrm{d}x$. For $d = 3$, we recover Eq. 2.31, while condensation is also possible for a harmonically-trapped two-dimensional gas at finite temperature[6]. However, $\zeta(1)$ diverges and thus macroscopic occupation of the ground state cannot be achieved for harmonically-trapped one-dimensional gas at a non-zero temperature in the thermodynamic limit ($N \to \infty$ while density remains constant, which requires that volume to also goes to infinity). Furthermore, Landau-Ginzburg theory of critical phenomena for phase transitions rules out the establishment of long-range order for Bose gases in 1D due to phase fluctuations which dominate even at $T = 0$ [130–132].

Although the above analysis approximated the discrete level structure of a Bose gas by a continuous distribution, and considered phase transitions to occur only in the thermodynamic limit, removing these assumptions gives a more realistic treatment of experimentally realisable systems [133, 134]. For a harmonically trapped gas of a finite number of atoms, macroscopic occupation of a single state is seen to be possible for one-dimensional systems due to a shift in condensation temperature for small N. For three-dimensional systems, finite number effects result in a slight lowering of critical temperature for the onset of condensation below that of Eq. 2.31, and while true phase transitions can only occur in the thermodynamic limit [133, 134], it can be shown that the behaviour for $N \gtrsim 10^4$ is virtually indistinguishable from that in the thermodynamic limit. As establishment of the order parameter and onset of long-range order upon macroscopic occupation of the ground state is possible for systems of finite N, this is seen as essentially being equivalent to the phase transition to BEC.

Following the same procedure for a 1D system, a transition temperature $T_c^{1\mathrm{D}}$ which marks the onset of a macroscopic occupation of the ground state of a harmonically

[6] In the absence of a trapping potential, condensation for a uniform 2D gas is only possible at $T = 0$, where the effective form of $g(\epsilon)$ mirrors that of a harmonically-trapped 1D gas [127].

trapped gas can be found from [133]

$$N = \frac{k_B T_c^{1\mathrm{D}}}{\hbar\omega_\parallel} \ln\left(\frac{2k_B T_c^{1\mathrm{D}}}{\hbar\omega_\parallel}\right). \tag{2.45}$$

Thus, a critical temperature can be reached for finite N, but fails in the limit that $N \to \infty$ while $N\omega_\parallel$ remains finite. The question of whether this constitutes true Bose-Einstein condensation in the sense of long-range order requires the influence of interactions to be considered, which will be discussed further in §2.4.1.

Systems of reduced dimensionality are rich with novel behaviour, in particular for the study of quantum statistics. The role of dimensionality on the phase transition to Bose-Einstein condensation can be investigated by measuring the correlation length of Bose gases, which depends on a critical exponent [135]. For uniform two-dimensional systems which cannot reach BEC at finite temperatures, 'quasi-condensate' superfluids can be formed at finite temperatures due to the Berezinskii–Kosterlitz–Thouless (BKT) transition which can be identified with coherence measurements [136, 137], while large numbers of vortices can also be induced in a 2D lattice of BECs in the BKT regime [138].

2.4.1 Quantum correlations in 1D Bose gases

The quantum correlation functions of ideal gases in the 3D limit was discussed in §2.1.1, where thermal gases display bunching characterised by $g^{(2)}(0) = 2$, while bunching is absent for condensates with long-range order such that $g^{(2)}(\Delta r) = 1$ for all Δr. However, long-range order cannot be established in a 1D system due to fluctuations in the order parameter [130, 131]. Interacting one-dimensional gases are nevertheless of interest because they provide a rare opportunity for exact solutions to be obtained for many-body Hamiltonians in certain regimes [139]. These include Tonks-Girardeau gases of bosons, where infinitely repulsive contact interactions cause the bosonic atoms to mimic the behaviour of fermions [140, 141], while a general class of Lieb-Liniger gases with contact potentials at $T = 0$ also allow correlation functions to be calculated [142–144]. Correlations at finite temperatures have also been explored for the Yang-Yang model [145] and Luttinger liquids [146]. However, the properties of systems outside these regimes are difficult to calculate, and extending the parameter space over which correlations in 1D can be calculated remains an active area of research.

As the aforementioned theoretical treatments are for 1D gases with a uniform linear density $n_{1\mathrm{D}}$, we must first check whether this is suitable for describing the more experimentally realistic case of a harmonically trapped Bose gas [147]. This requires the transverse harmonic oscillator length $l_\perp = \sqrt{\hbar/m\omega_\perp}$ to be much smaller than both λ_{dB} and the length scale of density fluctuations determined by the healing length $\xi^{\mathrm{heal}} = \hbar/\sqrt{2mn_{1\mathrm{D}}g}$ for interaction strength $g = 2\hbar\omega_\perp a$. In this case, a harmonically trapped 1D gas will behave like a uniform 1D gas on length scales smaller than the longitudinal harmonic oscillator length $l_\parallel = \sqrt{\hbar/m\omega_\parallel}$, which will naturally be much larger than $l_\perp$, when the 3D s-wave scattering length $a \ll l_\parallel$. However, the one-dimensional scattering length $a_{1\mathrm{D}} = \hbar^2/g$, which is the length scale of interactions between individual atoms in a 1D geometry, will be much larger than $l_\parallel$.

The properties of a uniform 1D gas with repulsive contact interactions at finite temperatures essentially depend on two dimensionless parameters [145], which are the cou-

pling parameter

$$\gamma = \frac{mg}{\hbar^2 n_{1D}}, \tag{2.46}$$

and the reduced temperature

$$\tau = \frac{T}{T_d} = \frac{2mk_BT}{\hbar^2 n_{1D}^2}. \tag{2.47}$$

The quantum degeneracy temperature $T_d = \hbar^2 n_{1D}^2 / 2mk_B$ corresponds to the temperature at which the average spacing between particles is equal to λ_{dB}.

These two parameters can be used to define several regimes, which are characterised by their second-order correlation functions [148]:

- Strong coupling $1 < \gamma < \infty$ gives the Tonks-Girardeau regime. For low temperatures where $\tau \ll \{\gamma^2, 1\}$, impenetrable contact interactions result in the 'fermionisation' of the degenerate Bose gas, for which $0 \leq g^{(2)}(0) < 1$ at finite T. At high temperatures where $\tau > 1$, bosons also act like a non-interacting Fermi gas where $0 \leq g^{(2)}(0) < 1$.

- In the high-temperature decoherent classical regime where $\tau \gg \max\{1, \gamma^2\}$, the thermal de Broglie wavelength is smaller than both the particle spacing and a_{1D}, and the behaviour of an ideal gas ($\gamma = 0$) is essentially recovered where $g^{(2)}(0) \approx 2$ [149]. The in-trap correlation length is $l_{corr} \approx \lambda_{dB}/\sqrt{2\pi}$, and $g^{(2)}(\Delta r) \to 1$ asymptotically over this length scale.

- For weakly coupled degenerate gases $\{\tau, \gamma\} < 1$, there are several regimes (or more accurately, a continuous spectrum of behaviours) which depend on the mechanism by which fluctuations are driven. The degenerate phase correlation length $l_\phi = \hbar^2 n_{1D}/mk_BT$ [146] sets the length scale of local coherence for weakly interacting gases at low temperatures, and the lack of long-range order can be understood from coherence not being able to extend over distances larger than l_ϕ.

  - A mean-field approach can be used for the low-temperature region for where $\tau \ll \gamma \ll 1$ in a similar way to the $T = 0$ limit, where quasi-condensation occurs such that the coherence is dominated by quantum phase fluctuations, and while $g^{(2)}(0) \approx 1$ locally, such clouds do not exhibit long-range order [150].
  - At higher temperatures where $\gamma < \tau < \sqrt{\gamma}$, fluctuations for mean-field quasi-condensates become predominantly thermal and $g^{(2)}(0) \gtrsim 1$.
  - Increasing the temperature further so that $\sqrt{\gamma} \ll \tau \ll 1$ results in the loss of phase coherence, and $g^{(2)}(0) \lesssim 2$ in the decoherent quantum regime. In this case, no quasi-condensate is present, and phase coherence occurs on length scales $l_\phi \sim \xi^{heal}$ such that short range correlations are similar to that of an ideal gas, even in the presence of a significant ground-state population [145].

While the discussion above is valid for trapped Bose gases, it is important to note that measurements of correlation functions are only possible in the far field for our experimental apparatus. This means that the spatial distribution at the detector will correspond to the in-trap momentum distribution. The lack of long-range order in 1D means that $g^{(2)}(\Delta k) \approx 2$ for all weakly-interacting states, and in particular the suppression of density fluctuations for trapped quasicondensates which implies $g^{(2)}(\Delta r) \sim 1$ for

small Δr does not translate to coherence in the far field. Therefore, it can be difficult to distinguish between different regimes by measuring the trapped momentum correlation functions $g^{(2)}(\Delta k)$ in the far field, which is especially so given the lack of sharp phase transitions for 1D gases in the weakly-interacting limit. The only difference between quasicondensates and ideal Bose gases in this case would be the characteristic length of the decay of the $g^{(2)}(\Delta k)$ function, which is $1/2l_\phi$ for the former as opposed to $1/l_\phi$ for the latter.

2.4.2 Transverse condensation of highly anisotropic quantum gases

Most cold-atom experiments trap Bose gases in elongated, 'cigar' shaped traps with cylindrical symmetry where the harmonic trapping frequency in the axial dimension $\omega_\parallel$ is considerably lower than that in the radial direction $\omega_\perp$. While the aspect ratio of these traps $\lambda = \omega_\perp/\omega_\parallel$ is often around 10 to 100, condensates of large numbers of atoms are routinely formed in accordance to the three-dimensional theory presented in §2.3.1 with no noticeable dependence on λ aside from the Thomas Fermi radii. Conversely, the dynamics in the radial dimension can be frozen out when $\hbar\omega_\perp > k_B T_c$, which produces a one-dimensional geometry where atoms do not have enough energy to populate more than one transverse mode, and long-range order is not possible.

Closer inspection of the thermodynamics of elongated Bose gases reveals another mechanism by which the dimensionality of a system can be lowered, where the gas can condense radially while remaining thermal axially, forming a 'multimode condensate' [151]. This so-called 'two-step condensation' occurs in a limited parameter space where the number of atoms in the gas N is slightly higher than the trap aspect ratio, and acts as an intermediate step between thermal and fully condensed gases as temperature is lowered. Note that this does not involve the freezing of dynamics radially, as this would prevent a true 3D BEC from forming at an appropriately low temperature.

For a fixed number of atoms N, any of the three regimes of 'single-mode' (i.e. true 3D) condensation, two-step condensation, and 1D gases can be reached by adjusting the trap aspect ratio $\lambda > 1$. The boundaries between these regimes can be quantified by considering the temperatures at which macroscopic ground state occupation occurs, where we will take T_c^{3D} to be that in Eq. 2.31, while T_c^{1D} is derived from Eq. 2.45, where $T_c^{1D} \approx N\hbar\omega_\parallel/k_B \ln(2N)$ for large N. Two-step condensation requires $T_c^{3D} > T_c^{1D}$ without $\hbar\omega_\perp > k_B T_c^{3D}$, the consequence of which being that the population of states excited in three dimensions saturates to a single state before the population of states excited in only one direction does [151]. As both T_c^{1D} and T_c^{3D} include a factor of N, we can define the range of λ for a given N such that two-step condensation can occur, which is

$$N\left[g_3(1)\right]^{1/2}\left[\ln(2N)\right]^{-3/2} < \lambda < \frac{N}{g_3(1)}. \tag{2.48}$$

Cooling a gas under these conditions will first result in the accumulation of atoms into a state condensed in two dimensions, but excited in the third, which occurs at $T \approx T_c^{3D}$. By further reducing the temperature such that $T < T_c^{1D}$, the atoms finally condensed into the full three-dimensional ground state of the system to form a BEC. It is also important to note that a significant transverse ground state population can be present if the two-step condensation process occurs near the 1D crossover as the temperature is reduced to approach $\hbar\omega_\perp/k_B$.

An experiment which probes this transition is presented in Chapter 5, where mea-

surements of the second-order correlation function show that coherence is established in the transverse direction, while the cloud continues to display bosonic bunching characteristic of thermal clouds in the axial dimension, if the conditions for two-step condensation are satisfied. In addition, the increase in radial transverse correlation length to essentially the size of the cloud allows for higher-order correlation functions to be measured axially with perfect contrast, as is detailed in §4.5.

2.5 Metastable helium

Although most experiments with ultracold atoms are performed with alkali or alkaline earth metals, in principle any bosonic species where the sum of the number of protons, neutrons and electrons in a neutral atom is an even integer can be cooled to quantum degeneracy to form a Bose-Einstein condensate. However, the ability to achieve this in practice depends largely on factors such as the elastic and inelastic collisional properties of a given species, as well as technical limitations such as the availability of stable and narrow linewidth lasers at the desired cooling transition wavelength. If such conditions can be satisfied, the cooling and trapping techniques discussed in the previous section will be effective in increasing the phase-space density of that species such that the phase transition to BEC can occur. Early experiments concentrated on the cooling and trapping of alkali metals[7] due to their simple single valence electron structure, with cooling transitions occurring at visible wavelengths for which lasers are readily available.

As cooling and trapping techniques developed, a greater variety of species have been successfully condensed. Many of these species have unique characteristics making them suitable for particular types of experiments, although some also present considerable challenges. The metastable helium used throughout this thesis is an especially notable case, as while loss due to Penning ionisation was initially thought to be the limiting factor for its cooling, this can be suppressed effectively enough to allow condensation to occur. Furthermore, cold atoms in a metastable state can be detected with single atom resolution, which is pivotal for quantum atom optics experiments such as quantum statistical measurements which will be the focus of much of this thesis.

2.5.1 Unique features of He*

A comprehensive review of metastable noble gases is available in Ref. [152], so only the key features of metastable helium will be mentioned here. At first glance, laser cooling of noble gases seems futile due to transitions from the atomic ground state occurring at extreme ultraviolet wavelengths, for which lasers are not commonly available. However, noble atoms can be excited to a metastable state with a high-voltage discharge or electron bombardment, from which transitions accessible with currently available lasers are present. Bosonic isotopes of noble gases lack hyperfine structure, as they do not carry a net nuclear spin, which simplifies their level structure and avoids the need for atoms to be repumped to close the cooling transition cycle, at the cost of an inability to achieve sub-Doppler cooling. While the outer shell of the core electron levels is not closed, metastable noble gases are quite similar to alkali metals as both have a single

[7] The first attempts of laser cooling were applied to hydrogen, which is chemically similar to alkali metals due to it having a single valence electron. However, as for noble gases, there are no readily accessible cooling transitions from the ground state.

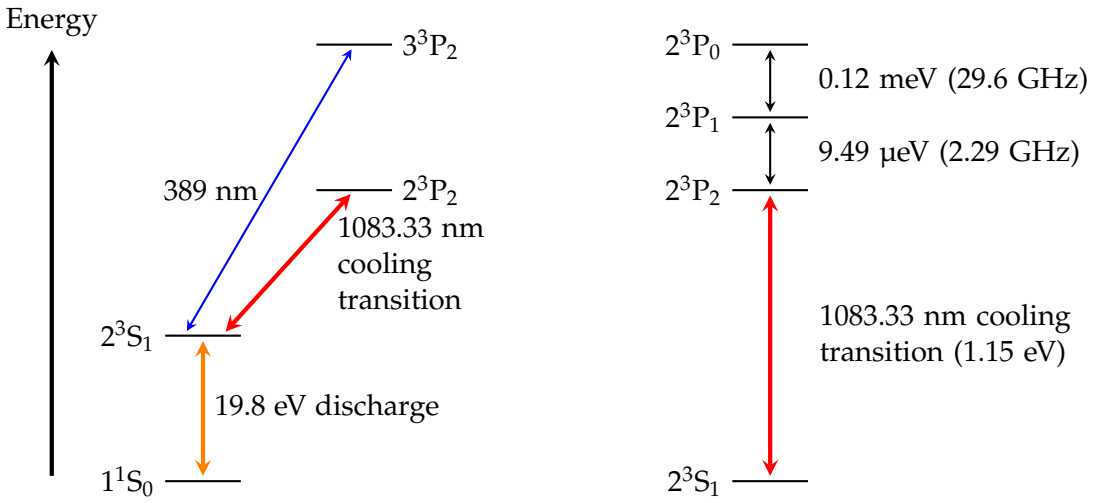

Figure 2.3: The level scheme for helium-4 is shown on the left (not to scale). Although cooling has been achieved for the 389 nm transition (blue), most experiments including all those described in this thesis will cool via the 1083 nm transition indicated in red. On the right, the 2^3P manifold is shown in more detail for the 1083 nm transition (also not to scale). The $2^3S_1 \rightarrow 2^3P_2$ transition is always used for cooling, however the $2^3S_1 \rightarrow 2^3P_1$ and $2^3S_1 \rightarrow 2^3P_0$ transitions, which are also readily accessible with our cooling fibre laser, can be used for Bragg and Raman transitions. Energy levels from `http://physics.nist.gov/PhysRefData/Handbook/Tables/heliumtable5.htm`. The Russell-Saunders spectroscopic notation used here is of the form $n^{2S'+1}L_J$ [119], where capital letters signify a sum over that quantity for all constituent particles, in particular $S' = \sum s$ for both the total spin of the core and valence electron. For states with $J \neq 0$, the degeneracy of different m_J states is lifted by the application of an external magnetic field.

'valence' electron. The level scheme of metastable helium-4 (He*) is illustrated in Fig. 2.3.

Among the metastable states available for bosonic isotopes of noble gases, helium-4 presents the most favourable properties for laser cooling. These include the lowest mass (and thus largest de Broglie wavelength at a given temperature), the simplest electronic structure, the longest-lived metastable state (2^3S_1, at 7870 s [153]), the highest internal energy which gives the best detection efficiency, strong interaction with magnetic fields due to the magnetic moment being two Bohr magnetons, and a low saturation intensity. The decay from the 2^3S_1 metastable state for He* is doubly forbidden by quantum-mechanical selection rules, as while the $2^1S_0 \rightarrow 1^1S_0$ transition is forbidden as angular momentum conservation does not allow spin to be carried away by a photon, $2^3S_1 \rightarrow 1^1S_0$ is suppressed further by spin polarisation in a magnetic field, giving this state a lifetime which is much longer than the duration of any experiment, and thus making it essentially the ground state of the system. In addition, the simple level structure of He* allows various quantum electrodynamical properties of this atom to be calculated very accurately, and compared to experiments.

Helium is the only metastable noble gas to have been cooled to quantum degeneracy thus far, which was first achieved by the École Normale Supérieure [48] and Institut d'Optique [47] groups in 2001. This was followed by condensate of He* by the Vrije

Universiteit group [154], here at ANU [155], and by a buffer gas method at Harvard University [156], while an experiment with ultracold helium has also been established at the University of Vienna [157]. One drawback with the use of He* is that the efficiency of exciting to the metastable state in a discharge source is very low, resulting in an atomic flux much smaller than is easily obtained for a vapour of alkali atoms produced by an oven.

2.5.2 Penning ionisation

The most notable feature of metastable helium is the 19.8 eV of internal energy carried by each atom in the 2^3S_1 state. This energy is enough to cause ionisation or electron ejection after collisions with other He* atoms, background particles, or the vacuum chamber itself, via a process called Penning ionisation. Loss due to collisions with any background atom or molecule X (excluding neon, due to its ionisation energy of 21.6 eV [158]) occurs via the mechanism

$$\mathrm{He}^* + \mathrm{X} \rightarrow \mathrm{He} + \mathrm{X}^+ + \mathrm{e}^-. \tag{2.49}$$

Otherwise, the dominant loss mechanism is Penning ionisation from the collision of two He* atoms via

$$\mathrm{He}^* + \mathrm{He}^* \rightarrow \mathrm{He} + \mathrm{He}^+ + \mathrm{e}^-, \tag{2.50}$$

while the associative Penning ionisation process also occurs at around 5% of the rate of Eq. 2.50 by [159]

$$\mathrm{He}^* + \mathrm{He}^* \rightarrow \mathrm{He}_2^+ + \mathrm{e}^-. \tag{2.51}$$

Other decay mechanisms such as radiative escape and fine structure changing collisions occur at a much smaller rate compared to these processes [159].

This loss can be characterised for a trapped cloud loaded at a rate L by considering the dependence of the population of the cloud as a function of time $N(t)$ as

$$\frac{\mathrm{d}N(t)}{\mathrm{d}t} = L - \alpha N(t) - \beta \int \rho^2(\mathbf{r}, t)\ \mathrm{d}^3\mathbf{r}. \tag{2.52}$$

The single body loss rate α will depend on collisions with background particles (and thus the density of the background gas X in Eq. 2.49, necessitating the attainment of ultra-high vacuum in the trapping chamber), while the two-body loss rate β accounts for Penning losses (Eqs. 2.50 and 2.51). In most cases, the density of the cloud will be small enough for loss due to collisions between three or more bodies to be negligible. By setting $L = 0$ and integrating over the spatial extent of the cloud characterised by an effective volume V, the decay in the cloud population can be found to be [160]

$$N(t) = \frac{2^{3/2}\alpha N(0) V}{[2^{3/2}\alpha V + \beta N(0)] \exp(\alpha t) - \beta N(0)}. \tag{2.53}$$

It was initially thought that the severity of the Penning loss mechanism, with a rate constant calculated to be $\beta > 5 \times 10^{-10}$ cm^{3}s^{-1} [161–163], would prevent the elastic collisions required for evaporative cooling to occur for this species. However, this rate constant can be reduced by five orders of magnitude with the application of an external magnetic field to polarise the spins of the particles [164], which conveniently occurs naturally in a magnetic trap. This suppresses the Penning ionisation process due to

spin conservation in Eqs. 2.50 and 2.51, as while the sum of the spins of the colliding trapped atoms is $S = m_J + m'_J = 2$, the right hand side of these equations has at most $S = 1$ as all the electrons in the ground state helium atoms are paired and antialigned. This reduction of the two-body loss rate for collisions between pairs of spin-aligned He* atoms is sufficient for the elastic collisions required for cooling and trapping to dominate over inelastic collisions. However, the effectiveness of this loss suppression is diminished for metastable noble gases more massive than helium, meaning that condensates for such species has not yet been achieved.

Loss rates for the unsuppressed collision pairs with $S = 0$ such as $(m_J, m'_J) = (0, 0)$ and $(-1, 1)$ result in two-body loss rates $\beta(m_J, m'_J)$ which have been measured to be consistent with theoretical predications at $\beta(0,0) = (6.6 \pm 0.4) \times 10^{-10}$ cm^{3}s^{-1} and $\beta(-1,1) = (7.4 \pm 1.0) \times 10^{-10}$ cm^{3}s^{-1} [165]. Conversely, for spin-polarised helium in the $m_J = 1$ state, theoretical studies have shown that $\beta(1,1) \sim 2 \times 10^{-14}$ cm^{3}s^{-1} [163, 164, 166], while the three-body loss rate is much smaller at $\gamma(1,1) \sim 10^{-26}$ cm^{6}s^{-1} [167, 168], which agrees well with experimental measurements of $\beta(1,1) = (2.9 \pm 2.0) \times 10^{-14}$ cm^{3}s^{-1} and $\gamma(1,1) = (1.2 \pm 0.7) \times 10^{-26}$ cm^{6}s^{-1} [169].

However, it is the large internal energy stored in He* atoms which permits single particle detection via Auger de-excitation (which proceeds in a similar manner to that in Eq. 2.49 for the interaction of He* with the detector surface) where detection systems for charged particles or energetic photons, such as those involving micro-channel plates, can be used. In particular, this gives helium relatively simple and flexible methods of single atom counting with high-resolution three-dimensional information [170], which is a unique feature among species used for quantum atom optics. This will be covered in more detail in §3.3, and is one of the most important considerations which influences the type of experiments performed with this species. In addition to this, we have utilised the Penning ionisation process to induce losses in clouds of He* to produce single atom sources, which is described in §7.2. This is of importance for the fundamental tests of quantum mechanics outlined in the previous sections, and in particular is pivotal to the realisation of Wheeler's delayed choice experiment, as discussed in Chapter 7.

Chapter 3

Experimental apparatus and methods

This chapter will provide a brief overview of the experimental apparatus and methods used to obtain the results described in this thesis. Of particular interest are the features unique to our use of metastable helium (He*), the most important of which being the single atom detection systems utilised. The physical processes resulting in cooling or trapping which were explained in the previous chapter will also be discussed in the applied context of the experimental setup. Each of our experiments will require the creation and subsequent manipulation of ultracold atomic clouds in magnetic and possibly also optical traps, and as trap stability will be a factor crucial to our experimental results, the implementation of several stabilisation mechanisms will also be discussed.

3.1 Helium BEC apparatus

Bose Einstein condensation in He* was first achieved at ANU in 2007 [155], and the experimental process used to produce condensates has remained largely unchanged since. The experimental procedure from which all of our subsequent experiments follow will only be outlined here, while more technical information about the apparatus can be found in the relevant references. The main features of the apparatus are illustrated in Fig. 3.1.

Experimental control

Achieving Bose Einstein condensation for He*, as well as the subsequent manipulation of ultracold clouds to perform novel experiments, requires a large and complicated experimental setup (see Fig. 3.1) which involves several stages of cooling and trapping. However, even the most elaborate of experimental procedures is essentially composed of the precise application of laser light, radio frequency (RF) radiation and magnetic fields to a source of He* atoms, as well as sequences of TTL triggers for various processes such as to initiate detector acquisition. These can be readily manipulated with the use of a desktop computer running National Instruments LabVIEW, which communicates to components in the experiment such as current controllers and acousto-optical modulator (AOM) drivers through a variety of digital and analogue output cards. This setup provides the precision, flexibility and stability over many experimental iterations typically required for our experiments.

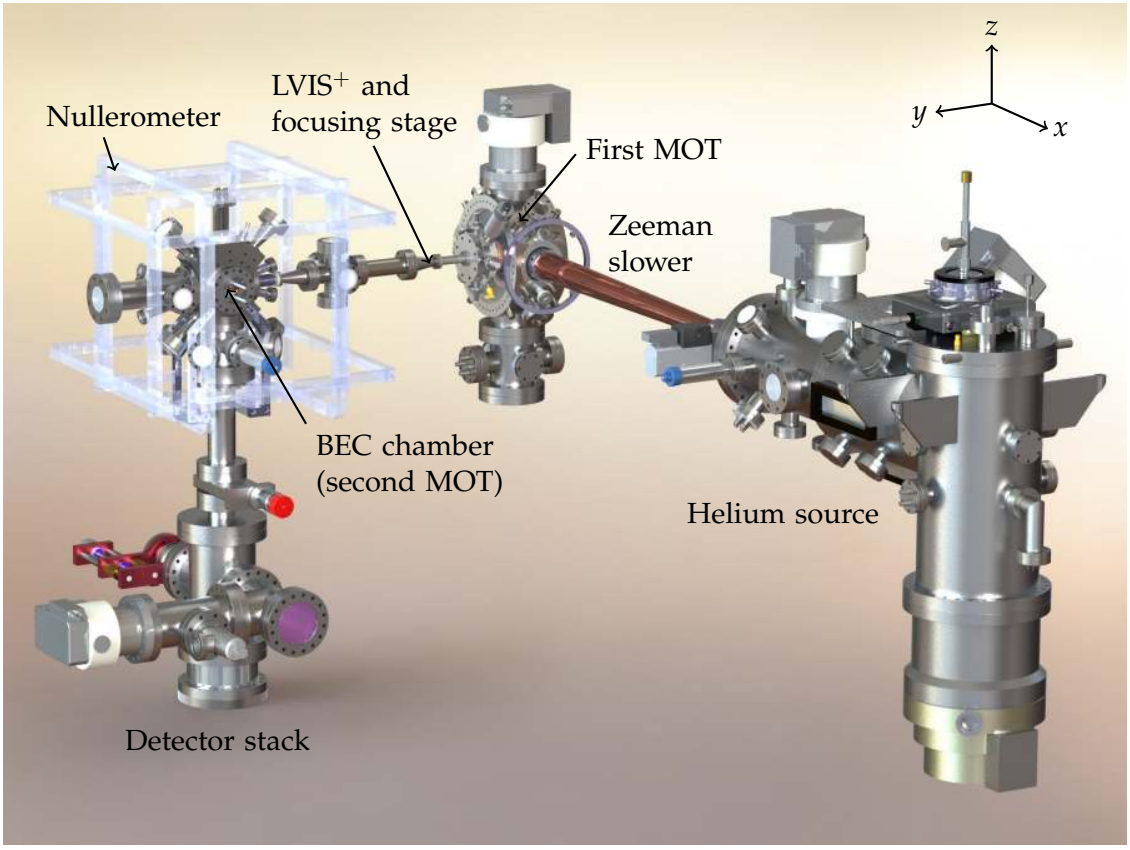

Figure 3.1: Solidworks schematic of the experimental apparatus. A more detailed schematic of the detector stack will be seen later in Fig. 3.8.

Vacuum system

As is the case for any ultracold atomic experiment, and especially so for metastable helium due to collisional losses via Penning ionisation (see §2.5.2), ultra-high vacuum (UHV) pressure must be maintained within the experimental chamber for cooling to occur. However, the excitation of helium from its true ground state to the metastable 2^3S_1 state in our atomic source (described below) is only $\sim$0.01% efficient [152], leaving a large background of other atomic states in the source chamber. Therefore, the experimental apparatus was designed to minimise the background pressure in the chamber where condensation is to be achieved. In addition to the large number of vacuum pumps used to remove particles from the chamber, and differential pumping stages to isolate the later stages from the background at the source, the 'line of sight' from the helium source to the first magneto-optical trap (MOT) is blocked, as is the direct path from the Zeeman slower to the second MOT where the final cooling to quantum degeneracy is performed. Instead, atoms in the desired He* state are selectively manipulated by laser light to pass through small apertures linking the different sections of the vacuum chamber, resulting in a partial pressure of helium below 5×10^{-12} Torr at the second MOT. This is many orders of magnitude better than what is possible further upstream, and is sufficient to allow ultracold atomic clouds with a single-body collisional lifetime of about 60 seconds to be produced.

Cooling laser

Although laser light will interact with the He* atoms to perform cooling at several locations in the experimental apparatus, all of this light is derived from a single 1083 nm 3 Watt fibre laser. This laser is locked to the $2^3S_1 \rightarrow 2^3P_2$ cooling transition, and is split into many arms which have their power and frequency controlled independently with AOMs.

3.1.1 Atomic beam used to load a MOT

Helium source and Zeeman slower

The cooling of our atomic samples starts with high-purity helium-4 gas being injected from a bottle at room temperature into a vacuum chamber cooled by a cryostat, where ground-state helium is excited to the 2^3S_1 state with a DC discharge, as is described in Ref. [171]. At this stage, the background pressure of helium is $\sim 10^{-5}$ Torr. The cryostat is cooled with liquid nitrogen rather than liquid helium, as the latter provides only a modest increase in atomic flux while requiring more frequent replenishment. The beam of helium which exits from the cathode nozzle then passes through a skimmer, followed by a collimation stage consisting of a 2D optical molasses which reduces the velocity spread of atoms in the transverse direction of the beam [172]. After this, a rotated 1D optical molasses stage deflects the beam of atoms in the 2^3S_1 state by $\sim 1.7^\circ$ to pass through a small aperture, while the background of other atomic species remain undeflected and thus removed from the experiment. The beam of atoms exiting the bending stage then passes down a Zeeman slower, which reduces the average longitudinal velocity of the beam from 10^3 ms^{-1} to around 70 ms^{-1} [173], while differential pumping between the source and collimation stage reduces the background pressure to 10^{-7} Torr.

First MOT and LVIS$^+$

The atomic beam is then loaded from the Zeeman slower into the first MOT, where the atoms are trapped and cooled to temperatures of a few mK. As the background pressure at this stage is still too high for a condensate to be formed, a beam of atoms from the first MOT is extracted as a low-velocity intense source (LVIS) [174] and loaded into a second MOT in the BEC chamber. This is achieved by having a mirror and $\lambda/4$ waveplate with a 1.5 mm circular hole to retro-reflect one of the MOT beams under vacuum, where the imbalance in radiation pressure allows very cold atoms to leak through the hole and proceed towards the second MOT at a 90° angle to the Zeeman slower. As with the bending stage, the lack of line of site in addition to the differential pumping after the first MOT allow pressures low enough for a BEC to be formed in the BEC chamber. The LVIS flux is increased by a very weak laser beam used to further imbalance the radiation pressure and 'push' the atoms to create what we call the LVIS$^+$. This loading is aided by a focusing stage, which consists of a 2D optical field and a anti-Helmholtz coil pair, which reduces the divergence of the LVIS$^+$ atomic beam.

Either of two metal tags mounted on translators at different positions inside the vacuum chamber can be inserted into the path of the LVIS$^+$ to measure the atomic flux, as the de-excitation of a He* atom via the Auger process creates a small current which can be read on a picoammeter. These tags, along with similar tags situated after the collimator and Zeeman slower, are invaluable for optimising the loading of the

second MOT, which is typically achieved by fine-tuning the alignment of the cooling laser beams.

Second MOT

As the beam of atoms transferred via the LVIS$^+$ has already been cooled significantly, the capture velocity and volume required to load these atoms into a second MOT is lower than for the first MOT. This allows us to use laser beams and anti-Helmholtz coils with very small radii ($\sim$7 mm) to create the second MOT in the BEC chamber [155]. A loading beam applied at 15° to the horizontal is added to the standard three counterpropagating pairs of beams to increase the loading efficiency. After the second MOT is loaded, a very low intensity ($I \sim 0.01 I_{\text{sat}}$) 1D in-trap Doppler cooling stage is applied to further reduce the temperature of the cloud from 1 mK to around 100 µK. The population of the trapped cloud can be monitored and optimised when required by measuring the amount of resonant light scattered off the trapped cloud with a photodiode.

3.1.2 BiQUIC magnetic trap

Once the second MOT is loaded into the anti-Helmholtz (quadrupole, Q) coil pair of the magnetic trap, a second pair (bias, B) of coils are used to create a purely magnetic trap in the bi-planar quadrupole Ioffe configuration (BiQUIC) [155], as is shown in Fig. 3.2. By minimising the trap coil radius, the amount of current required to provide sufficient magnetic field confinement is also decreased, which results in better trap stability. While other commonly used configurations such as cloverleaf traps typically require current of the order of hundreds of ampere, our BiQUIC trap requires a peak current of 40 A, which significantly reduces temperature fluctuations due to ohmic heating or eddy currents induced upon trap switch-off. The shot-to-shot reproducibility of the magnetic trap is also significantly enhanced by a temperature controlled water cooling system. Although the coils are small in both radius and pair separation (dimensions are specified in Fig. 3.2), which restricts the radius of any laser beam directed at the atom cloud, optical access is still available in each Cartesian axis of the chamber.

This coil configuration typically produces a cigar-shaped trap which has harmonic trapping frequencies of around $\omega_\perp = \omega_x = \omega_z = 2\pi \times 500$ to 550 Hz and $\omega_\parallel = \omega_y = 2\pi \times 50$ to 55 Hz in the radial and axial directions respectively (see Fig. 3.2). These trapping frequencies are measured by sinusoidally modulating the coil current, which results in a loss of atoms from the trap which is greatest when the modulation frequency matches that of the trap confinement. The geometry of the trap can also be adjusted by altering the ratio of currents passing through the two coil pairs, which we use to create a spherical 'sagged' trap with $\omega_x = \omega_z \approx \omega_y \approx 2\pi \times 80$ Hz and a trap centre displaced by several mm from the centre of the cigar-shaped trap, as shown in Fig. 3.2. This 'sagged' configuration is especially useful improving optical access to the magnetically trapped cloud, as is brings the trap centre closer to the middle of the quadrupole coil pair, through which dipole trapping and Bragg scattering beams can be applied, as will be seen in the following sections.

Magnetic trap stabilisation

Both the short-term and long-term stability of our magnetic trap are of vital importance to the quality of experimental results that can be obtained. While the latter is typically

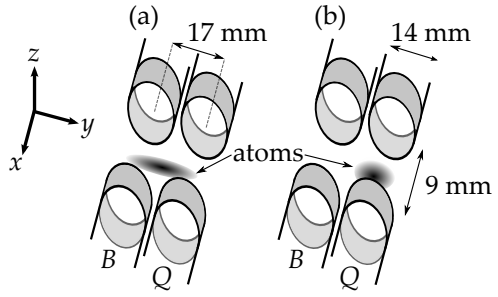

Figure 3.2: BiQUIC magnetic trap with bias (B) and quadrupole (Q) coil pairs, in (a) its normal 'cigar' configuration where the current passing through each coil pair is equal ($I_B = I_Q$), and (b) the 'sagged' configuration where $I_B < I_Q$.

limited by thermal drifts in the trap coils, sources of unwanted external magnetic fields can perturb the trap at both low and high frequencies. Passive solutions to this problem, including the use of mu-metal to shield nearby noise sources such as the turbo pumps, locating other noisy devices (typically involving 50 Hz hum from mains electricity) as far from the BEC chamber as possible, and having the BEC chamber itself made from titanium which has a low magnetic susceptibility, are limited in their success.

A critical feature of our experimental setup is the use of an active magnetic field stabilisation system, which we refer to as our 'nullerometer' [175]. Pickup coils are used to measure AC and DC magnetic field components in each Cartesian axis, and an actively regulated current controller drives Helmholtz coil pairs in each axis to cancel out magnetic field noise at frequencies from 0 Hz to about 3 kHz. This noise reduction is effective to ∼30 μG, or less than 1 kHz in the minimum of the trapping field, where a 1 G field results in a $h \times 2.8$ MHz trap bias energy[1]. The nullerometer also allows the bias magnetic field to be adjusted by a few gauss in each Cartesian axis, and is typically set to produce a trap bottom energy of around $h \times 1$ MHz, as while high bias fields reduce the trap confinement, bias frequencies lower than about 500 kHz leave the trap susceptible to Majorana (spin flip) losses. The direction of this bias field is also important for providing a quantisation axis for Bragg scattering, as will be seen in §7.3.2.

Evaporative cooling

An RF evaporation ramp is then used to continue cooling atoms to quantum degeneracy in the magnetic trap. A ramp defining radiation frequency as a function of time, which is an approximately exponential sweep over 17 seconds, is composed in LabVIEW and used to control an arbitrary waveform generator. The RF radiation is transmitted to an antenna situated in the bias coil of the BiQUIC trap, which outcouples atoms from the trap by spin flipping them into the field-insensitive $m_J = 0$ state. The lowest frequency of this ramp determines the final temperature of the cloud, and can be repeatably controlled to either side of the critical temperature (T_c is typically around 1 μK for our trap) for the formation of a BEC.

After the evaporative cooling process is complete, the trapped cloud of atoms can either be manipulated further – the manner of which is unique to each different experi-

[1]This is due to the gyrofrequency of an electron in a magnetic field being $f_g = qB/2\pi m$ for mass m, charge q and magnetic field B.

mental result – and then dropped under gravity to the detectors below. The properties of the cloud, typically including the temperature and condensate fraction, can be obtained from the density distribution of atoms measured on a variety of detectors in our system, details of which will be given in §3.3.

3.1.3 Optical dipole trap

The use of optical dipole traps can enable a great variety of experiments which require strongly-confining or high aspect-ratio trapping geometries, optical guiding, or the ability to hold atoms in the magnetic field insensitive $m_J = 0$ state, each which will be seen in later chapters of this thesis. Although magnetic traps are usually required to cool atoms to ultracold temperatures, we can transfer atoms from the BiQUIC trap to the focus of one or two laser beams which are red detuned from the atomic cooling transition. As with the magnetic traps, optimising the stability of our dipole traps is of critical importance, especially for correlation measurements which can be obscured by classical noise sources. In addition, the ability to change the trap depth over a wide range is a desirable property of optical traps, and will prove especially useful for creating quantum gases with unique correlation properties.

Dipole trapping lasers

Several different dipole trapping lasers have been used in our experimental setup. However, each are essentially of the same design, being fibre or diode lasers outputting 1550 nm light. This wavelength is far detuned to the red of the cooling transition at 1083 nm, resulting in an attractive trapping potential with minimal spontaneous scattering. The diode laser produces 120 mW beams, and our two different fibre lasers 5 W and 30 W beams respectively, where in general higher powers allow deeper and tighter traps to be easily produced, at the cost of poorer stability. In fact, the 30 W laser proved to be far too unstable to be used for trapping, while the 5 W laser benefited greatly from the installation of an optical isolator to eliminate feedback. While our earlier experiments used a single dipole trap derived from the 120 mW laser, later results which utilised a crossed-beam geometry required a larger amount of laser power, especially since each of the beams were to be derived from the same laser, and thus necessitated the use of the 5 W laser.

Beam setup and dipole trap stabilisation

A simplified schematic of the crossed-beam trap setup is shown in Fig. 3.3, while the single beam setup eliminates the 'horizontal' beam. Light from the fibre laser passes through an optical isolator, and then is telescoped with a lens pair and split into two paths with a polarising beamsplitter and $\lambda/2$ waveplate, the orientation of the latter tuning the power balance between the two arms. In each arm, the light is focused through an AOM which controls the light intensity entering the vacuum chamber, while the undiffracted portion of the beam is blocked by an iris. A small amount of light is picked off after each AOM and measured by a photodiode, while the remainder of each beam is collimated and then passes through a mechanical shutter to be focused into the BEC chamber. The focusing lenses, which are chosen so that the focus of the beam coincides with the centre of the BiQUIC trap, are mounted on linear translation stages incorporating micrometers to allow for precise adjustments to their alignment,

in three dimensions for the vertical beam and one dimension for the horizontal beam. Each of these translators are then locked in position once correctly aligned to reduce beam vibrations.

The intensity of each beam is controlled by the RF power delivered to an AOM by an AOM driver, which consist of an RF source such as a voltage-controlled oscillator (VCO) at the correct driving frequency of the AOM, an RF switch, linear attenuator and amplifier. The attenuation levels are manipulated by proportional-integral (PI) loop circuits which match external set points, typically produced by analogue voltage ramps sent from LabVIEW, with the light level measured on each photodiode. These 'noise-eaters' use operational amplifiers to actively compensate for the difference between the set point and measured light levels, at a bandwidth of $\sim$100 kHz. Each component of the feedback circuit was carefully optimised to maximise the dynamic range and minimise the noise floor of the PI controllers, which were ultimately limited to 2000 and $< 0.1\%$ of maximum power respectively.

Trap geometry

A comprehensive review of the properties of red-detuned optical dipole traps is provided in Ref. [176], the key points of which will be briefly reviewed here. The trap depth and harmonic confinement frequencies for a single, cylindrically-symmetric focused Gaussian beam are essentially set by the waist size and power of the beam. A Gaussian beam of power P propagating in the $\hat{z}$ direction with a focused $1/e^2$ radial spot radius of W_0 and Rayleigh length $z_R = \pi W_0^2/\lambda_{\text{dip}}$ for $\lambda_{\text{dip}} = 1550$ nm will have an intensity profile

$$I(r,z) = \frac{2P}{\pi W(z)} \exp\left(\frac{-2r^2}{W(z)^2}\right), \tag{3.1}$$

where the beam radius is $W(z) = W_0\sqrt{1+(z/z_R)^2}$. The dipole potential due to the red-detuned light field will be [120]

$$U_{\text{dip}}(r,z) = \frac{3\pi c^2}{2\omega_0^3}\frac{\Gamma}{\Delta} I(r,z) = \frac{\hbar\Gamma^2}{8\Delta I_{\text{sat}}} I(r,z), \tag{3.2}$$

where for ^{4}He* the transition linewidth is $\Gamma = 2\pi \times 1.6$ MHz and the saturation intensity is $I_{\text{sat}} = 2.7$ Wm^{-2}. In the absence of gravity, the trap depth will be

$$U_{\text{dip}}(0,0) = \frac{\hbar\Omega^2}{4\Delta}, \tag{3.3}$$

for Rabi frequency $\Omega = \Gamma\sqrt{I_0/2I_{\text{sat}}}$ and detuning $\Delta = \omega_{\text{dip}} - \omega_{\text{trans}}$ of the dipole beam from the atomic transition. As this potential provides a harmonic confinement of the form $U(r,z) \approx U_{\text{dip}}(0,0)\left(1 - 2(r/w_0)^2 - (z/z_R)^2\right)$, we can extract harmonic trapping frequencies

$$\omega_r = \sqrt{\frac{4U_{\text{dip}}(0,0)}{mW_0^2}}, \tag{3.4}$$

$$\omega_z = \sqrt{\frac{2U_{\text{dip}}(0,0)}{mz_R^2}}. \tag{3.5}$$

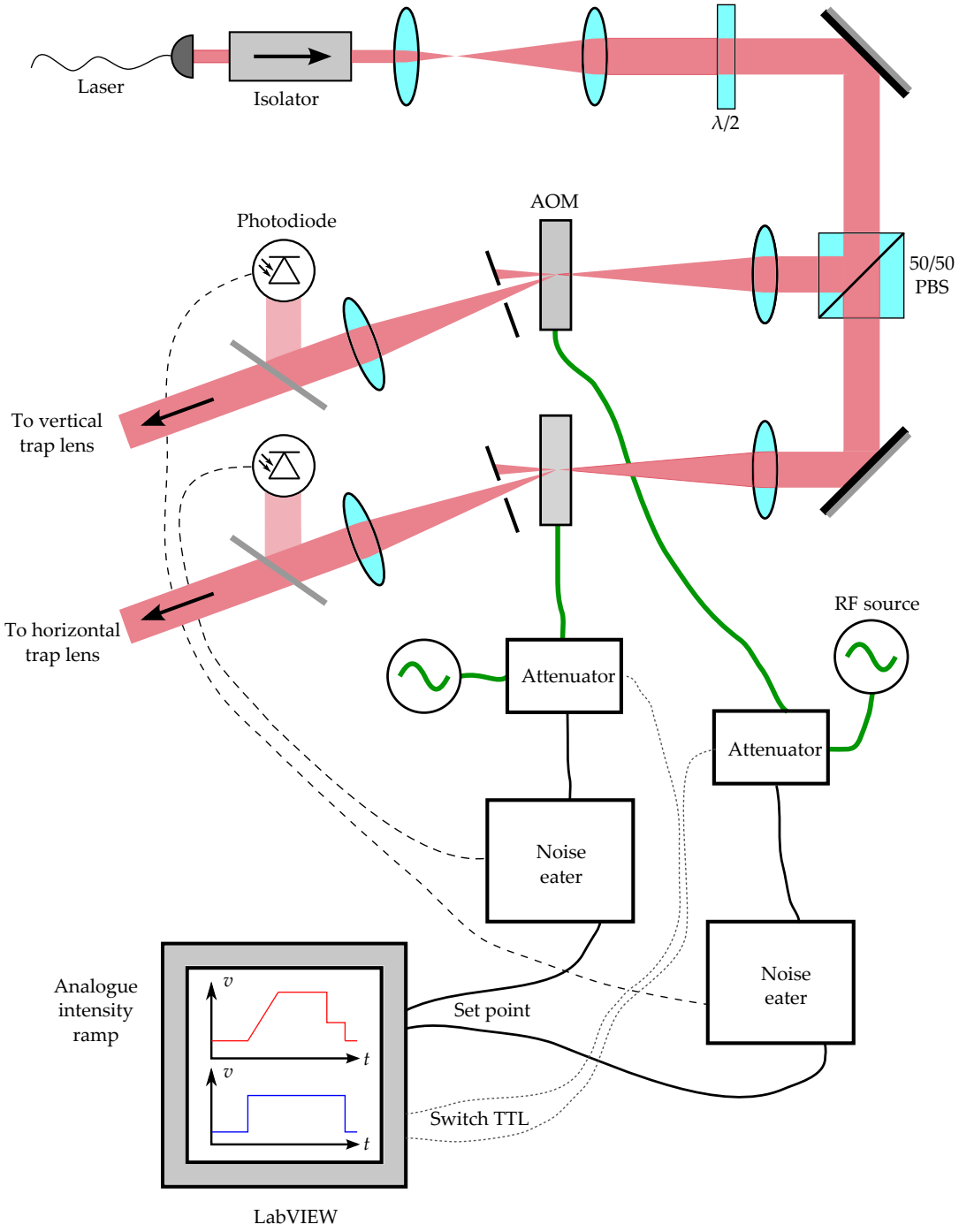

Figure 3.3: Schematic of the twin dipole beam setup, which enters the BEC chamber as shown in Fig. 3.5. The analogue set points and switch TTL waveforms can be controlled independently for the two beams. The AOMs detune the light by around 100 MHz, which is insignificant compared to the $\sim 10^{14}$ Hz detuning between the dipole laser and atomic cooling transition.

We can also include a gravitational potential $U_{\text{grav}}(z) = -mgz$, for gravitational acceleration $g = 9.8$ ms^{-2}, which is important for our vertically-aligned trap where the weak trapping axis is against gravity. In this case, the trap depth is reduced and confinement frequencies become position dependent, although this change is typically no more than 10%. A quadratic fit to the centre of the combined potential will again give the approximate trap frequencies, while the trap depth is the lowest energy required for a particle to escape the trap. This is shown in Fig. 3.4 for a spot size (20 µm) and range of powers powers (5 mW to 50 mW) typical for the vertical beam used in our experiments.

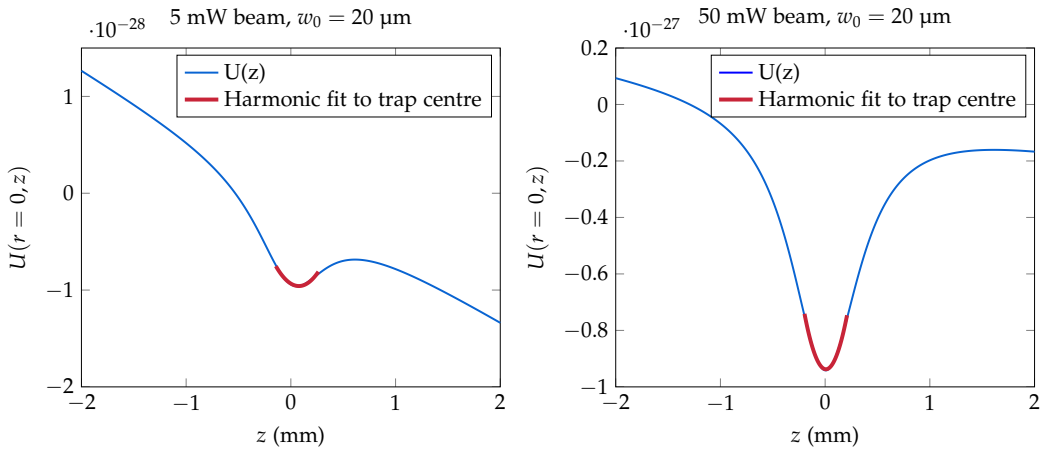

Figure 3.4: Axial potentials for dipole traps sagging under gravity, created with a beam of 1550 nm light with a 20 µm waist. For a 5 mW beam (left), the trap depth $U_{\text{depth}}/k_B \approx 2$ µK, while the trapping frequencies are $\omega_r = 2\pi \times 2.6$ kHz and $\omega_z = 2\pi \times 57$ Hz. For a 50 mW beam (right), the trap depth is 57 µK, and the trapping frequencies are $\omega_r = 2\pi \times 8.5$ kHz and $\omega_z = 2\pi \times 209$ Hz.

The focused spot radius of a collimated beam of radius W_{col} passing through a converging lens with focal length f_0 under the assumptions of standard Gaussian optics is $W_0 = \lambda f_0 / \pi W_{\text{col}}$, to which corrections can be applied for aberrations. Therefore, by measuring either the collimated beam radius or ideally the focused spot size of the beam, in addition to the total beam power, the trap parameters can be determined theoretically. However, the trap frequencies for each optical dipole trap can also be determined empirically by modulating the trap depth, in the same manner as for the magnetic trap. While this technique does not allow the frequencies of a crossed-beam trap to be measured directly, as the two beams intersect at right angles and are of considerably different trapping frequencies, the combined trap confinement can be determined by adding the frequencies of the two individual traps in quadrature.

Optical trapping of atoms

The vertical beam, first collimated to around 15 mm, is focused by either a 150 mm lens mounted above the BEC chamber, or a 75 mm lens inserted in a tube which is positioned close to the re-entrant window above the BiQUIC trap (see Fig. 3.5). This produces a spot of size 20−25 µm which is slightly elliptical due to the diffraction occurring in the AOM. Over a variety of slightly different implementations used for the results in this thesis, the power in the beam is typically less than 100 mW, which gives radial trapping frequencies which can reach ∼10 kHz, while a power of at least ∼5 mW is required to

provide axial confinement of at least 15 Hz which is required to hold the atoms against gravity. The horizontal beam is focused by a 500 mm lens to a 40 to 50 µm $\times \sim$120 µm spot, and provides radial trap frequencies up to $\sim$ 1 kHz at 500 mW.

To load a cloud of atoms into the optical trap, $\sim 10^6$ atoms are first cooled to around $T_c \approx 1$ µK in the magnetic trap. As the depth of a trap (in units of temperature, U_{depth}/k_B) must be at least an order of magnitude greater than the actual temperature of the cloud[2], it would not be possible to capture atoms directly from a MOT without a very powerful laser. After the RF evaporative cooling process, the vertical beam is typically ramped up over $\sim$100 ms to a power of about 60 mW, which provides a confinement of $\omega_r \approx 2\pi\times$ 6 to 7 kHz and $\omega_z \approx 2\pi \times 60$ to 80 Hz. This superposition creates a 'dimple' in the trapping potential, into which a condensate is almost always formed [177, 178].

After switching off the magnetic trap, around 10^4 atoms are held in the optical trap. The cloud can then be evaporatively cooled by ramping down the trap depth over a few 100 ms, which selectively releases the more energetic atoms in a similar fashion to RF evaporative cooling. While held solely in the vertical dipole beam, the atoms are confined at a very high aspect ratio, which is sufficient to allow lower-dimensional effects to be seen, as is investigated in the experiments described in §4.5 and Chapter 5. If instead we want to remain in the 3D regime, the horizontal beam can then be ramped up to typically $\sim$200 to 500 Hz, which allows the vertical beam to be further weakened to a similar radial harmonic frequency, so that the cloud is held in a roughly spherical potential.

3.2 Atom lasers

In general, atoms can be released from a trap by either suddenly switching the trap off, or by some process which outcouples a portion of a cloud from the trap. A review of atom lasers outcoupled from BECs is provided in Ref. [179], while the concept of an atom laser can also be extended to the outcoupling of thermal atoms which is possible by the same mechanisms. Atom lasers themselves can be interesting to study, where for example the correlation function of a pulsed atom laser (which will be covered in §4.2.1) was found to be coherent, which is consistent with the view that atom lasers are the matter wave equivalent of an optical laser and retain the coherence of the BEC from which they are extracted. Conversely, atom lasers can be used as an experimental tool to perform tasks such as outcoupling a small portion of a BEC to prevent the detector saturation that would otherwise occur if the entire cloud was dropped, to deplete the population of the trapped cloud, or to control the energy spread of atoms being measured at the detector. The thermal portion of a cloud can also be selectively outcoupled from the trap, which is particularly useful for experiments where the condensed and thermal portions of the cloud are to be investigated separately.

3.2.1 RF atoms lasers from magnetic traps

While there are many mechanisms by which atoms can be extracted from a magnetic trap, we typically use RF radiation to spin flip atoms to the field-insensitive $m_J = 0$ state in the same manner as for evaporative cooling. In this case, the frequency of RF radiation

[2]This is to ensure that the entire thermal distribution is captured.

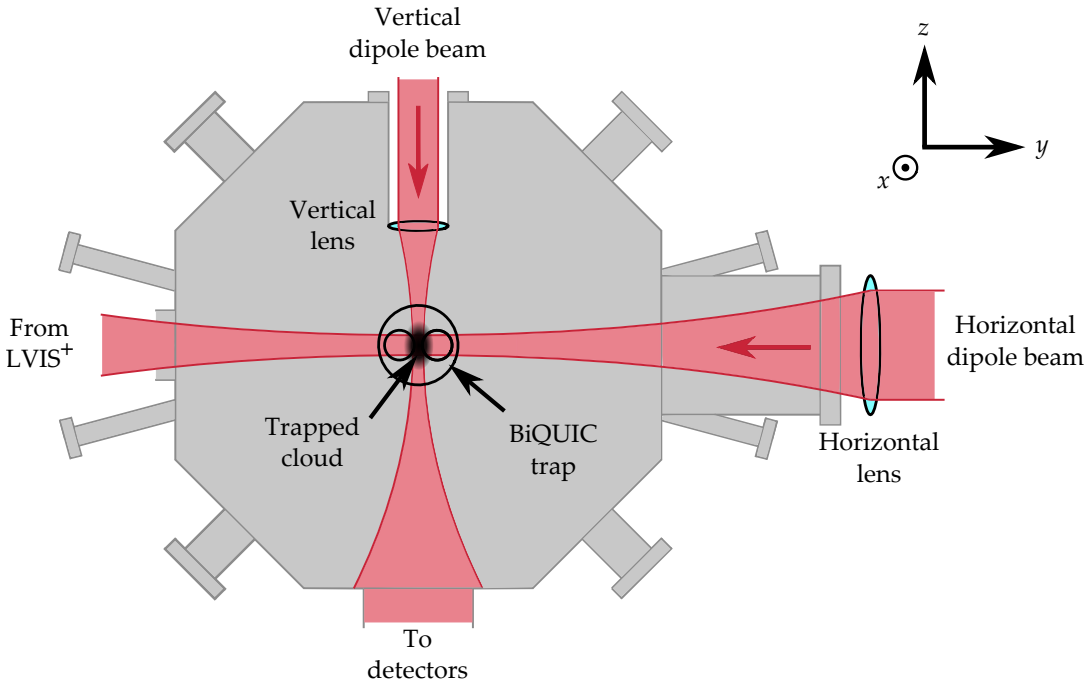

Figure 3.5: Atoms enter from the LVIS$^+$ to be loaded first into the BiQUIC trap inside the BEC chamber, and then transferred into a crossed-beam optical dipole trap. The foci of the vertical and horizontal dipole beams are aligned to coincide with the centre of the magnetic trap. As is depicted, the minimum distance from the trap centre to the vertical and horizontal lenses are approximately 75 mm and 500 mm respectively, while for some experiments a larger diameter $f = 150$ mm lens can be used for the vertical trap by mounting it above the BEC chamber. The cloud transferred to the dipole trap can then either be outcoupled and guided or dropped to the detectors below by lowering or switching off the trapping beam intensity.

applied can selectively outcouple atoms from a particular energy, or equivalently spatial location, within the Thomas-Fermi radius of the BEC. On the other hand, applying short Fourier-broadened pulses of RF can outcouple atoms approximately isotropically over a wide spread in energy. Due to the small mass of helium compared to other commonly laser-cooled atoms such as alkali metals, RF atom lasers tend to 'fountain' out of the trap and produce intensity profiles in the far field containing complicated fringe patterns, which was studied in depth in Ref. [180]. By outcoupling at energies above the chemical potential of the condensate, thermal atoms can be selectively extracted from the trap. These different scenarios are illustrated in Fig. 3.6.

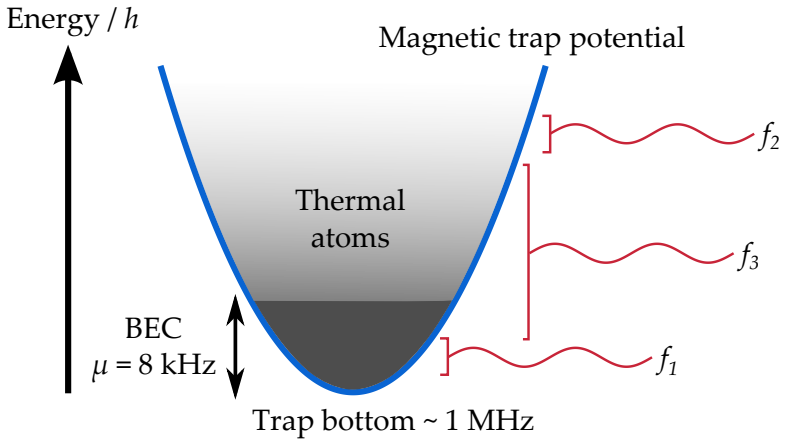

Figure 3.6: A cloud containing condensed (dark grey) and thermal (light grey) components are held in a harmonic magnetic trap (blue line). The red lines represent RF outcoupling over different frequency ($f = E/h$) ranges. Narrowband radiation at f_1 outcouples from within the BEC, and similarly for f_2 from the thermal component, while f_3 is Fourier broadened to outcouple both condensed and thermal atoms. The outcoupling frequencies are offset by the trap bottom, which is typically around 1 MHz. Note that the chemical potential of the BECs formed in our experiment is around $h \times 8$ kHz.

3.2.2 Atom lasers and waveguides from optical dipole traps

As was seen in the previous section, a reduction in dipole beam power leads to a lower trap depth, which can effectively provide a mechanism for evaporative cooling. This process can also be used to selectively outcouple the most energetic portion of the cloud, as is shown in Fig. 3.7. This technique will prove particularly useful for loading atoms into an optical waveguide, where the intensity of the vertical dipole beam is lowered such that it confines the cloud radially yet not axially, as will be seen in the experiments outlined in §§6.2.3 and 6.2.4.

3.3 Detectors for single metastable atoms

The principal motivation for performing quantum atom optics experiments with He* is the unique single atom detection capabilities available for this species. Most ultracold atomic experiments are performed with alkali metals, or less frequently alkaline earth or lanthanide metals, and use the interaction of these atoms with resonant light to perform

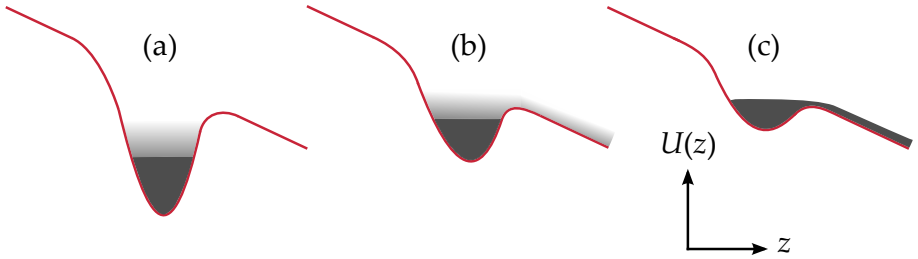

Figure 3.7: Cartoon representation of outcoupling atoms from an optical dipole trap, where the form of the combined optical and gravitational potentials $U(z)$ (red lines) are the same as those shown in Fig. 3.4. In (a), both the condensed (dark grey) and thermal (light grey) atoms are held in the trap. By lowering the trap depth adiabatically, first the thermal (b) and then condensed (c) portions of the cloud are outcoupled.

fluorescence or absorption imaging, while far detuned light can allow phase contrast imaging. An overview of this is presented in Ref. [126], and while in principle such techniques could be employed for the detection of He* atoms, the strong distortion due to radiation pressure suffered by He*, in addition to the poor performance of silicon-based CCD detectors at 1083 nm, has in the past limited the usefulness of imaging He* with resonant light [152]. However, with the increasing availability of high-quality InGaAs cameras, which are far more sensitive at 1083 nm than Si cameras, this form of imaging is beginning to be adopted in the He* community[3]. However, these detection techniques do not typically allow for single atom counting data to be obtained, and while mean-field atom optics effects can readily be observed, the measurement of full quantum statistics is usually not possible. The principal motivation for performing quantum atom optics experiments with He* is the unique single atom detection capabilities available for this species. Most ultracold atomic experiments are performed with alkali metals, or less frequently alkaline earth or lanthanide metals, and use the interaction of these atoms with resonant light to perform fluorescence or absorption imaging, while far detuned light can allow phase contrast imaging. An overview of this is presented in Ref. [126], and while in principle such techniques could be employed for the detection of He* atoms, the strong distortion due to radiation pressure suffered by He*, in addition to the poor performance of silicon-based CCD detectors at 1083 nm, has in the past limited the usefulness of imaging He* with resonant light [152]. However, with the increasing availability of high-quality InGaAs cameras, which are far more sensitive at 1083 nm than Si cameras, this form of imaging is beginning to be adopted in the He* community[4]. However, these detection techniques do not typically allow for single atom counting data to be obtained, and while mean-field atom optics effects can readily be observed, the measurement of full quantum statistics is usually not possible.

Measurements of quantum gases with single atom sensitivity have been possible with a variety of species, using techniques such as coupling to cavities [181, 182] and light sheets [183]. However, the energy stored internally in metastable atoms is sufficient to ionise other atoms or cause electron ejection from materials, and this allows the use

[3]Initial results using these devices by the Vassen (`http://www.nat.vu.nl/~wim/Cold_Atoms/cold2.html`) and Boiron/Westbrook/Aspect (`http://www.lumat.u-psud.fr/IMG/pdf/20120619/LUMAT_19Juin2012.pdf`) groups have been encouraging.

[4]Initial results using these devices by the Vassen (`http://www.nat.vu.nl/~wim/Cold_Atoms/cold2.html`) and Boiron/Westbrook/Aspect (`http://www.lumat.u-psud.fr/IMG/pdf/20120619/LUMAT_19Juin2012.pdf`) groups have been encouraging.

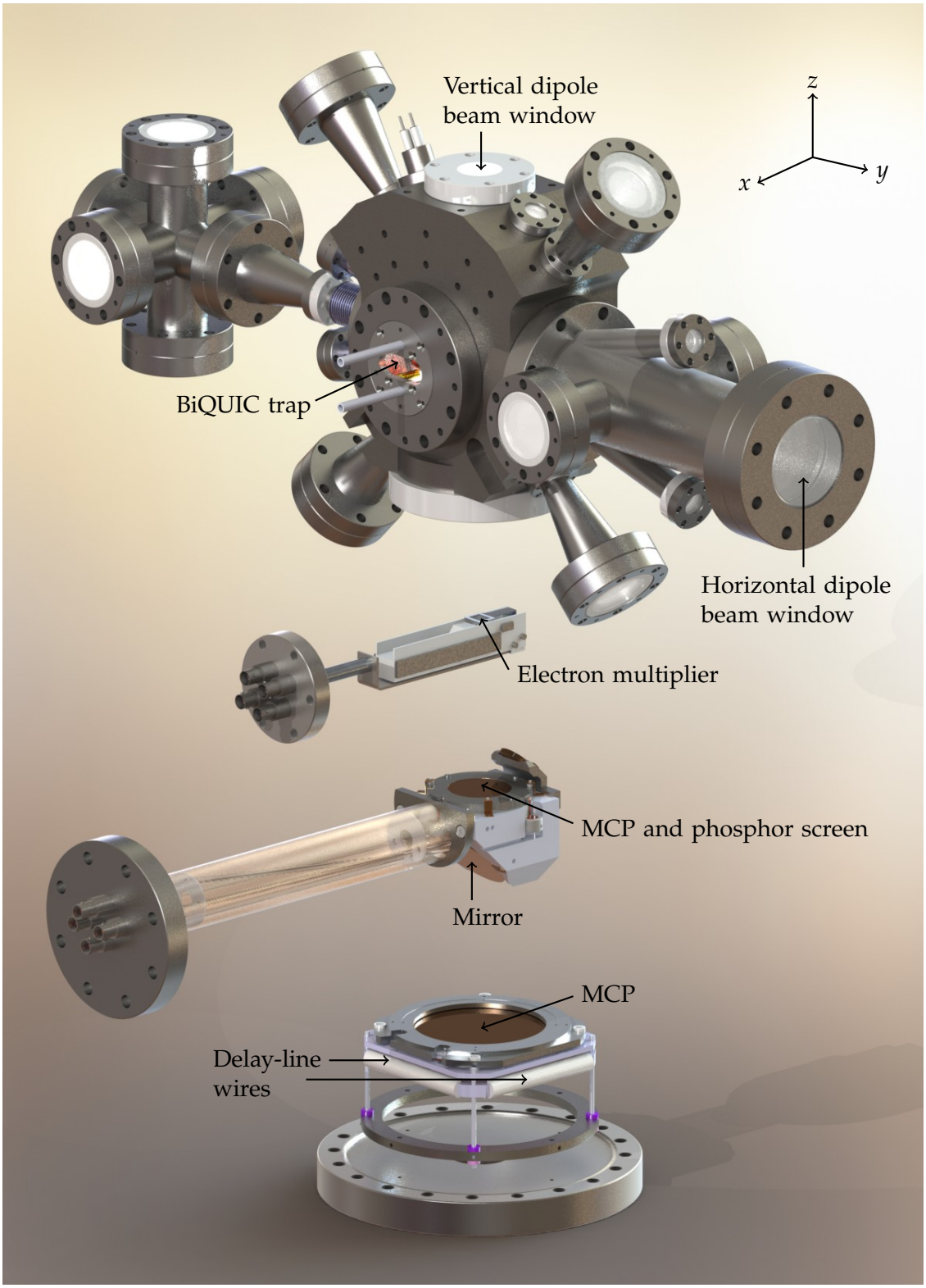

Figure 3.8: Cutaway Solidworks schematic of the detector stack (vertical positions of detectors not to scale). The electron multiplier and phosphor screen detectors are mounted on translators which allow them to be removed or inserted into the flight path of the atoms as they fall under gravity from the trap. The windows through which the vertical and horizontal dipole trapping beams are also indicated to supplement Figs. 3.3 and 3.5.

of detection systems based on electron multipliers, which is summarised in Ref. [152]. Such detectors, which have been commercially developed for applications with charged particles or energetic (UV or X-ray) photons, are appealing due to the flexibility of implementations available, where measurements of quantum gases with good temporal and spatial resolution over large spatial areas with modest incident fluxes are possible. In particular, micro-channel plates (MCPs) are well suited to imaging He* atoms, and a study of their performance with different coating materials and voltage configurations is available in Ref. [184].

Our experimental apparatus primarily makes use of the three different detectors shown in Fig. 3.8, each of which are based on electron multipliers. These detectors posses inherent strengths and weaknesses, and having a variety of detectors with complementary attributes is important for learning about the properties of the quantum gases produced, which is especially true given that we are currently unable to make in-trap measurements of our ultracold clouds.

3.3.1 Electron multiplier

Our discrete dynode electron multiplier, which is mounted approximately 135 mm below the trap, is often the first detector used to characterise the properties of our ultracold gases. Although this detector is not sensitive to spatial information, as it effectively integrates the cloud over a spatial area to give a time-of-flight profile, it has a larger open area fraction and thus higher quantum efficiency than is possible for an MCP, which is essentially a 2D array of electron multipliers. In addition, this detector can operate in either single atom counting (digital) or low-gain analogue modes, the latter of which allows atomic fluxes of up to $\sim 10^9$ Hz to be measured. The electron multiplier is most useful for measuring the temperature of clouds above quantum degeneracy, for investigating high-flux operations such as RF atom lasers outcoupled from the magnetic trap, or for accurately measuring the population of small clouds.

3.3.2 MCP and phosphor screen

An MCP and phosphor screen located $\sim$669 mm below the trap can be used for measurements in the spatial (x-y) plane of the atomic flight path at high flux. The MCP used for this detector, which has a 40 mm diameter and $\sim$50 µm spatial resolution, converts single atoms to spatially-localised charge pulses with a gain which is set by the potential across the MCP stack (typically -1500 V on the front, and ground on the back). These charge pulses are accelerated over 4600 V and collide with the phosphor screen which converts them to visible light, and this light is reflected by a mirror through a window in the vacuum chamber to a CCD camera which captures the illumination pattern.

As the electron multiplier saturates in single atom counting mode once a sizeable condensate fraction is produced, while the phosphor screen can measure flux of up to 10^{10} Hz with high dynamic range in analogue mode, the latter is especially useful for determining the condensate fraction of a cloud below T_c. This is achieved by visualising the bimodal density distribution, as is illustrated in Fig. 3.9. Although single atom counting can in principle be achieved with this detector, it requires both ultrafast cameras to capture the illumination of the screen with good temporal resolution, and extensive computation effort to extract the centroid of each detection event, which makes this approach generally prohibitive.

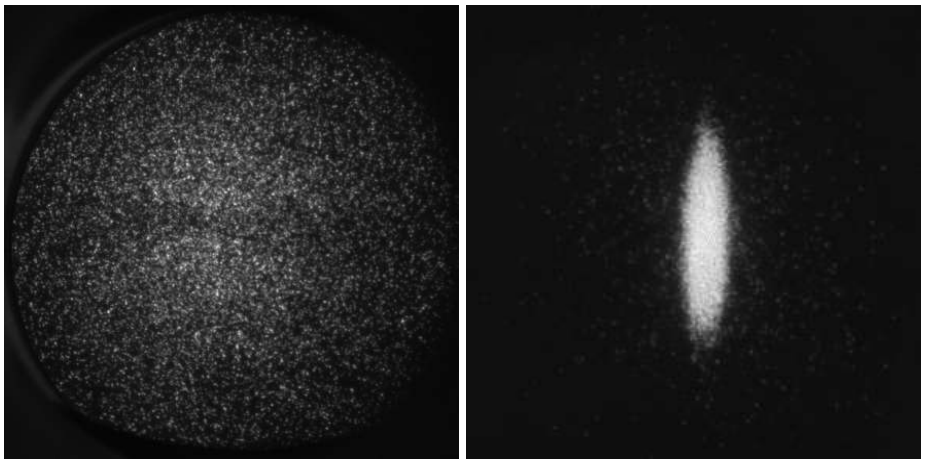

Figure 3.9: Images taken on the MCP and phosphor screen showing uniform illumination for a thermal cloud above the condensation temperature (left), and the Thomas-Fermi profile of a condensate with a small thermal fraction (right). Each glowing 'spot' on the detector represents the arrival of a single atom.

3.3.3 Delay-line detector

DLD apparatus

The use of an MCP and delay-line detector (DLD) allows the information available from the electron multiplier and phosphor screen to be obtained simultaneously for single atoms, making it the ideal detector to record data for quantum atom optics experiments. Photographs of our MCP and Roentdek DLD80 setup, which is mounted 852 mm below the traps, are shown in Fig. 3.10. A pair of 80 mm diameter MCPs with 30 µm pores and 60 µm pore spacing are stacked in the chevron configuration, where a potential of -2 kV is set on the top surface, while the back is grounded. This results in a gain of around 10^6 electrons liberated per incident He* atom, which can be increased to 10^7 if the top voltage is adjusted to -2.4 kV. These spatially-localised pulses of electrons are attracted to an orthogonal pair of helical delay-line anode signal wires, which are set to a potential of 300 V.

After the burst of charge reaches each of the two delay-line wires, a short ($\sim$5 ns wide) pulse of current propagates in both directions down each winding, and the time of arrival of the pulse on each of these four channels (X_1 and X_2 for one winding, and Y_1 and Y_2 for the other) is measured, as is illustrated in Fig. 3.11. Both of the delay-line wire loops actually consist of a pair of wires, where a second reference loop is set to 250 V, and the current pulse is extracted by a differential measurement between the signal and reference wires.

Signal processing

The process which converts the arrival of a current pulse at the end of each wire to a three-dimensional position and time of the atom's arrival is summarised in Fig. 3.12. The analogue signals on each channel of the delay-line wires exit the vacuum chamber via a feedthrough and undergo preamplification before being processed by a constant fraction discriminator (CFD). Single units which perform the preamplification and discrimination of the signal are commercially available, where we have used a Roentdek

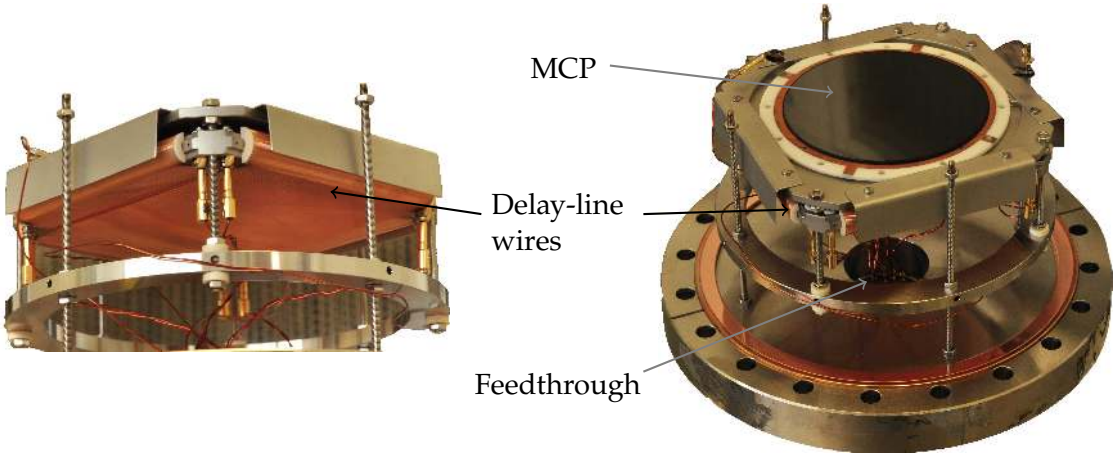

Figure 3.10: The delay-line detector assembly shown from below (left) and above (right). A pair of MCPs sit above the two orthogonal windings of delay-line wires in the chevron configuration. A feedthrough allows voltages to be applied to the MCPs and DLD wires, and carries the signals from the wires to be processed by various electronics.

DLATR-6 for our earlier results, before upgrading to a Roentdek ATR-19. The newer electronics have better specifications, the most noticeable of which being a reduction in cross-talk between the channels.

The amplification of each channel can be set in conjunction with the threshold of the CFD to optimise the ratio of genuine to false counts extracted. As there will naturally be a distribution in pulse amplitudes from the preamplifiers, the CFD is triggered at the zero crossing of the derivative of the signal, so that the pulse shape and not amplitude is what determines whether a count is recorded or not. The output of the CFD is a fast NIM logic pulse, which has a resolution of less than 1 ns and can distinguish between pulses at least 20 ns apart.

This signal is then transmitted to a time-to-digital converter (Roentdek TDC8P),

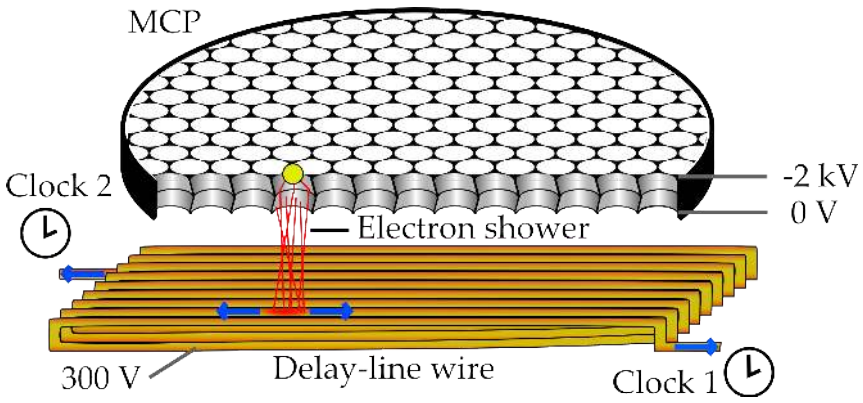

Figure 3.11: Cartoon representation of a single atom detection event on the DLD. A He* atom (yellow sphere) strikes the inside of one of the pores of the MCP stack (shown as a cutaway). This causes a shower of electrons in the pore to be accelerated from the MCP stack to the delay-line wires below (only one of the two windings shown) which are floated at 300 V. This spatially localised cascade of electrons then propagates to each end the wire where the DLD electronics process the signal.

which uses a precise frequency reference to convert the square NIM pulses to digital information containing the channel and a clock timestamp, which has 25 ps time bins and is accurate to 100 ps for signals at least 10 ns apart. The output of this card, which is mounted in a desktop PC, is captured as a text file by a C++ program, from which more meaningful information about the arrival time and position of each atom can be later calculated in C++ or MATLAB.

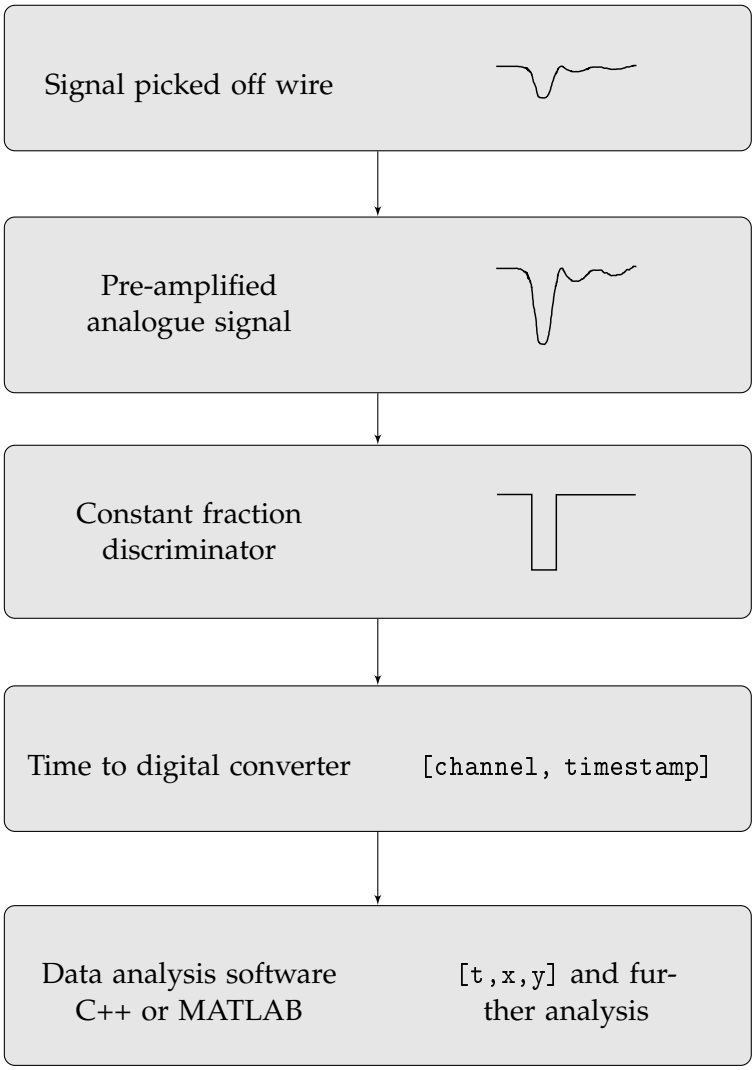

Figure 3.12: Flowchart outlining how signal from the DLD is processed.

Calculation of time and position of arrival for each atom

The data acquisition process is initiated by a master trigger, which provides a common external 'zero' time for each experimental cycle. After this trigger, the three-dimensional time and position of arrival for single atoms (t, x, y) can be uniquely determined from the output of the TDC. An arrival time for each atom can be derived from a signal capacitively picked off the MCP stack itself, which we can consider to be t. The signals registered on each of the four channels X_1, X_2, Y_1 and Y_2 will therefore all be after t, and the difference in time taken for the pulses to arrive at the end of each of the coils will

be proportional to the position of arrival on the MCP. The spatial position of the particle will thus be [170]

$$x = (X_1 - X_2)v_\perp, \tag{3.6}$$
$$y = (Y_1 - Y_2)v_\perp, \tag{3.7}$$

where $v_\perp = 5.26 \times 10^5$ ms^{-1} is the effective propagation velocity of the signal along the wires. Given that the two delay-line wire coils are the same length, the time taken for the signal to traverse along the entire wire length $T_{\text{sum}} = 80$ ns will be a constant, where

$$T_{\text{sum}} = X_1 + X_2 - 2t = Y_1 + Y_2 - 2t, \tag{3.8}$$

independent of arrival time or position. The redundancy in this information is useful for matching the signals for each channel of a given detection event in the high-flux 'multi-hit' regime, where the difference in arrival times for consecutive atoms is less than T_{sum}, or for reconstruction of detection events where only three channels successfully register a signal. However, this also allows us to determine (t, x, y) for each atom without using the MCP signal (Fig. 3.13), which typically has poorer a signal-to-noise ratio than the signals from the delay line wires, the latter being sufficiently reliable and fail for only a few percent of detection events. In this case, we can determine the arrival time from

$$t = \frac{1}{2}\left(X_1 + X_2 - T_{\text{sum}}\right) = \frac{1}{2}\left(Y_1 + Y_2 - T_{\text{sum}}\right). \tag{3.9}$$

In principle, multiple hits separated by at least 10 ns can be distinguished, however we artificially impose a 100 ns electronic dead time to remove false counts due to ringing in the electronics. As the MCP itself saturates when the average interval between successive particles is 1 µs, this restriction does not significantly change the atomic flux measurable.

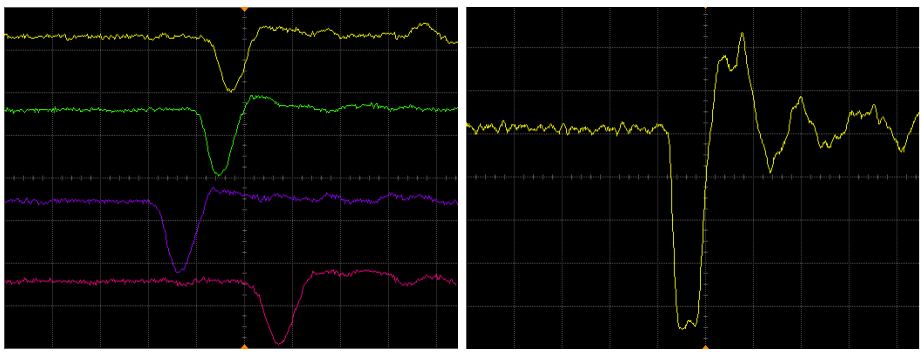

Figure 3.13: Pre-amplified pulses from the four corners of DLD, shown on a 20 ns time scale at 200 mV per division (left). Signal from the MCP is not typically used in data analysis due to the ringing on the pulses, shown with a 20 ns time scale at 100 mV per division (right).

DLD specifications

The spatial resolution of the delay-line detector is quoted by the manufacturer to be < 100 µm with a linearity of 0.2 mm across the 80 mm diameter, a temporal resolution of a few nanoseconds, and a dead time of 20 ns. A calibration aperture mask was used to verify that the resolution is around 130 µm, which is limited by both the MCP pore

size and specifications of the signal processing electronics, with no observable error in linearity.

The maximum flux that can be measured across the entire detector is less than 1 MHz, although the MCPs can be saturated for around 1 ms within the charge depletion area of a pore which detects a single atom. Therefore, there is no hard limit to the flux that can be measured accurately, although severe saturation can be observed in the bulk profile of the cloud for fluxes exceeding 2 MHz. We typically aim to only measure atomic fluxes of less than 1 MHz to avoid this problem. The dark count rate of $\sim$20 Hz across the entire detector is usually negligible for our results, and therefore high-contrast images with minimal noise can usually be produced.

Perhaps the greatest limitation of the delay-line detector system is the quantum efficiency (QE) of detection, which is estimated to be around 20%. While the open area of the MCP stack restricts this to a theoretical maximum of about 50%, another research group which uses a similar detector setup has estimated their QE to have a lower limit of 10% [185]. In principle, this could be directly measured from the single atom source which will be discussed in §7.2, however this test has not yet been undertaken. While a poor QE prevent experiments such as some configurations of loophole-free entanglement measurements from being successfully performed, for each of the results presented in this thesis – in particular, bunching measurements – a low QE only has the effect of reducing data acquisition rates, and has no influence on the conclusions drawn from the data.

Chapter 4

The Hanbury Brown-Twiss effect and higher-order correlation functions

The measurement of quantum correlations in ultracold atoms heralded the genesis of the field of quantum atom optics, just as the first measurements and theoretical treatment of the Hanbury Brown-Twiss effect instigated quantum optics over 50 years ago. In this chapter, several experiments which significantly improved our ability to observe atomic correlation are discussed. In particular, by increasing data acquisition rates and observable bosonic bunching amplitudes, higher-order correlation functions were measured to directly test the validity of Wick's theorem for ultracold atoms.

The experiments described in this chapter have been published in:

- A. G. Manning, S. S. Hodgman, R. G. Dall, M. T. Johnsson, and A. G. Truscott, "The Hanbury Brown-Twiss effect in a pulsed atom laser," *Optics Express* **18**, 18712 (2010).
- S. S. Hodgman, R. G. Dall, A. G. Manning, K. G. H. Baldwin, and A. G. Truscott, "Direct measurement of long-range third-order coherence in Bose-Einstein condensates," *Science* **331**, 1046 (2011).
- A. G. Manning, W. RuGway, S. S. Hodgman, R. G. Dall, K. G. H. Baldwin, and A. G. Truscott, "Third-order spatial correlations for ultracold atoms," *New Journal of Physics* **15**, 013042 (2013).
- R. G. Dall, A. G. Manning, S. S. Hodgman, Wu RuGway, K. V. Kheruntsyan, and A. G. Truscott, "Ideal n-body correlations with massive particles," *Nature Physics* **9**, 341 (2013).

A popular summary of this research is presented in:

- S. S. Hodgman, R. G. Dall, A. G. Manning, M. T. Johnsson, K. G. H. Baldwin, and A. G. Truscott, "Characterizing Atom Sources with Quantum Coherence," *Optics and Photonics News* **22**, Issue 12, pp. 37 (2011).

4.1 Quantum correlations with ultracold atoms

Experiments measuring quantum correlation effects in atomic gases have provided strong evidence that the analogy often drawn between quantum optics and quantum atom optics is appropriate. Dilute ultracold atomic systems, where interactions between atoms are naturally weak, provide an ideal opportunity to not only observe Hanbury Brown-Twiss bunching in bosons, but to investigate a rich variety physical effects which are not possible for photons. These include the comparison of quantum statistics for bosons and fermions, studies of the influence that dimensionality has on quantum statistics, and probing states containing order such as Mott insulators and weakly-bound Feshbach molecules. Alternatively, the ability to tune interactions away from the ideal gas limit also allows novel features such as the 'fermionisation' of bosons in the Tonks-Girardeau regime to be realised.

In addition to the interest in learning about the fundamental coherence of ultracold atoms, there is also a strong motivation to develop correlation function measurements as a tool to reveal new information about atomic systems. However, until recently such measurements have required lengthy data acquisition times and painstaking data analysis to yield correlation function measurements with bunching visibilities which are small compared to the ideal limit of theoretical predictions. This is largely due to the difficulty in measuring individual atoms, which demands the use of detectors which are not suited to imaging the large atomic clouds that we typically create in our magnetic trap (N of order 10^6, $T_c \approx 1\mu$K), where a resolution of order the atomic de Broglie wavelength λ_{dB} would be required to observe bunching in-trap. For example, our experimental setup comprises a microchannel plate (MCP) and delay-line detector (DLD) stack as our primary means for imaging atoms in correlation measurements (please refer to §3.3 for more details). This detection system offers a great deal of flexibility with the types of measurements we can perform, however the limited flux that can be measured ($\sim$1 MHz count rate) and good yet not perfect spatial resolution ($\sim$100 µm, while the temporal resolution is four orders of magnitude better) do not permit the direct measurements of the aforementioned clouds at a resolution of order $\lambda_{\mathrm{dB}} = \hbar\sqrt{2\pi/mk_BT} \sim 1$ µm and where atomic fluxes can exceed 100 MHz. Alternative detection methods also have significant drawbacks, which are outlined in the following sections. Consequently, there have been relatively few experiments undertaken which make use of bunching measurements to probe novel coherence properties of atomic gases.

In the following sections, several experiments which address these limitations are discussed. A unique feature of our He* BEC apparatus is the very large distance ($\sim$850 mm) over which atoms fall under gravity from either a magnetic or optical dipole trap to the DLD. Under most circumstances, this means that we view the cloud in the 'far field' of the trap, where the position distribution of atoms at the detector represents the in-trap momentum distribution. A longer fall time gives a lower energy spread in the cloud per unit volume, which increases the correlation length over which boson bunching can be observed. Ensuring that this correlation length exceeds the spatial resolution of the DLD prevents the bunching signal from being 'washed out', and addressing this issue will prove to be a factor of great importance to the experiments presented in this chapter.

Another consideration is the amount of data needed to measure nth order correlations $g^{(n)}$ with good signal-to-noise, and furthermore the amount of computational effort and difficulty they require to compute. The 'brute force' approach that we took for our earlier results, which typically involved acquiring data over many thousands

of experimental cycles, taking days or weeks to complete, served us well in our initial attempts to measure second- and third-order correlation functions. We were able to increase the effective experimental duty cycle compared to previous experiments by creating a pulsed source from clouds of around 10^6 atoms at temperatures near T_c in our magnetic trap. RF outcoupling was used to release 30 or more pulses of atoms from the trap, which allowed us to acquire data from a larger portion of each ultracold cloud of He* that we produce without experiencing detector saturation. In addition, we were able to verify that this RF outcoupling procedure was coherent, in the sense that the correlation properties of the cloud were unchanged by it. This is of particular interest for the case of a pulsed atom laser, where second order coherence was found to be maintained despite the mean field interactions experienced by the outcoupled atoms. The exceptional stability of our BiQUIC magnetic trap allowed us to extend this procedure to measure the long-range third order correlation function $g^{(3)}(\Delta\mathbf{r}_1, \Delta\mathbf{r}_2)$ with ultracold atoms for the first time. This was found to be consistent with Glauber's theory for thermal clouds, and confirmed that $g^{(n)}(\Delta\mathbf{r}_1, \ldots, \Delta\mathbf{r}_{n-1}) = 1$ holds to order higher than $n = 2$ for the first time in a coherent state of matter such as a BEC. However, data analysis was an onerous task due to the sheer number of atoms required to plot each correlation function in this manner.

In general, the bunching amplitude measured will depend not only on the ratio of correlation length to detector resolution, but also the volume of the bins used to compute the correlation histograms. When searching for n-tuples of atoms to calculate $g^{(n)}(\Delta\mathbf{r})$, we must find n different atoms within a three-dimensional volume such that the particles are separated by no more than the size of the bin in two dimensions, with the third dimension providing the independent variable $\Delta\mathbf{r} = \Delta r\hat{\mathbf{e}}_j$ $(j = x, y, z)$ of the histogram. The size of the bin must be carefully chosen to optimise the signal-to-noise measured for the correlation function. Large bins encompass more atoms and thus reduce statistical errors, but if the bin is large compared to the correlation length then n-tuples of atoms which are not interfering are included, and thus the bunching amplitude measured will be reduced, the basic concept of which is illustrated in Fig. 4.1. Therefore, the greatest improvements in the bunching amplitude measured are the result of increasing the ratio of 'correlation volume' (i.e. the correlation length in each Cartesian axis) to the physical size of the atomic cloud at the detector.

As we will see in §4.1.1, the correlation length after the time of flight to the detector is proportional to the harmonic frequency of the trap from which the atoms are released, and inversely proportional to the square root of temperature. Therefore, releasing atoms from a tighter trap, or cooling to a lower temperature, will produce a source with a larger correlation volume in the far field. Although the lowest thermal temperature possible is obviously limited to T_c, at which point the cloud undergoes the transition to BEC where bunching is no longer present, for clouds in the magnetic trap we can cool to well below our typical $T_c = 1$ μK for $\sim 10^6$ atoms by reducing the number of atoms held in the trap, as $T_c \propto N^{1/3}$. By doing this, we formed small clouds at ~ 95 nK which allowed us to measure amplitudes for $g^{(2)}$ and $g^{(3)}$ at least five times greater than for previous experiments. This experiment was also unique in its measurement of long-range higher-order correlations in the spatial plane of the detector, as opposed to the previous measurements in the time-of-flight axis of the cloud falling under gravity.

However, the most striking improvement in bunching signal measured was achieved by transferring the ultracold atomic cloud from the magnetic trap to an optical dipole trap. Our vertically-aligned dipole trap has a much higher radial confinement than is

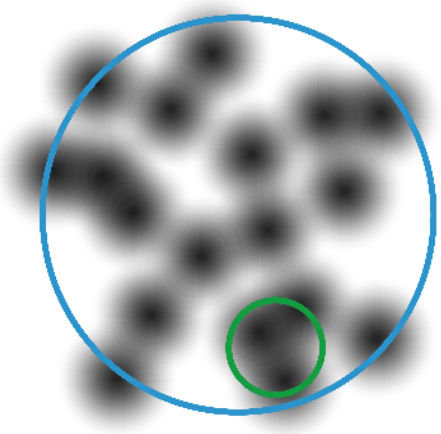

Figure 4.1: For atoms with de Broglie wave packets depicted in black, a large bin size (blue) will capture more n-tuples of particles, but few of the particles within such a bin have overlapping wavefunctions. However, while a smaller bin (green) increases the average interference between atoms landing in such an area, the amount of data required to achieve robust statistics when calculating correlation functions is considerably more than for the larger bin.

possible for the BiQUIC magnetic trap, with the highest tightest trapping frequencies now along the axes of the detector with the poorest resolution, which helps circumvent the limitations of our DLD. In addition, the temperature of clouds held in our dipole trap are typically less than a few tens of nanokelvin, and although this introduced some effects due to one-dimensional physics, it still resulted in bunching according to Glauber's theory. Furthermore, data acquisition rates were considerably improved due to the substantial increase in correlation length. This setup provided us with the ability to measure correlation functions in the ideal limit, where the prediction of Wick's theorem that $g^{(n)}(0) = n!$ was measured directly. Because the correlation length of these clouds in the radial dimension approached the physical size of the cloud, and the computation of correlation functions required smaller numbers of atoms to be measured, we observed correlation functions up to order $n = 6$, which provides the most rigorous test yet of Glauber's theory of quantum statistics.

In addition to the experimental results presented in this chapter, the use of correlation functions as a tool to investigate features of ultracold atomic clouds will be studied in detail in Chapters 5 and 6, and consequently much of what is discussed in the sections below will be relevant to those experiments.

4.1.1 Theoretical modelling of correlation functions for thermal atoms

In this section, we will review extensions to the theory outlined §2.1.1 to include a treatment suitable for noninteracting ultracold atoms in three dimensions. This material is studied in great detail in Ref. [34] and [186], therefore we focus on key points which are relevant to the experimental results discussed in the following sections. The majority of the concepts from the optical case carry over for atoms, while the most obvious difference is the ballistic expansion of atoms as they fall under gravity from the trap to the DLD below. These theoretical studies assume an ideal gas model, which is appropriate for our experimental conditions as the average particle spacing at the detector (of order

100 µm) is much larger than the inter-particle scattering length for He* (7.5 nm).

Bose-Einstein condensates, which are the atomic analogue of an optical laser and are thus the archetype of a coherent state, are theoretically predicted to be coherent to all orders, which is quantified by a complete absence of bunching, where $g^{(n)}(\Delta\mathbf{r}_1,\ldots,\Delta\mathbf{r}_{n-1}) = 1$. In practice, it is difficult to produce atomic systems where $N_0/N = 1$ and there is no thermal component present. However, as the density of the condensed portion of the cloud is much greater than the thermal component (which is especially so in the far field once the atoms have reached the DLD), and the nth order correlation function measures the likelihood of n particles being close together, the contribution from the condensate will almost inevitably dominate the correlation function observed under most circumstances when a macroscopic condensed portion of the cloud is present.

For purely thermal atomic clouds at temperatures well above T_c, we begin by recalling from §2.1.1 the basic form of the second order correlation function $g^{(2)}(\Delta\mathbf{r})$ in the high temperature limit

$$g^{(2)}(\Delta\mathbf{r}) \equiv g^{(2)}(\mathbf{0},\mathbf{r}) = 1 + \frac{\left|G^{(1)}(\mathbf{0},\mathbf{r})\right|^2}{\rho(\mathbf{0})\rho(\mathbf{r})}, \tag{4.1}$$

where $G^{(1)}(\mathbf{0},\mathbf{r})$ is the unnormalised first order correlation function and $\rho(\mathbf{r}) = G^{(1)}(\mathbf{r},\mathbf{r})$ is the density at position $\mathbf{r}$. If the chemical potential of the system is insignificant, $G^{(1)}(\mathbf{0},\mathbf{r})$ takes a Gaussian form with respect to $\mathbf{r} = x\hat{\mathbf{x}} + y\hat{\mathbf{y}} + z\hat{\mathbf{z}}$ which allows us to cast Eq. 4.1 in a simple form in Cartesian coordinates

$$g^{(2)}(\Delta x,\Delta y,\Delta z) = 1 + \exp\left[-\left(\frac{\Delta x}{l_x}\right)^2 - \left(\frac{\Delta y}{l_y}\right)^2 - \left(\frac{\Delta z}{l_z}\right)^2\right], \tag{4.2}$$

for correlation lengths l_j in the j direction. We typically define these coordinate axes to coincide with the trap geometry. Clearly, as the spatial separation between pairs of particles becomes much larger than the corresponding correlation length in each axis, $g^{(2)}(\Delta\mathbf{r}) \to 1$ monotonically and interference is no longer observed.

Glauber's theory also allows correlation functions to be defined to orders higher than $n = 2$ (see §2.1.1), which will be measured in several of the experiments discussed in this chapter. As with the second-order function, these can be decomposed into first-order correlation functions by Wick's theorem, from which we can obtain the third-order function (*cf.* Eq. 2.24)

$$\begin{aligned} g^{(3)}(\Delta\mathbf{r}_1,\Delta\mathbf{r}_2) \equiv g^{(3)}(\mathbf{0},\mathbf{r}_1,\mathbf{r}_2) = {} & \frac{\left|G^{(1)}(\mathbf{0},\mathbf{r}_1)\right|^2}{\rho(\mathbf{0})\rho(\mathbf{r}_1)} + \frac{\left|G^{(1)}(\mathbf{0},\mathbf{r}_2)\right|^2}{\rho(\mathbf{0})\rho(\mathbf{r}_2)} + \frac{\left|G^{(1)}(\mathbf{r}_2,\mathbf{r}_1)\right|^2}{\rho(\mathbf{r}_1)\rho(\mathbf{r}_2)} \\ & + 2\Re\left\{\frac{G^{(1)}(\mathbf{0},\mathbf{r}_1)G^{(1)}(\mathbf{0},\mathbf{r}_2)G^{(1)}(\mathbf{r}_2,\mathbf{r}_1)}{\rho(\mathbf{0})\rho(\mathbf{r}_1)\rho(\mathbf{r}_2)}\right\} + 1. \end{aligned} \tag{4.3}$$

Expressions for the nth order correlation function contains $n!$ terms, so functions for $n > 3$ will not be covered here for the sake of brevity, however they can be derived in the straight forward yet cumbersome manner explained in §A.2. Nevertheless, such correlation functions for thermal distributions continue to take on a form composed of a sum of Gaussian functions which are characterised by the same correlation lengths l_j

as before. For example, the form for the two-body function in Eq. 4.2 can be extended to the third-order correlation function, which for a measurement in the x axis is

$$g^{(3)}(\Delta x_1, \Delta x_2) = 1 + \exp\left[-\left(\frac{\Delta x_1}{l_x}\right)^2\right] + \exp\left[-\left(\frac{\Delta x_2}{l_x}\right)^2\right] + \exp\left[-\left(\frac{\Delta x_1 - \Delta x_2}{l_x}\right)^2\right] + 2\exp\left[-\left(\frac{\Delta x_1}{\sqrt{2}l_x}\right)^2 - \left(\frac{\Delta x_2}{\sqrt{2}l_x}\right)^2 - \left(\frac{\Delta x_1 - \Delta x_2}{\sqrt{2}l_x}\right)^2\right]. \quad (4.4)$$

In particular, it is important to realise that the form of the $g^{(n)}$ function will depend on how the $\Delta\mathbf{r}_j$ are defined. This will be clarified in later sections where correlation functions for $n > 2$ are encountered.

In trap, the correlation length is $l_{x,y,z} = \lambda_{\mathrm{dB}}/\sqrt{2\pi}$ for de Broglie wavelength $\lambda_{\mathrm{dB}} = \hbar\sqrt{2\pi/mk_BT}$, where T is the temperature, k_B the Boltzmann constant, and m the particle mass[1]. As previously mentioned, for ^{4}He at 1 µK (which is a typical temperature for T_c for large clouds in our magnetic trap), $l_{x,y,z}$ is of order one micrometre, which makes bunching very difficult for us to observe in trap. However, by considering the cloud expanding ballistically from a harmonic potential, it is found that the in-trap momentum distribution maps directly to the far field position distribution at the detector. Here, the coordinates for the correlation functions are rescaled from the near field r_j to the far field $\tilde{r}_j$ by $\tilde{r}_j \approx r_j/\omega_j t_{\mathrm{ToF}}$, for trapping frequency ω_j in the j direction, and flight time t_{ToF}, which for our experiment is rather large at 0.416 seconds. In such a case, we can relate the z coordinate, which is by convention parallel to gravity, with an arrival time on the detector such that $z \approx v_z(t - t_0)$ for trap release time t_0 (where $v_z = gt_{\mathrm{ToF}} = 4.08\ \mathrm{ms}^{-1}$ for gravitational acceleration g), and thus $\tilde{t} \approx (t - t_0)/\omega_z t_{\mathrm{ToF}}$.

The correlation lengths in the far field are scaled similarly, where $\tilde{l}_j \approx l_j\omega_j t_{\mathrm{ToF}}$. In practice, our long fall distance ensures that the correlation time $\tilde{t}_c$ is equivalent to $\tilde{l}_z/v_z$. In the high temperature limit, we can equate this with $\tilde{l}_j = p_j t_{\mathrm{ToF}}/m$ for momentum 'correlation length' $p_j = \hbar/s_j$ where $s_j = \sqrt{k_BT/m\omega_j^2}$ is the size of the trapped cloud. This allows us to write the correlation length in a form which clarifies the experimental parameters which influence it, namely

$$\tilde{l}_j = \frac{\hbar t_{\mathrm{ToF}}}{ms_j} = \frac{\hbar t_{\mathrm{ToF}}\omega_j}{\sqrt{mk_BT}}. \quad (4.5)$$

As the trapped size of the cloud s_j is typically the only degree of freedom in an experimental procedure, improving the bunching signal observed will depend on reducing s_j by decreasing the source temperature, and increasing the confinement of the harmonic trap. We can physically interpret this increase in correlation length with fall distance by considering the momentum spread of atoms within a spatial volume of a fixed size. In this case, the correlation length can be written as $\lambda_{\mathrm{dB}}/\sqrt{2\pi} = \hbar/\Delta p_{\mathrm{loc}}$ where Δp_{loc} is the local momentum spread. As the cloud expands, the momentum spread per unit volume decreases as the velocity components separate, decreasing the energy spread per volume. This also illustrates the difference between a dropped cloud and a continuously outcoupled beam of atoms. For the latter, the momentum components in the direction of the beam do not separate, and thus the correlation length in that direction does not increase with distance when falling under gravity, making continuous beams of atoms

[1]The mass of ^{4}He is 6.64×10^{-27} kg.

often unsuitable for correlation measurements. Also, please note that from now on we will no longer denote far field coordinates with a tilde, as all of our measurements are taken in the far field.

4.1.2 Correlation data analysis and Monte Carlo simulations

We now turn our attention to how correlation functions can be computed from experimental data, and also how we can theoretically simulate experimental imperfections which reduce the bunching amplitude measured. Data acquired with the DLD is essentially the arrival time and spatial position of individual atoms as they reach the detector, in the form of a coordinate triplet (t, x, y). As we can only measure atomic densities $\rho(\mathbf{r})$, the nth order correlation function that we compute will be of the form

$$g^{(n)}(\Delta\mathbf{r}_1, \ldots, \Delta\mathbf{r}_{n-1}) = \frac{N \sum_N \langle \rho_N(\mathbf{0}) \rho_N(\mathbf{r}_1) \rho_N(\mathbf{r}_2) \ldots \rho_N(\mathbf{r}_{n-1}) \rangle}{\langle \sum_N \rho_N(\mathbf{0}) \sum_N \rho_N(\mathbf{r}_1) \sum_N \rho_N(\mathbf{r}_2) \ldots \sum_N \rho_N(\mathbf{r}_{n-1}) \rangle}, \tag{4.6}$$

which sums over N realisations of the experiment. Roughly speaking, this gives us the 'average of the correlations' normalised by the 'correlation of the average', where $\langle \ldots \rangle$ is the average over the detector.

However, without arbitrarily large amounts of data available to compute these correlation functions, data must be binned so that the numerator and denominator of Eq. 4.6 take the form of discrete histograms. Essentially, we choose one axis which acts as the independent direction along which we form the histogram (i.e. $|\Delta\mathbf{r}| = \Delta r_j$ for $j \in (t, x, y)$), and form a bin in the plane orthogonal to this direction. For example, if we take $j = t$, then to compute $g^{(2)}(\Delta t)$ we determine if the separation in the x-y plane between each a pair of atoms is less than a set distance (the 'bin size'): if so, a count is added to the histogram array element appropriate for the temporal separation Δt between the two atoms; while if the x-y separation is too large, the pair of atoms is discarded from the correlation measurement. In effect, we bin in all three dimensions, however the bin size in the dimension of the histogram (in this example, t) must be much smaller than the correlation length in that dimension, otherwise no bunching will be observed.

The procedure is extended to higher-order correlation functions by repeating this process for the separation between first and second, second and third, and so on for pairs within an n-tuples of atoms. This has the effect of integrating the correlation function Eq. 4.6 over the bin volume in space:

$$g^{(n)}(\Delta r_{j,1}, \ldots, \Delta r_{j,n-1}) = \frac{N \int_{\text{bin}} \sum_N \langle \rho_N(\mathbf{0}) \rho_N(\mathbf{r}_1) \rho_N(\mathbf{r}_2) \ldots \rho_N(\mathbf{r}_{n-1}) \rangle \, \mathrm{d}^3\mathbf{r}}{\int_{\text{bin}} \langle \sum_N \rho_N(\mathbf{0}) \sum_N \rho_N(\mathbf{r}_1) \sum_N \rho_N(\mathbf{r}_2) \ldots \sum_N \rho_N(\mathbf{r}_{n-1}) \rangle \, \mathrm{d}^3\mathbf{r}}. \tag{4.7}$$

The difference between the numerator and denominator of Eq. 4.7 is that the numerator only searches for n-tuples of counts within a single experimental iteration, while the denominator finds n-tuples over an entire ensemble of realisations. In effect, the former only looks for groups of atoms which could possibly interfere, while the latter will provide a bulk density correlation profile in the absence of any bunching, which allows us to normalise $g^{(n)}$.

By integrating the correlation function over the bin volume, its average value will be decreased as the interference monotonically reduces at larger separations. In particular, if the size of the bin is large compared to the correlation length discussed in §4.1.1, the contrast C of the measured correlation function in the j direction $g_m^{(2)}(\Delta r_j)$ will be

reduced from its ideal theoretical value $C=1$, such that Eq. 4.2 is altered to

$$g_m^{(2)}(\Delta r_j) = 1 + C \exp\left[-\left(\frac{\Delta r_j}{l_j}\right)^2\right], \tag{4.8}$$

for some value of bunching amplitude C between 0 and 1. An example of the dependence of C on the bin size in one dimension is illustrated in Fig. 4.2, while some actual experimental data analysed with different bin sizes is shown in Fig. 4.3.

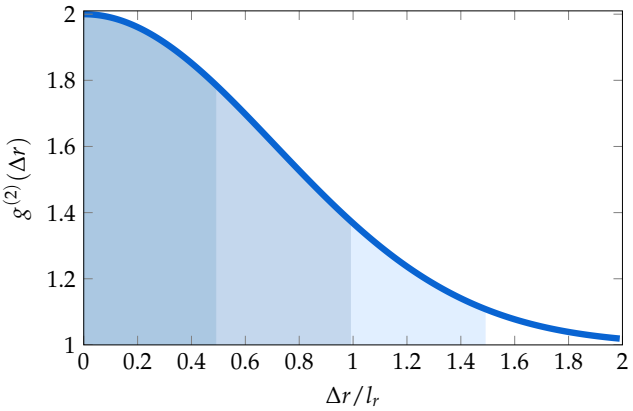

Figure 4.2: If we average a generic form for $g^{(2)}(\Delta r)$ over different domains, we can see how changing the bin size in one dimension will effect the bunching contrast C. If our bin size R is $0.5l_r$, we can expect $C = 0.907$, while for $R = l_r$ we have $C = 0.743$, $R = 1.5l_r$ gives $C = 0.570$ and $R = 2l_r$ gives $C = 0.441$. When binning in three dimensions, the decrease in C with larger bins is even more severe.

This analysis provides the basis for our theoretical modelling of the atomic systems studied experimentally, and typically is found to be in good agreement with the correlation functions obtained from our measurements. However, although this accounts for the most significant cause of bunching contrast reduction seen in our data, there are a few additional factors which become important for understanding why our pulsed atomic source data has a low bunching contrast. These include the effects of local detector saturation, where there is a reduced likelihood of measuring multiple particles at separations of order the spatial MCP pore centre-spacing (60 µm) or the electronic dead time (100 ns). The finite spatial resolution of the DLD, while typically smaller that the bin radius in our data analysis, can 'smear out' the spatial distribution of atoms measured on the detector and make pairs of atoms appear to be separated by slightly larger distances than they actually are, can also be included.

These effects are incorporated in a Monte Carlo simulation of the integrated correlation function[2] in the form of Eq. 4.7 to calculate the expected value of the bunching amplitude C for a given experimental setup. We can ensure that the effect of these well-known parameters on the model is generally minor by allowing them to vary within experimentally realistic ranges. Generally, it is local saturation which has the greatest impact on the value of C calculated, while the other parameters cause smaller changes.

It is also important to be aware that the higher-order correlation functions mea-

[2]This is favoured over an analytic model as the integrals are over non-trivial domains, especially for higher-order correlation functions, and thus become cumbersome to compute.

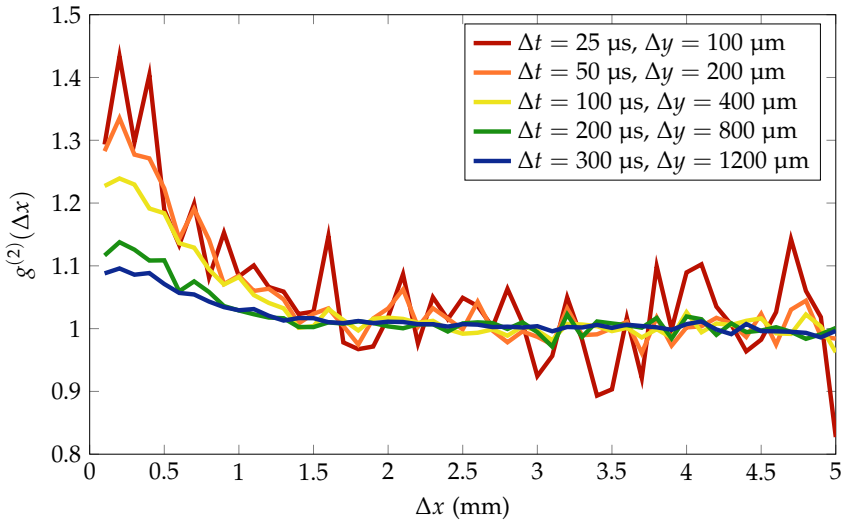

Figure 4.3: The effect of bin size on the correlation function measured, illustrated by calculating $g^{(2)}(\Delta x)$ with actual data from the experiment detailed in §4.4. The correlation lengths for this data are $l_t = 300$ µs and $l_y = 120$ µm. The smallest bins (red) result in the largest bunching contrast, but also a large amount of statistical noise, while the smallest bins (blue) give the lowest amount of scatter and the smallest value of C. The best choice of bin size will maximise the ratio of C to shot noise.

sured or simulated may change in appearance depending on the definition of independent variables Δr_i or Δt_i along which the histograms are calculated. In particular, we typically plot higher-order functions $g^{(n)}(\Delta r_1, \ldots, \Delta r_n)$ as a diagonal cross-section $g^{(n)}(\Delta r) = g^{(n)}(\Delta r, \ldots, \Delta r)$ due to our inability to visualise plots in higher dimensions. If we are to for example compute $g^{(3)}(\Delta t_1, \Delta t_2)$ for a triplet of particles arriving at times t_1, t_2 and t_3, defining $\Delta t_2 = t_3 - t_1$ rather than $\Delta t_2 = t_3 - t_2$, or substituting $|\Delta r|$ for Δr, will change the form of the correlation function. In particular, the two-body correlation length l_c may no longer be extracted from a Gaussian fit to $g^{(n)}(\Delta r)$, depending on the definition of each Δr_i in Eq. 4.4. While the two-body correlation length is the quantity of most obvious physical significance, ensuring that the form of the correlation function does not change qualitatively with small adjustments to the data analysis parameters such as bin sizes is a useful diagnostic to distinguish genuine bunching from systematic errors.

A final preliminary consideration which is worthwhile to mention is the effect of detector quantum efficiency on the correlation functions measured experimentally. One might naïvely consider that correlation functions are composed of well-defined n-tuples of particles, where the failure to measure a particle will reduce the bunching contrast C measured. However, bunching in the normalised correlation function will exist irrespective of a random and isotropic failure to detect individual atoms. As we recall from §2.1.1, a source which distinguishes individual particles will have different quantum statistics to the sources used for the results obtained for this thesis, which are indistinguishable bosons. Naturally, this is no longer true for sources with unique properties such as those displaying number squeezing due to a pair-production process [185]. So, while our detector efficiency is around 20%, this only results in a slower data acquisition rate.

Under some circumstances, effects such as trap instabilities and temperature fluctua-

tions can present themselves as a correlation signal which mimics bosonic bunching. To distinguish these effects from genuine quantum interference, it is important to select an appropriate length scale over which to investigate the correlation function and integrate the bins of the histogram. By choosing a bin size of order the extent of such a source of fluctuations, it is possible to exaggerate its effect on the measurement of $g^{(n)}$. The dependence of the bunching contrast C on the bin volume can actually provide a valuable diagnostic for this, as C failing to change in the expected manner with different bin sizes can indicate that extraneous effects are influencing the correlation function computed. Fig. 4.3 illustrates this effect in the limit where the bin size is the dominant factor which determines the observed bunching contrast.

4.1.3 Previous atomic correlation measurements

It is only with recent advances in atomic cooling and single particle detection that bosonic bunching has been observed with neutral atoms. Such measurements have been achieved with a variety of atomic species and detection methods, a brief summary of which will be given here. The key points which determine the success of these experiments are the comparison of the correlation volume of the atomic source, and the detection and data analysis method used. Correlation measurements in ultracold atoms offer a rich variety of different behaviours, many of which are not possible for optical sources, such as dependence on trapping geometries and dimensionalities, the presence of interactions, and the comparison of bosonic and fermionic statistics.

First-order coherence

Although we consider Bose-Einstein condensates to be a coherent state, analogous to the optical laser, early experiments only revealed the anisotropic density distribution typical of a condensed cloud, and were unable to test the coherence or long-range order of such a cloud. To probe the quantum nature of a BEC, an important step is to demonstrate first-order or phase coherence, which as we saw in §2.1.1 is a necessary but not sufficient criteria for establishing that a BEC is a truly coherent state. This was first achieved by creating two spatially separated condensates, and allowing them to interfere and produce a high-contrast fringe pattern in the resulting density profile [187] in a similar manner to Young's double slit experiment. The fringe pattern extended across a large portion of the spatial profile of the cloud, which strongly suggested that long-range order is present in a BEC. Further studies utilising Bragg spectroscopy showed that phase coherence does indeed exist over the entire condensate [188, 189]. Among other experiments which used measurements of first-order coherence to probe the state of matter waves, a guided atom laser was diffracted by a transmission grating to produce a distinctive interference pattern [190], which is a topic that will be studied in more detail in §6.1.

First observation of two-body bunching in metastable neon

The first measurement of the Hanbury Brown-Twiss effect with atoms was achieved with a beam of metastable neon [54], an atomic species which shares many properties with He* such as the ability to use microchannel plates to detect individual atoms [152]. As neon has not yet been cooled to quantum degeneracy, the atomic source used for this

experiment was restricted to the relatively high temperature attainable for a magneto-optical trap (MOT) of order millikelvin, and therefore the correlation length over which bunching can be observed was very small. This resulted in significant experimental challenges, such as the need to carefully engineer the detection system to match the wavefront of the atomic beam, and a lengthy data acquisition process to achieve even a qualitative indication of bosonic bunching, which makes this observation all the more remarkable. However, this style of experiment was superseded in favour of experiments using sources with much larger correlation lengths.

Hanbury Brown-Twiss effect and fermionic antibunching in metastable helium

As clouds of metastable helium can be cooled to temperatures where the correlation length is large compared to the resolution of detectors with single atom sensitivity, it is an ideal species for correlation measurements. A milestone experiment which built upon the observation of bunching in a beam of neon was the use of clouds of ultracold ^{4}He* dropped under gravity onto an MCP and delay-line detector to quantitatively compare the second order correlation function for Bose condensed and thermal atomic clouds [55]. By directly comparing the bunching signal for thermal atoms to the second-order coherence of the BEC, the quantum coherence of a condensate was unambiguously established. Similarly, the uniquely quantum-mechanical behaviour of 'anti-bunching' was observed in a thermal source of fermionic ^{3}He* using a similar experimental technique [56].

Continuous beams of rubidium measured with a cavity

The time-of-flight flux of single atoms can also be detected with a high-finesse cavity, which was used to measure the quantum statistics of a beam of ^{87}Rb atoms outcoupled from a magnetic trap with RF radiation [182]. Although measuring single atoms in such a way is a considerable feat due to the precise engineering required, there are several disadvantages which prevent this method from being a useful generally-applicable tool for measuring correlation functions. The small size of the cavity restricts the portion of atomic flux captured, while a lack of spatial selectivity and a dead time many orders of magnitude higher than for a MCP-DLD system are still incurred. Thermal bunching could therefore not be measured with this setup, due to the correlation function washing out to $C = 0$ over the area of the cavity. However, a pseudothermal beam was produced from a condensed source by outcoupling atoms with narrowband RF radiation carrying random noise to produce a beam with a small enough energy spread to observe a bunching signal, which was in contrast to a coherent atom laser which showed no bunching. While this did not directly compare the quantum statistics of thermal and condensed sources, it does highlight that the energy spread of the source determines the bunching signal observed.

Underlying structure such as lattices and molecules

The measurement of higher-order correlation functions can be used to extract information from an atomic system that phase interferometry cannot reveal. Such measurements can not only be derived from single atom counting measurements, but also from the autocorrelation of atomic shot noise present in absorption imaging [191]. A particularly striking example of this is when there is underlying structure to an atomic sample in

position space in the near field, which is obscured in a density measurement in the far field which represents the in-trap momentum distribution. The array structure of ^{87}Rb atoms released from an optical lattice in the Mott insulator regime has been recovered by computing the spatial correlation function in the far field, where a correlation function showing a high-contrast array of localised bunching peaks was retrieved from a featureless density absorption image [192], and similarly for anti-bunching in ^{40}K [89].

Structure in an atomic cloud can also exist due to the pairing of weakly-bound molecules coupled by a magnetic-field Feshbach resonance. When such molecules dissociate, the two atoms of different spin states which constituted the pair will be correlated. This is clearly observed in an experiment using absorption imaging to detect pairs of ^{40}K atoms [90], where a strong noise interference peak is seen in the spatial correlations between atoms in these two spin states.

Investigation of coherence across the BEC threshold

The emergence of phase (first-order) coherence as a Bose gas is cooled below the condensation temperature was demonstrated by measuring the visibility of a 'double-slit' style experiment which outcoupled atoms from a trap simultaneously at two different RF frequencies [193]. The beating of these two outcoupled matter wave beams creates an interference pattern in a similar way to Young's experiment, with a visibility dependent on both the energy separation of the two beams and the temperature of the cloud. While fringes with relatively low visibility were observed for clouds with $T > T_c$ over small energy separations, highly visible fringes at larger separations became apparent as the cloud is cooled to quantum degeneracy. This is analogous to the comparison of incoherent light, which can exhibit limited coherence for sources with a sufficiently narrow bandwidth, with truly coherent light which possesses true long-range order.

Although the coherence properties of noninteracting ultracold Bose gases are well understood in both the high temperature $T \gg T_c$ and well below BEC threshold $T \ll T_c$ limits, complications arise which require modifications to the correlation function theory presented above for temperatures around T_c. This was investigated for ^{87}Rb released from a chip trap capable of creating confining potentials ranging from the 3D to quasi-1D geometries, where Hanbury-Brown Twiss bunching was measured as a function of T/T_c using fluorescence imaging [194]. The study concluded that bunching was observed for each geometry at temperatures below T_c, which was attributed to a persistent multimode state occupation in the weak (x) axis of the cigar-shaped trap. This may occur due to the presence of 1D characteristics for the trapped gas in all geometries, given the smooth transition between the ideal Bose gas and quasicondensate regimes for an elongated gas as is discussed in §2.4.1. Furthermore, a dip of $g^{(2)}(0 < \Delta x < l_x) < 1$ became increasingly pronounced at lower temperatures below T_c due to the beating of different axial modes, which is in contrast to many other experiments which report that $g^{(2)}(\Delta r) = 1$ for essentially any cloud with a macroscopic ground-state occupation.

4.2 Hanbury Brown-Twiss correlations in a pulsed atomic source

Our first experimental measurement of quantum correlation functions was made by outcoupling atoms from an ultracold cloud held in a magnetic trap. With this procedure,

we were able to test the coherence of an atom laser outcoupled isotropically with radio frequency (RF) radiation (see §3.2.1), and directly compare this with the bunching observed in a pulsed thermal source. By outcoupling from the cloud isotropically, rather than from a spatially localised region, we are better able to test the long-range order of the entire cloud, and also confirm that the mean-field interactions experienced by the atoms during outcoupling do not alter their correlation properties. This procedure also has the practical benefit of acquiring experimental data much quicker than was possible in previous correlation measurements with dropped clouds of He* [55].

4.2.1 Experimental method

As will be the case with every result presented in this thesis, we began by cooling a cloud of He* to a temperature near the BEC critical temperature of our magnetic trap, where $T_c \sim 600$ nK for this particular experiment, as described in §3.1.2 and Ref. [155]. Such clouds typically contained around 10^6 atoms held with harmonic trapping frequencies $\left(\omega_x, \omega_y, \omega_z\right) = 2\pi \times (500, 50, 500)$ Hz. Whether we cooled to above or below T_c, which was controlled by adjusting the evaporative cooling procedure, determined if we created a BEC from which an atom laser could be produced, or a thermal source. When forming a condensate, we ensured that N_0/N was large, which was satisfied given that $T/T_c \sim 0.2$, so that the density profile and therefore also the correlation function was dominated by the condensed portion of the cloud.

Once the evaporative cooling process was finished, we applied a sequence of 30 Fourier-broadened pulses of RF radiation to spin-flip atoms from the $m_J = 1$ to the $m_J = 0$ state and thus release them from the magnetic trap. These RF pulses were modulated by a 20 µs square wave, which gave them a Fourier frequency spread of $\Delta f \approx 300$ kHz , which is large compared to the chemical potential of the condensates (≈8 kHz), and will interact with the majority of thermal atomic clouds (with an energy spread of $\sim h \times 30$ kHz) formed in our magnetic trap under these conditions. This means that atoms were outcoupled isotropically across the entire cloud. The short duration of the pulses necessitated the use of a 30W amplifier to increase the RF power available, so that a reasonable number of atoms were outcoupled. The power of RF pulses was ramped up from the first to last pulse in an attempt to outcouple approximately the same number of atoms in each pulse, although later pulses tended to release fewer atoms as the cloud held in the trap was depleted, as can be seen in Fig. 4.5. We also ensured that the portion of atoms outcoupled was only a few percent of the entire cloud, so that the outcoupling process had little impact on the energy distribution of atoms remaining in the trap. By applying these pulses at 29 ms intervals, we ensured that the clouds did not overlap after their expansion during the time-of-flight from the trap to the DLD, which is illustrated in Fig. 4.4.

We acquired 1700 experimental realisations for both $T > T_c$ and $T < T_c$, from which second order correlation functions for thermal and Bose-condensed atoms respectively were computed in the manner described in §4.1.2. The stability of our magnetic trap allowed the formation of either thermal or condensed clouds to be made in a controllable and repeatable manner over data runs spanning many tens of hours.

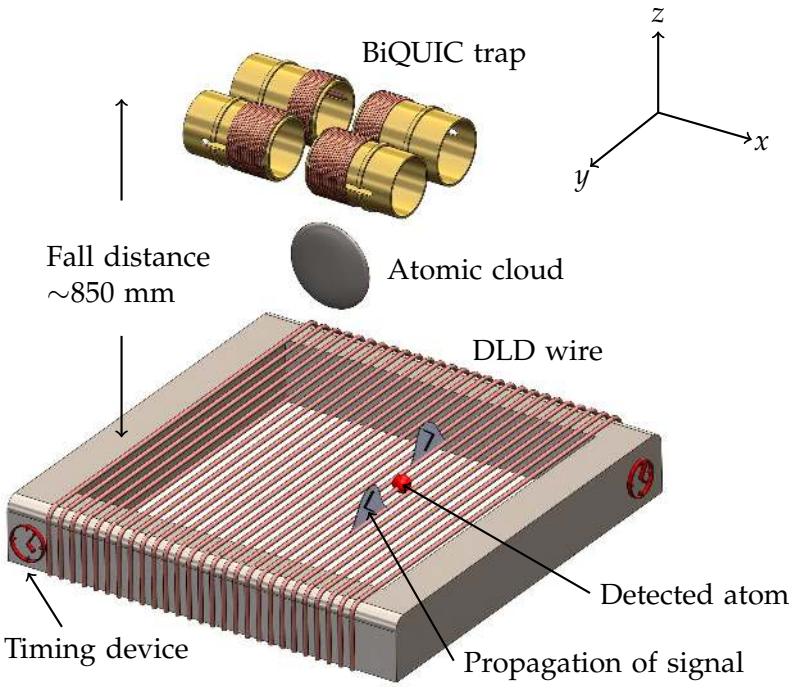

Figure 4.4: Experimental setup for pulsed-source correlation function measurement. Atoms are outcoupled from the BiQUIC magnetic trap with RF radiation, and fall ~850 mm under gravity to the DLD below (MCP not shown). When the signal from a single atom detection event lands on the DLD wire (only one of the two windings is shown), a signal propagates along the wire to the timing electronics, which record information from which the three-dimensional time and position of the atom's arrival on the detector can be calculated. The coordinate axis relates to the orientation of the trapping frequencies. Note that the atomic cloud, which is cigar-shaped with a long axis in the $\hat{y}$ direction in-trap, represents a BEC in the 'far field' in this illustration.

4.2.2 Results

Before correlation functions were computed for this data, it was instructive to analyse the density distribution of atoms measured on the detector. An example of this is the time-of-flight profile shown in Fig. 4.5, which is the average of 10 experimental cycles for thermal atom pulses. Each pulse of atoms arrives at the detector in a ~20 ms window, due to ballistic expansion during the time of flight, and successive pulses were found to not overlap at the detector. If this were not the case, a reduction in correlation length would be expected, due to the same loss of energy selectivity that occurs for a continuous beam. Also, fitting the time-of-flight profile allowed a temperature for the atomic pulses can be obtained, which was measured to be 850±100 nK for thermal atoms. Later pulses were found to be slightly colder than earlier ones, due to the gain of our 30W amplifier being greater at higher frequencies, which preferentially outcoupled hotter atoms and left less energetic particles in the trap. Finally, it was important to verify that the flux of atoms measured on the DLD was less than 1 MHz, to ensure that the detector did not saturate. In Fig. 4.5, we see that the atomic flux was typically no more than 150 kHz, except for the final high flux peak which was the atoms not removed by the RF pulses being dropped onto the DLD. This final pulse was omitted from correlation

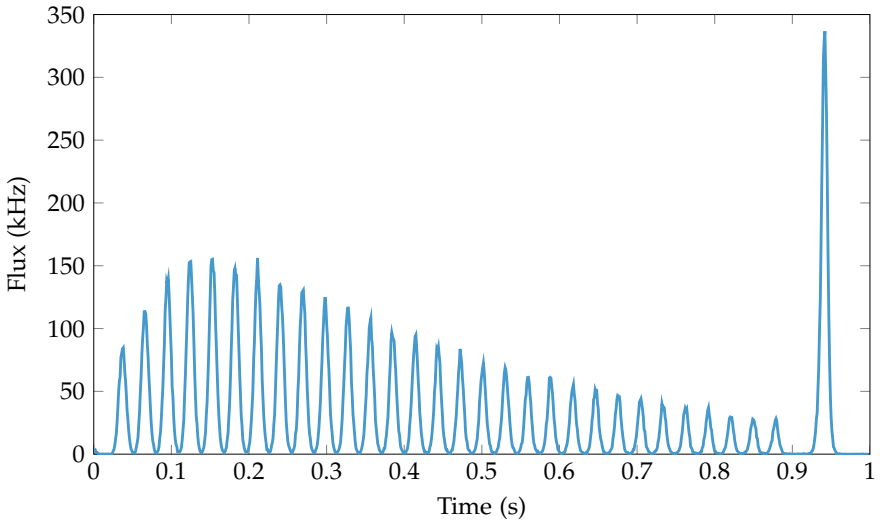

Figure 4.5: Time-of-flight flux of thermal atoms on the DLD. A similar profile is seen for the pulsed atom laser, however the pulses are narrower in that case.

function measurements. However, the majority of atoms in the trap contributed to the correlation function measurements, making more efficient use of the atoms each cloud than was possible for previous experiments [195].

We chose to compute correlation functions in the z axis, or equivalently in the time of arrival t at the DLD. Because the magnetic trap is tightest in the x and t directions and therefore the correlation lengths will be greatest in these axes in the far field, and the DLD has superior resolution in t compared to the x-y plane, this is the natural choice for this experimental setup. The correlation function histograms in the form of Eq. 4.7 were computed using 700 µm bins in x and y, while the t axis was binned in 20 µs increments. These binning parameters were determined empirically to optimise the signal-to-noise of the $g^{(2)}(\Delta t)$ functions calculated, shown in Figs. 4.6 and 4.7, which resulted in $\sim 10^5$ correlated pairs per 20 µs time bin.

The bunching amplitude and correlation time were measured for the thermal atoms by fitting the form of Eq. 4.8 to the correlation function plotted in Fig. 4.6. This resulted in a contrast of $C = 0.024$, and a correlation time of $l_t = 102$ µs. Using Eq. 4.5, we expect the correlation time[3] to be 120 ± 20 µs, and the Monte Carlo simulation outlined in §4.1.2 for these parameters predicted that $C = 0.04$. The discrepancies between the theoretical and measured values for the correlation time and amplitude could be attributed to temperature fluctuations, which alter the performance of the normalisation procedure. The same correlation function computation procedure was then applied to the pulsed atom laser data, as shown in Fig. 4.7. As expected, no bunching was present for this source, which was confirmed by a fit of Eq. 4.8 to the data giving $C = 0$.

4.2.3 Discussion

Although the thermal bunching amplitude of 0.024 measured in this experiment is small compared to the ideal value of $C = 1$, it is consistent with our simulated value as we make use of spatial bins of 700 µm, which are larger than the correlation lengths in

[3] As noted before, we convert between length and time scales with a factor of velocity, which for our apparatus is ≈ 4.08 ms^{-1} at the DLD.

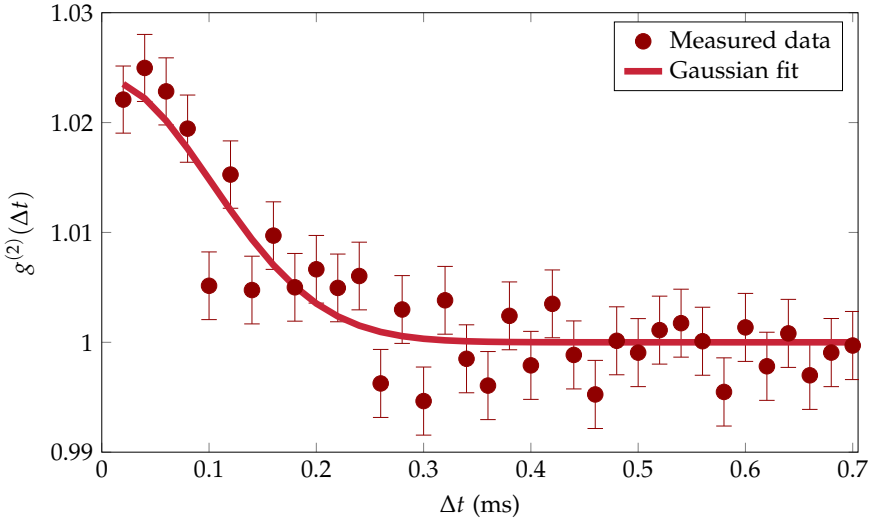

Figure 4.6: Plot of second order correlation function $g^{(2)}(\Delta t)$ for thermal atoms at $T = 850$ nK, where the error bars represent shot noise.

the x-y plane of $l_x = 490$ µm and $l_y = 49$ µm. Because our thermal temperature of 850 nK is not significantly higher than $T_c \approx 600$ nK, it is not possible to increase the thermal correlation length significantly by cooling the clouds further without forming a condensate fraction. Subsequent experiments which overcome this limitation will be discussed in §4.4 and §4.5.

This thermal bunching measurement also cannot be readily improved by outcoupling atoms in a continuous beam. Although the correlation lengths in the x-y plane will remain the same as before for this situation, in the z axis the correlation time becomes $l_t = \hbar/\Delta E$ where $\Delta E = mv\Delta v$ [186]. Using $v = \sqrt{2k_BT/m}$ and $\Delta v = 2v/g$ [196], we find $l_t \approx 22$ µs for a continuous beam under our experimental conditions[4]. In addition to this, the small mass of helium causes its outcoupling surfaces to have much higher curvature than those for other species such as rubidium [180], causing atoms to fountain upwards and further increase the effective energy spread of the beam. This means that the approach taken for other previous experiments such as [182] would require an unreasonably large amount of experimental data to observe bunching due to the poor bunching amplitude C expected.

With this setup, we can circumvent some of the limitations of previous experiments where detector saturation [55, 56] or low flux measurement rates [182] made obtaining enough experimental data to calculate $g^{(2)}(\Delta t)$ an undesirably lengthy process (of order weeks). We have instead measured a bunching signal similar to that seen in other He* experiments [55, 56] with an order of magnitude faster data acquisition rate afforded by the stability of our magnetic trap. Data could have conceivably been taken even faster, as illustrated by the peak count rate in Fig. 4.5 being somewhat less than the saturation flux of 1 MHz, however we wanted to ensure that the portion of the cloud outcoupled was small for each pulse. This is important because the dynamics of RF outcoupling from within the Thomas Fermi radius of a BEC is quite different to a sudden trap switchoff, due to mean field interactions and the possibility for collective excitations within the cloud [197], as well as the stability of the cloud over the 1 s interval between

[4]This is incorrectly stated to be 100 ns in [59].

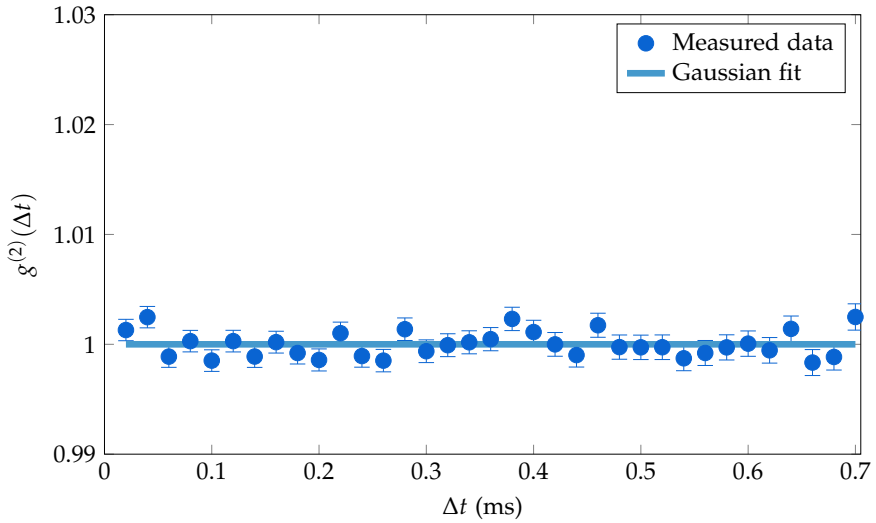

Figure 4.7: Second order correlation function $g^{(2)}(\Delta t)$ for a pulsed atom laser, where the error bars represent shot noise.

the first and last outcoupled pulse. Also, Penning ionisation could be induced between the atoms outcoupled via spin flipping to the $m_J = 0$ state, where the resulting ions could cause perturbations to the atoms remaining in the trap. The coherence of our pulsed atom laser source shows that RF outcoupling provides a minimally destructive probe of the coherence of the cloud. As the aforementioned fountaining of outcoupled atoms shows that helium is a species typically more susceptible to decoherence than other commonly used atom species such as alkali metals, this result indicates that other species should also retain coherence when outcoupled with broadband RF radiation.

Although the observation of bunching in this system is difficult, by measuring a clear two-body interference signal for thermal atoms, in contrast to a pulsed atom laser which displays no bunching, we can confirm that pulsed outcoupling does provide an unperturbed measurement of coherence. As we have improved upon data acquisition rates for correlation measurements, we can apply this technique to expand our knowledge about atomic coherence, as we will see in the next section.

4.3 Direct measurement of long-range third-order coherence in Bose-Einstein condensates

A key consequence of Glauber's theory of coherence (which was described in detail in §2.1.1) was that the distinction between classical and quantum correlation functions is truly unambiguous for the interference of n-tuples of particles, as opposed to more familiar first order correlation measurements. Although measurements of second-order correlations such as that in the previous section provide enough information to distinguish between thermal and Bose condensed atomic samples, verification that coherent states lack bunching to all orders of n in an important step towards confirming Glauber's theory is appropriate for Bose Einstein condensates. Furthermore, the small bunching contrast does not directly demonstrate that $g^{(n)}(\mathbf{0}, \ldots, \mathbf{0}) = n!$ holds for thermal atoms as a consequence of Wick's theorem.

Previous to this experiment, three-body loss rate measurements had hinted at the effect of higher-order correlation functions in atomic samples [198, 199]. Although such loss rates do give an indication of the interference of three atoms, and succeeded in demonstrating the distinction between thermal and condensed sources of atoms, they give no indication of the long-range coherence of the cloud. Such measurements are inevitably influenced by the strong interactions experienced on length scales tens of times the s-wave scattering length a [34, 200], where a is of order nanometres (for He*, this is 7.5 nm [201]). Also, localised correlation measurements do not necessarily reveal information about long-range order, such as for one-dimensional systems where true condensates with long-range order cannot be created, but a measurement of $g^{(n)}(0,\ldots,0)=1$ can still be made in trap with quasicondensates which display local coherence [202]. By allowing the atoms to ballistically expand during their fall under gravity from the trap to the detector, the physical size of the cloud increases considerably from being around 10-100 μm in trap to larger than 1 cm at the detector. Thus, the average particle spacing is around 0.1 to 1 mm, and typical correlation lengths are typically[5] between 0.1 to 10 mm, both of which are considerably larger than the distance over which interactions influence the correlation properties of the cloud. Therefore, the unperturbed long-range coherence of the cloud can be probed in the far field where the effect of interactions is negligible.

By measuring the third-order correlation function in the same manner that the second-order function was measured in §4.2, we show that $g^{(3)}(\Delta t_1,\Delta t_2)=1$ for a pulsed atom laser, and compare the second- and third-order correlation functions for thermal atoms to show that a scaling consistent with Wick's theorem exists. As the computation of third-order correlations requires about an order of magnitude more data than for the second-order function, the increase in data acquisition rate achieved by a pulsed source was required for this experiment to be feasible for clouds with $\sim 10^6$ atoms in our magnetic trap.

4.3.1 Experimental method

To obtain a pulsed source of ultracold atoms from which second- and third-order correlation functions were computed, we followed essentially the same experimental method as outlined in §4.2.1. In this experiment, we outcoupled 2 to 3% of atoms from the magnetic trap with trapping frequencies $(\omega_x,\omega_y,\omega_z)=2\pi\times(565,51,565)$ Hz with each of 30 pulses of RF radiation. The pulse duration of 5 μs gave a Fourier broadened frequency spread of $\Delta f\sim 1.2$ MHz , which exceeds the energy spread of the thermal cloud ($\sim h\times 30$ kHz) and chemical potential of the BEC ($\approx$8 kHz). As before, we chose to cool the atomic cloud to either above or below $T_c\approx 1$ μK in a repeatable manner, where the thermal clouds in this experiment were at a temperature of $\sim 1.3\pm 0.2$ μK. Note that the experimental parameters are slightly different to those for the previous experiment, due to small changes in the number of trapped atoms and the geometry of the magnetic trap itself, while similar changes will also inevitably occur for subsequent experiments. To obtain reasonable signal-to-noise levels for the third-order correlation function, we acquired data over $\sim$24,600 experimental iterations for thermal clouds, while only $\sim$3,700 realisations were required for the pulsed atom laser due to the much higher density of such clouds, yielding many more triplets of atoms within a given bin volume.

[5] In §4.2 we have $l_z=l_t v\approx 500$ μm, while in subsequent sections we will see experiments where l_r exceeds 1 mm.

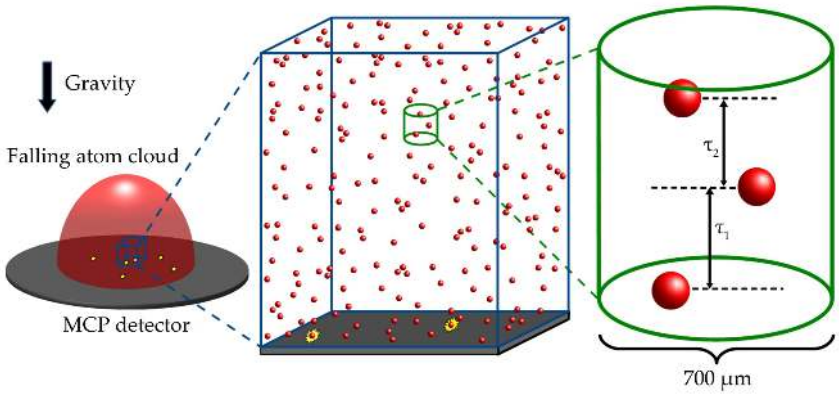

Figure 4.8: Calculating the correlation function in time $g^{(3)}(\Delta t_1, \Delta t_2)$ from a cloud of He* atoms (represented by red spheres) as they arrive at the detector (indicated with yellow flashes) requires that a two-dimensional area be considered in the plane of the detector for each atom measured (in this case, a bin of radius 700 μm shown in green), and histogram of the differences in arrival time (labelled τ_1 and τ_2) for two more atoms arriving subsequently on the detector is computed.

Fig. 4.8 illustrates the data analysis procedure outlined in §4.1.2 that is used to calculate the third-order correlation function from our experimental data. The unnormalised third-order correlation function $G^{(3)}(\Delta t_1, \Delta t_2)$ is a histogram of the distribution of time separations between three atoms arriving on the detector within a bin of size 700 μm in the x-y plane for each experimental iteration. This is normalised by repeating this same process for the distribution of atoms over every experimental realisation in the data set, to give the product of bulk intensity profiles $\rho(0)\rho(\Delta t_1)\rho(\Delta t_2)$, from which the normalised third-order correlation function $g^{(3)}(0, \Delta t_1, \Delta t_2) = G^{(3)}(\Delta t_1, \Delta t_2)/\rho(0)\rho(\Delta t_1)\rho(\Delta t_2)$ is obtained.

4.3.2 Results

The third-order correlation functions for thermal and Bose-condensed sources are presented in Fig. 4.9 and Fig. 4.10 respectively. These plots show a distinct contrast between the bosonic bunching present for the thermal atoms and the lack of bunching for the atom laser. The observation of $g^{(3)}(\Delta t_1, \Delta t_1) = 1.000 \pm 0.001$ in Fig. 4.9 for all $\Delta t_1, \Delta t_2$ confirms that Bose Einstein condensates are coherent to third order as expected. However, the size of the bins required to compute the correlation functions with acceptable signal-to-noise are large compared to the correlation length of the thermal atoms, which decreases the peak bunching amplitude from the predicted $g^{(3)}(0,0) = 6$ to 1.061 ± 0.006 in a similar manner to that seen for the second-order correlation measurement described in the previous section.

From the factorised form of the third order correlation function, which was derived

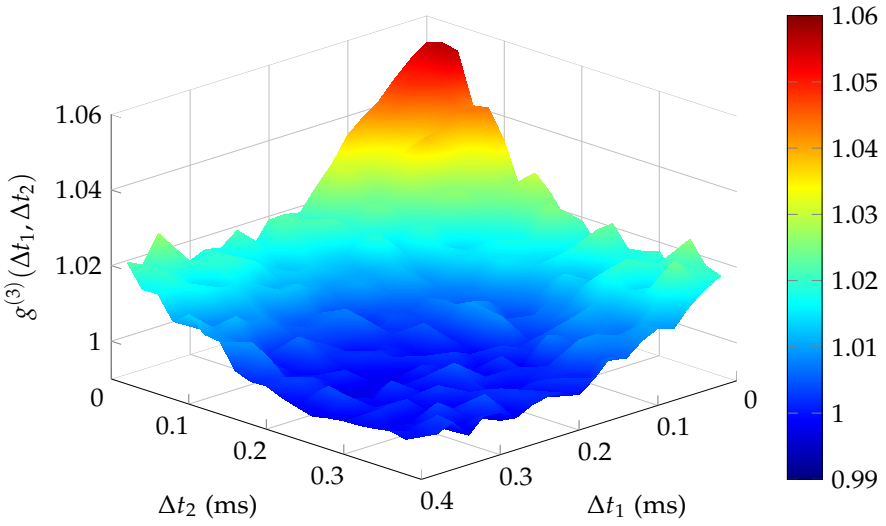

Figure 4.9: Normalised third-order correlation functions $g^{(3)}(\Delta t_1, \Delta t_2)$ for ensembles of thermal atoms.

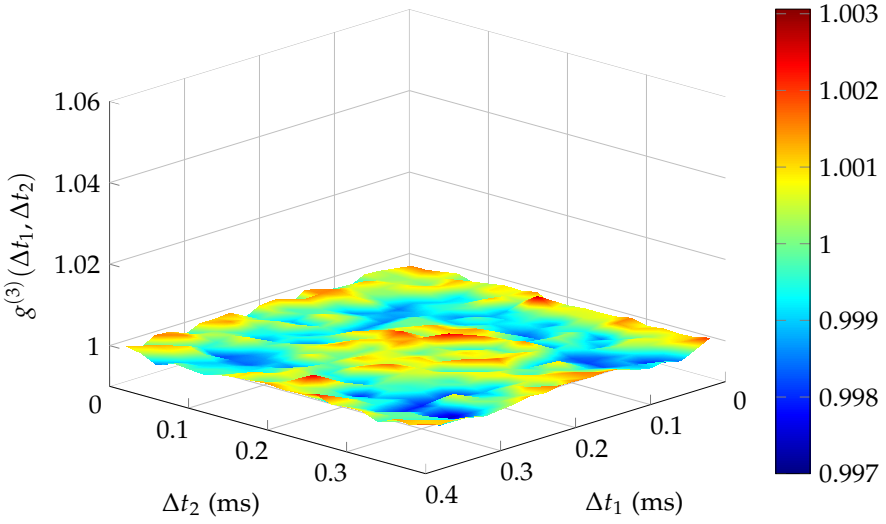

Figure 4.10: Normalised third-order correlation functions $g^{(3)}(\Delta t_1, \Delta t_2)$ for Bose-condensed atoms.

	Experiment	**Theory**
$g^{(2)}(0)$	1.022±0.002	1.025±0.005
l_t	90±10 µs	80±20 µs
$g^{(3)}(0,0)$	1.061±0.006	1.075±0.015
$(g^{(3)}(0,0)-1)/(g^{(2)}(0)-1)$	2.8±0.3	3.0±0.3

Table 4.1: Comparison of theoretical and experimental correlation parameters

in §2.1.1,

$$g^{(3)}(\Delta t_1,\Delta t_2)=\frac{\left|G^{(1)}(\Delta t_1)\right|^2}{\rho(0)\rho(\Delta t_1)}+\frac{\left|G^{(1)}(\Delta t_2)\right|^2}{\rho(0)\rho(\Delta t_2)}+\frac{\left|G^{(1)}(\Delta t_2-\Delta t_1)\right|^2}{\rho(\Delta t_1)\rho(\Delta t_2)} + 2\Re\left\{\frac{G^{(1)}(\Delta t_1)G^{(1)}(\Delta t_2)G^{(1)}(\Delta t_2-\Delta t_1)}{\rho(0)\rho(\Delta t_1)\rho(\Delta t_2)}\right\}+1, \tag{4.9}$$

we see that if either of Δt_1 or Δt_2 is much larger than l_t, then $G^{(1)}$ terms containing that time separation will tend towards zero and not contribute to the bunching signal measured in $g^{(3)}(\Delta t_1,\Delta t_1)$. For example, if we take $\Delta t_2 \gg l_t$, then Eq. 4.9 simplifies to

$$g^{(3)}(\Delta t_1,\Delta t_2)_{\Delta t_2\to\infty}=\frac{\left|G^{(1)}(\Delta t_1)\right|^2}{\rho(0)\rho(\Delta t_1)}+1=g^{(2)}(\Delta t_1). \tag{4.10}$$

Therefore, Eq. 4.10 confirms the intuitive notion that 'three-particle interference with one particle far away will be two-particle interference'. This is clearly illustrated in Fig. 4.9, where for $\Delta t_2 > 200$ µs, the peak bunching amplitude is $C \approx 0.02$, considerably lower than for $g^{(3)}(0,0)$ but similar to the value of $C = 0.024$ obtained in our previous experiment[6].

We show this explicitly in Fig. 4.11 by averaging $g^{(3)}(\Delta t_1,\Delta t_2)$ for either Δt_1 or Δt_2 larger than 200 µs to obtain effectively $g^{(2)}(\Delta t)$ for both thermal and Bose condensed atoms. A maximum two-body bunching contrast derived from a Gaussian fit of $C = 0.022\pm0.002$ was measured for the thermal clouds, while a complete absence of bunching is again observed for the atom laser. The correlation time l_t was found to be 90±10 µs for thermal atoms. We can compare the two-body correlation function directly with the three-body function shown in Fig. 4.12 by taking a diagonal cross section $g^{(3)}(\Delta t) = g^{(3)}(\Delta t,\Delta t)$ through the data shown in Figs. 4.9 and 4.10, which highlights the bunching peak of $g^{(3)}(0,0) = 1.061\pm0.006$ for thermal atoms and lack of bunching in a BEC. Although a 'three-body correlation time' can be measured as the width of a Gaussian fit to $g^{(3)}(\Delta t)$ for thermal atoms, its value of 120 µs is largely an artefact of the binning regime used to plot $g^{(3)}(\Delta t_1,\Delta t_2)$, and is a factor of $\sqrt{2}$ larger than $l_t = 90$ µs due to this.

By applying the model described in §4.1.2, we can compare the measured and theoretical values of bunching contrast and correlation length for this experiment, which are given in Table 4.1. In particular, we are able to directly compare $g^{(2)}(0)$ and $g^{(3)}(0,0)$ to verify that the predictions of Eq. 4.9 and its simplification to Eq. 4.10 are correct.

[6]The temperature of the thermal cloud was about 35% lower in that experiment, which accounts for the higher bunching amplitude measured when using bins of the same size.

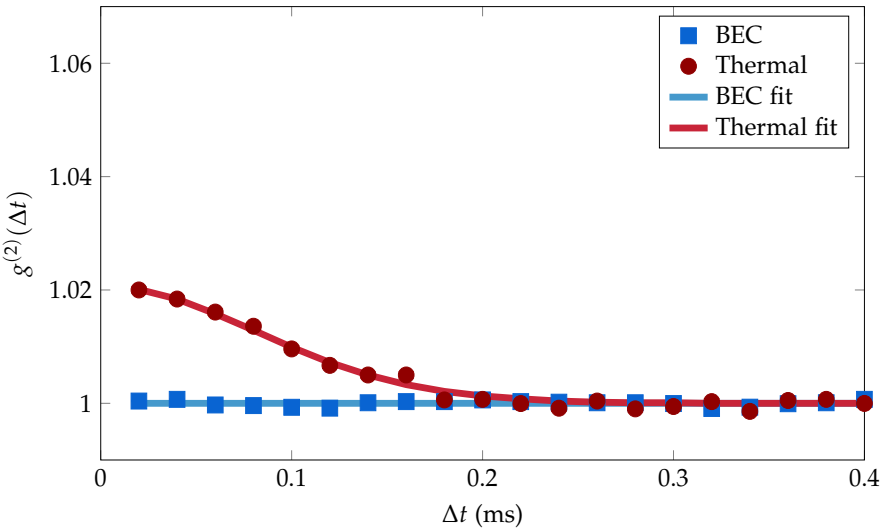

Figure 4.11: Second-order correlation function $g^{(2)}(\Delta t)$ ($g^{(3)}(\Delta t_1, \Delta t_2)$ averaged over Δt_1 and $\Delta t_2 > 200$ µs), for both thermal (red circles) and Bose condensed (blue squares) atoms. The red and blue lines are Gaussian fits to the thermal and BEC data, while the error bars (which are barely visible in this plot) represent shot noise.

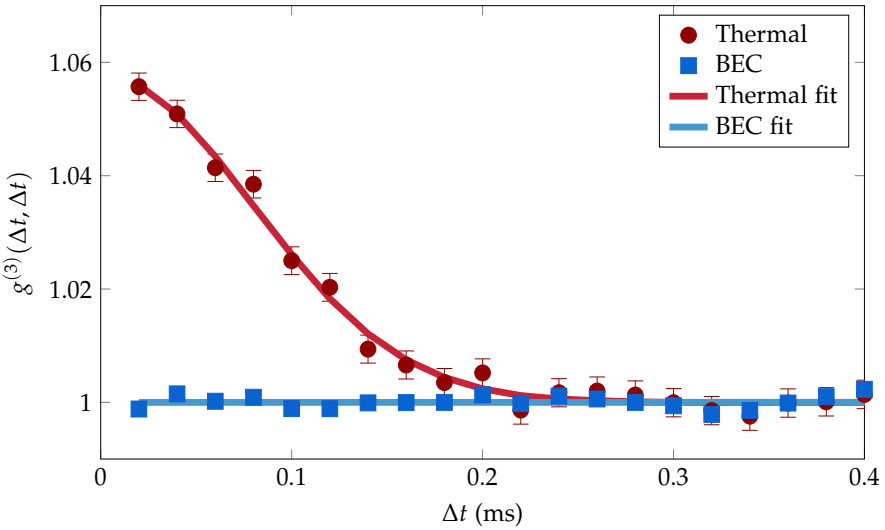

Figure 4.12: Diagonal section ($\Delta t_1 = \Delta t_2$) of $g^{(3)}(\Delta t_1, \Delta t_2)$ for thermal (red circles) and Bose condensed (blue squares) atoms. The red and blue lines are two-dimensional Gaussian surface fits to the thermal and BEC data, while the error bars represent shot noise.

4.3.3 Discussion

The results summarised in Table 4.1 confirm that we have successfully measured the long-range third-order correlation function, and allow us to verify its relationship with the second-order function. Although the peak bunching amplitudes of $g^{(3)}(0,0) = 1.061 \pm 0.006$ and $g^{(2)}(0) = 1.022 \pm 0.002$ do not match the ideal theoretical value predicted by Wick's theorem of $g^{(n)}(0,\ldots,0) = n!$, the ratio $(g^{(3)}(0,0)-1)/(g^{(2)}(0)-1)$ allows the scaling between correlation function orders to be verified. Importantly, this ratio is less sensitive to imperfections in the normalisation procedure and the effects of bunching contrast reduction due to the relatively large bin size required than a direct measurement of C. As normalisation imperfections are responsible for the errors quoted for our experimental measurements, taking the ratio of second- to third-order peak bunching amplitudes helps to reduce the effect of such a systematic error. These results thus confirm the quantum theory of boson statistics is applicable to weakly interacting atomic gases, where a Bose Einstein condensate possesses long-range coherence to at least order $n = 3$, while the bunching observed in thermal clouds is consisted with Eq. 4.9.

Although the time required to obtain enough experimental data ($\sim$250 hours) was considerably longer than for our previous measurement of $g^{(2)}$, and highlights the usefulness of our pulsed outcoupling method, the time required to compute the correlation functions was the limiting factor in this experiment. This dissuaded us from improving the signal-to-noise of this measurement, or even calculating order correlation functions, by continuing with this pulsed source method. The following sections will describe experiments which address this limitation, and allow higher-order correlation functions with better signal-to-noise to be measured.

4.4 Large bunching amplitude third-order spatial correlations

In this experiment, we aim to significantly increase the correlation length of our atomic samples to enable a long-range third-order quantum correlation measurement to be taken in the spatial plane of a detector for the first time. Not only does this improvement in observed bunching contrast make data acquisition and computation much quicker, but also allows us to measure the individual moments of the correlation function that give rise to Wick's theorem, which has previously been achieved in trap [203] but not yet over long ranges. With this, three-body effects such as collisions [198, 199, 204] and Efimov trimers [102, 205, 206] could possibly be investigated. Measuring correlation functions in the spatial plane of the detector also gives greater flexibility in the trapping geometries can be utilised, where for example systems of reduced dimensionality [202] which display different quantum statistics in the weak and strong axes of the trap due to the lack of long-range order could be studied. Indeed, this will be important for an investigation of transverse condensation in the following chapter of this thesis. In addition, the visibility of spatial imaging techniques such as ghost imaging is enhanced with the use of higher-order correlation functions [85].

As we saw in §4.1.1, in the 3D limit for an ideal thermal gas, correlations in each axis for clouds dropped under gravity are the same apart from the scaling of the correlation length due to the trapping frequencies. Previous measurements with photons were able to confirm that photon coincidence count rates in the spatial plane of a detector are consistent with previous measurements of temporal correlations to third order [85]. For

our MCP and DLD system, as the detector resolution is far poorer in the x-y plane than it is for t, computing long-range second- and third-order correlation functions in this plane requires correlation lengths which far exceed this resolution limit to prevent bunching from being washed out. We achieve this by cooling clouds in our BiQUIC magnetic trap containing far fewer atoms than for previous experiments ($\sim 10^3$ rather than $\sim 10^6$), which drives T_c down by an order of magnitude. As $l_r \propto T^{-1/2}$ (Eq. 4.5), we can now cool thermal clouds to temperatures where the correlation length in the x direction is now 1.3 mm, much larger than the spatial detector resolution of ∼100 µm, and results in a peak bunching amplitude far greater than that which was seen with our previous pulsed source technique.

4.4.1 Experimental method

Once again, we produced ultracold atomic clouds of $\sim 10^6$ atoms at temperature just above $T_c \approx 1$ µK in our BiQUIC magnetic trap. However, rather than outcoupling pulses of atoms from the magnetic trap with bursts of RF radiation, the population of the trap was attenuated while continuing to cool the cloud in a manner which ensured that the temperature remained above T_c at all times. We recall from §2.3.1 that $T_c \propto N^{1/3}$, which sets the lowest possible thermal temperature as a function of trap population, and by reducing the population to $\sim 10^3$ atoms we achieved an ultimate critical temperature of ∼100 nK. To achieve this, the cloud was attenuated over the final 2.7 seconds of evaporative cooling by outcoupling atoms uniformly from the trap with 54,000 pulses of RF radiation, which were significantly Fourier broadened due to their short duration of 100 µs. During this process, the evaporative cooling was adjusted to compensate for the decrease in trap population, and resulted in thermal clouds with a temperature of $\approx 95 \pm 10$ nK. The reduction in temperature was limited by the stability of the trap, which was already highly stabilised by our nullerometer (see §3.1.2). About 4,000 experimental realisations of such clouds were then dropped under gravity to the MCP and DLD below, where single atoms were detected as per the experiments previously discussed.

We then computed second- and third-order correlation functions along the x axis in a manner similar to previous experiments. The x axis was chosen due to the trapping frequency in that direction being 550 Hz where the correlation length was theoretically predicted to be ∼1.5 mm, as opposed to 50 Hz in the y direction which gave a correlation length of order the detector resolution (∼140 µm). We chose bins of 250 µs in time[7], 1 mm in y and histogram in increments of 200 µm in the x direction, the latter being restricted to at least the detector resolution of ∼100 µm. The bin sizes were chosen to maximise the ratio of $g^{(3)}(\Delta x_1 = 0, \Delta x_2 = 0)$ to shot noise. The dependence of second-order bunching amplitude on bin size for this data set was illustrated previously in Fig. 4.3, however repeating this process for third-order correlation functions lead to poorer signal-to-noise for for this data than is seen for $g^{(2)}(\Delta x)$.

4.4.2 Results

The second-order correlation function $g^{(2)}(\Delta x)$, complementary to those shown in Fig. 4.3 but with the bin size specified in the experimental method, is shown in Fig. 4.13. A Gaussian fit to this profile measured a bunching contrast of $C = 0.131 \pm 0.015$, and a correlation length of 1.30 ± 0.03 mm, which is in good agreement with the results of the

[7] This corresponds to 1 mm in the z direction, with a fall velocity of ≈ 4 ms^{-1}.

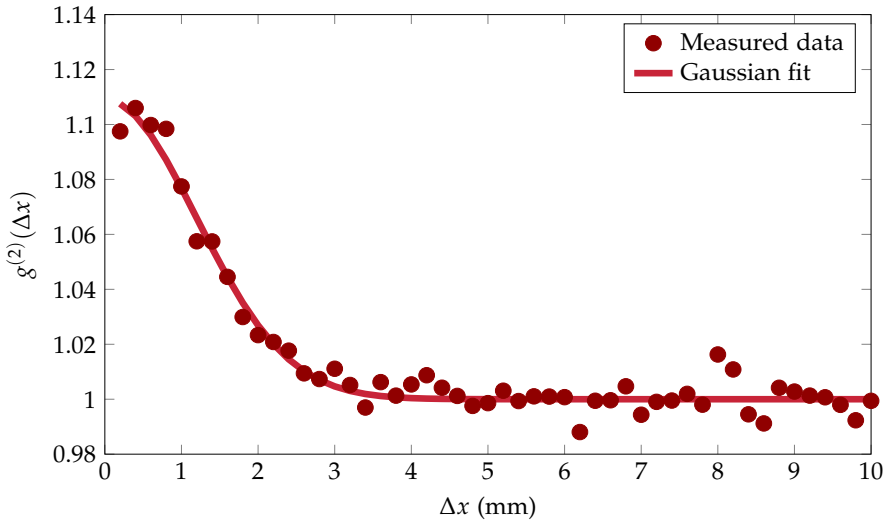

Figure 4.13: Normalised second-order spatial correlation function $g^{(2)}(\Delta x)$ for ∼95 nK thermal atoms.

theoretical model discussed in §4.1.2 which predict $C = 0.14 \pm 0.02$ and $l_x = 1.5 \pm 0.2$ mm for these experimental conditions. Although this bunching contrast still falls short of the ideal value of $C = 1$, we see that increasing the correlation length of our atomic sample to a much larger fraction of the bin size gives a much stronger bunching peak than that measured for our previous experiments with smaller correlation lengths, which were restricted to $C < 0.024$.

The third-order correlation function computed under the same conditions is also shown in Fig. 4.14. As with our measurement of $g^{(3)}(\Delta t_1, \Delta t_2)$ in Fig. 4.9, the independent axes of this plot represent the separation in the x axis between the first and second atoms in the triplet ($\Delta x_1 = x_2 - x_1$), and between the second and third atoms ($\Delta x_2 = x_3 - x_2$). The experimental data in this figure (left) is displayed alongside a fit to this surface (right), which is of the form of Eq. 4.9 and has free parameters for the bunching amplitudes due to the two- and three-body moments, as well as the correlation length. For clarity, a plan view of the same data is presented in Fig. 4.15, which confirms that the measured correlation function (left) matches the form of the theoretical model (right). This fit yielded a peak three-body bunching amplitude of $g^{(3)}(0,0) = 1.44 \pm 0.02$, which is consistent with the prediction of the theoretical model of 1.47 ± 0.05. As with our previous third-order bunching measurement, $g^{(2)}(0)$ is recovered for either $g^{(3)}(0, \Delta x_2 > l_x)$ or $g^{(3)}(\Delta x_1 > l_x, 0)$.

A feature of the data plotted in Figs. 4.14 and 4.15 which was not present in our temporal third-order correlation function measurements shown in Fig. 4.9 is a ridge of bunching observed along the $\Delta x_1 = \Delta x_2$ diagonal. This occurs in the spatial correlation data due to a lack of monotonic ordering in x position of consecutive atoms within a triplet, where an ordering is naturally present in time for our previous experiment. This means that if $\Delta \mathbf{x}_1 = -\Delta \mathbf{x}_2$, there can exist a two-body bunching enhancement due to the first and third atoms, while the second particle is far enough separated to not contribute to the bunching. If $\Delta \mathbf{x}_1 = \Delta \mathbf{x}_2 > l_x$, then all three particles are mutually far apart and no bunching exists, which is why the contrast of the diagonal ridge is roughly half that of $g^{(3)}(0, \Delta x_2 > l_x)$ or $g^{(3)}(\Delta x_1 > l_x, 0)$.

Due to the significant increase in three-body bunching amplitude for this data set

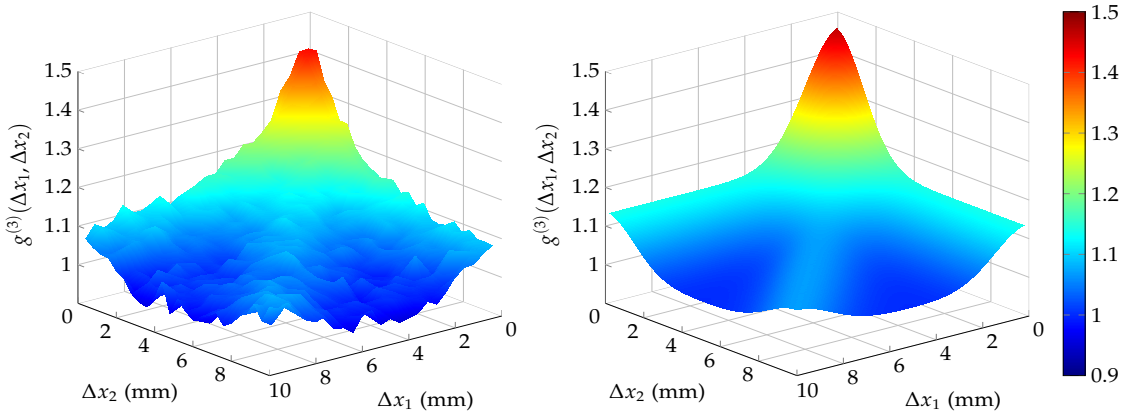

Figure 4.14: Normalised third-order spatial correlation function $g^{(3)}(\Delta x_1, \Delta x_2)$ for the experimental data (left) and theoretical simulation (right). Note the diagonal ridge corresponding to bunching between the first and third particles when $\Delta x_1 = \Delta x_2$.

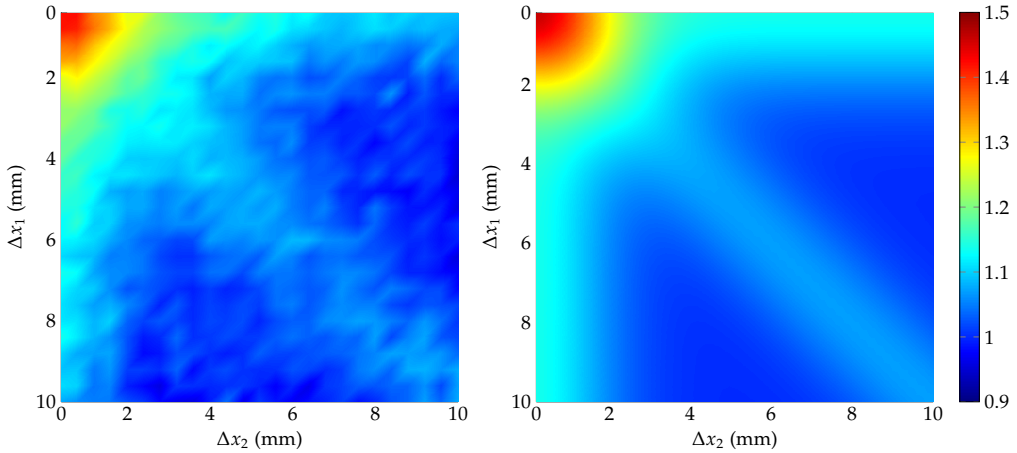

Figure 4.15: Normalised third-order spatial correlation function $g^{(3)}(\Delta x_1, \Delta x_2)$ for the experimental data (left) and theoretical simulation (right) in plan view.

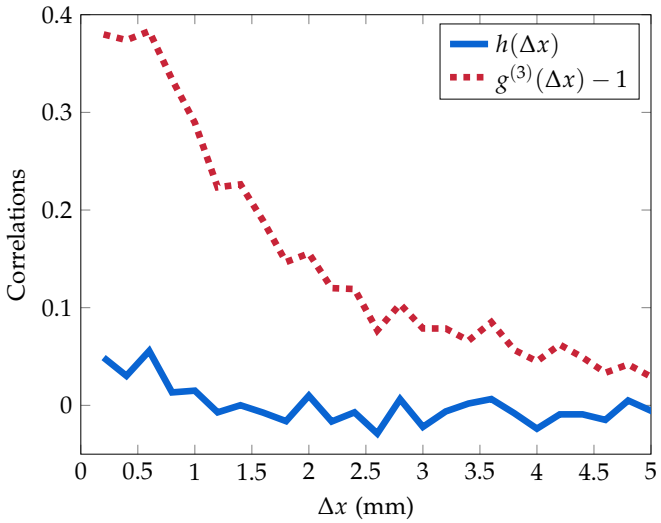

Figure 4.16: Comparison of the entire third-order correlation function $g^{(3)}(\Delta x, \Delta x) - 1 = g^{(3)}(\Delta x) - 1$ (dashed red line) and the three-body moment $h(\Delta x, \Delta x) = h(\Delta x)$ (solid blue line).

compared to that described in §4.3, we are now able to successfully measure the three-body moment of the third-order correlation function for the first time. We can rearrange Eq. 4.9 to isolate this moment $h(\Delta x_1, \Delta x_2)$,

$$\begin{aligned} h(\Delta x_1, \Delta x_2) &= 2\Re\left\{\frac{G^{(1)}(\Delta x_1)G^{(1)}(\Delta x_2)G^{(1)}(\Delta x_2 - \Delta x_1)}{\rho(0)\rho(\Delta x_1)\rho(\Delta x_2)}\right\}, \\ &= g^{(3)}(\Delta x_1, \Delta x_2) - \left[\frac{\left|G^{(1)}(\Delta x_1)\right|^2}{\rho(0)\rho(\Delta x_1)} + \frac{\left|G^{(1)}(\Delta x_2)\right|^2}{\rho(0)\rho(\Delta x_2)} + \frac{\left|G^{(1)}(\Delta x_2 - \Delta x_1)\right|^2}{\rho(\Delta x_1)\rho(\Delta x_2)} + 1\right], \end{aligned} \tag{4.11}$$

and compare this to $g^{(3)}(\Delta x_1, \Delta x_2) - 1$, as shown in Fig. 4.16. The definition of $h(\Delta x_1, \Delta x_2)$ implies a theoretical value of $h(0,0) = 2$, however we find it to be around 0.05, which is suppressed due to our binning regime even more severely than seen for the two-body bunching component shown in Fig. 4.13. However, this is to be expected as $h(\Delta x, \Delta x)$ requires the mutual overlap of three particles, which results in a far lower contrast three-body bunching signal than for interference between the first and second or second and third particles which contribute to the two-body correlation function.

4.4.3 Discussion

This result clearly shows that engineering a source with the largest possible correlation length gives not only a far better thermal bunching amplitude than for our pulsed source method ($g^{(3)}(0,0) = 1.44$ rather than 1.061), but also requires considerably less data and therefore less computational effort. In this experiment, only 4,000 experimental cycles were obtained as opposed to 24,600 for our previous experiment, with each cycle resulting in around three orders of magnitude fewer atoms measured. It may seem counter-intuitive that discarding atoms can significantly improve the signal-to-noise of our correlation functions measurements, however the order of magnitude

increase in correlation length along each axis ensures that we achieve far greater wavefunction overlap at the detector for a given bin size, which is not surprising given the conclusions drawn in §4.1.2. In doing so, this also allowed the three-body moment of the correlation function to be measured, which was not possible with our previous data.

High-contrast correlation measurements in the spatial plane of a detector paves the way to further experiments which probe novel phenomena. These include investigation of the correspondence between Hanbury Brown-Twiss bunching and speckle in a guided atomic source (which will be discussed in §6.2.4) and the observation of transverse condensation in an elongated quantum gas (Chapter 5). This technique could also enable additional experiments such as the use of ghost imaging to test Bell's inequality, which has been previously achieved with photons [207].

4.5 Thermal bunching up to sixth order in the ideal limit

Although the experiment described in the previous section represented a significant improvement in our ability to measure quantum correlation functions, it remained unable to observe bunching in the ideal limit of $g^{(n)}(0,\ldots,0) = n!$, and did not provide the opportunity to investigate correlation functions at orders higher than $n = 3$. However, it emphasised that the best approach for observing higher-order bunching in the limit where detector resolution or binning does not suppress the bunching contrast is to create an atomic source with the largest possible correlation length, even if this comes at the expense of the number of atoms in the cloud. While the previous result reached the limit of what could be achieved with our magnetic trap, optical dipole traps (see §3.1.3 for more details) are capable of confining clouds at considerably lower temperatures (of order a few tens of nK for our experimental setup, as opposed to ∼100 nK for our BiQUIC trap), and with much tighter radial confinement ($\omega_\perp$ can be up to 8 kHz for our dipole trap, while our magnetic trap is typically at most around 500 Hz). As we recall from Eq. 4.5, both of these will result in a considerable increase to the bunching correlation length. Although the axial trapping frequency is typically around a quarter of that for the magnetic trap, the dipole trap is oriented such that this is aligned in the z axis, which has a far better detector resolution than in the x-y plane and will therefore not restrict the bunching measured with this trap, while the radial correlation lengths will greatly exceed the spatial resolution of the MCP and DLD system.

We use an optical dipole trap in this manner to measure thermal long-range quantum correlation functions in the ideal limit up to sixth order. This is made possible not only by the tight radial trapping frequency ($\omega_\perp = 2\pi \times 2050$ Hz) and low temperature of the cloud (63 nK), which in the 3D limit would result in an extremely large correlation length of around 7.4 mm in the plane of the detector, but also by the role of dimensionality, which was introduced in §2.4. As the dipole trap is very elongated in the z direction, with an aspect ratio of $\omega_\perp/\omega_z > 100$, we are able to enter a regime where the cloud becomes partially condensed into the transverse axis of the trap, while remaining thermal in the longitudinal axis [151], as is discussed in §2.4.2. The phase transition into a transversely-condensed state will be studied in more detail in an experiment described in Chapter 5, which shows that a gas in this state saturates the population of transversely excited states into the radial ground state of the potential, behaving like a harmonically trapped ideal Bose gas. However, the longitudinal behaviour is intermediate between a highly degenerate ideal Bose gas and a weakly interacting quasicondensate, where the

broad crossover [208] between these two regimes is influenced by small number effects due to the fact that the clouds used in this experiment only contain ~ 330 atoms.

This results in a cloud which possesses a transverse correlation length which essentially covers the entire extent of the cloud, but lacks macroscopic occupation of the ground state of the 3D potential, and therefore means that a true Bose-Einstein condensate with long-range order is absent. As both the ideal Bose gas and weakly interacting quasicondensate regimes exhibit the usual Hanbury Brown-Twiss bunching of $g^{(n)}(0) = n!$ in the far field [208], an intermediate state between these two cases allowed quantum correlations to be measured with near-perfect contrast due to the transverse correlation length of the cloud being much larger than the bin size required to compute correlation functions. As this correlation length extended over a large portion of the cloud, correlation functions up to order $n = 6$ could be computed without the loss of signal-to-noise encountered for previous experiments with smaller bunching amplitudes.

This measurement represents not only the first measurement of atomic correlation functions above order $n = 4$ (where temporal correlations up to fourth order have been measured for trapped thermal atoms [209]), but also the first time thermal bunching has been observed in the ideal limit of $g^{(n)}(0, \ldots, 0) = n!$ for each order up to $n = 6$ for atomic species. In addition to providing the most rigorous validation yet of the applicability of Wick's theorem to Glauber's theory of coherence with massive particles, this also demonstrates that atomic measurements are competitive with state-of-the-art quantum optics experiments using photons for testing fundamental quantum physics.

4.5.1 Experimental method

Ultracold clouds of $\sim 10^6$ ^{4}He atoms were first cooled to just above the BEC transition temperature $T_c \approx 1$ μK as usual. A dimple trap was then formed by ramping up[8] the intensity of a beam of 1550 nm laser light focused in the direction of gravity over 100 ms, to form an optical dipole trap which captured about 10^4 atoms. Once atoms had been transferred to the optical trap, the magnetic trap is switched off, after which the trapped atoms were evaporatively cooled further by ramping down the intensity of the dipole trapping beam over 200 ms. At this stage, the dipole trap provides an approximately harmonic confinement of $(\omega_x, \omega_y, \omega_z) = 2\pi \times (2350, 1800, 15)$ Hz.

However, the superposition of an optical trap over the magnetic trap acts like a dimple trap, and almost inevitably results in condensation of the cloud [210, 211]. To avoid this, a short pulse of near-resonant light (detuned to the red of the $2^3S_1 \rightarrow 2^3P_2$ transition by about 700 MHz) was then applied to remove some atoms from the trap to ensure that the cloud remains thermal in the axial direction. This process was tuned to preferentially remove the condensed component of the cloud due to a superradiant-like effect [212], where the recoil velocity of the atoms absorbing a photon is enough to eject the atom from the trap without heating the rest of the cloud. Similarly to the experiment in the previous section, the removal of atoms lowers T_c so that a lower thermal temperature can be achieved. The dipole trap is then suddenly switched off, and the atoms fall $\sim$850 mm under gravity to the MCP and DLD below, as depicted in Fig. 4.17.

[8] As the trapping frequencies which we produce with this trap are $\bar{\omega} \sim 500$ Hz, this ramp should occur over a time scale much longer than $1/(500\ \mathrm{s}) = 2$ ms to be essentially adiabatic.

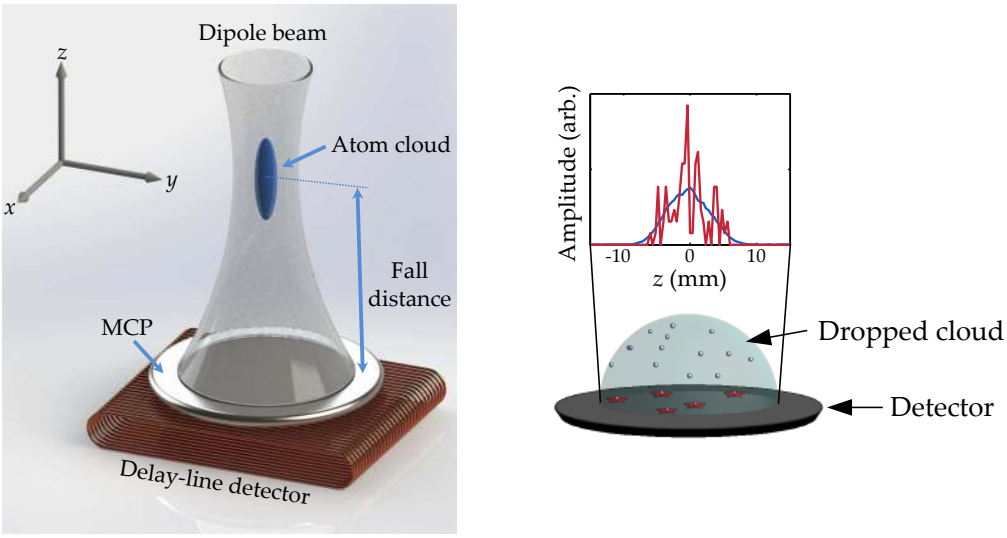

Figure 4.17: (Left) Ultracold atoms are held in an optical dipole trap, at the focus of a red-detuned laser beam. When the beam is switched off, the cloud drops ∼850 mm under gravity to the MCP and DLD system. (Right) The inset shows a typical single longitudinal profile of the cloud at the detector (red line), and an average profile of many experimental iterations (blue line).

We acquired ∼2,000 experimental realisations to calculate correlation functions in the z axis. The second and third order correlation functions were computed with bins of size 1 cm in the x and y directions in the manner described for previous experiments, while the functions for $n=4$ to $n=6$ were calculated with an autocorrelation procedure which differs slightly from our usual computation of correlation functions. In the latter case, the atoms were first binned temporally, then sorted in 8 mm bins in the x-y plane, which reduced the computational effort required to calculate these correlation functions. This had minimal effect on the correlation functions produced because the bins were much smaller than the correlation length in these axes, which was confirmed by a direct comparison of the two methods for $n=2$ and $n=3$.

4.5.2 Results

Before calculating the quantum correlation functions for this experimental data, the temperature of the clouds produced was measured from the time-of-flight profile. This was achieved by fitting an ideal 3D Bose gas model, where trap frequencies, atom number and temperature could each by altered within experimentally realistic bounds, and was found to be 63 nK for the clouds consisting of ~ 330 atoms. Furthermore, the experimental time-of-flight profile matched the shape of a thermal distribution, and a bimodal profile distinctive of a cloud with a condensate fraction with suppressed density fluctuations was not observed, which confirms that the cloud is thermal and thus incoherent in the z axis. If we compare this temperature to the condensation temperatures in 1D

	Experiment	**Theory**
$g^{(2)}(0)$	2.05±0.09	2
$g^{(3)}(0)$	6.0±0.6	6
$g^{(4)}(0)$	23±3	24
$g^{(5)}(0)$	111±16	120
$g^{(6)}(0)$	710±90	720

Table 4.2: Comparison of the maximum correlation function amplitude for orders $n=2$ to 6 with the ideal theoretical values of $g^{(n)}(0)=n!$.

and 3D (refer to §2.4), which are [151]

$$T_c^{3D} \approx \frac{\hbar}{k_B}\left[\frac{N\omega_z\omega_y\omega_z}{g_3(1)}\right]^{1/3}, \tag{4.12}$$

$$T_c^{1D} \approx \frac{N\hbar\omega_z}{k_B \ln(2N)}, \tag{4.13}$$

where $g_3(1)\approx 1.202$, we find that $T_c^{3D}\approx 124$ nK and $T_c^{1D}\approx 37$ nK. A final condition that prevents radial dynamics from being 'frozen out' by the trap dimensionality, which is $\omega_\perp/\omega_z \approx 137 < Ng_3(1)\approx 397$ [151], ensures that these quantum gases satisfy the requirements for transverse condensation, which will be explored in more detail in Chapter 5. The quantum state of the gas should thus be influenced by one-dimensional physics due to the fact that $T_c^{1D} < T < T_c^{3D}$, resulting in a lack of longitudinal coherence as is discussed in Chapter 5. In particular, as $k_B T/h = 1300$ Hz $< \omega_\perp/2\pi = 2050$ Hz, a significant occupation of the transverse ground state will exist, and as we will see in Chapter 5 the transverse correlation length is larger than the size of the cloud in the x-y plane.

The result of computing the quantum correlation functions $g^{(n)}(\Delta z) \equiv g^{(n)}(\Delta z,\ldots,\Delta z)$ for $n=2$ to 6 is shown in Fig. 4.18, and the resulting peak correlation function amplitudes derived from Gaussian fits to these functions are given in Table 4.2. It is clear that the bunching observed is in agreement with the prediction due to Wick's theorem that $g^{(n)}(\Delta z)=n!$ in the ideal limit, when binning and detector resolution do not 'wash out' the interference measured. A Gaussian fit to the width of the second-order correlation function gives a correlation length of 394 μm.

A full surface plot of $g^{(3)}(\Delta z_1,\Delta z_2)$ is shown in Fig. 4.19 to compare this result with our previous measurements of the third-order correlation function in Figs. 4.9 and 4.14. A marked increase in both signal-to-noise and bunching amplitude is seen for the optically-trapped clouds, where the latter is improved from the peak bunching amplitude in our previous result of $g^{(3)}(0,0)=1.44$. Plotting the complete fourth-, fifth-, and sixth-order correlation functions, $g^{(4)}(\Delta z_1,\Delta z_2,\Delta z_3)$, $g^{(5)}(\Delta z_1,\Delta z_2,\Delta z_3,\Delta z_4)$, $g^{(6)}(\Delta z_1,\Delta z_2,\Delta z_3,\Delta z_4,\Delta z_5)$ fully without merely taking the cross-sections shown in Fig. 4.18 require four-, five- and six-dimensional plots respectively and are therefore not possible. As with previous results, the 'nth-order correlation lengths' discussed in relation to Fig. 4.12 remain dependent on the binning regime chosen, in an extension to the scaling seen in the form of Eq. 4.4. In addition, features in the surface plot of the third-order function such as the bunching observed for $g^{(3)}(\Delta x,\Delta x)$ in Fig. 4.14 are avoided so that the cross-sections shown in Fig. 4.18 illustrate the most important information contained in the correlation functions, namely a comparison of $g^{(n)}(0)$ with $g^{(n)}(\Delta z > l_z)$ which ensures that the peak bunching amplitude has been measured correctly, while

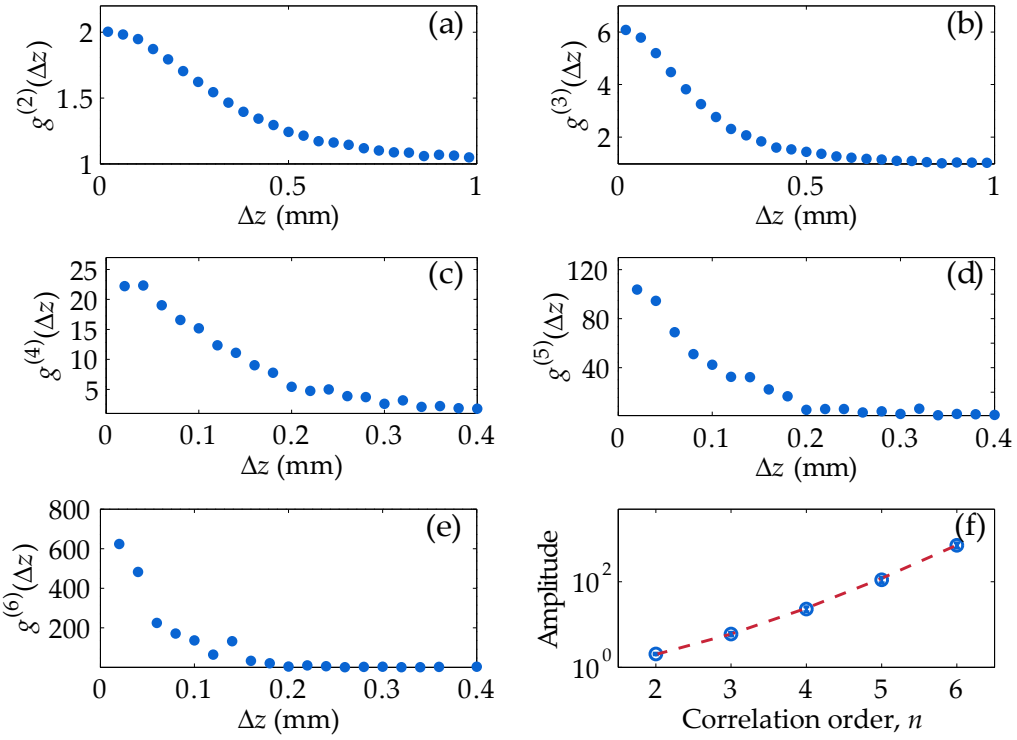

Figure 4.18: Second-order (a) through to sixth-order (e) correlation functions $g^{(n)}(\Delta z)$ measured. In (f), the peak correlation function amplitude (blue circles) for each order is compared to the ideal $n!$ scaling (dashed red line) on a logarithmic scale.

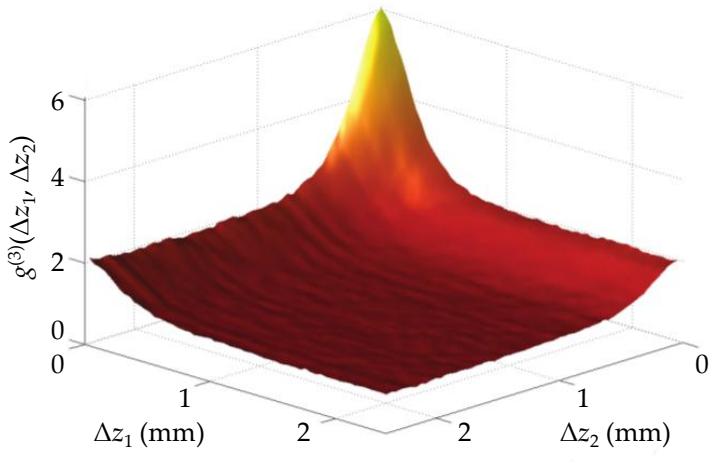

Figure 4.19: Surface plot of the three-body correlation function $g^{(3)}(\Delta z_1, \Delta z_2)$.

remaining simple to interpret.

4.5.3 Discussion

The peak amplitudes of each nth-order correlation function summarised in Table 4.2 provide the strongest direct evidence yet that the application of Wick's theorem in Glauber's theory of quantum coherence is valid. Although measuring Hanbury Brown-Twiss bunching in quantum gases has proven to be difficult in previous experiments, where the bunching contrast measured was restricted to small fractions of the ideal values, this result allows quantum atom optics experiments to be directly compared to traditional photon quantum optics, where high-contrast bunching measurements are far less challenging. In particular, our measurement of $g^{(6)}(0) = 710 \pm 90$, which implies that the density-normalised likelihood of measuring six particles in close proximity is almost three orders of magnitude greater than that for six particles at separations larger than l_z, is to our knowledge in excess of even state-of-the-art photonic measurements.

Similarly to the conclusions drawn about the experiment described in the previous section, we find that increasing the correlation length of the cloud further at the expense of number of atoms continues to give improvements in both bunching amplitude and signal-to-noise. In this case, we acquire half the number of experimental iterations compared to §4.4, where each shot contains a third of the number of atoms, and find that correlations with ideal amplitude persist for each moment in the sixth-order correlation function. Roughly speaking, the effect of bunching itself compensates for the reduction in statistics due to the increased number of independent variables $\Delta z_1, \ldots, \Delta z_{n-1}$ required to describe n-tuples of particles within a bin as n increases. Therefore, the signal-to-noise does not degrade at higher orders, which is in contrast to the experiment in the previous section where the three-body moment h in the third-order correlation function was heavily attenuated from its ideal value, which implies that measurements of fourth-order correlations with that data would have poor signal-to-noise. While we expect that correlation functions to seventh- and even higher-orders could be computed in principle for the optically-trapped clouds, the limited atomic flux prevented normalisation of the correlation functions from being reliable at higher orders.

This experiment has also served as a preliminary investigation of transversely-condensed quantum gases. Although dimensionality was not the focus of this partic-

ular result, the partial condensation of the cloud in the transverse direction of the trap resulted in a cloud with ideal coherence properties for measuring axial correlation functions, as the bin size in the x-y plane was far smaller than $l_\perp$. The correlation length in the axial direction provides further information about the quantum state of the clouds, which is intermediate between an ideal Bose gas and a weakly-interacting quasicondensate. The correlation length for a quasicondensate in the far field can be estimated from the in-trap momentum correlation scale of $\Delta k \sim 1/2l_\phi$ [146] with $\Delta z = \hbar \Delta k t_{\mathrm{ToF}}/m$, where $l_\phi = \hbar^2 n_{1D}/mk_BT$ is the in-trap length scale of phase coherence for a quasicondensate. Under the local density approximation, the 1D density $n_{1D} \approx 2.0$ atoms/μm leads to a correlation length of ~ 860 μm for the quasicondensate regime, while for an ideal Bose gas $l_z \approx 95$ μm, so our measured correlation length of 394 μm is consistent with the gas being in an intermediate state between these two limiting regimes. Furthermore, the very weak confinement in the z direction against gravity will result in the cloud 'sagging' in the optical trap, and therefore not provide the harmonic trapping confinement which is assumed for our theoretical predictions.

The behaviour of the gas can also be characterised by the dimensionless parameters for interaction strength and temperature from Eqs. 2.46 and 2.47 respectively. In this case, the interaction parameter is small at $\gamma = mg/\hbar^2 n_{1D} \simeq 0.006$, while the dimensionless temperature is $\tau = 2mk_BT/\hbar^2 n_{1D}^2 \simeq 0.26$. As this temperature is around three times larger than the crossover temperature which is $\tau_C \sim \sqrt{\gamma} \approx 0.078$ [150], it can be seen that the system is indeed an intermediate between the decoherent quantum (approximately ideal Bose gas where $\tau \gg \sqrt{\gamma}$) and quasicondensate ($\tau \ll \sqrt{\gamma}$) regimes [149, 150].

4.6 Summary

In this chapter, several experiments which each successively improve our ability to measure higher-order quantum correlation functions have been described. The coherence of a pulsed atom laser outcoupled with RF radiation was verified, and directly compared to a pulsed thermal source. Long-range third-order correlations were measured for atomic systems for the first time temporally, where the coherence of a BEC was confirmed to third order, followed by a measurement of third-order thermal bunching in the spatial plane of the detector with significantly improved amplitude and correlation length. Finally, an optical dipole trap was used to create an atomic source with a transverse correlation length which extended over the entire cloud radially, which allowed thermal correlation functions to be measured in the ideal limit and thus confirmed the applicability of Wick's theorem for ultracold gases.

These experiments have not only added to the growing body of fundamental knowledge about correlations in quantum gases, but have also developed techniques which allow correlation measurements to be a useful experimental tool to probe the state of ultracold atomic systems. Several fundamental tests of quantum mechanics with photons, including realisations of Einstein-Podolsky-Rosen entanglement [213] and violations of Bell's inequalities [20, 83], rely on accurately measured correlations for quantum systems, and thus improvements in the measurement of atomic correlation functions could allow similar tests with massive particles [104]. Higher-order correlation measurements could also be useful for investigating p- and d-wave pairings [214] which may clarify the mechanism of high-temperature superconductivity.

The next chapter of this thesis will carry on the theme of using Hanbury Brown-

Twiss bunching as a probe for quantum systems, by using correlation measurements to reveal the novel phenomenon of transverse condensation in an elongated Bose gas. Systems of lower dimensionality can access a wide variety of regimes displaying unique coherence behaviour which is not possible in 3D, while the transitions between these regimes can in many cases be revealed with bunching measurements. A particular example of a system influenced by dimensionality was explored in §4.5 of this chapter, and it will be seen in the following chapter that the ideal bunching seen for this system is a consequence of the saturation of the transverse ground state of the cloud, which nevertheless remains incoherent longitudinally.

Chapter 5

Using quantum correlations to probe transverse condensation of an elongated Bose gas

While most of the correlation experiments in Chapter 4 were performed for systems well described by classical Boltzmann gas theory, a rich variety of different coherence regimes can be explored for systems near transition points in degeneracy or dimensionality, as was discussed in §2.4.1. An example of such a system was seen in §4.5, where a low temperature cloud held in a highly elongated trap was seen to be extraordinarily conducive to high-contrast Hanbury Brown-Twiss interference measurements, and enabled bunching for an incoherent gas in the ideal limit where $g^{(n)}(0) = n!$ to be observed up to order $n = 6$. Although accounting for the effects of dimensionality or the proximity to quasicondensation was not pivotal to understanding that particular result, such striking correlation behaviour does encourage further study of the consequences of these influences.

In this chapter, ultracold Bose gases confined in high aspect ratio cigar-shaped traps at temperatures near quantum degeneracy are investigated. By producing systems in a parameter space where the number of atoms in the cloud is of order the trap aspect ratio, while the cloud remains in the 3D regime despite being close to the 1D crossover, the phenomenon of transverse condensation can be observed. In this case, the gas saturates the transverse ground state of the potential, while remaining incoherent axially, which is consistent with the results seen in §4.5. Here, the quantum state of the gas is probed with a measurement of long-range second-order correlation functions over a range of temperatures and trap populations, which quantifies the disparate behaviour between the longitudinal and radial axes characteristic of transverse condensation.

The experiment described in this chapter has been published in:

- Wu RuGway, A. G. Manning, S. S. Hodgman, R. G. Dall, A. G. Truscott, T. Lamberton, and K. V. Kheruntsyan, "Observation of Transverse Bose-Einstein Condensation via Hanbury Brown-Twiss Correlations," *Physical Review Letters* **111**, 093601 (2013).

The behaviour of trapped ultracold Bose gases can be accurately described by three-dimensional ideal Bose gas theory for a wide range of experimentally-produced systems, where the weak inter-atomic interactions present are assumed to be negligible. Each of the correlation measurements performed with clouds held in our cigar-shaped magnetic trap described in Chapter 4 of this thesis fall under this category, where considerations such as the trap geometry or the finite number of atoms in the system have little bearing on the physical processes observed. In particular, the phase transition to Bose-Einstein condensation for an ideal gas (§2.3.1) where long-range order is established occurs simply due to quantum statistics, and does not require the influence of interactions.

For thermal clouds at a temperature T somewhat above the critical temperature for the transition to BEC, Hanbury Brown-Twiss bunching characteristic of a classical Boltzmann gas can be observed, according to the theory covered in §4.1.1. In this case, bunching occurs over an in-trap correlation length of $l_{\mathrm{trap}}^{(\mathrm{cl})} = \lambda_{\mathrm{dB}}/\sqrt{2\pi}$, for thermal de Broglie wavelength λ_{dB}. As we recall from Eq. 4.5, this scales over the time of flight $t_{\mathrm{ToF}} = 416$ ms to the detector in the far field of the trap to

$$l_j^{(\mathrm{cl})} = \frac{\hbar\omega_j t_{\mathrm{ToF}}}{\sqrt{m k_B T}}, \tag{5.1}$$

where ω_j is the harmonic trapping frequency in the Cartesian direction j.

However, as was discussed in §2.4, the dimensionality of a quantum gas can potentially be altered by the geometry of the trap it is confined in. In an anisotropic trap where the transverse and longitudinal trapping frequencies ($\omega_\perp$ and $\omega_\parallel$ respectively) are sufficiently different, dynamics can be frozen out in the direction j if the confinement in that direction is strong enough to prevent multiple thermal modes in that direction from being populated, which occurs when $\hbar\omega_j \gg k_B T$ (an overview of trapped gases in lower dimensions is presented in Ref. [215]). In particular, an elongated cigar-shaped geometry where $\omega_\perp \gg \omega_\parallel$ can lead to a one-dimensional cloud where excitations are only possible in the longitudinal axis of the trap, while $\omega_\perp \ll \omega_\parallel$ leads to a two-dimensional 'pancake' geometry where dynamics are suppressed in one dimension.

An important consequence of changing the dimensionality of a harmonically-trapped Bose gas is an alteration to the density of states (Eq. 2.43), which in turn changes the critical temperature T_c for condensate formation (Eq. 2.44). As we recall from Eq. 2.31, in three dimensions this takes the familiar form in the thermodynamic limit[1] of

$$T_c^{3D} = \frac{\hbar\bar{\omega}}{k_B}\left[\frac{N}{g_3(1)}\right]^{\frac{1}{3}}, \tag{5.2}$$

for N atoms, where $g_3(1) \approx 1.202$ and $\bar{\omega} = (\omega_x\omega_y\omega_z)^{1/3}$ is the geometric mean of the three trap frequencies ω_j ($j = x, y, z$). While condensation is also possible for a harmonically-trapped 2D gas, it can not occur for harmonically-trapped 1D gases in the thermodynamic limit. However, removing the restriction of being in the thermodynamic limit results in the possibility of macroscopic occupation of the ground state of a

[1] The thermodynamic limit describes systems where the number of particles goes to infinity, while the peak density remains constant.

1D system at the critical temperature

$$T_c^{1D} \approx \frac{N\hbar\omega_z}{k_B \ln(2N)}. \tag{5.3}$$

While it is well established that three-dimensional Bose-Einstein condensates possess long-range coherence characterised by the quantum correlation functions $g^{(n)}(\Delta\mathbf{r}) = 1$ to all orders of n, it was seen in §2.4.1 that the coherence of one-dimensional Bose gases depends on dimensionless parameters for interaction strength γ and temperature τ [216–218]. A variety of regimes can be realised, from high temperature and weakly interacting gases which behave in a way similar to ideal Bose gases, to strongly interacting and low temperature Tonks-Girardeau gases which mimic the anti-bunching behaviour of fermions, to weakly-interacting but degenerate gases which display a range of behaviours depending on the dominant source of fluctuations. The latter of these regimes includes the phenomenon of quasicondensation, where density fluctuations are suppressed and thus such clouds mimic the density profile of a BEC before expansion, while phase fluctuations cause coherence to only be possible over small, localised regions of the cloud. Therefore, while essentially no Hanbury Brown-Twiss bunching should be observed in trap, regions which are not phase coherent eventually overlap during ballistic expansion of the cloud and result in bunching being seen in momentum space, which is what would inevitably be measured by our detector situated in the far field of the trap.

Previous studies of quantum correlations influenced by system dimensionality

Several experiments have explored aspects of the effect of dimensionality on the coherence of ultracold Bose gases. A measurement of bunching in quasicondensates for times of flight intermediate between the near and far fields was achieved for ^{87}Rb atoms released from a quasi-one-dimensional chip trap, using a light sheet to detect individual atoms [202]. Phase fluctuations due to thermal excitations in BECs have also been characterised over a range of temperatures and geometries, where fluctuations are found to be more prevalent at large aspect ratios [219]. Other experiments have explored the role of dimensionality by measuring in-trap collisional loss rates, in a manner similar to an experiment which compared three-body loss rates for condensed and thermal sources of bosons [198]. Although such experiments are not capable of determining long range order, and can be significantly influenced by interactions due to the short spatial scales being probed, measurements of density fluctuations do give an indication of quantum-statistical properties over short ranges.

Bosons confined in a 1D geometry incorporating an optical lattice can also display behaviour normally associated with fermions such as anti-bunching in the strongly-interacting Tonks-Girardeau regime, as was discussed in §2.4.1. A characteristic of such gases is the dependence of the axial radius of the trapped cloud on interaction strength, which was observed in a system lacking strong confinement in one axis [220]. Tonks-Girardeau gases in an optical lattice have also been observed to have a momentum distribution characteristic of strongly-interacting Bose gases, which differs from that for a fermionic system [221]. First-order correlation measurements of phase coherence can reveal information about the excitation spectrum of strongly interacting 1D gases held in a lattice, where Bragg spectroscopy has been used to probe the transition between the superfluid and Mott insulator states [222]. This study also observed the increase

in fluctuations for 1D systems lacking long-range coherence, while the transition to a 3D state resulted in a significant change to the correlation length of the system. Tonks-Girardeau gases can also be identified by a reduction in many-body loss rates indicative of anti-bunching [143, 199, 204].

Several experimental studies have demonstrated that the exactly-solvable theory of 1D Bose gases with repulsive contact potentials developed by Yang and Yang [223] is capable of describing the behaviour of such gases over a wide range of conditions. Agreement with the measured in-trap spatial density profiles of a weakly interacting, nearly one-dimensional gas provided the first test of Yang-Yang theory [224]. Furthermore, measurements of atom number fluctuation in a 1D gas were able to demonstrate that Yang-Yang theory correctly accounts for the crossover from weakly interacting quasicondensation to strongly-interacting gases displaying fermionic behaviour [225]. Calculations of theoretical second-order correlation functions with Yang-Yang theory have found good agreement with the behaviour predicted in the limiting regimes of quasicondensation and ideal Bose gas theory [145], while the Luttinger liquid approach has also been used in the weakly interacting limit [146], as described by the parameter ranges outlined in §2.4.1.

Another interesting transition can be realised in a two-dimensional gas, where for temperatures around the Berezinskii-Kosterlitz-Thouless (BKT) transition point, different regimes such as the superfluid and non-superfluid quasicondensate states occur. Each of these regimes have characteristic correlation properties, which were identified in an experiment which split a 2D gas with an optical lattice and interfered the clouds to measure fringe visibility and the proliferation of free vortices as a function of temperature [136], while another experiment measured the correlation length of a 2D gas using Raman scattering to create a phase interferometer [137]. It has also been shown that the critical number for the onset of a bimodal density distribution is not well predicted by ideal gas theory, while the BKT model provides a much better description of this phase transition [226].

Transverse condensation of Bose gases

A Bose gas confined to an anisotropic trap which is able to undergo complete three-dimensional Bose-Einstein condensation can also access an intermediate state between incoherence and full long-range order. In this case, the gas can condense into the tightly confining axes of the trap while remaining thermal in the weak axis, as was first predicted by van Druten and Ketterle [151] and is discussed in detail in §2.4.2. For a general class of elongated cigar-shaped traps, condensation can proceed in two steps if the three-dimensional critical temperature T_c^{3D}(Eq. 5.2) is higher than than in one dimension T_c^{1D} (Eq. 5.3). Transverse condensation can then occur when $T_c^{1D} < T < T_c^{3D}$, where the transverse ground state of the gas becomes saturated. If the gas is then cooled further to $T < T_c^{1D}$, a full 3D condensate is then produced.

For this to be apparent, the gas should remain in the 3D regime where $k_B T \gtrsim \hbar\omega_\perp$. This requirement, in addition to the bounds on temperature, place restrictions on the number of atoms in the system N and the aspect ratio of the trap $\lambda = \omega_\perp/\omega_z$, where $\omega_\perp \equiv \omega_x = \omega_y$ is the frequency in the transverse direction, assuming a radially symmetric confinement. This can be expressed in terms of placing bounds on λ for a given N

such that transverse condensation is possible, which we recall from Eq. 2.48 is

$$\lambda_{\min} \equiv N\left[g_3(1)\right]^{1/2}\left[\ln(2N)\right]^{-3/2} < \lambda < \frac{N}{g_3(1)} \equiv \lambda_{\max}. \tag{5.4}$$

As with the phase transition to a normal 3D condensate, the critical transition to transverse condensation is quantum degeneracy driven, and does not occur as the result of interactions [208].

When analysing the correlation behaviour of quantum systems at temperatures near to quantum degeneracy, it no longer suffices to assume that ideal Bose gases are well described by taking the high-temperature Boltzmann limit. Specifically, the theory developed in Refs. [34] and [186] first considers an ideal Bose gas, which is described by a first order correlation function of

$$\begin{aligned} G^{(1)}(\mathbf{r},\mathbf{r}') =& \frac{1}{\pi^{3/2}}\sum_{j=1}^{\infty}\exp\left(\frac{j\tilde{\mu}}{k_BT}\right)\prod_{\alpha=x,y,z}\frac{1}{\sigma_\alpha\sqrt{1-\exp\left(-2\tau_\alpha j\right)}} \\ &\times\exp\left[-\tanh\left(\frac{\tau_\alpha j}{2}\right)\left(\frac{r_\alpha+r'_\alpha}{2\sigma_\alpha}\right)^2-\coth\left(\frac{\tau_\alpha j}{2}\right)\left(\frac{r_\alpha-r'_\alpha}{2\sigma_\alpha}\right)^2\right], \end{aligned} \tag{5.5}$$

where $\tau_\alpha = \hbar\omega_\alpha/k_BT$, $\tilde{\mu} = \mu - \hbar\sum_\alpha \omega_\alpha/2$, and the harmonic oscillator length is $\sigma_\alpha = \sqrt{\hbar/m\omega_\alpha}$. The density of the gas can then be determined from $\rho(\mathbf{r}) = G^{(1)}(\mathbf{r},\mathbf{r})$. However, the theory used to describe most of the correlation measurements in this thesis, which was discussed in §4.1.1, simplifies Eq. 5.5 to the limit where $\mu \to -\infty$ for a high-temperature Boltzmann gas. This eliminates the need to sum over j, and results in

$$G^{(1)}(\mathbf{r},\mathbf{r}') = \frac{N}{\lambda_{\mathrm{dB}}^3}\prod_{\alpha=x,y,z}\tau_\alpha\exp\left[\frac{\tau_\alpha}{2}\left(\frac{r_\alpha+r'_\alpha}{2\sigma_\alpha}\right)^2-\pi\left(\frac{r_\alpha-r'_\alpha}{\lambda_{\mathrm{dB}}}\right)^2\right]. \tag{5.6}$$

When the expression in Eq. 5.6 is normalised by density, the familiar correlation length of $l_{\mathrm{trap}}^{(\mathrm{cl})} = \lambda_{\mathrm{dB}}/\sqrt{2\pi}$ is recovered for a trapped Boltzmann gas, while the characteristic length of the correlation function for an ideal Bose gas in Eq. 5.5 will not necessarily be described by such a simple relationship. Thus, the longitudinal correlation length for a transversely condensed gas would be expected to deviate from that for a classical Boltzmann gas, as $T < T_c^{3D}$ in this case.

The ground state population of an ideal Bose gas can be extracted from the density distribution of the cloud, by determining what fraction of the system is in the lowest energy state with a density profile [186]

$$\rho_0(\mathbf{r}) = \frac{\exp\left(\tilde{\mu}/k_BT\right)}{1-\exp\left(\tilde{\mu}/k_BT\right)}\prod_{\alpha=x,y,z}\frac{\exp\left(-r_\alpha^2/\sigma_\alpha^2\right)}{\left(\sqrt{\pi}\sigma_\alpha\right)^3}. \tag{5.7}$$

The ground state fraction can be found for a classical gas from the appropriate Boltzmann factor, which implicitly accounts for the role of dimensionality in the system.

Competition between formation of quasicondensates and BECs

An important consideration for describing the behaviour of elongated, transversely-condensed clouds is to quantify whether quasicondensation or true Bose-Einstein condensation is likely to occur as the cloud is cooled. As we saw in §2.4.1, such systems can

be characterised by dimensionless parameters for interaction strength (Eq. 2.46)

$$\gamma = \frac{mg}{\hbar^2 n_{1D}}, \tag{5.8}$$

where the interaction strength is $g = 2\hbar\omega_\perp a$, n_{1D} is the linear density, and a is 3d s-wave scattering length, which is 7.5 nm for He* [201]; and a density-independent temperature parameter $\mathcal{T}$, derived from τ in Eq. 2.47 such that

$$\mathcal{T} = \frac{\tau}{\gamma^2}. \tag{5.9}$$

In the limit of weak interactions where $\gamma \ll 1$, a 1D gas can either undergo condensation to the ground state of the system which is driven by quantum degeneracy, or interaction-driven quasicondensation [208].

For a weakly-interacting 1D system with a uniform density distribution, the transition to quasicondensation occurs in a continuous manner as T drops below $T_d\sqrt{\gamma}$, where the quantum degeneracy temperature T_d is [208]

$$T_d = \frac{\hbar^2 n_{1D}^2}{2mk_B}. \tag{5.10}$$

Similar behaviour occurs for a harmonically-confined 1D gas, which unlike the uniform gas can also undergo condensation for an ideal Bose gas at the temperature T_c^{1D} (Eq. 5.3). The factor which determines which of these behaviours dominates is the longitudinal trapping frequency ω_z, where weak confinement will be shown to leads to quasicondensation, while strong confinement gives statistically-induced condensation.

The crossover temperature T_{co} and number N_{co} for quasicondensation for weak longitudinal traps can be determined using the local density approximation (LDA). This requires that the characteristic length of density fluctuations $l_c \simeq \hbar/\sqrt{m\,|\mu_0|}$, where $\mu_0 \approx gn$ is the chemical potential at the centre of the cloud, is much smaller than the length scale of density variations, which is given by $L \simeq \sqrt{|\mu_0|\,/m\omega_z^2}$ for incoherent clouds or $L \simeq \sqrt{2n_{co}g/m\omega_z^2}$ for quasicondensates with density n_{co}. The LDA can be shown to hold if

$$\omega_z \ll \omega_{co} \equiv \left[\frac{m(gk_BT)^2}{\hbar^5}\right]^{1/3}. \tag{5.11}$$

in which case quasicondensation occurs in the same fashion as for a uniform gas.

For large enough values of the density-independent temperature parameter ($\mathcal{T} > 10^3$), the interaction-induced crossover to quasicondensation can be shown to dominate over the formation of a BEC if Eq. 5.11 is satisfied, while a statistically-driven BEC will form if $\omega_z \gg \omega_{co}$ [208]. Such behaviour is also expected to extend to the boundary between 1D and 3D geometries where $T \sim \hbar\omega_\perp$, where quasicondensation is also able to occur in 3D. Furthermore, the quasicondensate transition is predicted to retain properties influenced by 1D physics even if $k_BT > \hbar\omega_\perp$.

An experimental study to test this regime measured density fluctuations in an ideal gas through the transition from an ideal gas to quasicondensation, with a range of trap geometries from 1D to nearly 3D [227] such that the freezing of dynamics due to dimensionality is strong but not perfect. This experiment was performed in a parameter space conducive to transverse condensation, and was thus able to probe the interplay between lower-dimensional and 3D physics at the quasicondensate crossover. It was found that

a continuous change in behaviour occurs across the dimensional crossover temperature $T_{\mathrm{DC}} \sim \hbar\omega_{\perp}/k_B$, and that while the transition to quasicondensation at the 1D to 3D crossover is always dictated by 1D effects, it occurs via degeneracy-driven transverse condensation in the 3D limit, and by interactions in the 1D limit, as expected. In all cases, a modified Yang-Yang theory using ideal Bose gas theory for excited states in the transverse axis was able to successfully describe the behaviour of the gas. Measurements of in-trap loss rates have also been used to probe the behaviour of quasi-condensates across the transition from 1D to 3D geometries, in regimes where either degeneracy or interactions drive phase transitions [203].

5.1 Direct observation of transverse condensation in an elongated Bose gas

In this experiment, the quantum state of Bose gases in trap geometries near the 1D to 3D crossover, and at temperatures close to quantum degeneracy, will be investigated with measurements of second-order correlation functions in the far field. This will allow the coherence of the cloud to be tested along both the transverse and longitudinal axes, which will be able to unambiguously identify the phenomenon of transverse condensation. This study extends the investigation presented in §4.5, which only considered coherence in the longitudinal axis, by comparing radial and axial correlation functions at a variety of temperatures.

5.1.1 Experimental method

The experimental method for investigating transverse condensation in an elongated Bose gas essentially followed the same procedure that was used to observe ideal longitudinal thermal bunching up to sixth order in §4.5.1. While the aspect ratio of the magnetic trap of around $\lambda \approx 10$ is far too low for this experiment to be feasible, highly anisotropic one-dimensional ($\lambda > 100$) traps can easily be produced with red-detuned dipole laser beams. Small clouds of about 10^4 atoms were first loaded from a magnetic trap with a temperature of around 1 μK into a dimple trap at its maximum trap depth. Near-resonant but low intensity ($I \approx 0.01\, I_{\mathrm{sat}}$) light was then applied to reduce the number of atoms N in the cloud, which ensured that $\lambda \sim N \approx 10^2$ to 10^3 was achieved independently of trap strength.

The depth of the dipole trap was then reduced to evaporatively cool the trapped cloud to different levels (refer to §3.1.3), which resulted in a range of trap depths, temperatures, and cloud populations. The three different settings used in this investigation are described in Table 5.1, and include the fully three-dimensional high-temperature and number regime (a), clouds which are cooled such that a macroscopic portion of the population is in the transverse ground state of the potential (b), and clouds which are cooled even further so that the majority of the cloud is in the transverse ground state (c). Justification for the names given to these regimes will be provided in the following sections.

The trap aspect ratio for each experimental configuration in Table 5.1 was seen to satisfy the bounds placed by Eq. 5.4, which ensured that transverse condensation is possible for temperatures between the 1D and 3D critical temperatures. The values for N quoted in Table 5.1 are corrected by a factor of the quantum efficiency of the delay-

Regime	N	$(\omega_x, \omega_y, \omega_z)/2\pi$	λ_{min}	λ	λ_{max}
(a) 3D thermal, no TC	2800	$(5400, 4500, 38)$ Hz	121	130	2330
(b) Partial TC	820	$(2700, 2300, 21)$ Hz	45	119	682
(c) Full TC	370	$(2350, 1700, 13)$ Hz	24	154	307

Table 5.1: The three different regimes entered in this experiment, each having undergone different degrees of transverse condensation (TC).

line detector, which according to a variety of other measurements performed with our detector is is assumed to be $\sim$20%. The coherence of the cloud can then be measured in the transverse (x or y axes) and longitudinal (z) directions by calculating second-order momentum space correlation functions in the same manner as the other experiments described in Chapter 4. To achieve this, a data set of at least 10^3 experimental iterations was obtained for each of the three experimental settings.

5.1.2 Results

To first confirm the thermal and incoherent nature of the gas in the longitudinal direction, and compare this to the ideal nth order bunching result in §4.5, second-order correlations are measured in the z axis of the system. In this case, the bins used to compute the correlation functions are 5 mm in both the x and y directions for data set (a), and 10 mm for (b) and (c). These correlation functions (A) to (C) are illustrated in Fig. 5.1, accompanied by the corresponding longitudinal density profiles (a) to (c). The density distribution is well described in each regime by ideal Bose gas theory with Eq. 5.5, and the temperatures measured for each system thus correspond to these fits. We can then compare these measured longitudinal temperatures with the 3D and 1D transition temperatures in Eqs. 5.2 and 5.3, the result of which is shown in Table 5.2. Here, we can see that $T > T_c^{1D}$ in all cases, and while $T < T_c^{3D}$ for (b) and (c), no bimodality is evident in the density profiles (B) and (C) in Fig. 5.1, which indicates that a macroscopic occupation of the longitudinal or full 3D ground state is not present. Also, note that while we are inevitably close to the 1D crossover, $k_B T \gtrsim \hbar\omega_\perp$ in all cases.

Regime	T	T_c^{3D}	T_c^{1D}	T/T_c^{3D}	$k_B T/\hbar\omega_\perp$
(a) 3D thermal, no TC	1.7 µK	620 nK	592 nK	2.74	7.18
(b) Partial TC	155 nK	214 nK	111 nK	0.72	1.29
(c) Full TC	63 nK	124 nK	37 nK	0.52	0.66

Table 5.2: Temperature measurements in each regime, the corresponding 1D and 3D transition temperatures, and a comparison of temperature with the 3D transition point and transverse confinement.

The correlation functions (a) to (c) in Fig. 5.1 confirm that long-range order is not present in any of the three regimes, and instead display a bunching signal characteristic of an incoherent Bose gas. The ratio of the correlation length to bin size in the x-y plane, and consequently the bunching amplitude, increases with decreasing temperature. However, we recall that the correlation length for a classical Boltzmann gas (Eq. 5.1) in the x-y plane of the bins, which determines the bunching contrast, depends on both temperature T and predominantly the radial trapping frequency $\omega_\perp$ such that $l^{(\text{cl})} \propto \omega_\perp T^{-1/2}$. For our dipole trap setup, a decrease in temperature is accompanied by a reduction in trapping frequencies during the evaporation process, such that the trans-

verse classical correlation length only increases by a factor of around two between (a) and (c) and is thus unable to account for the marked difference in bunching amplitude observed between these regimes. This provides further evidence that the coherence in the transverse direction of the cloud is not behaving in a manner associated to a classical Boltzmann gas. In particular, we see that regime (c) provides perfect a bunching amplitude of $g^{(2)}(0) = 2$ and a correlation length of 394 µm, with a quantum gas which matches that used to obtain perfect bunching up to sixth order in §4.5. Otherwise, the bunching amplitude is attenuated due to the effect of binning in the same fashion as other experiments described in Chapter 4.

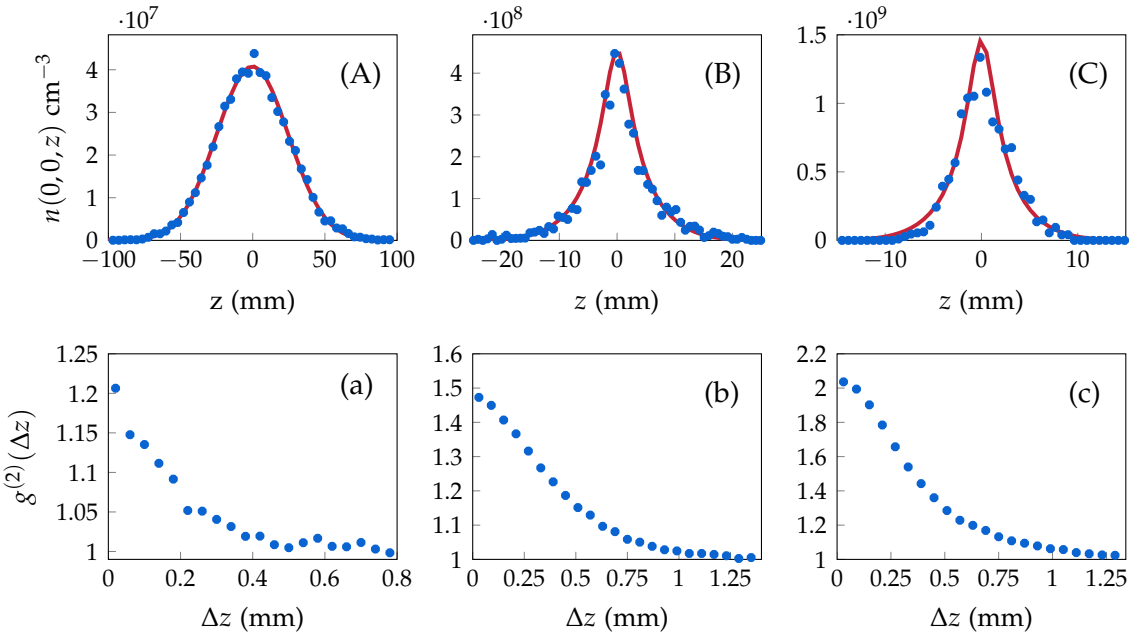

Figure 5.1: (Top row) Longitudinal cross sections of the density distribution of the cloud at the detector $n(0,0,z)$ (blue circles), and theoretical fits using the ideal Bose gas model (red lines) for the three sets of data described in Table 5.1. (Bottom row) The corresponding longitudinal second order-correlation functions $g^{(2)}(\Delta z)$.

Correlation functions can then be computed in a similar manner for the radial dimension x (which should show essentially the behaviour as the y direction), using bins which are 6 mm in y and 160 µm in z. The result of this is shown in Fig. 5.2, where the data points correspond to the same regimes are before. In particular, it is seen that the measured correlation $l_x^{(\mathrm{corr})}$ diverges from that for a classical Boltzmann gas (Eq. 5.1) as the gas is cooled. In the high-temperature limit (a), the measured correlation length coincides with the predicted classical length, signifying that the gas is indeed an ideal Boltzmann gas as expected. However, when T drops below T_C^{3D} for points (b) and (c), the measured transverse correlation length becomes significantly larger than that for a classical gas, which is accompanied by a macroscopic occupation of the transverse ground state. For (b), the ground state occupation is 51% according to the ideal Bose gas model, as opposed to 29% for a Boltzmann gas, while the discrepancy in the correlation length increases for (c), where the ideal Bose gas model predicts a ground state population of 82% compared to 61% for a classical gas. This trend is captured by a theoretical

curve of $l_x^{(\mathrm{corr})}/l_x^{(\mathrm{cl})}$ against T/T_c^{3D}, which includes a weak dependence on atom number when $T < T_c^{3D}$ and is thus produced by an average over experimental parameters for (b) and (c), including their respective uncertainties. In all cases, the transverse correlation function is well represented by ideal Bose gas theory.

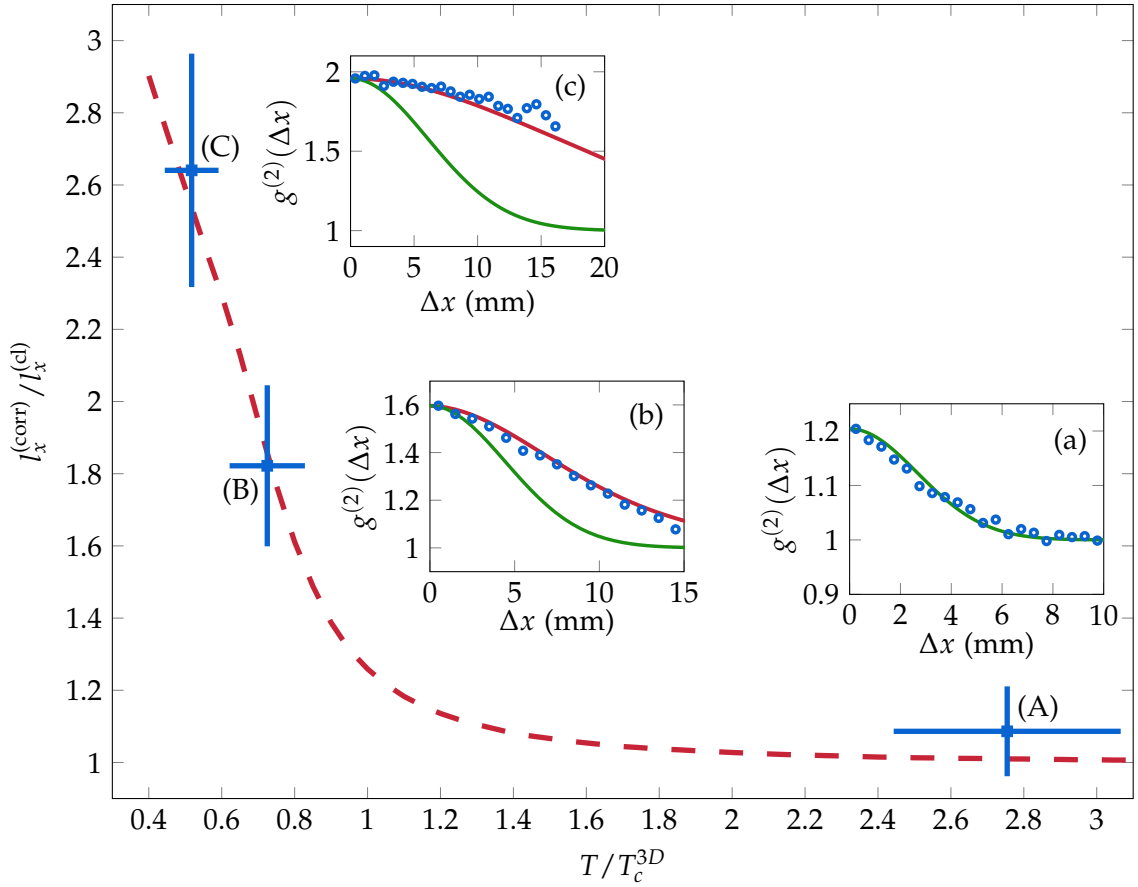

Figure 5.2: For the three points (A) to (C) which correspond to different temperatures normalised against the 3D transition temperature T/T_c^{3D} according to Table 5.2, the radial correlation length $l_x^{(\mathrm{corr})}$ measured from the transverse correlation functions $g^{(2)}(\Delta x)$ is compared to the correlation length for a classical Boltzmann gas $l_x^{(\mathrm{cl})}$. Here, we see that the scaled transverse correlation length $l_x^{(\mathrm{corr})}/l_x^{(\mathrm{cl})}$ increases with decreasing normalised temperature. The error bars on these points account for the uncertainty in T (10%), N (25%), ω_i (10%), and $l_x^{(\mathrm{corr})}$ (5%). The dashed red line is derived from a fit to the RMS width of correlation functions simulated using the full ideal Bose gas theory in Eq. 5.5, compared to the classical limit in Eq. 5.6. The insets (a) to (c) show the measured transverse correlation function corresponding to each point (A) to (C). The red and green lines are theoretical curves for an ideal Bose gas and classical Boltzmann gas respectively, where the two curves coincide for the high-temperature gas (a).

5.1.3 Discussion

The results in Fig. 5.2 show that the behaviour in the transverse axis of the trap is well described by ideal Bose gas theory for a degenerate system, where radial coherence can be identified given that the transverse correlation length exceeds the size of the cloud once $T < T_C^{3D}$, as was seen most strikingly in regime (c). This implies that the saturation of the transverse population of the system occurs due to the quantum degeneracy effects characteristic of ideal Bose gases, rather than being driven by interactions. As the transversely-condensed gases in regimes (b) and (c) are inevitably close to the 1D crossover at $k_B T \sim \hbar\omega_\perp$, a transverse ground state population would also be present due to the dimensionality constraints on the system. However, while this is accounted for by the classical estimate of the ground state population, the larger ground state occupation predicted by the ideal Bose gas model shows that a sizeable portion of this population is due to transverse condensation driven by quantum statistics.

In contrast, the longitudinal behaviour in Fig. 5.1 is obviously incoherent. More specifically, the longitudinal coherence, especially for temperatures below T_c^{3D}, is intermediate between that for an ideal Bose gas and a weakly-interacting 1D quasicondensate. This conclusion can be arrived at by considering the correlation length for the coldest cloud (c), where the measured correlation length of 394 µm is between that for an ideal Bose gas at 95 µm, and the predicted correlation length of a 1D quasicondensate of 860 µm, as was discussed previously in §4.5.3. Given that $\tau \approx 0.26$ and $\gamma \approx 0.006$, the system is not described exclusively by either the quasicondensate ($\tau \ll \sqrt{\gamma}$) or ideal Bose gas ($\tau \gg \sqrt{\gamma}$) regimes.

Although the quantum degeneracy temperature is $T_d = 243$ nK, the temperature of cloud (c) still exceeds to the threshold for the smooth transition to quasicondensation for a uniform (untrapped) gas at $T_d\sqrt{\gamma} = 18.8$ nK due to the small interaction strength. The density-independent temperature parameter in Eq. 5.9 is $\mathcal{T} \approx 7200$ for (c), so the more accurate treatment for a harmonically trapped system could also give insight into the longitudinal behaviour of the cloud. Once again, we see that the crossover for the axial trapping frequency in Eq. 5.11 is $\omega_{\rm co} = 2\pi \times 85.6$ Hz, which is of order $\omega_z = 2\pi \times 13$ Hz and is thus not unambiguously in either the quasicondensate or ideal Bose gas regimes. As Hanbury Brown-Twiss bunching of $g^{(2)}(0) = 2$ is expected in the far field for both of these cases [146], the behaviour in the longitudinal axis of the cloud resides in the broad crossover between these regimes.

The distinction between the second-order correlation functions in the longitudinal and transverse axes also gives a clear indication of transverse condensation. The perfect longitudinal bunching signal measured in regime (c) up to sixth order in §4.5 can be explained by a high level of radial coherence, which allows the reduction in bunching amplitude due to binning to be circumvented. It must be noted here that the lack of precise agreement between $g^{(2)}(\Delta x = 0)$ and $g^{(2)}(\Delta z = 0)$ for the three regimes in Figs. 5.1 and 5.2 respectively is due to these correlation plots being computed with different bin sizes.

The temperature T_c^{3D} considered to mark the onset of condensation in 3D is defined in the thermodynamic limit where $N \to \infty$ while density remains constant, and while this approximation remains appropriate for systems with as few as 10^4 atoms, smaller

systems require an adjustment of the critical temperature to [133]

$$T_{3D}^{*} \approx T_{C}^{3D}\left[1-\frac{0.7275\sum_{i}\omega_{i}}{3N^{\frac{1}{3}}\left(\prod_{i=x,y,z}\omega_{i}\right)^{\frac{1}{3}}}\right]. \tag{5.12}$$

Using this, we find that $T_{3D}^{*} \approx 0.63T_{C}^{3D}$ for (c), while $T_{3D}^{*} \approx 0.74T_{C}^{3D}$ for (b) and $T_{3D}^{*} \approx 0.82T_{C}^{3D}$ for (a). This lowering of the transition temperature accounts for the observation in Fig. 5.2 that $l_{x}^{(\mathrm{corr})}$ diverges away from $l_{x}^{(\mathrm{cl})}$ at a temperature distinctly lower than T_{c}^{3D}.

5.2 Summary

In this experiment, we have used Hanbury Brown-Twiss correlations to probe the statistically-driven phenomenon of transverse condensation in an ultracold elongated Bose gas. While the cloud was found to be almost completely coherent radially, the longitudinal correlation behaviour remains incoherent for temperatures above the 1D transition temperature, despite the temperature of the system being below the 3D transition temperature. It was also shown that the transverse behaviour of the cloud is well described by ideal Bose gas theory, which diverges from the theory of classical Boltzmann gases at such low temperatures.

Following from the theme in Chapter 4, increasing the radial correlation length of a quantum gas, which in this case exceeds the size of the cloud in two dimensions due to a macroscopic occupation of the transverse ground state, has been seen to allow large bunching amplitudes with minimal noise to be measured in the longitudinal direction. Such systems will be useful for studies of atomic coherence tomography, in a similar vein to that performed in optics [228]. Further studies could more thoroughly investigate the different phases possible for ultracold gases, especially the variety of behaviours present in lower dimensions, and could incorporate more rigorous tests of theory such as Yang-Yang thermodynamics. Similarly, the approach of producing systems with remarkably long correlation lengths in certain axes may also be applied to allow the measurement of second-order correlations in 2D systems, which could be important for clarifying the mechanism of the BKT crossover. The topic of correlation functions in systems with novel dimensionality properties will extend to the next chapter of this thesis, where the coherence of matter waves guided by an optical potential will be investigated.

Chapter 6

Macroscopic imaging of matter-wave interference

In this chapter, several manifestations of matter-wave interference which are observable at a macroscopic level will be explored. By imaging an atom laser onto a transmission mask, a diffraction pattern can be formed in the far field on either of our spatially-sensitive detectors. This provides the opportunity to not only determine first-order coherence immediately from a single density profile, but to also derive information about the density matrix of an atomic system by reconstructing its Wigner function.

Our vertically-aligned optical dipole trap also allows us to observe matter-wave interference directly, by guiding atoms falling under gravity onto our detectors with single atom resolution. The energy selectivity and collimation of atomic matter waves is improved by controllably loading atoms with a small energy spread into the waveguide via a form of evaporative cooling. The modal structure occupied by atoms in a waveguide can be studied by either directly imaging the density profile, or by analysing Hanbury Brown-Twiss bunching, where the correspondence between bunching and macroscopically-visible speckle patterns is apparent. A unique feature of our experimental setup is the ability to measure the transverse mode profile directly, as our detectors are in the plane orthogonal to the wave guide. The ability to both control and probe the modal structure of matter-wave guides is encouraging for a wide range of applications, including the development of high-precision yet compact sensors, and the generation of entanglement.

The experiments described in this chapter have been published in:

- R. G. Dall, S. S. Hodgman, A. G. Manning, and A. G. Truscott, "Observation of the first excited transverse mode in guided matter waves," *Optics Letters* **36**, 1131 (2011).
- R. G. Dall, S. S. Hodgman, A. G. Manning, M. T. Johnsson, K. G. H. Baldwin, and A. G. Truscott, "Observation of atomic speckle and Hanbury Brown-Twiss correlations in guided matter waves," *Nature Communications* **2**, 291 (2011).

6.1 Transverse interference profile of an atom laser incident on transmission mask

While the coherence measurements undertaken in the previous chapters resulted in correlations on a microscopic scale, matter-wave interference can also be observed directly on a macroscopic scale. Striking fringe patterns were achieved in an early experiment which demonstrated the interference of two Bose-Einstein condensates [187], and the transverse coherence of a guided matter wave has been measured by diffracting atomic beams on a transmission mask [190], where an atom laser produced a distinct interference pattern which was absent for a thermal beam. In an extension to the previous result obtained in our lab which is described in Ref. [190], diffraction patterns of atom lasers passing through a transmission mask have been measured, with the aim to extract the Wigner function of the quantum gas. The main difference between these two experiments is that the present result outcouples atoms from a magnetic trap without forming a waveguide, while the previous method guided atoms from an optical dipole trap through the transmission mask. Although analysis on this new data is yet to be completed, the images obtained also serve as an intuitive introduction to the concepts of the experiment described in §6.2.4, which measure the second-order correlation function of guided matter waves.

Experimental method

A BEC of $\sim 10^6$ atoms is first prepared in the usual manner, however the balance of currents in the quadrupole and bias coils of our BiQUIC trap (see §3.1.2) are adiabatically adjusted over 200 ms after having formed a condensate. This is to transform the trap from the 'cigar' configuration[1] to the 'sagged' configuration, with harmonic frequencies of $\omega_x = \omega_z \approx \omega_y \approx 80$ Hz which results in a reduction in energy spread for the outcoupled atoms. An atom laser is then formed by outcoupling atoms from the magnetic trap with a one-second pulse of RF radiation to reduce Fourier broadening, and thus obtain an approximately Gaussian atom laser density profile. In particular, atoms are outcoupled from the outer shell of the Thomas Fermi profile of the condensate, which minimises the momentum spread due to the reduction in mean-field interactions experienced (refer to §3.2.1). The transverse profile of such an atom laser is shown with the transmission mask removed in Fig. 6.1.

The outcoupled atom laser falls 118 mm under gravity onto a Quantifoil R 2/2 holey carbon film transmission mask, which is an array of 2 µm circular holes with 4 µm centre spacing, supported by a grid of copper wires with a density of 200 wires per inch. The size of the atom laser as it reaches the mask is around $R_x = 0.5$ mm and $R_y = 1.1$ mm, compared to the 2 mm radius of the Quantifoil. Images of the interference pattern produced by diffraction of the atom laser are then recorded on both the phosphor screen (Fig. 6.2) and delay-lined detector, located 669 mm and 852 mm from the trap centre respectively.

In addition, the process was repeated with thermal atomic beams derived from fully thermal clouds where $T \approx 2$ µK, and for the coldest thermal atoms at $T \approx 600$ nK from a cloud containing a condensed fraction (refer to Fig. 3.6), which are shown in Fig. 6.3. The diffraction patterns produced for thermal atoms have considerably worse fringe

[1] The 'cigar' configuration has $\omega_x = \omega_z \approx 500$ Hz and $\omega_y \approx 50$ Hz.

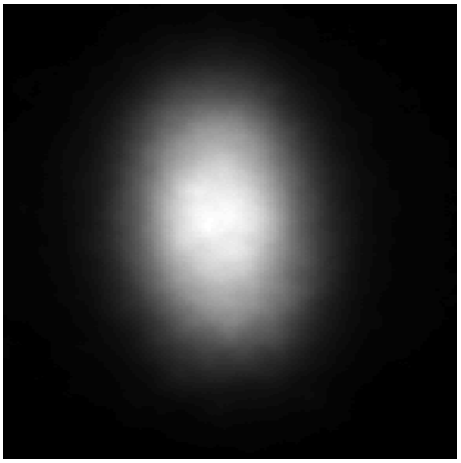

Figure 6.1: The average of the atom laser profiles for five experimental iterations on the MCP and phosphor detector with the Quantifoil removed. A Gaussian fit to the profile gives radii of $R_x = 1.2$ mm and $R_y = 2.6$ mm.

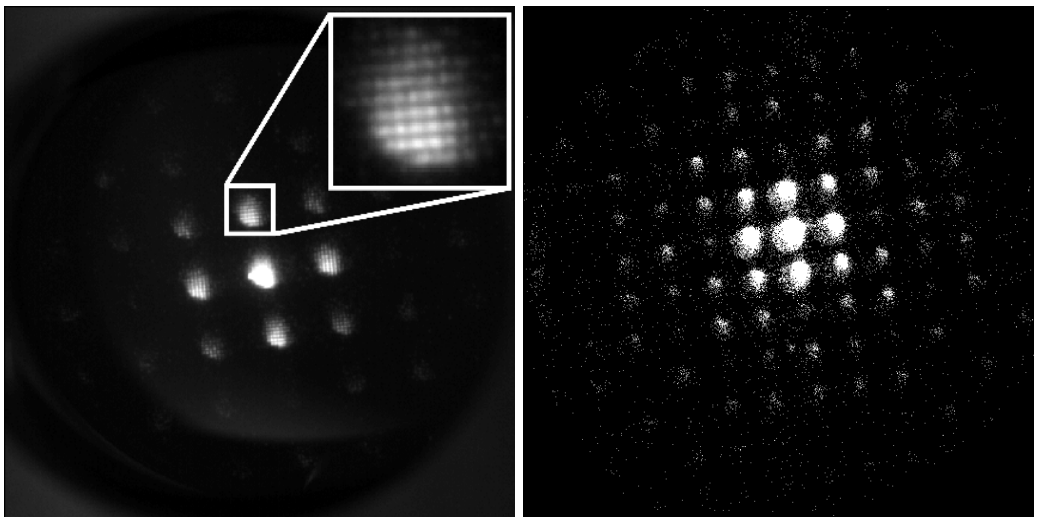

Figure 6.2: Diffraction image for an atom laser passing through Quantifoil from the average of 14 shots on the MCP and phosphor detector (left). The diffraction pattern in the left image extends to the edge of the 4 cm diameter detector, which matches the size of the image. The inset shows the additional high-frequency fringe pattern with 127 µm spacing present on each diffraction order, due to the copper wire grid. On the right, data for the same parameters is shown on the delay-line detector, with a colour map which saturates the central interference modes but shows that these modes extend to the edge of the 8 cm diameter detector.

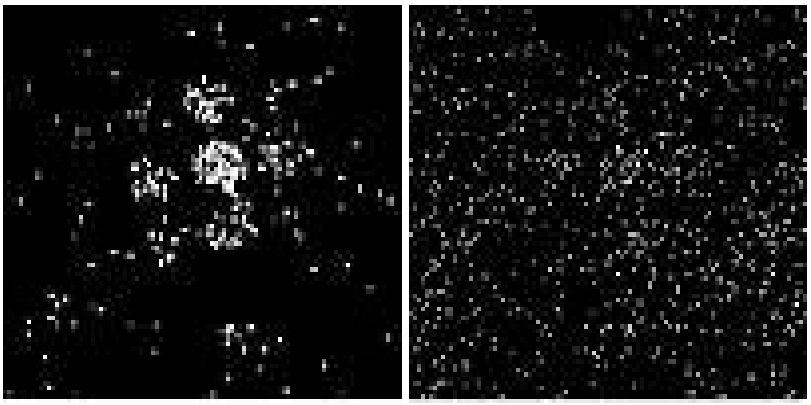

Figure 6.3: Diffraction images for around 20 shots of thermal atomic beams taken with the delay-line detector, cropped to the central 4 cm square portion, at 600 nK (left) and 2 μK (right). For the colder atoms, a central mode and ring of first order diffraction modes can be resolved, while the hotter atoms show no interference at all.

visibility than those for the atom laser.

Extraction of Wigner function

At the time of writing, data analysis is being performed by the group of Robert Scholten at the University of Melbourne to extract the Wigner function of the atom laser from the diffraction image shown in Fig. 6.2. The Wigner function $W(\mathbf{r},\mathbf{p})$ is a quasi-probability distribution which serves as a middle ground between a Schrödinger wavefunction, which cannot allow both position $\mathbf{r}$ and momentum $\mathbf{p}$ to be well defined simultaneously, and a classical phase-space density distribution lacking uncertainty [229, 230]. It was first developed by Wigner to account for quantum corrections to classical statistical mechanics where connections between the two regimes are apparent [231], such that for example the quantum-mechanical averages $\langle\mathbf{r}\rangle = \iint \mathbf{r}W(\mathbf{r},\mathbf{p})\,\mathrm{d}\mathbf{r}\,\mathrm{d}\mathbf{p}$ and $\langle\mathbf{p}\rangle = \iint \mathbf{p}W(\mathbf{r},\mathbf{p})\,\mathrm{d}\mathbf{r}\,\mathrm{d}\mathbf{p}$ can be obtained.

The Wigner function is also related to the density matrix $\hat{\rho}$ and first-order correlation function $G^{(1)}(\mathbf{r}_1,\mathbf{r}_2)$ through a Fourier transform [34, 232]

$$W(\mathbf{r},\mathbf{p}) = \frac{1}{(2\pi\hbar)^3}\int \left\langle \mathbf{r}+\mathbf{r}'\right|\hat{\rho}\left|\mathbf{r}-\mathbf{r}'\right\rangle \mathrm{e}^{2\mathrm{i}\mathbf{p}\cdot\mathbf{r}'/\hbar}\,\mathrm{d}\mathbf{r}', \tag{6.1}$$

$$G^{(1)}(\mathbf{r}_1,\mathbf{r}_2) = \int \mathrm{e}^{-\mathrm{i}\mathbf{p}\cdot(\mathbf{r}_1-\mathbf{r}_2)/\hbar} W\left(\mathbf{p},\frac{\mathbf{r}_1+\mathbf{r}_2}{2}\right)\mathrm{d}\mathbf{p}. \tag{6.2}$$

While quantum wavefunctions cannot be directly measured, the density matrix of an ensemble is the most complete knowledge that can be obtained from a classical mixture of states. In turn, the Wigner function, which reveals information about the density matrix, also cannot be observed directly. However, it can be reconstructed from an ensemble of measurements by tomographic analysis of quadrature operators, which are linear combinations of position and momentum operators [233, 234].

Previous experiments have been able to extract the Wigner function for atomic systems. This was achieved for a thermal beam of metastable helium incident on a double-slit [232], from which non-classical behaviour related to the interference of atoms in a superposition of states was observed. Another experiment probed spin-squeezed states

of a two-component BEC [235], where multi-particle entanglement was implied from the Wigner function which was reconstructed by spin-noise tomography [236].

Our experiment has the distinct advantage of measuring the density distribution of ultracold gases with single atom resolution, which may aid in improving the accuracy of the Wigner function obtained. A connection with the results of previous chapters is also present, where full quantum state tomography can in principle be achieved with the measurement of higher-order correlation functions [104]. Furthermore, the Wigner function reveals information important for quantum atom optics experiments measuring effects such as correlations, squeezing and entanglement [237, 238], which may help drive further discoveries in this active and fast developing field.

However, without further analysis being performed, the contrast in first-order correlation function between the coherent atom laser and incoherent thermal beam is immediately obvious from the diffraction pattern visibility. The coherence of the atom laser extends essentially across its entire profile, and provides a high-contrast interference pattern. Conversely, for thermal clouds the correlation length is of order the de Broglie wavelength which is $\sim$1.1 µm for atoms at 600 nK and 0.62 µm at 2 µK, resulting in the 'washing out' of the interference pattern from the 2 µm Quantifoil holes. This distinction will be examined further in §6.2.4, where guided atom lasers are shown to be second-order coherent, while Hanbury Brown-Twiss bunching of thermal atoms can be observed directly from measured density distributions in a matter wave analogue to optical speckle.

6.2 Modal structure of matter-wave guides

6.2.1 Wave guiding

Waveguides are commonly used to carry a variety of waves such as sound and electromagnetic radiation, and can be found in a range of everyday applications such as loudspeakers and optical fibres. An important characteristic of wave guides is that they typically support discrete modes of wave propagation, which is familiar in the context of musical instruments. Waveguides are now ubiquitous with the use of optical fibres in telecommunications, an important property of which being whether the fibre provides either single-mode or multi-mode support. Analysis of individual higher-order modes of propagation can be used to investigate the profile of waveguides [239], or to achieve novel effects such as the slowing of light [240], improvements in strain sensing [241] and gravitational wave detection [242]. Furthermore, entanglement can be generated between different spatial modes of a single laser beam [243], which significantly reduces the complexity of developing multimode quantum communication systems.

Guiding of matter waves

Guiding can also be achieved with matter waves, by forming a confining potential on a length scale similar to the de Broglie wavelength of the massive particles. Such potentials for ultracold atoms can be produced in a variety of ways, such as with red-detuned optical dipole laser beams, blue-detuned evanescent waves, magnetic fields, and hollow optical fibres. In particular, this allows for the miniaturisation and integration of cold atom experiments on microchips, where macroscopic transport of clouds can be achieved [190, 244–254]. The modes supported by a waveguide will depend on the form

of the confining potential, where circularly-symmetric potentials will support Laguerre-Gaussian transverse modes for sources with a Gaussian intensity profile, while elongated guides which range from elliptical to rectangular have Hermite-Gaussian modes [255]. These are both referred to as transverse electromagnetic modes (TEM) in an optical context, while in the limit of a weakly-guiding potential which lacks a sharply-changing potential these are sometimes referred to as linearly-polarised (LP) modes. When a source is loaded into a waveguide, it can occupy either a single mode or a superposition of modes, depending on the energy spread of the source and mode-matching of the transfer.

Early experiments with cold thermal atoms were not able to achieve good mode selectivity [245, 246, 250, 256, 257] due to the relatively large kinetic energy of the cloud which results in a poor coupling of the gas to the guide. However, Bose-Einstein condensates can be guided with a large occupancy of the lowest energy mode [251, 258], which has been achieved to 85% efficiency for alkali atoms [252, 253], and 65% for a previous experiment in our lab with He* [190]. Waveguides also allow low-divergence atom lasers with clean spatial profiles [190] and divergence consistent with the Heisenberg limit [259] to be produced, in comparison to freely propagating atom lasers with expanding density profiles containing interference fringes due to effects such as mean-field lensing and four-wave mixing [180, 260, 261]. Effects which degrade the profile of atom lasers are especially pronounced for helium, given its low mass. Thus, similarly to the commonly used method in optics, coupling to a waveguide can act as a filter to isolate a single clean mode of propagation.

While the guiding of matter waves is still a relatively new field, applications are already being realised which take advantage of the ability to transport atoms over macroscopic distances, often in setups which attempt to counteract acceleration due to gravity [262]. Such techniques are especially appealing for interferometers, which surpass the sensitivity of their optical counterparts, in addition to enabling measurements of local gravity fields [259, 263]. Matter-wave guiding may lead to improvements in the precision, interrogation time and possibly sensitivity of atom interferometers [179], while miniaturised chip-based interferometers with magnetic field waveguides have already demonstrated the ability to split, reflect and recombine condensates [264]. Important components of interferometers such as Bragg reflection [265], beam splitting or switching [266], and guiding in a one-dimensional hollow-core photonic bandgap fibres [267] have also been realised in optical waveguides, which may lead to quasi-continuous sources of matter waves. Other studies have theoretically investigated important considerations ranging from control of the mode quality and flux of guided matter waves [268], to the determination of the longitudinal coherence length or even generation of entanglement [269] with guided atom lasers.

Of particular relevance to the experiments described in this chapter was the study of the transverse coherence of an atom laser guided by a red-detuned optical dipole potential performed previously in our lab [190], which is discussed in detail in the PhD thesis of Sean Hodgman [270]. This result showed the transverse interference pattern of matter waves guided vertically under gravity through a Quantifoil transmission mask to demonstrate the contrast in first-order coherence between condensed and thermal atoms, much like the result shown in §6.1. In addition, the modal occupancy of the guide was determined from the transverse density profile of a guided atom laser with single atom sensitivity, in contrast to many other experiments which image the longitudinal density profile by absorption imaging [179], often with guides aligned perpendicular to

gravity [258].

Optical wave guides formed by red-detuned dipole potentials are especially appealing due to the superior confinement strength, flexibility and mode profiles possible compared to magnetic potentials [262, 271]. In addition, outcoupling from the trap to the waveguide does not result in a change of state or interactions with large mean-field potentials [179]. The experiments described in this section which investigate the excitation of higher order modes in a guide, as well as probing the modal structure of guided matter waves by measuring Hanbury Brown-Twiss bunching, extend naturally from the work presented in [190]. Confirming that coherence is maintained during matter-wave transmission is critical to demonstrate the applicability of guiding for interferometers, while higher-order modes may prove to be beneficial for such sensors, or possibly may enable entanglement to be generated in matter waves.

6.2.2 Experimental method for guiding matter waves in an optical dipole potential

Each of the experiments described in the remainder of this chapter are based on the following procedure. After cooling a cloud of atoms in the BiQUIC magnetic trap to just above $T_c \approx 1$ μK, atoms are loaded into a single optical dipole trap produced by a 1550 nm laser beam focused to a ∼20 μm spot, which is aligned vertically in the direction of gravity (see §3.1.3). The transfer occurs with 60 mW of laser power, which produces a trap with harmonic confinement frequencies $(\omega_x, \omega_y, \omega_z) \approx 2\pi \times (5900, 8000, 55)$ Hz and ∼7 μK depth, and atoms condense into the dimple formed by the superposition of the optical and magnetic traps[2]. The asymmetry of the trap $\omega_x \neq \omega_y$ is the result of the distortion of the beam by the acousto-optical modulator (AOM) which controls the beam power entering the BEC chamber. The BiQUIC trap is then switched off, and around 10^4 atoms which remain in the $m_J = 1$ state required for magnetic trapping are held in the dipole trap, and the combination of the magnetic field produced by the nullerometer and other stray fields continue to suppress losses from Penning ionisation.

After reducing the optical power of the dipole trap by adjusting the AOM diffraction efficiency, the most energetic portion of the cloud will leak out of the trap under gravity in the z direction, as shown in Fig. 3.7. However, if the dipole beam is not switched off and remains at an intensity only slightly less than that required to trap the atoms, the outcoupled gas will still be confined in the x-y plane by the potential and is thus guided to the detector below. The energy spread and mode occupancy of atoms released from the trap into the waveguide can be manipulated by adjusting how the trap depth is ramped between the capture power of 60 mW and the guiding power of ≈5 mW, as described in Fig. 6.4. At 5 mW of laser power, a guiding potential with transverse confinement $(\omega_x, \omega_y) = 2\pi \times (1700, 2300)$ Hz is produced, while the axial confinement of $\omega_z = 2\pi \times 16$ Hz is only just sufficient to hold the condensate while allowing thermal atoms to escape the trap (for further details, see §3.2.2).

If condensed atoms are loaded into the waveguide adiabatically, only the lowest mode of the potential should be populated, while higher-order modes can be excited due to a small amount of heating occurring in the trap or non-adiabatic transfer, in addition to transfer of the thermal component of the gas. As the atoms fall under gravity away from the trap centre, after about 20 ms the radial confinement also becomes too

[2] We find that the portion of the cloud loaded into a dimple trap is not strongly dependent on the initial temperature in the magnetically trapped cloud, which may be above or below T_c.

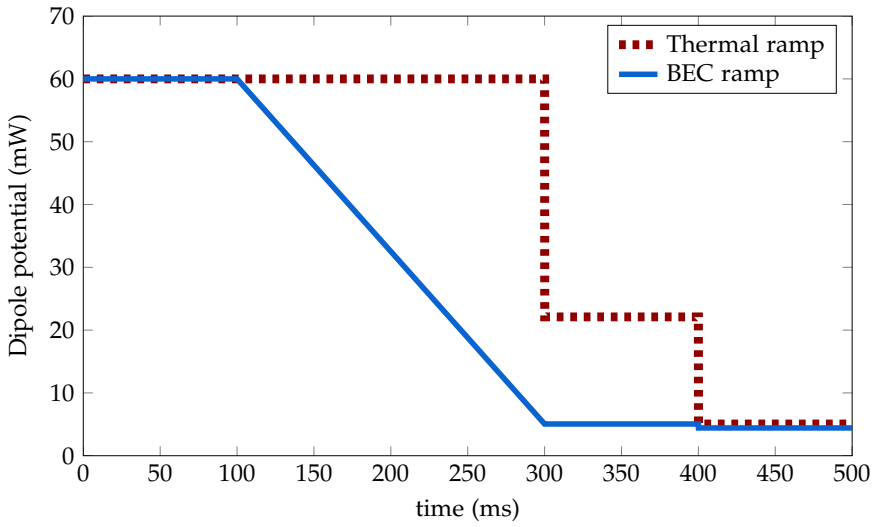

Figure 6.4: Intensity ramps of the dipole beam to load either a single-mode condensate (blue) or multi-mode thermal cloud (red) into the waveguide. At time $t = 0$, the magnetic trap is switched off, and the atoms are held for 100 ms to ensure that thermal equilibrium is reached. Evaporative cooling occurs between 100 ms and 300 ms, where condensates are adiabatically cooled into the ground state of the potential in the blue ramp, while a non-adiabatic quench cooling step occurs for the thermal ramp at 300 ms. After holding the cloud for another 100 ms to re-establish equilibrium, atoms are loaded into the guide at $t = 400$ ms. A laser power of 5 mW is required to retain the coldest (condensed) atoms in the trap, and consequently the blue trace evaporatively cools to just about 5 mW to increase the portion of the atom laser guided in the lowest energy mode, before dropping to just below 5 mW at 400 ms to produce a guided atom laser. On the other hand, the middle step of the red ramp between 300 ms and 400 ms determines the energy spread of thermal atoms loaded into the guide, while the guiding process for times after 400 ms occurs at a trap power just above 5 mW which continues to trap the condensate. Guided thermal clouds will consequently not be at equilibrium, as they do not include the low energy tail of the thermal distribution which is retained along with the condensate.

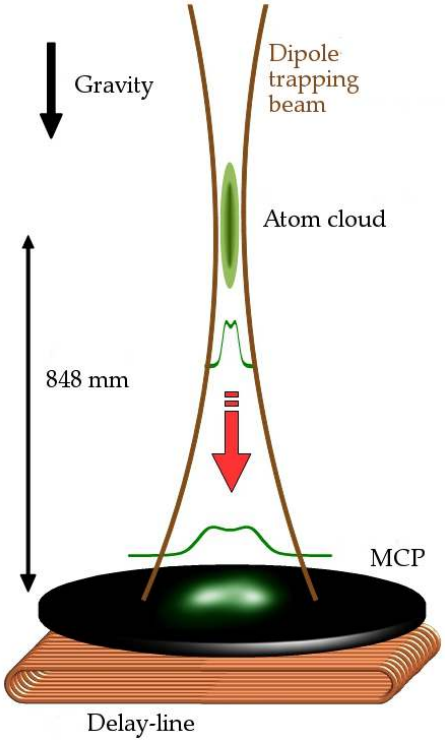

Figure 6.5: Atoms are released from the optical dipole trap at the focus of a red-detuned laser beam and fall under gravity towards either the delay-line detector (shown) or a phosphor screen (not shown) below. Atoms remain guided by the optical potential for the first ∼20 ms of their time of flight to the detector, which nevertheless results in a collimated beam even after the long fall time to the detector (416 ms for the DLD, and 360 ms for the phosphor screen).

weak to guide the atoms as the focused laser beam diverges, and the atoms expand ballistically. The atoms can then be imaged on either the phosphor screen or the delay-line detector (DLD) to record the spatial density distribution of the cloud, while correlation measurements require the use of the DLD to gain temporal information, which is illustrated in Fig. 6.5. A unique feature of our experimental setup is the ability to measure the transverse density distribution with single atom counting, which enables the modal structure to be investigated in the experiments described in the following sections, both of which are based on the same optical waveguide setup.

6.2.3 Observation of the first excited mode of an atomic wave guide

Many matter-wave guiding experiments have concentrated on obtaining the largest population of the lowest energy mode by reducing the energy spread of atoms loaded into the guide, as well as optimising the adiabaticity of the transfer. However, this approach does not immediately carry over to allowing particular higher-order modes to be controllably excited, due to difficulties in mode matching. Techniques analogous to those typically used in optics such as varying the angle at which light is coupled to a fibre [239] are similarly unsuitable. Atomic gases generally have a broad momentum distribution which makes it difficult to selectively excite waveguide modes with a cloud at equilibrium, however this has been achieved here by loading a thermal portion of a

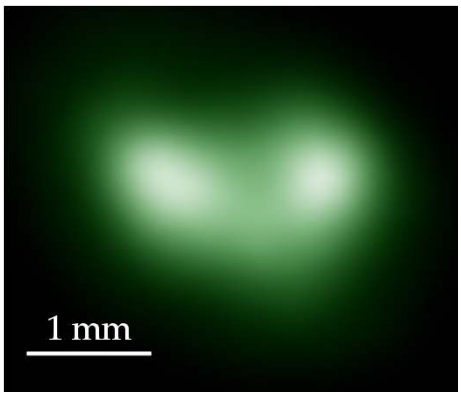

Figure 6.6: False colour density distribution of guided atoms dominated by the dual-lobed first excited mode of the guiding potential.

cloud which is not in equilibrium, but has an energy distribution which approximately matches the energy of the first excited transverse mode of the guide.

The method to load a thermal distribution into an optical waveguide described in the caption of Fig. 6.4 allowed the first excited mode of our slightly asymmetric waveguide (with an aspect ratio of $\omega_x/\omega_y = 0.74$) to be predominantly loaded, which corresponds to the TEM_{01} mode of an optical fibre. The nth-order of transverse TEM_{0n} mode $\Psi_n(x)$ for guides with slightly weaker confinement in the x direction is given by [272]

$$\Psi_n(x) = \sqrt{\frac{1}{2^n n!}} \left(\frac{m\omega_x}{\pi\hbar}\right) \mathrm{e}^{-\frac{m\omega_x x^2}{2\hbar}} H_n\left(\sqrt{\frac{m\omega_x}{\hbar}}x\right), \tag{6.3}$$

where H_n is the nth-order Hermite polynomial, and m is the atomic mass. The energy spread of atoms loaded into the guide is set by the change in confinement potential occurring during outcoupling step at 400 ms shown in Fig. 6.4, while sufficient trap depth must be maintained after this to retain the lowest-order mode in the trap, as otherwise this mode would dominate the distribution. This is conceptually similar to a method of producing higher-order laser modes by attenuating the fundamental mode of a cavity [273].

It was found that guiding the coldest possible thermal cloud at a thermal temperature of around 100 nK allowed the largest occupation of the first excited mode in the waveguide. The result of this is obvious from the density distribution recorded on the DLD shown in Fig. 6.6, which clearly shows a dual-lobed profile reminiscent of the TEM_{01} laser mode. As this image is the average of 2,000 experimental iterations, this demonstrates the precision and repeatability of the procedure.

The integrated linear density profile can then be decomposed into a linear combination of the modes described by Eq. 6.3, by allowing the width of the lowest-order ($n = 0$) mode and the occupancies of the lowest six modes to be free parameters in a least-squares fit. The result of this is shown in Fig. 6.7, and the distribution of mode populations (Fig. 6.8) confirms that the first excited $n = 1$ mode dominates the profile with 47 ± 2 % occupation, while the $n = 0$ and $n = 2$ modes each contribute about a quarter of the mode occupation and modes $3 \leq n \leq 5$ have negligible populations.

The transverse radius r of the guided cloud at the detector can be related to the average mode occupancy $\langle n \rangle$ by the virial theorem for non-interacting atoms, where

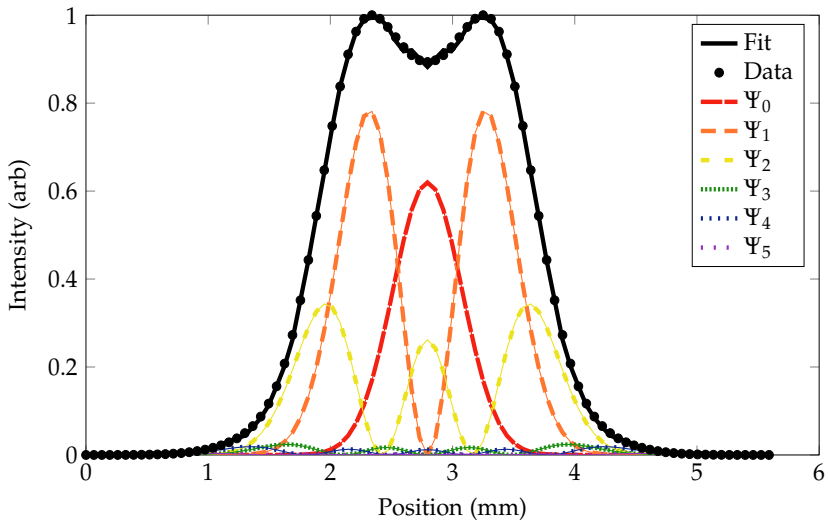

Figure 6.7: Decomposition of the measured linear density profile (black) into the lowest six supported modes (Ψ_0 to Ψ_5).

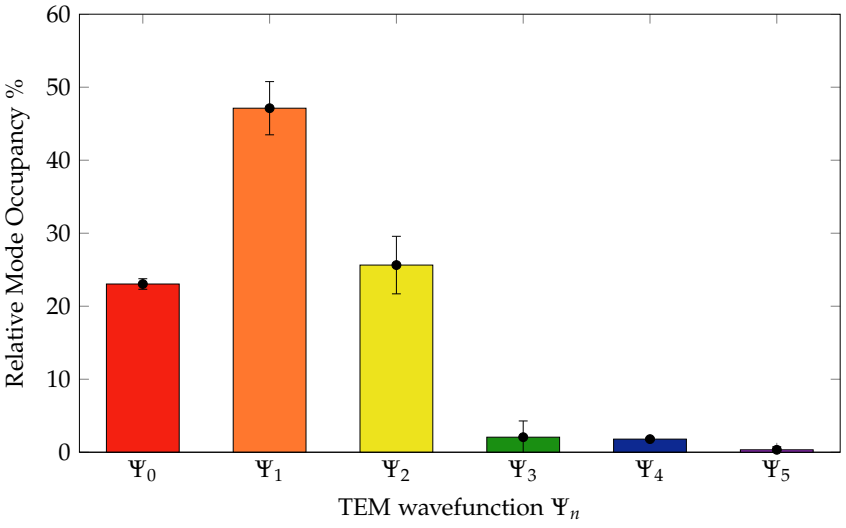

Figure 6.8: Occupancies of the modes Ψ_0 through to Ψ_5 corresponding to the decomposition seen in Fig. 6.7. Error bars correspond to the allowable range of the free parameters in the least-squares fit.

[252]

$$\frac{1}{2}m\left(\frac{r}{t}\right)^2 = \frac{\hbar\omega_r}{2}\left(\langle n\rangle + \frac{1}{2}\right), \tag{6.4}$$

for fall time t between the trap and detector, where $\omega_r \approx 2\pi\times 50$ Hz is the radial harmonic potential experienced by the atoms as they exit the guide. Given the mode occupancies measured in Fig. 6.8, an average mode occupancy of $\langle n\rangle = 1.13$ is calculated, which is in agreement with the $\sim$2 mm spot seen on the detector in Fig. 6.6.

In principle, the relative occupation of the Ψ_1 mode could be improved further by evaporating the cloud to a colder thermal temperature in the optical trap before loading the guide. However, this would result in a smaller number of atoms being loaded into the guide for each experimental iteration, and would therefore require a data set larger than the 2,000 experimental realisations obtained here to perform an accurate modal decomposition of the density distribution. Furthermore, the non-adiabatic transfer from the trap to the guide will inevitably result in a range of modes being excited in the waveguide. Nevertheless, this result represents the first instance of a single higher-order mode dominating the distribution of a guided matter wave.

6.2.4 Measurement of Hanbury Brown-Twiss bunching in guided matter waves

A key characteristic which determines the suitability of matter-wave guiding to applications such as interferometry is whether such sources can be guided coherently. The previous experiment undertaken by the ANU group which demonstrated a 65% occupancy of the lowest mode of a guided atom laser also produced a diffraction pattern with 91% fringe visibility by imaging the guided atom laser onto a Quantifoil transmission mask [190, 270]. Conversely, a guided thermal beam did not produce a diffraction pattern, demonstrating the contrast in coherence between the two sources. Here, this result is extended to measure the second-order correlation function of guided matter waves, which unlike first-order correlation measurements serves as an unambiguous test of true quantum coherence (see §2.1.1 for more details).

As was discussed in §4.1.2, the amplitude of Hanbury Brown-Twiss bunching measured for a given data analysis bin size is related to how strongly particles interfere within this set spatial volume, and therefore provides a test of the coherence of a source. This was used to compare the bunching amplitude to the average modal occupancy of atoms loaded into a waveguide. Furthermore, it was possible to directly observe bunching due to the macroscopic speckle pattern captured in the density distribution of guided thermal atoms.

Observation of macroscopically-visible Hanbury Brown-Twiss bunching

Optical speckle is a familiar effect which can be produced by scattering a laser beam off a diffuse material to produce a fixed interference pattern [274]. Conversely, temporally-varying speckle patterns can be produced from fluctuations in incoherent light sources [275] as a result of the Hanbury Brown-Twiss effect. As was seen in §4.1.1, smaller sources of incoherent bosons result in larger coherence lengths over which bunching can be observed, while sources with a large spread in kinetic energy result in the microscopic correlations lengths usually measured for second-order correlation functions. A variety of experiments discussed in Chapter 4 yielded correlation lengths of less than

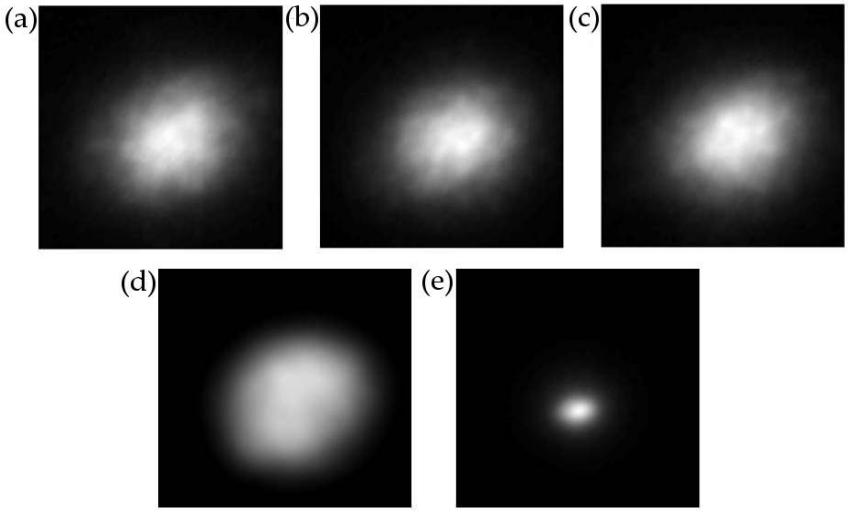

Figure 6.9: Individual experimental iterations of guided multi-mode thermal beams (a) to (c) show a distinct speckle pattern, while the average of twenty shots does not contain any visible interference (d). A single-mode guided atom laser (e) results in a considerably smaller Gaussian profile which lacks any resolvable interference. Each image is of a 3 mm by 3 mm section of the phosphor screen.

one millimetre, which did not permit the direct observation of bunching in a measured density distribution, while single-mode condensates do not exhibit Hanbury Brown-Twiss bunching. On the other hand, an experiment which did result in a macroscopically large transverse correlation length (§4.5) was achieved with clouds without sufficient density for this effect to be visible at the detector. However, the carefully controlled energy spread of atoms loaded into the waveguide results in a relatively small number of modes being occupied, which allowed the first macroscopic observation of Hanbury Brown-Twiss bunching to be made in an atomic system.

The optimal experimental procedure for visualising atomic speckle was achieved with a slight variation to the method described in §6.2.2. In this case, a dipole trap with a $1/e$ diameter of 30 µm was used to guide around 10^5 thermal atoms in a waveguide with confinement $(\omega_x, \omega_y) = 2\pi \times (1075, 1500)$ Hz to the phosphor detector now situated $\sim$180 mm below the trap. As is always the case for guided thermal atoms from our dipole trap, a sufficient trap depth was maintained to ensure that the condensed fraction of the cloud was not outcoupled. The speckle pattern can only be observed on time scales which are set by the correlation time t_c in the direction of gravity, and taking a photograph of the phosphor screen with an exposure time of order $t_c \sim 100$ ms allows the speckle pattern to be captured.

The resulting random speckle pattern for several experimental iterations is shown in Fig. 6.9 (a) to (c), while an average of twenty shots given in Fig. 6.9 (d) washes out the pattern. For reference, an atom laser predominantly guided in the lowest mode of the detector is also shown in Fig. 6.9 (e). The average mode occupancy is obtained from Eq. 6.4 in a similar manner to the experiment investigating the first excited mode of a waveguide, and was found to be $\langle n \rangle \approx 15$. While guided matter waves populating too many modes of the guide result in the speckle pattern washing out, enough different modes must be present to carry the fluctuations which cause interfere to be macroscopically visible.

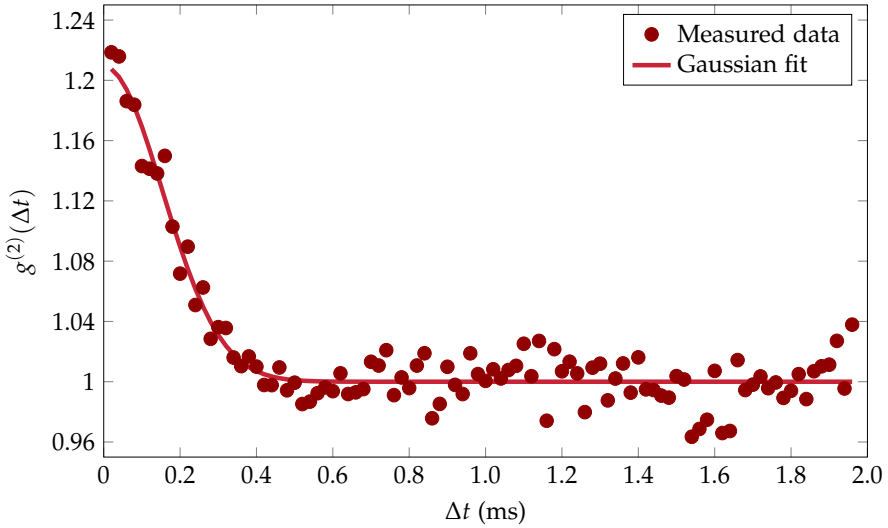

Figure 6.10: Longitudinal second-order correlation function for guided thermal matter waves with the lowest achievable average mode occupancy, resulting in a maximum bunching amplitude of $g^{(2)}(\Delta t = 0) = 1.21$. The error in the data points is predominantly shot noise.

Correspondence between second-order correlations and average modal occupancy of guided matter waves

To better quantify the Hanbury Brown-Twiss bunching present in guided matter waves, second-order correlations were measured by imaging the atomic beams on the delay-line detector using the experimental method described in §6.2.2. The modes occupied by atoms is the waveguide can again be precisely controlled in the manner described in Fig. 6.4, where the energy spread of thermal atoms loaded into the guide depends on the depth of the evaporation step. Smaller evaporation steps lead to a larger spread in the energy of atoms in the guide, and consequently this higher average transverse mode occupancy results in a shorter correlation length and less pronounced bunching signal. This was measured for a variety of different evaporation depths for thermal atoms, and compared to a guided atom laser created by evaporating the trapped cloud to a pure condensate, and then adiabatically transferring the condensate to the waveguide using the procedure described in Fig. 6.4.

An example of the second-order correlation function measured in longitudinal time-of-flight axis over ∼2,000 experimental iterations is shown in Fig. 6.10. This particular data set has the lowest average mode occupancy possible for a thermal beam in our experimental setup, with a transverse temperature of around 150 nK which resulted in only the lowest three modes of the form of Eq. having significant occupations. For hotter clouds which load atoms into a larger number of modes, the average mode occupancy is derived from the size of the cloud at the detector from Eq. 6.4, where the discrepancy between this method and a full modal decomposition was estimated to be around 10%. The transverse correlation length was obtained by assuming that the cloud expands ballistically after exiting the guide around 20 ms after being released from the trap, which gave a correlation length of between 200 and 370 µm in the x-y plane of the detector.

The resulting change in peak bunching amplitude $g^{(2)}(\Delta t = 0)$ as a function of average mode occupancy $\langle n \rangle$ is shown in Fig. 6.11. Each point represents an individual

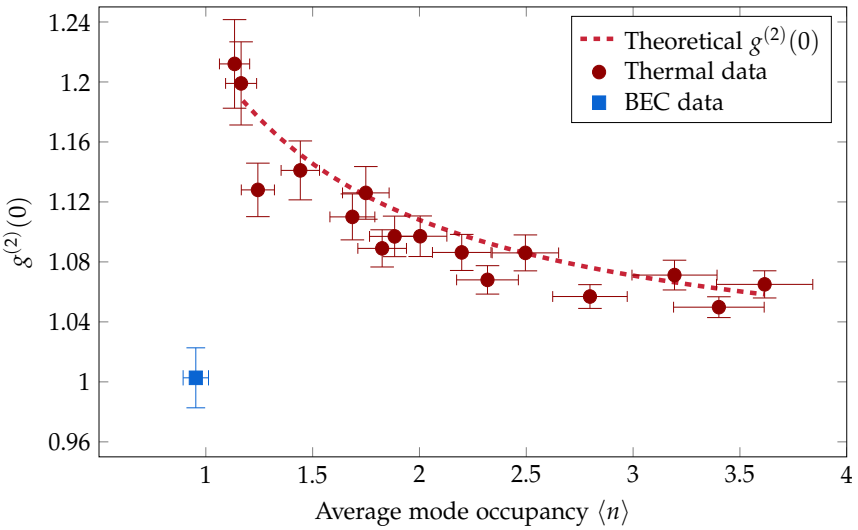

Figure 6.11: Comparison of peak bunching amplitude $g^{(2)}(\Delta t = 0)$ with average mode occupancy $\langle n \rangle$ for guided ultracold gases. The dashed line represents a theoretical model of the bunching expected for this system. Thermal beams (red) which retain the condensed portion of the cloud in the trap show stronger bunching at lower $\langle n \rangle$, while a guided atom laser (blue) corresponds to a distribution which is dominated by the lowest-order mode of the guide and shows no bunching, confirming that it is second-order coherent. The error bars are the result of uncertainty in the amplitude fitted to the forms of $g^{(2)}(\Delta t)$ and the fits which determine the average mode occupancy.

correlation function computed for ∼2,000 experimental runs, where a decrease in mode occupancy leads to a stronger bunching signal being measured due to the increase in correlation length. The range of $\langle n \rangle$ in this plot corresponds to the range of energy spreads possible, where the largest occupancy is the result of releasing the entire thermal portion captured in the dipole trap into the guide without any evaporation. Although a perfectly single-mode atom laser should result in $\langle n \rangle = 0$, our atom laser has $\langle n \rangle \lesssim 1$ due to a combination of residual thermal atoms and a slightly non-adiabatic transfer into the waveguide. However, the distinction between the guided atom laser and the coldest possible thermal cloud is clear from the contrast in bunching amplitudes, even though there is a relatively small change in spot size or equivalently average mode occupancy between these first two points in Fig. 6.11. The theoretical curve[3] is based on the theory presented in §4.1.2.

6.3 Summary

Several different instances of macroscopically-observable matter-wave interference have been investigated, which show great promise for future applications. If the Wigner function can be extracted from an atom laser produced in our experiment, the information derived from this may assist with subsequent measurements of a variety of exotic quantum effects. The combination of accurate quantum state tomography and the high-resolution single atom measurement capabilities of metastable helium would be highly

[3]This model was produced by Mattias Johnsson.

conducive to future quantum atom optics experiments, including those concerned with the generation of entanglement and testing of Bell's theorem.

Characterising the coherence and modal support of guided matter waves is also valuable for the development of devices such as atom interferometers. Atom interferometry is currently a particularly active area of research, and improvements which could be achieved with the use of waveguides in either the precision of results obtained or the compactness of the experimental apparatus would be welcome. Other imaging techniques such as atom holography and ghost imaging may also benefit from the use of wave guides. The selective excitation of higher-order guided matter-wave modes, which was achieved to 47 ± 2 % in the first excited mode, may lead to further advances in interferometry or the generation of entanglement, analogously to similar results achieved with light. Furthermore, the modal occupation of a waveguide has been probed with Hanbury Brown-Twiss bunching, which provides a robust diagnostic of the coherence of matter waves that cannot necessarily be obtained directly from a density image. Hanbury Brown-Twiss bunching has also been observed directly from atomic speckle in a density profile for guided matter waves with certain mode occupancies which facilitate interference visible on a macroscopic scale.

Chapter 7

Towards Wheeler's delayed choice *gedankenexperiment*

Wheeler's famous delayed choice *gedankenexperiment* (see §2.1.2 for background information about this) represents an important treatment of the role of complementarity in quantum mechanics. Although Wheeler devised this test in 1978 [108], it was not until 2007 that a true experimental realisation of this was achieved for photons [21]. The main obstacle which restricted many previous experiments to only demonstrating certain aspects of Wheeler's experiment was the requirement to eliminate a variety of 'loophole'-like conditions to ensure that no local realistic theory could explain the results of the experiment, in a similar manner to tests of Bell's inequality. Two of the more important conditions that are needed are a single-particle source, and a 'delayed choice' of experimental configuration which is both truly random, and relativistically separated from the entry of the particle to the interferometer.

Experiments attempting to realise this *gedankenexperiment* with atoms face challenges common with other investigations in atom optics. While reflection, splitting and single-particle production and detection are possible for atomic sources, they are significantly more difficult than what is regularly achieved for light. However, an advantage of using ultracold atoms is that their velocity is insignificant compared to the speed of light, which eliminates any relativistic ambiguity. In this chapter, the steps required to accomplish Wheeler's experiment for atoms are described, and some preliminary results investigating the *gedankenexperiment* are presented which indicate that a complete realisation is within reach.

An experiment described in this chapter is being prepared for the following publication:

- A. G. Manning, R. Khakimov, R. G. Dall, and A. G. Truscott, "A Source of Single Metastable Atoms in the Nanokelvin Regime," *Physical Review Letters* **113**, 130403 (2014).
- A. G. Manning, R. Khakimov, R. G. Dall, and A. G. Truscott, "Wheeler's Delayed Choice *Gedankenexperiment* with a Single Atom," under review (2014).

7.1 Overview of proposed method to realise Wheeler's experiment with ultracold atoms

Before proceeding to a technical description of the experimental method, a brief conceptual overview will be given here. The approach taken is based on the version of Wheeler's experiment shown in Fig. 7.1, which compares a particularly simple setup for an experiment with photons (a) to an equivalent atomic experiment (b). In a similar manner to the scheme shown in Fig. 2.2, a delayed choice is made as to whether to 'close' or leave 'open' an interferometer to determine whether interference is seen or not. In either experimental setup, if information about the path taken by a photon (or atom) is removed by the presence of a double slit (Fig. 2.2) or beamsplitter (Fig. 7.1) to 'close' the interferometer, interference should be observed which is indicative of wave behaviour. Conversely, the removal of the 'mixing' device which leaves the interferometer 'open' re-establishes information about which way the quanta went, and results in particle behaviour being seen. In the experiment with the double slit, this distinction exists in the presence of either a fringe pattern or a pair of spatially localised spots, which is built up over many experimental iterations with single photons. The experimental approach to be undertaken relies on a phase ϕ being imposed upon one arm of the interferometer, where the probability of measuring the quanta in either port (be it for the photodiodes PD1 and PD2, or momentum modes $|0\rangle$ and $|\hbar k_{\mathrm{rec}}\rangle$) will be $\sin^2(\phi)$ and $\cos^2(\phi)$ respectively for the 'closed' configuration of the interferometer. The dependence on ϕ is not present for the 'open' configuration, where ideally the quanta should be measured in either port 50% of the time.

To realise the atomic experiment shown in Fig. 7.1 (b), several considerations need to be addressed. The experiment must be performed with only one atom present in the interferometer at a time, to ensure that Bohr's idea of complementarity is unambiguously tested, which essentially requires a source of single trapped ultracold atoms to be produced. This single ultracold atom must then be accurately and controllably split and mirrored, which can be achieved with $\pi/2$ and π Bragg pulses respectively where a momentum kick is imparted on the atom by a coherent two-photon scattering process. The delayed choice of whether the second $\pi/2$ pulse is present to mix the arms of the interferometer must be made in a random way relativistically separated from the entry of the atom to the interferometer, to exclude justifications for the experimental result which invoke Einstein's argument of local reality. While this aspect of the experiment is challenging for photons travelling at the speed of light, this is not so problematic for atoms moving at speeds no greater than a few metres per second. Commercially available quantum random number generators (QRNG) are capable of producing the random choice on a microsecond time scale, which is sufficient for setting the interferometer configuration after the π pulse is applied by triggering a switch which transmits or blocks the second $\pi/2$ pulse. The state of the switch can also be recorded so that the two configurations can be distinguished after each experimental iteration.

Finally, measuring single atoms with sufficient spatial resolution to distinguish the two momentum modes $|0\rangle$ and $|\hbar k_{\mathrm{rec}}\rangle$ can be achieved easily with our MCP and delay-line detector (DLD). As the atoms fall though a 416 ms time of flight between the trap and DLD, the two momentum modes will be separated by a distance of the order of centimetres. At such a separation, the two modes are easily resolved on the DLD, which also facilitates single atom counting. Wheeler's experiment can thus be carried out over

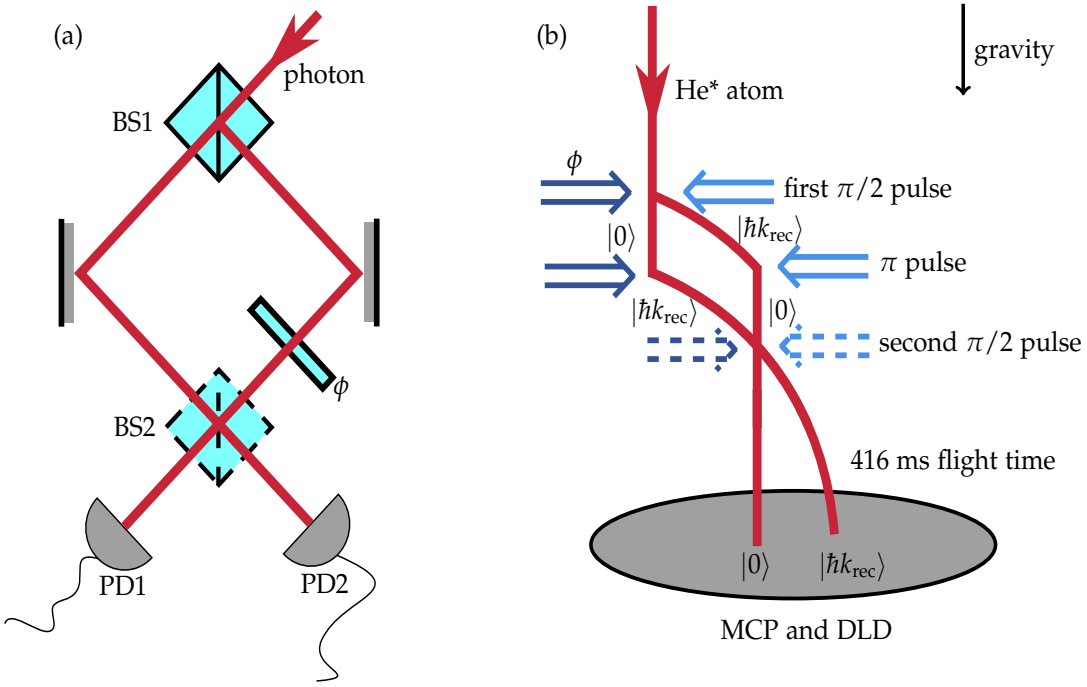

Figure 7.1: The idealised Mach-Zehnder interferometer version of Wheeler's delayed choice *gedankenexperiment* for photons (a) and atoms (b). For the experiment with light, a single photon enters the interferometer on the first beamsplitter (BS1), after which time a choice about the presence or removal of the second beamsplitter (BS2) is made before the photon reaches it. If BS2 is present, wave interference should be observed from a dependence of the probability that the photon is measured on either photodiode PD1 or PD2 on the angle of a $\lambda/2$ waveplate (ϕ). However, with BS2 removed, the probability of measuring the photon on PD1 or PD2 is independent of ϕ. The atomic experiment replicates this scheme with the use of Bragg scattering pulses which provide either beam splitting with a $\pi/2$ pulse, or mirroring with a π pulse, which transfer the probability amplitude of a single atom between two momentum modes $|0\rangle$ and $|\hbar k_{\mathrm{rec}}\rangle$. A phase relative ϕ between the two modes of the atomic wavefunction is imprinted with the first $\pi/2$ pulse, and after applying the π pulse mirror, a decision is made whether to apply the second $\pi/2$ pulse to mix the arms of the interferometer. After this process, the two momentum modes separate during the time of flight to the delay-line detector (DLD), where they arrive at two spatially and temporally separated locations. The probability of a count arriving in either location of the DLD is then either dependent on the phase ϕ applied by the first beamsplitting Bragg pulse if the second $\pi/2$ pulse is applied, or otherwise will be independent of ϕ.

many experimental iterations by measuring the probability of detecting atoms in either spatial location on the DLD as a function of a relative phase ϕ set by the first $\pi/2$ Bragg pulse, for interferometer configurations which are randomly toggled between 'open' and 'closed'. In the following sections, the experimental procedure to satisfy each of these requirements individually are discussed, before being combined for the acquisition of a preliminary measurement of Wheeler's experiment for massive particles.

7.2 Single-atom source

Among the most immediately obvious consequences of quantum theory is that sources of light or atoms should be considered as being composed of discrete particles, and it is common to invoke the notion of a single particle in theoretical treatments of quantum processes. However, the experimental production of deterministically-delivered single photons was certainly not trivial to achieve. Early experiments desiring single-photon outputs were only capable of ensuring that a single photon is present in the experiment on average, by simply reducing the intensity of the source. However, it was the interaction of light with atoms which allowed true single-photon sources to be produced, based on the emission of a photon as an excited atomic system relaxes back to its ground state. Experimental setups which are able to trap single ultracold atoms have also been developed recently, and are beginning to be used for fundamental studies which strive towards the creation of quantum logic devices [276].

7.2.1 Single-photon sources

One of the earliest experiments which investigated the behaviour of individual photons was a study by Taylor which produced an interference pattern in the same manner as for Young's experiments, except that there was typically only a single photon in the experiment at a time [277]. While this was not performed with a true single-photon source, it did indicate that wave behaviour persists even for single particles, and gave one of the first hints of complementarity. The invention of the laser and subsequent theoretical work exploring quantum optics such as that of Glauber motivated the search for single-photon sources, however it was not until 1974 that a true single photon source was generated [278], and sources of single photons on demand took a further two decades to be developed [279, 280]. The generation and detection of single photons is now routinely achieved (a range of review publications are available for general information on this topic such as Refs. [281–283]) with sources such as colour centres, quantum dots, single atoms, single ions, single molecules, and atomic ensembles. Single photon sources can emit in either a probabilistic manner, or more commonly are heralded where a pair of photons are produced, where one photon is used to signal the presence of its twin.

As was seen in §2.1.1, number-squeezed sources of bosons such as Fock states were shown by Glauber's theory of quantum coherence to be highly non-classical, which can be identified from a measurement of the second-order correlation function where $g^{(2)}(\Delta t = 0) < 1$, and in particular $g^{(2)}(0) = 0$ for single-particle states. This was first demonstrated by the measurement of fluorescence of individual atoms in a laser beam [79], where the finite lifetime of spontaneous emission prevents multiple photons from being scattered by an atom in an arbitrarily small interval. Later, true single-photon sources have been used to confirm the result of Taylor's single particle interference experiment [111], and have been key to several experiments such as tests of Bell's inequal-

ity [19, 284]. Beyond fundamental tests, sources of single photons are also important for the development of applications in quantum information such as cryptography.

7.2.2 Previous single-atom sources

While early experiments demonstrated the coupling of single atoms to optical cavities [181, 285], single trapped atoms at ultracold temperatures where wavelike properties will be easily observed are required to attempt Wheeler's experiment. Single neutral atoms have been captured from a MOT at the focus of very small volume dipole trap [286], which resulted in non-classical second-order correlations where $g^{(2)}(\Delta t = 0) < 1$ as expected. Single atoms have also been captured from a MOT and deterministically transported over macroscopic distances with standing-wave dipole traps [287]. Further experiments have loaded single atoms into arrays of optical traps [288–291] and in particular the lattice sites of a Mott insulator [57, 292], or have used light-assisted collisions to isolate individual atoms by depleting a cloud initially containing a large number of atoms [290, 293]. While the efficiency of loading single atoms in a trap is usually limited to 50% due to depletion of the cloud occurring in a pairwise manner, a loading efficiency of over 80% has been achieved with finely-tuned light-assisted collisions [294].

Recent experiments have cooled single atoms to the vibrational ground state of an optical potential using Raman sideband cooling [295, 296], while a scheme has been proposed to achieve this with electromagnetically-induced transparency in a cavity [297]. Studies of cavity quantum electrodynamics which couple single atoms to cavities have also allowed single atoms to be entangled with single photons [298], and have observed squeezed light emitted from a single atom [299]. Furthermore, the interface between single trapped ultracold atoms and a photonic crystal cavity has been investigated in the limit of strong coupling, to allow the cavity field to be probed at a resolution below the diffraction limit [300].

7.2.3 Experimental method

A property unique to helium among the bosonic species which have been cooled to quantum degeneracy is the large amount of internal energy stored in each atom. This leads to the Penning ionisation process described in §2.5.2, where the collision of two He* atoms results in ionisation and the loss of both atoms from the trap. While this is normally suppressed for collisions between pairs of spin-aligned atoms where $\sum m_J \neq 0$ by spin polarisation with the application of an external magnetic field[1] to allow the standard cooling and trapping processes to proceed, removal of this magnetic field provides a mechanism by which trapped clouds can be attenuated to a single atom. As for many of the single-atom experiments described above, a trap containing either one or zero atoms can be produced, assuming that the one-body loss rate is negligible on this time scale, by simply allowing Penning ionisation to proceed in a cloud initially containing a large number of atoms.

The $1/e$ lifetime for condensed atoms in the $m_J = 1$ substate was measured to be $\sim$16 s for our optical trap[2]. Assuming that the overall decay of the trapped cloud is

[1] The atoms held in a magnetic trap will naturally be in the $m_J = 1$ state, as atoms in the $m_J = 0$ state will not be trapped, while atoms in the $m_J = -1$ state will be ejected from the trap.

[2] The lifetime for $m_J = 1$ atoms in the BiQUIC trap is $\sim$40 s. That the lifetime of the cloud in the optical dipole trap is considerably shorter than for the magnetic trap could be attributed to some form of

not dominated by the one-body loss rate α, the lifetime for atoms in the $m_J = 0$ state is expected to be several orders of magnitude smaller. This follows from the disparity between the loss rate of collision pairs in that state of $\beta(m_J = 0, m'_J = 0) = (6.6 \pm 0.4) \times 10^{-10}$ cm^3/s [165] and the rate for spin polarised pairs of $m_J = 1$ atoms where $\beta(1,1) = (2.9 \pm 2.0) \times 10^{-14}$ cm^{3}s^{-1} [163, 164, 166]. If α can be considered to have a negligible effect on the trap lifetime, the $m_J = 0$ lifetime should be of order $16\,\text{s}/[\beta(0,0)/\beta(1,1)] \sim 10^{-2}$ s, as the density of Bose-Einstein condensates, and hence the effective volume in Eq. 2.52, is only weakly dependent on number (refer to §2.3.1). In this case, allowing Penning ionisation to proceed unabated allows the attenuation of the cloud to a single atom to occur over an experimentally reasonable time span. The difference in loss rates will be less pronounced if the one-body lifetime $1/\alpha$ is indeed not negligible compared to the 16 s lifetime for the $m_J = 1$ cloud. Note that the trap lifetime will in any case be considerably shorter than the radiative lifetime of 7870 s for atoms in the 2^3S_1 metastable state [153].

As the Penning ionisation process will occur primarily for pairs of atoms in the $m_J = 0$ state, the magnetic trap cannot be used to hold such atoms, and instead we transferred the atoms into the vertically-aligned optical dipole trap[3] (see §3.1.3) which can hold any m_J magnetic substate. After evaporatively cooling $\sim 10^6$ atoms to around T_c in the BiQUIC trap, the proportion of current passing through the two pairs of coils in the BiQUIC magnetic trap configuration was then ramped over 500 ms. This moved the centre of the magnetic trap a few millimetres to become coincident with the middle of the BEC chamber, as is shown with the 'sagged' configuration of the trap in Fig. 3.2. This allowed greater optical access to the trapped cloud for both the dipole trapping beams and the Bragg scattering laser beams which will be later used to create an interferometer.

About 10^4 atoms were then loaded into the vertically-aligned dipole trap which was ramped up to maximum power over 200 ms to form a combined dimple trap, as has been the procedure for many of the experiments in this thesis such as that in §4.5. After switching off the magnetic trap, the power of the vertical beam was ramped down over 100 ms to produce a trap with harmonic frequencies of $(\omega_x, \omega_y, \omega_z) \approx 2\pi \times (1800, 1800, 12)$. The trap remained at this power for 2 s, where the trap depth is smaller than the chemical potential of the condensate formed in this dimple trap (refer to §3.1.3), which allowed most of the thermal component of the cloud to exit the trap. This ensured that the cloud contains predominantly condensed atoms, with a higher two-body collision rate than is possible for a thermal cloud. Throughout this process, the nullerometer was used to produce a constant bias magnetic field of around 0.125 Gauss.

After ramping the trap back to its maximum power, the spin of these atoms, which remain in the $m_J = 1$ magnetic substate after transfer to the optical trap, was then flipped to the $m_J = -1$, 0 and 1 states. This was achieved with the application of 11 highly amplified bursts of Fourier-broadened RF radiation with 25 μs duration at a frequency of ∼350 kHz, which corresponds to the Zeeman energy of the atoms in the

'anomalous heating', which appears to be a commonly encountered yet not currently understood problem [176].

[3] Earlier attempts at this experiment, and the results presented in the following sections where Bragg pulses are applied to the cloud, were performed with the dual beam dipole trap. However, the single beam setup described here may result in improved trap stability due to the elimination of relative motion between the two laser beams. Conversely, the dual beam trap results in a reduction in the anisotropy in trapping frequencies, which allows a trap depth sufficient to hold the atoms to be achieved with a far lower dipole beam power than for either beam separately. This means that the cloud will not expand rapidly during the time of flight under gravity from the trap to the detectors below.

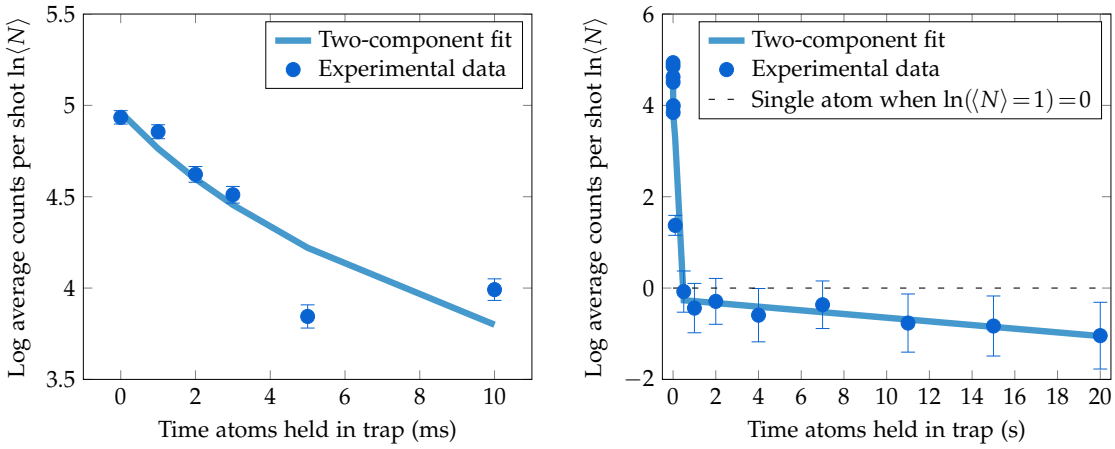

Figure 7.2: Logarithm of the trap population, adjusted by an assumed quantum efficiency of detection of 20%, of $m_J = 0$ atoms as a function of time held in the trap. For times of less than 0.5 s (left), the two-body loss rate is dominant, which fits to a $1/e$ lifetime of 9.5 ms, while for later times (right) the single body loss rate becomes dominant and fits to a $1/e$ lifetime of 24.9 s. The error bars indicate statistical uncertainty, and the dashed line shows the threshold below which no more than a single atom is present in the trap on average.

bias magnetic field. As the dipole trap can hold atoms of any magnetic substate, a strong linear magnetic field was applied by passing current through the bias pair of coils in the BiQUIC trap to remove atoms in the $m_J = \pm 1$ substates from the trap. The magnetic field then remained on to prevent atoms in the $m_J = 0$ substate from undergoing a Majorana flip back to the $m_J = \pm 1$ states. The trap was then ramped back down to a depth just above the chemical potential of the condensate, and the cloud was held for a variety of different durations of up to 20 seconds before being released by reducing the trap depth further and allowing the cloud to fall under gravity to the delay-line detector below.

The number of counts was then recorded in the smallest possible spatial and temporal window which encapsulates the unattenuated cloud of 20 ms $\times$ 5 mm $\times$ 5 mm on the detector, to reduce the effect of dark counts. The gain of the micro-channel plates was adjusted by tuning the voltage applied to improve the signal-to-noise ratio measured with this data, as although a higher gain increases the quantum efficiency of measuring single atoms, it also increased the dark count rate. An optimal balance between these factors was found at a gain of 2050 V, instead of the 2000 V typically used, although the improvement seen was not significant. It is predicted that for a sufficiently long hold time, a single atom should remain in 50% of experimental cycles, and no atoms otherwise, depending on whether we start with an odd or even number of atoms in the optical trap respectively.

A measurement of the trap lifetime for this Penning ionisation loss procedure is shown in Fig. 7.2, where the atoms were held in the trap for different durations between the spin flipping and trap switchoff. The bimodal nature of the trap loss is evident from the two distinctly different loss rates occurring before and after hold times of ~ 0.5 s, where loss is dominated by binary collisions at earlier times with a $1/e$ lifetime of 9.5 ms, which subsides at later times as the population of the trapped cloud is reduced such that the $1/e$ lifetime increase to 24.9 s.

The one- and two-body loss rates (α and β) for the cloud can be derived from the

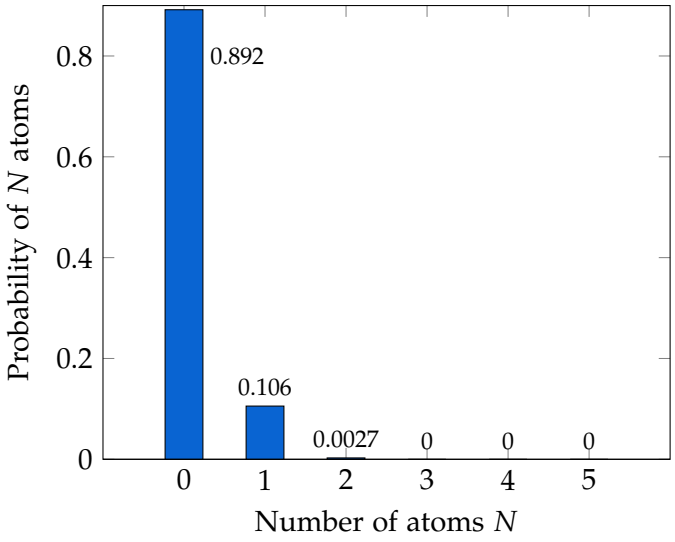

Figure 7.3: Probability of measuring N atoms in a given experimental iteration (not adjusted for detection efficiency), obtained by holding the $m_J = 0$ atoms in the trap for at least one second.

bimodal fit to the trap population as a function of time (Eq. 2.53) illustrated in Fig. 7.2. In this case, the two-body loss rate β is set to zero once the average count rate drops below one atom per iteration (adjusted for detection efficiency) after a hold time of 0.5 s. The biggest uncertainty in determining β is from accurately characterising the trap volume V, which is assumed to take on a Thomas-Fermi density profile with radii R_{TF} given by Eq. 2.36, where for simplicity then chemical potential μ is assumed to be a constant independent of atom number, as from Eq. 2.35 we see that $\mu \propto N^{2/5}$ and thus $R_{\mathrm{TF}} \propto N^{1/5}$. With this, we find that $\alpha = 0.0402$ which corresponds to a one-body lifetime of $1/\alpha = 24.9$ s, and we can estimate the value for the two-body loss rate to be $\beta(0,0) \approx 1 \times 10^{-9}$ cm^3/s, which is within a factor of two of the result obtained from previous measurements [165].

To determine whether a true single-atom source is being produced, a histogram of the likelihood $P(N)$ of N atoms being measured in a single shot averaged for hold times of one second or more is shown in Fig. 7.3. While the count rate for the lifetime data in Fig. 7.2 has been adjusted for the quantum efficiency of the delay-line detector, which is estimated by a variety of other measurements to be 20%, this compensation has not been applied to the $P(N)$ data in Fig. 7.3. However, in both cases a background dark-count rate of 0.00175 counts per shot has been subtracted. Although an ideal detector should result in $P(0) = P(1) = 0.5$ and $P(N > 1) = 0$, the limited detector efficiency reduces the average number of atoms measured such that $P(1) \approx 0.1$. This agrees well with the data in Fig. 7.3, and while a pair of counts is measured in 0.27% of experimental cycles, the rate of double counts corrected by compensating for the quantum efficiency is 1.35%, such that $P(1)/P(N > 1) \approx 8$ and thus the source is found to produce single atoms predominantly but not exclusively.

As was mentioned previously, a clear characteristic of a non-classical Fock state of particles is a sub-Poissonian correlation function where $g^{(2)}(0) < 1$. A distinct advantage of assessing the single atom source in this way is that it allows us to quantify its fidelity in a manner not limited by the quantum efficiency of the delay-line detector. A measurement of this is shown in Fig. 7.4, where the form of the correlation function is now

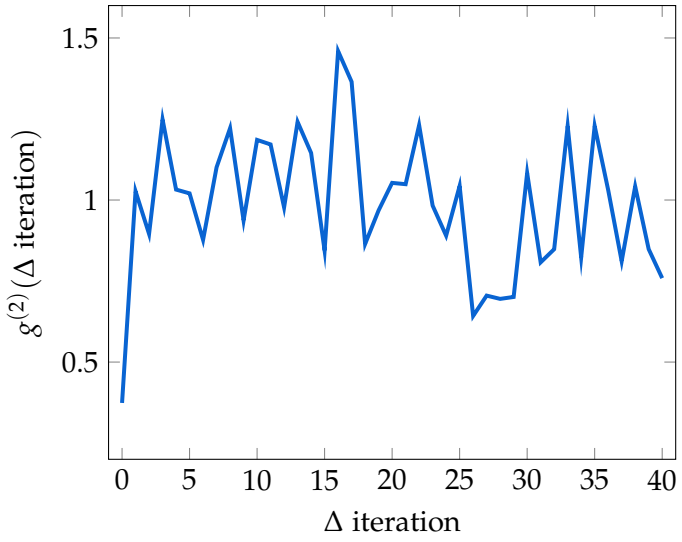

Figure 7.4: Second order correlation function $g^{(2)}$ measured for the single atom source as a function of increment between experimental iterations.

not directly comparable with those presented in Chapter 4. In the present case, we are simply concerned with how many particles are present in each experimental iteration, as is indicated by the dependent axis used for the plot, which also eliminates any notion of a 'correlation time'. Instead, what this plot shows is that any pair of particles measured is more likely to occur by one particle being in each of two separate experimental iterations, rather than both the particles occurring in the same iteration. While ideally we should find that $g^{(2)}(0) = 0$, which corresponds to $P(N > 1) = 0$ in Fig. 7.3, we find that $g^{(2)}(0) \approx 0.37$ which confirms that we have a strongly sub-Poissonian but imperfect source of single atoms[4].

In principle, this method should be robust against experimental drifts in temperature and number, which can often be troublesome for data sets which are acquired over the course of several weeks, as would be the case for Wheeler's experiment. The atoms produced by this method are very cold, and an ensemble of single atom measurements has an energy spread which can be characterised by a thermal temperature of around 10 nanokelvin, which is consistent with the energy spread of the trapped cloud before attenuation. Assuming that this energy spread places an upper bound on the 'temperature' of the single-atom source, the large de Broglie wavelength of at least $\sim$ 14 µm (compared to 0.027 µm for He* atoms in a 1 mK MOT) of these atoms at this temperature confirms their suitability for measuring wave behaviour. This approach also has the advantage of enabling experiments with single atoms to be performed with atoms trapped in the same way as for large clouds, without resorting to the specialised trapping geometries used in other single-atom experiments.

7.3 Atom interferometry

A fundamental tenet of atom optics is the interchangeable nature of matter and particles, where a standing wave of light can be used to diffract atoms in the same way that a

[4]The stability of the dipole trap setup was further optimised after the submission of this thesis to obtain a considerably improved single-atom source, where $g^{(2)}(0) = 0$. These results are available in Ref. [66].

matter grating can diffract light. The interaction of atoms and light has been covered previously in §2.2, where the scattering of individual photons was seen to apply a force on an atom to manipulate its motion. In this section, the two-photon Bragg scattering process will be discussed in the context of its application to the atom interferometry required to realise the experimental setup shown in Fig. 7.1. More detail on this topic can be found in the comprehensive overview of atom interferometry available in Ref. [263].

7.3.1 Two-level atoms and Rabi oscillations

We will begin by considering a two-level atom, where monochromatic radiation can be used to drive the atom between these two levels which we will denote $|1\rangle$ and $|2\rangle$. If these two states have energies $E_1 = \hbar\omega_1$ and $E_2 = \hbar\omega_2$, then the atomic wavefunction will take the general form $\psi(\mathbf{r},t) = c_1(t)\,|1\rangle\, e^{-i\omega_1 t} + c_2(t)\,|2\rangle\, e^{-i\omega_2 t}$, where normalisation requires that $|c_1(t)|^2 + |c_2(t)|^2 = 1$ at all times. If light of angular frequency ω_{laser} is incident on an atomic system with a resonant transition frequency $\omega_{\text{atom}} = \omega_2 - \omega_1$ which is initially in the state $\psi(\mathbf{r},0) = |1\rangle$, then at a later time the population of the state $|2\rangle$ will be [120]

$$|c_2(t)|^2 = \left(\frac{\Omega}{\Omega_R}\right)^2 \sin^2\left(\frac{\Omega_R t}{2}\right). \tag{7.1}$$

The detuning of the laser from the atomic transition $\delta = \omega_{\text{laser}} - \omega_{\text{atom}}$ results in a shift in the frequency of the population oscillation from the natural Rabi frequency Ω to the generalised Rabi frequency $\Omega_R = \sqrt{\Omega^2 + \delta^2}$. Resonant pulses ($\delta = 0$) of different durations result in Rabi oscillations of the atomic system, where in particular pulse durations of $t_\pi = \pi/\Omega$ result in a complete population transfer between $|1\rangle$ and $|2\rangle$, while a duration of $t_{\pi/2} = \pi/2\Omega$ creates an equal superposition of the two states where $|c_1(t)|^2 = |c_2(t)|^2 = 0.5$.

7.3.2 Bragg and Raman scattering for three-level atoms

Although two-level atoms with transitions driven by a single laser beam results in momentum being transferred from the photon to the atom, and is the fundamental mechanism of laser cooling, it does not allow the coherent transfer of atoms from one discrete momentum mode to another. However, a two-photon scattering processes driven by a pair of laser beams can facilitate this by having the atom absorb a photon from one laser beam, and emit into the other beam, resulting in an impulse on the atom due to momentum conservation. At the same time, angular momentum and energy must be conserved for the transition between the two states $|1\rangle$ and $|2\rangle$, which can be achieved with suitable beam polarisations and detuning between the two lasers. The atom can either undergo Bragg scattering where $|1\rangle$ and $|2\rangle$ have the same internal state but different momentum and energy, or can also transfer between different internal states in a process referred to as Raman scattering.

Although the two states $|1\rangle$ and $|2\rangle$ are typically different (or even the same) magnetic substates of a given electron configuration separated by a relatively small energy, transitions between them can be driven optically via an intermediate state $|3\rangle$. This requires a three-level atom such as that illustrated in Fig. 7.5 to be considered. A laser with angular frequency ω_{L1} can be used to drive a transition between $|1\rangle$ and $|3\rangle$ by the absorption of a photon, while another laser with angular frequency ω_{L2} can drive

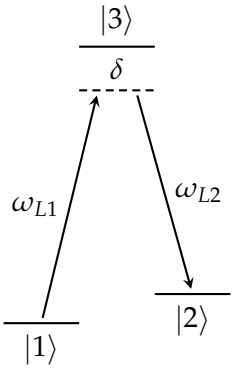

Figure 7.5: Two-photon Bragg or Raman transition between states $|1\rangle$ and $|2\rangle$ via an intermediate state $|3\rangle$ which does not become populated.

the transition from $|3\rangle$ to $|2\rangle$ by stimulated emission. In particular, if the single photon detuning $\delta \approx \omega_{L1} - (E_3 - E_1)/\hbar \approx \omega_{L2} - (E_3 - E_2)/\hbar$ is much larger than the than the two-photon detunings $\delta_{12} = (\omega_{L2} - \omega_{L1}) - (E_2 - E_1)/\hbar$, then the scattering process couples the states $|1\rangle$ and $|2\rangle$, while any lasting population of the intermediate state $|3\rangle$ is adiabatically eliminated. Furthermore, larger values of δ result in a reduction of undesirable spontaneous emission [120].

Under these conditions, the Bragg or Raman scattering process essentially becomes a two-level process with an effective detuning $\delta_{\text{eff}} = (\Omega_{13}^2 - \Omega_{32}^2)/4\delta + \delta_{12}$ and Rabi frequency $\Omega_{\text{eff}} = \Omega_{13}\Omega_{32}/2\delta$, where Ω_{13} is the Rabi frequency of the two-level transition from $|1\rangle$ to $|3\rangle$, and similarly for Ω_{32} [301]. Two-photon scattering pulses are usually of a short duration with large Fourier broadening so that transitions occur over a wide range of atomic velocities. However, each two-photon process results in the same exchange of energy and momentum between the atoms and light, and allows the population of the two modes to oscillate in the same way as for the two-level atom. Atoms can also undergo multiple two-photon scattering events which result in higher-order momentum modes being populated, however the efficiency of scattering into high momentum modes is highly dependent on the initial momentum spread of the cloud and the Rabi frequency of the scattering beams [302, 303], and this phenomenon will be avoided in our experiment.

7.3.3 Mach-Zehnder interferometers for atoms

Assuming that the Bragg or Raman two-photon scattering process only couples the states $|1\rangle$ and $|2\rangle$, an interferometer can be formed which coherently transfers the population of these two states in a way which depends on an externally imposed phase. The Mach-Zehnder interferometer shown in Fig. 7.1 can be created by a sequence of three Bragg or Raman pulses. Assuming that the atoms start in the $\psi(0) = |1\rangle$ mode, applying a resonant $\pi/2$ pulse of duration $t_{\pi/2} = \pi/2\Omega_{\text{eff}}$ and phase ϕ_{BS1} creates an equal superposition of the two momentum modes [301]

$$\psi = \frac{1}{\sqrt{2}}\left(|1\rangle - \mathrm{i}e^{-\mathrm{i}\phi_{\text{BS1}}}|2\rangle\right). \tag{7.2}$$

Some time T after applying this beamsplitting pulse, the two states acquire a phase factor $\delta T/2$, such that

$$\psi = \frac{1}{\sqrt{2}}\left(\mathrm{e}^{\mathrm{i}\frac{\delta T}{2}}\,|1\rangle - \mathrm{i}\mathrm{e}^{-\mathrm{i}\left(\frac{\delta T}{2}+\phi_{\mathrm{BS1}}\right)}\,|2\rangle\right). \tag{7.3}$$

A second $\pi/2$ pulse with phase ϕ_{BS2} results in

$$\psi = \mathrm{i}\mathrm{e}^{\mathrm{i}\frac{\delta T}{2}}\left[\sin\left(\frac{\delta T}{2}\right)|1\rangle - \cos\left(\frac{\delta T}{2}+\frac{\phi_{\mathrm{BS1}}-\phi_{\mathrm{BS2}}}{2}\right)|2\rangle\right]. \tag{7.4}$$

Thus, the population of the modes oscillate after this sequences of pulses as

$$|c_2|^2 = \frac{1}{2}\left[1+\cos\left(\delta T+\phi_{\mathrm{BS1}}-\phi_{\mathrm{BS2}}\right)\right]. \tag{7.5}$$

The population of each mode $|c_2|^2$ and $|c_1|^2 = 1-|c_2|^2$ essentially depend on two variables, which are the phase picked up by the evolution of the atomic wavefunctions δT, and the difference in phase between the two $\pi/2$ pulses $\phi_{\mathrm{BS}} = \phi_{\mathrm{BS1}} - \phi_{\mathrm{BS2}}$. For many applications for interferometers, especially those used for precision measurements of quantities such as gravity, it is the former of these terms that is of interest, as this will contain information about the quantity being measured. However, for the present experiment this quantity is simply a constant, and it is the externally-applied phase difference ϕ_{BS} which is of importance, as it is analogous to the $\lambda/2$ waveplate shown for the optical experiment in Fig. 7.1. The addition of a π pulse of duration $t_\pi = \pi/\Omega_{\mathrm{eff}}$ after the first beamsplitting pulse, to reflect the momentum two modes such that they again overlap for the second $\pi/2$ pulse to form an atomic Mach-Zehnder interferometer, simply results in a change in the evolution phase term δT and does not alter the result of Eq. 7.5.

As the intensity, frequency and phase of the two Bragg/Raman beams are controlled by diffraction with AOMs, the interferometer phase ϕ_{BS} can be set by the phase of the RF signal used to drive each AOM, as is shown in Fig. 7.6. This requires that the duration, phase and lag between the two RF signals is accurate and reproducible to within a fraction of a period of the RF wave, which is of order 10 ns. The frequency difference δf between the two AOMs directly corresponds to the detuning between the beams. This is set by the requirement of simultaneous energy and momentum conservation, where a recoil in momentum $p_{\mathrm{rec}} = \hbar k_{\mathrm{rec}}$ due to the two-photon scattering process corresponds to a recoil energy $E_{\mathrm{rec}} = p_{\mathrm{rec}}^2/2m = h\delta f$. It is also worth noting that a closed Mach-Zehnder interferometer can be formed without adjusting the frequency of the two beams for each of the π and two $\pi/2$ pulses, as the momentum transferred to the atom results in a Doppler shift for the laser beam which reverses the direction in which the momentum transfer occurs for subsequent pulses.

7.3.4 Interferometry with metastable noble gases

Interferometry with ultracold metastable noble gases (general information about which can be found in Refs. [152, 301]) has distinct advantages compared to more commonly used alkali metals. Aside from the single atom counting capabilities of species such as metastable helium and neon, the small mass of these atoms results in large de Broglie wavelengths for a given temperature, which makes wave interference easier to observe,

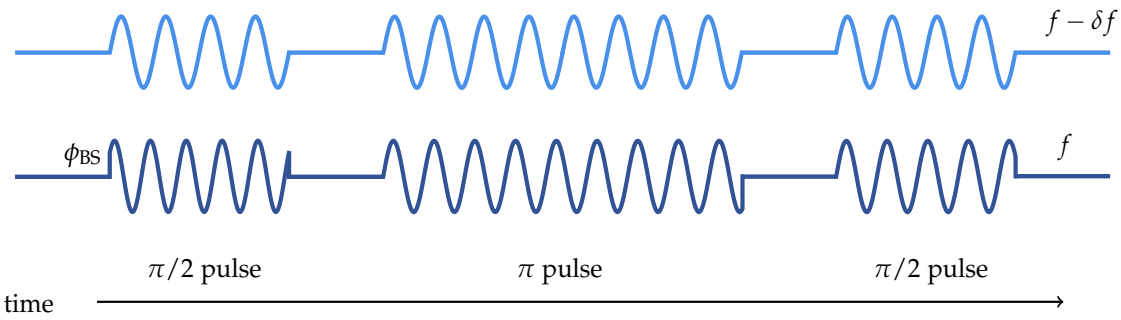

Figure 7.6: Cartoon representation of how phase is controlled in an atomic interferometer with the RF signal used to drive the AOM for each beam at frequencies f and $f - \delta f$ respectively. A relative phase of ϕ_{BS} exists between the initial phases of the first $\pi/2$ pulse, while the initial phase of each other pulse is set to a constant value, which we choose to be zero.

and large recoil velocities for a given wavelength of scattered light which increases the 'open area' of Mach-Zehnder-type interferometers. Early experiments which optically pumped Ne* into a state with $J = 0$ which is insensitive to electromagnetic fields were able to explore a variety of interferometry effects, including the demonstration of Young's experiment with a double-slit aperture [304] and holography [305–308], in addition to the previously discussed Hanbury Brown-Twiss demonstration [54].

Interferometry using Bragg or Raman transitions has also been achieved for He*, in a number of experiments which have explored the collision of condensates. The spontaneous four-wave mixing process, which is analogous to optical parametric down-conversion[5], can be induced by two-photon scattering which splits the cloud into two momentum components which interact through s-wave collisions [310, 311]. The conservation of momentum and energy required for these s-wave collisions was shown to result in number squeezing between modes with opposite momentum [185] and consequently a violation of the Cauchy-Schwarz inequality for number correlations between such modes [92]. These results are particularly important for the current quest for testing Bell's inequality with matter waves, as violation of the Cauchy-Schwarz inequality is a prerequisite for entanglement.

7.3.5 Experimental method

Before attempting the full realisation of Wheeler's experiment, we first characterised our ability to create a Mach-Zehnder interferometer with momentum transfer from stimulated Bragg scattering. As we saw in §7.2.3, the single atom source used in Wheeler's experiment will be in the $|J = 1, m_J = 0\rangle$ state, and it is advantageous for the two-photon scattering process to return the atoms to this state, as it is insensitive to perturbations from external magnetic fields. However, to characterise the interferometer we used large clouds in the $|1, 1\rangle$ state, which is not only the state held by the magnetic trap but also one which suppresses loss due to Penning ionisation, and will therefore allow accurate preliminary measurements with large numbers of atoms to be obtained quickly.

We therefore applied Bragg transitions between the 2^3S_1 and 2^3P_2 manifolds, as is shown in Fig. 7.7. Although transitions between the 2^3S_1 and 2^3P_0 manifolds contain fewer levels which can be accidentally accessed by imperfect energy and polarisation

[5] This was studied in detail in Ref. [309].

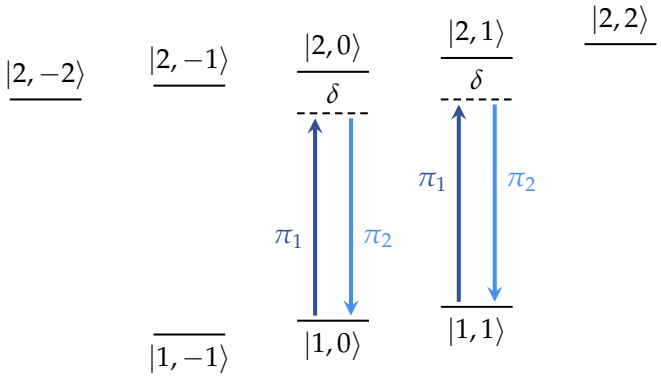

Figure 7.7: Energy level scheme for Bragg transitions in metastable helium between $|J, m_J\rangle$ states in the 2^3S_1 and 2^3P_2 manifolds. This diagram only refers to internal states, and the external states of the interferometer are not degenerate due to a difference in their kinetic energy, where the π_1 transition is driven by the beam of frequency f, while the π_2 transition is driven at $f - \delta f$. Note that transitions from $|1,0\rangle \leftrightarrow |2,0\rangle$ and $|1,1\rangle \leftrightarrow |2,1\rangle$ can each be driven individually with the same beam setup, depending on the magnetic substate of the atoms scattered.

selectivity, the chosen manifolds allow calibration measurements to be taken easily for large numbers of atoms. This is achieved by simply neglecting to transfer the atoms into the $|1,0\rangle$ state, while retaining the same settings for the Bragg beams, except for the requirement to tune the beam duration or power to compensate for the different transition strengths. As acquisition of data to explore Wheeler's experiment will take several weeks, this is an important step to characterise the interferometer and identify and minimise long-term systematic experimental drifts. The detuning δ was set $\sim$16 GHz to the red of the transition at 1083.331 nm, as the transition from $2^3S_1 \rightarrow 2^3P_1$ is only 2.3 GHz to the blue of the $2^3S_1 \rightarrow 2^3P_2$ transition, while the $2^3S_1 \rightarrow 2^3P_0$ transition is a further 30 GHz to the blue (refer to Fig. 2.3).

Bragg beam setup

The geometry of the Bragg beam setup is shown in Fig. 7.8. As the atoms are nearly at rest when the Bragg pulses are applied, and therefore experience no Doppler shift with respect to the laser beams, they will preferentially absorb from the more energetic 'bottom' Bragg beam with wavevector $\mathbf{k}_1$, which drives the π_1 transition (refer to Fig. 7.7). This laser beam is diffracted with an AOM which detunes the light by $f = 120$ MHz. The two-photon process is completed by stimulated emission into the other 'top' Bragg beam with wavevector $\mathbf{k}_2$, which is detuned δf less than 120 MHz, such that energy conservation is satisfied by the atom gaining a kick in kinetic energy of $E_{\text{kin}} = h\delta f$. As the beams are not aligned symmetrically about the horizontal axis, the momentum kick $\mathbf{p}_{\text{rec}} = \hbar(\mathbf{k}_1 - \mathbf{k}_2)$ will have components in both the horizontal ($\hat{y}$) and vertical ($\hat{z}$) directions, such that the resulting momentum modes $|0\rangle$ and $|\hbar k_{\text{rec}}\rangle$ will be separated in both time and space at the detector.

As the two Bragg beams enter the BEC chamber through windows already occupied with beams used for laser cooling in the second MOT, these cooling beams are reflected into the chamber by mirrors attached to flipper mounts. This is so that the cooling beams can be translated out of the way, and the Bragg beams can be reflected into the

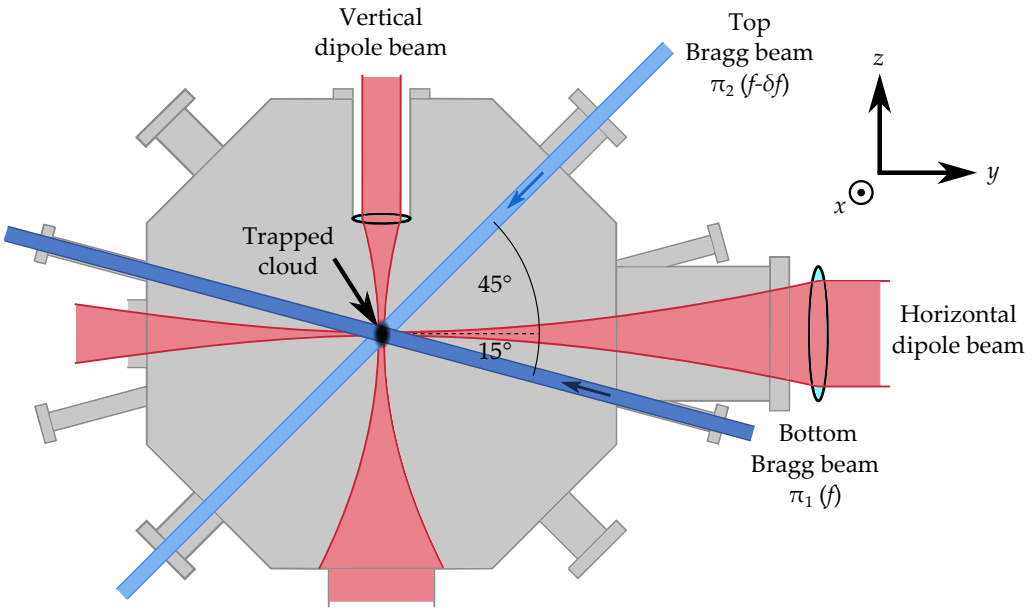

Figure 7.8: Experimental setup of the Bragg beams (related to the dipole trapping beam setup in Fig. 3.5). Each Bragg beam is considerably larger than the cloud held in the crossed dipole trap, to ensure that the light intensity is uniform across the cloud. The polarisation of each Bragg beam is linear in the $\hat{z}$ direction, to match the bias field applied by the nullerometer.

chamber by stationary mirrors to reduce vibrations in these beams. The angle between the two Bragg beams of 60° is also fixed by these windows, and was chosen so that the momentum recoil $\mathbf{p}_{\text{rec}}$ was large enough to distinguish the two modes, yet not sufficient to kick the atoms beyond the detector radius.

Throughout the entire experimental procedure, the nullerometer is used to not only cancel magnetic field noise, but to also define a bias magnetic field at the optical trap centre in the $\hat{z}$ direction. As the transitions illustrated in Fig. 7.7 do not change the magnetic substate of the atoms, each of these will be π transitions driven by linearly polarised light which carries no angular momentum. The polarisation of each beam is set to align with the magnetic field bias with a $\lambda/2$ waveplate. Also note that the presence of this bias field lifts the degeneracy of the different m_J states for atoms held in the optical trap.

The Bragg scattering laser light is provided by a 1 W ytterbium fibre laser operating at 1083 nm. As the light output is far detuned from the $2^3S_1 \rightarrow 2^3P_2$ transition, it is not locked to the transition and thus resulted in wavelength drifts of around 5%. The laser power was found to drift by up to ∼15% over the time scale of typical experimental runs, and therefore a slow feedback loop was implemented to correct this. A small amount of light was picked off the laser beam and its power measured on a photodiode, which was used to tune an attenuator which controls the RF power delivered to each AOM. This setup reduced long term power drifts by at least 50%. While these specifications are not ideal, they should not compromise our ability to demonstrate the distinction between particle and wave behaviour if an interferometer with at least 50% contrast can be produced.

Conservation of energy and momentum

To determine the detuning δf between the two Bragg beams, we need to ensure that energy conservation is satisfied for a given recoil momentum. The recoil momentum $p_{\text{rec}} = \hbar\,|\mathbf{k}_1 - \mathbf{k}_2|$ is the result of absorbing a photon from one beam, and emitting into the other beam. For an angle of 60° between the two beams, $|\mathbf{k}_1 - \mathbf{k}_2| = k_{1,2}$ and thus

$$k_{\text{rec}} = \frac{2\pi}{\lambda} = 5.8 \times 10^6 \text{ m}^{-1}, \tag{7.6}$$

$$v_{\text{rec}} = \frac{\hbar k_{\text{rec}}}{m} = 0.092 \text{ ms}^{-1}, \tag{7.7}$$

$$\delta f = \frac{E_{\text{rec}}}{h} = \frac{m v_{\text{rec}}^2}{2h} = 42 \text{ kHz}. \tag{7.8}$$

The recoil velocity has components in the $\hat{y}$ and $\hat{z}$ direction of $v_{y,\text{rec}} = v_{\text{rec}} \cos(5\pi/12) = 2.4 \text{ cm}^{-2}$ and $v_{z,\text{rec}} = v_{\text{rec}} \sin(5\pi/12) = 8.9 \text{ cm}^{-2}$ respectively. This results in a 1 cm spatial separation and 9.3 ms temporal separation between the two momentum modes after the time of flight to the DLD, which is sufficient for the two modes to be distinguished.

We can also estimate the time t_π required for a π pulse. First, recall that the natural linewidth of the 2^3S_1 and 2^3P_2 transition is $\Gamma = 2\pi \times 1.6$ MHz, and the saturation intensity for the $|1,1\rangle \to |2,2\rangle$ transition is $I_{\text{sat}} = 167$ μWcm^{-2} [152], from which the saturation intensity for other transitions can be obtained with the relevant line strength [119]. For 3 mW beams with a 5 mm radius, the Rabi frequency for each individual transition is

$$I_{\max} = \frac{P}{\pi r^2} = 3.8 \text{ mWcm}^{-2}, \tag{7.9}$$

$$\Omega_{13,32} = \Gamma \sqrt{\frac{I_{\max}}{2 \times 2 I_{\text{sat}}}} \approx 240 \text{ MHz}. \tag{7.10}$$

The extra factor of two in the Rabi frequencies is from the Clebsch-Gordan coefficient for the $|1,1\rangle \to |2,1\rangle$ transition (see p. 54 of Ref. [119]). The $|1,0\rangle \to |2,0\rangle$ transition has a coefficient of 1.5, which can be compensated for by tuning the laser beam intensity or Bragg pulse duration so that the same experimental procedure can be used for either transition. From this, we can find the effective two-level Rabi frequency and π time

$$\Omega_{\text{eff}} = \frac{\Omega_{13}\Omega_{32}}{2\delta} \approx 290 \text{ kHz}, \tag{7.11}$$

$$t_\pi = \frac{\pi}{\Omega_{\text{eff}}} \approx 10.9 \text{ μs}. \tag{7.12}$$

It is also important to consider how many photons will be scattered spontaneously over the duration of a π pulse, which will be [309]

$$N_{\text{sp}} \approx \Gamma \frac{\Omega_{13}\Omega_{32}}{4\delta^2} t_\pi = 1.6 \times 10^{-4}. \tag{7.13}$$

As $N_{\text{sp}} \ll 1$, the interaction between the atoms and laser light will be dominated by stimulated Bragg scattering, and thus a significant a reduction of the efficiency of momentum transfer operations which create the Mach-Zehnder interferometer is not experienced.

Pulse train

Of crucial importance to our ability to create a Bragg interferometer is the generation of a train of RF pulses in the style shown in Fig. 7.6 used to drive the AOMs which manipulate the two Bragg beams. The amplitude, frequency and phase of these RF pulses directly influences these parameters for the laser beams diffracted by the AOMs, and therefore must be precisely controlled and stable over many experimental iterations. While the absolute phase of the interferometer (set by the δT term in Eq. 7.5) is not of importance, the two AOMs must also be phase locked to ensure that the relative phase ϕ_{BS} is well defined.

We define the RF waveform with three pulses (a $\pi/2$, π, $\pi/2$ sequence) as an array of voltages with 2 GSa/s resolution, and upload these waveforms to a two-channel Agilent 81150A arbitrary wavefunction generator. These pulses will be at a frequency of 120 MHz for the 'bottom' π_1 beam, and 119.958 MHz for the 'top' π_2 beam, the latter of which incorporates the $\delta f = 42$ kHz detuning determined by Eq. 7.8. The two RF signals then pass through a separate RF switches and 2 W RF amplifiers to each of the AOMs. The coaxial cables which carry this RF signal were made as short and as close to equal length as possible to reduce systematic phase shifts between the two AOMs, as the signal propagates at $\sim 10^8$ ms^{-1} and thus a 10 cm mismatch results in a 1 ns lag between the two channels. In addition, these cables were carefully shielded to eliminate pickup from environmental noise sources.

An advantage of this approach is that the two channels of the signal generator are inherently phase locked and respond to the same external trigger to initiate the pulse train. While the absolute triggering time of the RF output is not of critical importance (the delay between the trigger from the experimental control and the pulse is in any case very small at around 40 ns), the relative lag between the two channels determines the phase sensitivity of the interferometer. The pulses produced by the waveform generator were measured by an oscilloscope with 1 GHz bandwidth to have a few percent jitter in amplitude and phase, however the RF amplifiers introduce around 5% amplitude jitter to the signal without distorting the wave phase.

Experimental procedure

The performance of the Bragg scattering process was first characterised with clouds containing a large number of $m_J = 1$ atoms, in the same trap that will eventually be used for the single $m_J = 0$ atoms when performing Wheeler's experiment. This experiment followed the same procedure as that in §7.2.3 to produce trapped clouds of atoms, however for this and subsequent experiments a dual beam dipole trap was used. In this case, the reduction in trap depth in the vertically-aligned trap after transfer from the magnetic trap was compensated for by an increase in power for the horizontal beam, such that the trap volume was much less elongated with trapping frequencies of $(\omega_x, \omega_y, \omega_z) = 2\pi \times (500, 500, 300)$. The lower trapping strength in the x and y axes resulted in a slower expansion of the condensed cloud during the time of flight to the detector, which allowed us to more easily resolve the two momentum modes in that plane. A lower momentum spread for the source resulting from smaller trapping frequencies also improves the fidelity of Bragg scattering [303]. In addition, the stages to transfer the spin, push the remaining $m_J = \pm 1$ atoms away, and then hold atoms in the trap for up to 20 seconds to attenuate the cloud were eliminated. Note that for this

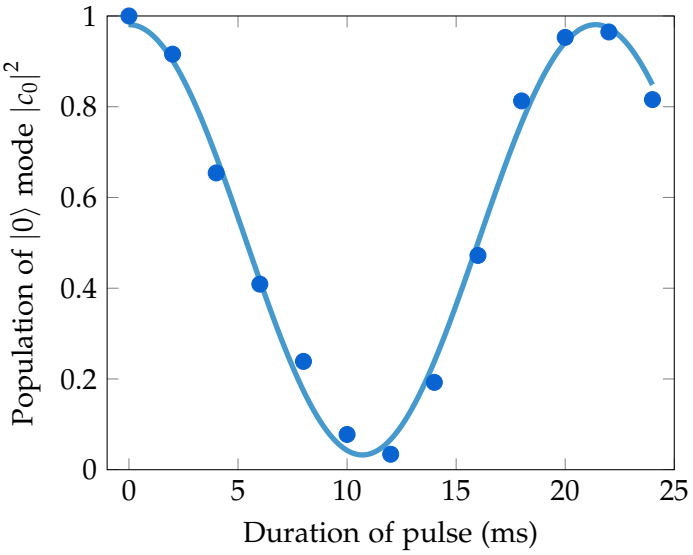

Figure 7.9: Rabi flopping of the population of the $|0\rangle$ mode for a single Bragg pulse with maximum beam intensity. The circular points are experimental measurements, and the sinusoidal fit line gives a transfer efficiency of 94.8% and π time of $t_\pi = 10.7$ µs, after which time almost the entire cloud is reflected into the $|\hbar k_{\text{rec}}\rangle$ mode.

measurement the atoms remain in the $m_J = 1$ magnetic substate, and the presence of the bias magnetic field applied by the nullerometer to set the quantisation axis for the Bragg beams restricts the Penning ionisation rate.

After allowing the resultant cloud contained in this manner to re-equilibrate in the dual beam trap over 100 ms once the final confinement geometry is reached, both trapping beams were switched off to allow the $\sim 10^3$ atoms to fall under gravity to be measured on the delay-line detector below. Around 2 ms after the atoms are released, the arbitrary waveform generator was triggered to output the train of RF pulses used to drive the two AOMs, which applied the Bragg pulses to the atomic cloud. Before attempting a full Mach-Zehnder interferometer, a single pulse gated by RF switches was used to map out the Rabi flopping between the $|p = 0\rangle$ and $|\hbar k_{\text{rec}}\rangle$ momentum modes as a function of pulse duration. The portion of the cloud occupying these two modes was determined from counting the number of atoms measured in the two physically separated pulses measured on the DLD.

The result of this measurement is shown in Fig. 7.9. A sinusoidal oscillation of the occupation of the $|0\rangle$ momentum mode is clearly seen as the duration of the Bragg pulse changes, which fits to a transfer efficiency of 94.8% and a π time of $t_\pi = 10.7$ µs. Similar results were obtained for a variety of Bragg laser powers and single photon detunings δ, which resulted in the π time scaling accordingly. The optimal population transfer was found to occur for a relative beam detuning of $\delta f = 42$ kHz, as expected from Eq. 7.8.

The full Mach-Zehnder interferometer can then be realised by applying the full sequence of three Bragg pulses to the atoms. In this case, it was found that halving the intensity of the two Bragg beams to double the π time to $\approx$22 µs, achieved by altering the RF power delivered to the AOMs, resulted in an increase in interference visibility. Thus, a first 11 µs $\pi/2$ pulse, followed by a 30 µs flight time, then the π pulse, another 30 µs pause and then the final $\pi/2$ pulse results in the population transferring between

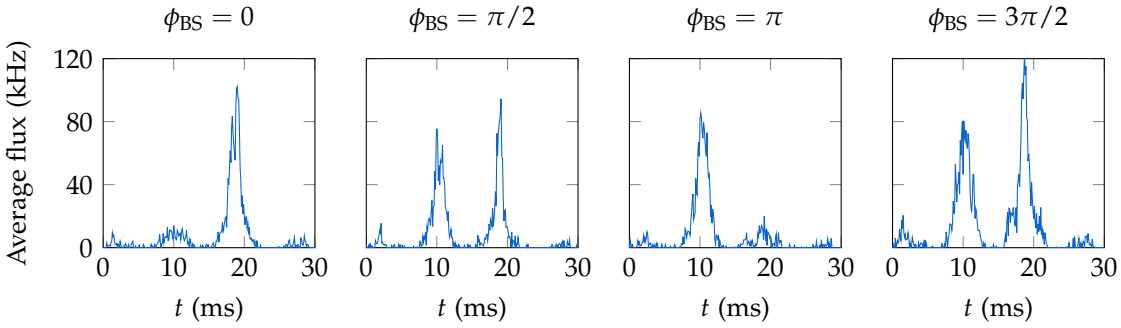

Figure 7.10: Transfer of population for the three-pulse Mach-Zehnder interferometer between the $|0\rangle$ and $|\hbar k_{rec}\rangle$ momentum modes arriving on the detector at 10 ms and 19 ms respectively, as a function of the interferometer phase ϕ_{BS}. Note that a small portion of the cloud undergoes multiple two-photon scattering processes, or scatters in the opposite direction to the majority of the atoms, and arrive with momentum $|-\hbar k_{rec}\rangle$ at 1 ms or $|2\hbar k_{rec}\rangle$ at 28 ms.

the two momentum modes as shown in Fig. 7.10 for a sequence of different externally applied phases ϕ_{BS}. As is also the case for the single-pulse Rabi flopping measurement, the two pulses are separated on the DLD by around 1 cm in the x-y plane, causing a small amount of overlap in that plane, but are also clearly distinguished by a 9 ms separation in flight time, as expected from the recoil velocity of the two-photon scattering process. A very small portion of the cloud is seen to scatter into other momentum modes such as $|-\hbar k_{rec}\rangle$ and $|2\hbar k_{rec}\rangle$, and these higher-order modes will be ignored for the following experiments.

The result of mapping out the population transfer over a full range of external phases is shown in Fig. 7.11. The expected form for this is $|c_0(\phi_{BS})|^2 = 0.5\sin(\pi\phi - 0.5\pi) + 0.5$, due to the presence of a constant phase offset which is set to $\delta T = 0.5\pi$. A sinusoidal fit to the population is in good agreement with the expected form at $|c_0(\phi_{BS})|^2 = 0.425\sin(0.954\pi\phi_{BS} - 0.502\pi) + 0.510$, and gives an interferometer contrast of 85% which should be sufficient for realising Wheeler's experiment. If the second $\pi/2$ pulse used to recombine the two momentum modes is not present, the average population of the $|0\rangle$ mode was found to be 0.491.

7.3.6 Discussion

Each of the controllable experimental parameters, such as the effective Rabi frequency and time of flight before and between the Bragg pulses, were optimised to achieve the best possible interferometer visibility. Allowing the atoms to expand for more than a few milliseconds after trap switch-off severely diminished the transfer efficiency, as did long times of flight between successive Bragg pulses. Higher Rabi frequencies resulting in shorter π times generally gave better fringe contrast for the interferometer, at the cost of a greater sensitivity to errors or drifts in the Bragg beams which result in greater proportional errors in Ω_{eff}. It was found that a single pulse Rabi flopping contrast of 88% was obtained for $t_\pi = 44$ µs, compared to 93% for $t_\pi = 25$ µs and 98% for $t_\pi = 10$ µs, where greater Fourier broadening for shorter pulses may have ensured that a larger velocity range within the cloud is scattered, as the finite momentum width of the cloud reduces the efficiency of Bragg scattering [303]. Also, a lower effective

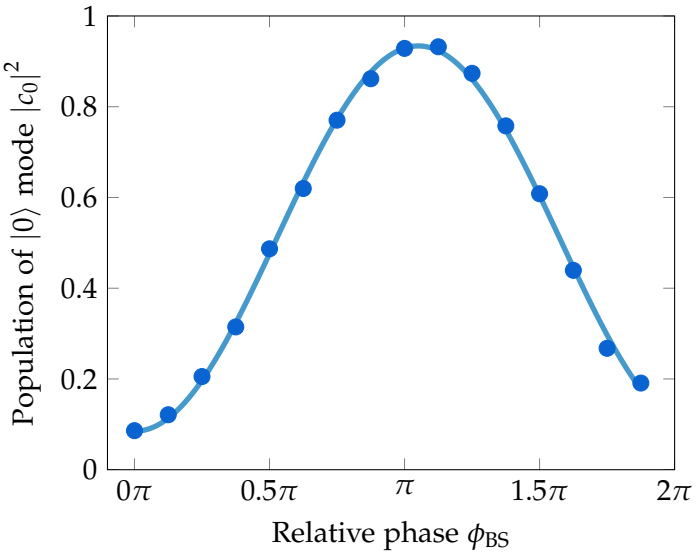

Figure 7.11: Population transfer for an interferometer with different externally-applied phases ϕ_{BS}, derived from a sequence of measurements of the type shown in Fig. 7.10. The experimental points fit to a sinusoidal function $|c_0(\phi_{BS})|^2 = 0.425 \sin(0.954\pi\phi_{BS} - 0.5021\pi) + 0.510$.

Rabi frequency and consequently larger π time is known to result in a reduction of Bragg mirror fidelity [303]. The π time of 22 µs was chosen as the optimal compromise between these competing factors. The two-photon detuning δ was chosen to be large at 16 GHz to reduce the sensitivity of Ω_{eff} to long-term drifts in laser wavelength output, in addition to reducing the spontaneous scattering rate.

The results obtained, particularly that shown in Fig. 7.11, indicate that the Bragg interferometer should be capable of facilitating a measurement of Wheeler's experiment in its current configuration. On the time scale of this measurement of a few hours, the effective Rabi frequency did not change significantly for the chosen experimental parameters, which is important considering that the true realisation of Wheeler's experiment will require several weeks of data acquisition. The value of $|c_0(\pi/2)|^2$, which should be 0.5, was measured to match this average value and fluctuate by less than 10% RMS or about $\pm$20% peak to peak over a 12 hour experimental run, where this measurement was subject to an error of about 10% due to shot noise.

7.4 Wheeler's delayed choice *gedankenexperiment*

7.4.1 Proposed experimental method

The basic premise of the full realisation of Wheeler's experiment is to apply the full Mach-Zehnder interferometer sequence of Bragg pulses to a single atom, where a decision of whether to switch the second $\pi/2$ pulse to recombine the two momentum modes is made randomly after the first two Bragg pulses are applied. As it will take several weeks to acquire enough data to fully map out the dependence of $|c_0|^2$ on ϕ_{BS} for single atoms, we will begin by simply repeating the interferometry experiment described in the previous section, but with the addition of a random delayed choice of the interferometer configuration. This will allow us to assess the suitability of this proposed experimental

method for attempting to realise the idealised version of Wheeler's experiment.

As before, clouds of $\sim 10^3$ atoms in the $m_J = 1$ state are released from the crossed dipole trap, and the train of Bragg pulses is initiated 2 ms after trap switch-off. The random choice of interferometer configuration is made 17 µs after the π pulse, by retrieving a random bit from a commercially available id Quantique Quantis OEM quantum random number generator[6] (QRNG). This device produces a truly random stream of binary digits as a NIM logic signal at an average bandwidth of 4 MHz. The random choice is then obtained by triggering a digital latch to store the value of the NIM signal as a TTL logic level. This TTL signal is used to set whether an RF switch in line with the drive signal to the AOMs is to transmit the second $\pi/2$ Bragg pulse, which determines whether the interferometer is in the open or closed configuration for each experimental cycle. As the average period of the QRNG bit generation (250 ns), delay between the latch being triggered and storing the random bit (50 ns), and rise time of the switch (6 ns) are all much shorter than the interval between the random choice and application of the first (69 µs) or second (13 µs) $\pi/2$ pulses, the choice is both 'delayed' after and relativistically separated from the first pulse, yet will be implemented well before the second pulse.

The atoms are measured on the DLD as before, however the configuration of the interferometer is also recorded by the delay-line electronics so that the result of the random choice for each experimental iteration can be recovered. The TTL signal from the digital latch is sent to a pulse generator, where a high level results in a sequence of NIM pulses being registered on a channel of the time to digital converter not used for the delay-line wires (see §3.3.3), while a low level does not generate such pulses. Thus, during the data analysis process undertaken using the files written to our data acquisition PC, the presence of these pulses identifies the interferometer configuration for each shot.

The result of this delayed choice interferometer for clouds with a large number of atoms is shown in Fig. 7.12. The experimental data for the interferometer in the closed configuration fits to a sinusoidal form of $|c_0(\phi_{\mathrm{BS}})|^2 = 0.332 \sin(1.031\pi\phi - 0.4500\pi) + 0.508$, which is quite similar to the form seen in Fig. 7.11 as expected. In this case, the fringe contrast is now 66.4%, where a reduction in contrast from the previous measurement of 85% could be attributed to long-term drifts in the power and frequency of the Bragg laser. When the second $\pi/2$ pulse is absent, a constant $|c_0(\phi_{\mathrm{BS}})|^2 = 0.5$ is expected, however a small yet systematic phase dependence is observed. This anomalous effect could also be the result of changes in the Bragg beams which alter the π time, such that the 22 µs pulse applied no longer acts as a perfect mirror, and similarly for the 11 µs beamsplitting pulse. Other possible causes of this include leakage of RF signal through the switch, or imperfect synchronisation between the RF signals for the two AOMs.

In any case, while this result does not perfectly match the form expected for when the mixing $\pi/2$ pulse is not present, it still displays an unmistakable contrast between the two interferometer configurations. We will therefore apply the same process to single atoms in an attempt to realise Wheeler's experiment. This is based on the aforementioned procedure for large clouds of $m_J = 1$ atoms, however incorporates a spin-flipping operation and subsequent holding of $m_J = 0$ atoms the trap for 20 seconds to attenuate the cloud to a single atom, as described earlier in §7.2. The population of atoms in each

[6] Technical information about this device can be found at `http://www.idquantique.com/component/content/article.html?id=9`.

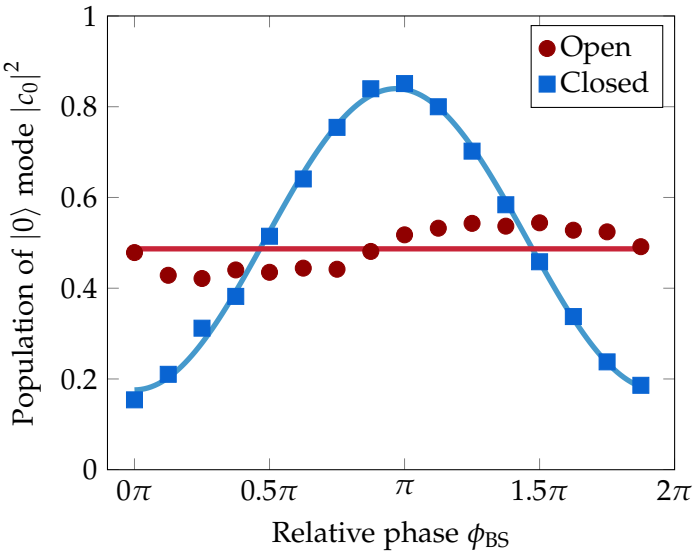

Figure 7.12: Delayed choice interferometer experiment with large atomic clouds. Red circles are for the interferometer in the open configuration, the average of which is 0.487. The blue squares are for a closed interferometer, which fits to the form $|c_0(\phi_{BS})|^2 = 0.332\sin(1.031\pi\phi - 0.4500\pi) + 0.508$.

arm of the interferometer is measured by counting the atoms detected in a 2.4 mm by 2.4 mm window in the x-y plane, and a 6 ms interval around each momentum mode arriving on the DLD. From this, the average dark count rate is removed, which corresponds to around 20% of the rate of genuine counts in that window.

The data taken by the time of writing, shown in Fig. 7.13, is clearly not a conclusive result due to a considerable presence of both systematic and statistical errors. This experiment was undertaken with a previous generation of our single-atom source, which resulted in an average count rate of only 0.04 atoms per iteration with considerably poorer long-term stability than the newer method described in §7.2.3. Each point on the plot corresponds to data taken over the course of between one and two days, which allows long-term drifts in the laser to accumulate and alter the interferometer performance. Furthermore, the small number of counts and relatively large error due to dark counts contribute to the large amount of scatter seen in the data, especially for the open configuration. However, fits to the form of the data for the two interferometer configurations are not inconsistent with those measured for the $m_J = 1$ atoms, which encourages the notion that acquiring a larger data set after having further reduced drifts in the Bragg beams and implementing the new optical trap setup may yet lead to a positive result.

7.5 Summary and future directions

The results presented in this chapter indicate that a full realisation of Wheeler's famous *gedankenexperiment* should soon be possible. While this experiment is currently being undertaken, there are some technical problems currently being addressed which should improve the measurement presented in Fig. 7.13. The stability of the dipole traps has recently been optimised by replacing the AOM units, while further improvements to stabilise the power and frequency of the Bragg laser are also being considered, including

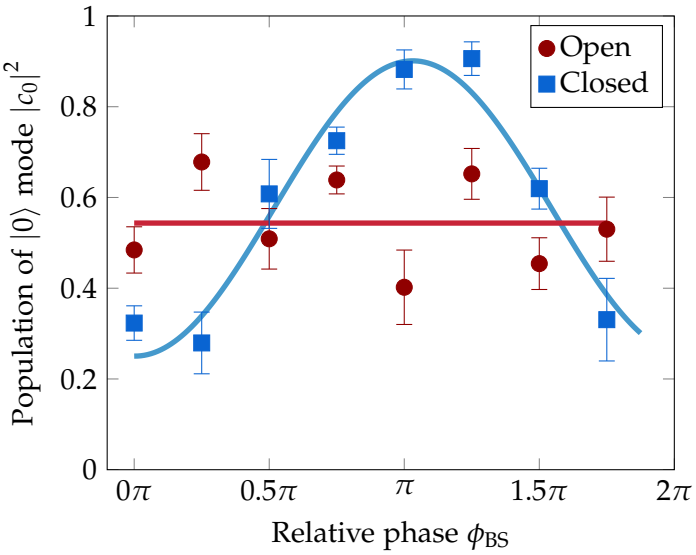

Figure 7.13: Preliminary data for Wheeler's delayed choice *gedankenexperiment*. Red circles for the open interferometer configuration have an average value of 0.5436, while the blue squares for closed interferometers fit to the form $|c_0(\phi_{BS})|^2 = 0.325\sin(0.972\pi\phi - 0.501\pi) + 0.576$. The error bars correspond to shot noise.

the addition of noise-eaters to stabilise the beam power, and an increase in the detuning of the beams. Another substantial improvement to this experiment would be to replace the use of the Agilent arbitrary wavefunction generator with a low-noise direct digital synthesis (DDS) signal generator. This allows analogue sinusoidal waveforms to be generated from digital signals which are programmed on a PC or field-programmable gate array, with fast phase and frequency switching at high resolution and with low noise. The RF source for each of the two AOMs can be synchronised to the same master clock to ensure a well-controlled relative phase relationship.

At the time of writing, a dual channel Analog Devices AD9910 DDS setup is being prepared to provide the three RF Bragg pulses. While the sample rate of 1 GSa/s is not an improvement over the Agilent function generator, the jitter specifications for the DDS are considerably better than those quoted for the Agilent device of 1 ns peak-to-peak, which is ∼10% of the RF period. Good quality reference clocks, from which the analogue signal are produced, typically have RMS jitter of less than 35 ps over long-term usage[7]. While other sources of jitter such as truncation due to the finite word size of the digital signal and a lack of signal oversampling with respect to the master clock can also be introduced, similar setups have achieved phase stability of less than 400 ps jitter between the two channels [312], which is ideal for interferometry applications. Further improvements could conceivably be achieved with a more thorough filtering of the RF signal to remove spurious frequency components, however the AOMs themselves act as narrow-band filters which isolate the desired driving frequency.

In conclusion, this proposed method strives towards the goal of observing exciting new phenomena with massive particles, and shows that the capabilities of experiments in quantum atom optics are quickly catching up to their photonic counterparts. This

[7]See `http://www.analog.com/library/analogDialogue/archives/38-08/dds.pdf` for general information about direct digital synthesisers.

also gives the opportunity to explore and exploit the unique features of atomic species when undertaking fundamental tests of quantum mechanics, and to confirm the applicability of key quantum concepts to particles with mass and internal structure. Once this experiment has been completed[8], novel extensions such as quantum eraser schemes could be considered, which further widens the scope of matter-wave experiments, and may provide insights into the possibility of other long sought after experiments such as tests of Bell's inequality with massive particles.

[8]In the months following the submission of this thesis, work continued on this experiment which improved the stability of the single-atom source considerably and allowed a data set to be collected which conclusively demonstrated the anticipated result of Wheeler's experiment, consistent with the conclusions suggested by the data shown in Fig. 7.13. The results of this are contained in an article currently under review.

Chapter 8

Conclusion

The field of quantum atom optics has progressed rapidly since the first experimental realisation of Bose-Einstein condensation in a dilute atomic gas, such that it is now catching up to the state-of-the-art of quantum optics experiments with light. Recent experiments have not only sought to demonstrate that the same quantum-mechanical processes which occur for photons are also applicable to quantum gases, but have also broken new ground to incorporate rather than ignore the internal structure and external interactions unique to atomic samples. While the intrinsic difficulty of the manipulation and detection of atomic clouds can be challenging, especially considering the relative simplicity and maturity of similar experiments with light, it provides the opportunity to investigate a rich variety of novel phenomena for massive particles. Therefore, the development of techniques to improve our ability to perform fundamental tests of quantum mechanics with atomic gases, and the subsequent application of these techniques to investigate new systems, have been the two main objectives of this thesis.

8.1 Summary of the work presented in this thesis

The results presented in this thesis clearly highlight the unique advantages of our use of ultracold metastable helium to investigate different aspects of quantum atom optics. In particular, much of the experimental apparatus was designed specifically to enable novel correlation measurements to be performed, where the stability and flexibility of the trap configuration, the detector setup, and the large time of flight between trap and detector result in high signal-to-noise correlation measurements with single atom counting. This allowed the variety of experiments detailed in Chapter 4 to be performed which investigate fundamental properties of quantum correlations in ultracold Bose gases. The coherence of a pulsed atom laser was compared to that of a truly thermal atomic source for the first time, and it was found that outcoupling atoms from a Bose-Einstein condensate with RF radiation does not result in the loss of coherence for such a source. Using this pulsed RF method, long-range temporal third-order correlations were measured in an atomic sample, which demonstrated that the bunching observed for thermal atoms is consistent with Wick's theorem, while condensates were confirmed to be coherent to third order.

Another experiment measured significantly improved second- and third-order bunching contrast by cooling thermal clouds to an order of magnitude colder temperature than our previous experiments, resulting in a correlation length which exceeded the spatial resolution of the detector and thus enabled bunching to be measured in the spatial plane of the detector. Finally, loading atoms into an optical dipole trap allowed

us to create an atomic source with a correlation length which exceeded the radial size of the cloud, such that axial correlations from second- to sixth-order could be measured for the first time, and with nearly perfect contrast. These studies have provided the most rigorous test yet to confirm the suitability of Glauber's theory of quantum coherence for atomic gases, and the applicability of Wick's theorem to such correlation function measurements. Furthermore, correlation measurements were used in Chapter 5 to show that this elongated system had undergone the degeneracy-driven transition to transverse condensation, where the population of the transverse ground state of the system was saturated, while the cloud remained incoherent in the longitudinal axis with a behaviour in the broad crossover between the ideal Bose gas and weakly-interacting quasicondensate regimes.

External potentials can be applied to quantum gases to facilitate macroscopic imaging of matter-wave interference. The modal structure of an optical waveguide was investigated in Chapter 6, both via direct imaging of the longitudinal density profile of the guided atomic source, and with the measurement of Hanbury Brown-Twiss bunching which is directly related to the macroscopically-visible speckle pattern observed in the gas. The average modal occupancy, as well as the most predominantly occupied mode of the waveguide, can be manipulated by precisely controlling the depth of our optical dipole trap. This allowed us to demonstrate that sources occupying a large number of modes result in a poorly resolved bunching signal which improves as a result of better energy selectivity with a smaller but still multimode occupation, while single-mode guided atom lasers were found to be coherent.

A full realisation of Wheeler's delayed choice *gedankenexperiment* should soon be possible with the procedure described in Chapter 7. The individual steps of the experiment such as the single atom source and Bragg interferometer have been developed, and preliminary measurements for the complete experiment indicate that a conclusive result should be obtained once a few technical problems are solved. A successful realisation of this experiment would be an important result in quantum atom optics, and would add further evidence to support the assertion that our current understanding of quantum phenomena such as complementarity is correct.

8.2 Future directions

The experiments described in this thesis have developed new techniques which allow ultracold gases to be manipulated and probed, and many of the procedures could be extended to explore new phenomena, in addition to the completion of several as-yet incomplete investigations. It would be interesting to further pursue the aim of extracting the Wigner function from the diffraction pattern produced by our atom laser, and extend this to a study of quantum state tomography. Correlated pair production by atomic four-wave mixing could lead to the observation of a rich variety of different phenomena, and would enable quantum atom optical analogues of quantum optics experiments which rely on pairs of photons produced by parametric down-conversion. The flexibility in trap geometries for optical dipole potentials, in addition to the freedom to apply either Bragg or Raman scattering to the quantum gas, could be pivotal to some of the experiments discussed below.

Further work to solve technical issues with our experimental setup should first be undertaken to strive towards completion of Wheeler's experiment. In particular, the

performance of the single atom source should be improved, which could be achieved by reducing trap instability, while an increase to the quantum efficiency of the delay-line detector may be possible by fine-tuning the detector electronics and MCP gain. Producing a reliable single-atom source could enable other investigations, such as an accurate measurement of the quantum efficiency of our different single-atom detectors, or even a single-atom realisation of Young's experiment. Furthermore, reducing long-term drifts and short-term instability in the Bragg interferometer will improve the interference visibility of the 'closed' configuration of the experimental setup. By addressing these considerations, not only could the Wheeler experiment be completed[1], but other similar experiments could be considered.

Among the potential novel investigations which could naturally follow from the setup for the Wheeler experiment would be an observation of the Hong-Ou-Mandel effect [33] with an atomic source. This effect describes the phenomena where pairs of indistinguishable and strongly correlated particles enter a 50:50 beamsplitter, such that when one particle is incident on each port of the beamsplitter, both particles always exit from the same port, despite each particle individually having a 50% probability of exiting via either port. While parametric down-conversion is used to produce a source of correlated photon pairs, and analogous effect can be achieved for ultracold atoms with four-wave mixing collisions, which can be induced by Bragg scattering [313]. In the spontaneous regime, an *s*-wave scattering halo of correlated atom pairs is produced, which can be mirrored and recombined with further Bragg pulses. Cross correlations between opposite momentum modes should reveal a reduced likelihood of one particle exiting each port in accordance with the Hong-Ou-Mandel effect.

Quantum entanglement is a fascinating non-classical result of quantum theory which has stimulated a considerable amount of theoretical and experimental work. Recently, several experiments have tested Bell's theorem for photons while closing each of the so-called 'loopholes' such as fair sampling and local communication in different experimental realisations, although no single experiment was able to close each loophole simultaneously [314]. One of the long-standing objectives of quantum atom optics is to confirm that macroscopic entanglement can be observed with massive particles. To date, several of the pre-requisites of a quantitative test of Bell's theorem have been satisfied, where sub-Poissonian statistics [225], spin squeezing [315] and inseparable quantum states [315, 316] have been demonstrated. However, tests of the EPR entanglement criterion, which can be defined for imperfectly entangled systems [317], and Bell's inequality are yet to be conclusive. Furthermore, other avenues to tests of macroscopic or mesoscopic quantum behaviour for ultracold gases are being developed, such as the investigation of Leggett-Garg inequalities [318] and weak quantum measurements [319, 320].

Extensions of the Hong-Ou-Mandel effect in principle allow tests of Bell's inequality to be performed [321], while Rarity and Tapster proposed a related scheme to test Bell's inequality by measuring phase and momentum [83] as opposed to the majority of experiments which measure spin quadratures. In the Rarity and Tapster scheme, coincidences between pairs of photons created by parametric down-conversion are measured as a function of an externally applied phase to one arm of the interferometer which allows a violation of the CHSH inequality [322], which is suitable for a test of Bell's the-

[1]Further work conducted after the submission of this thesis by the ANU group has addressed these issues and allowed this experiment to be completed.

orem, to be observed. An atomic analogue of the Rarity and Tapster scheme has been devised for atoms [214], in which four-wave mixing provides the correlated atom pairs, and Bragg scattering applies the required mirror and beamsplitter operations as with the Wheeler and Hong-Ou-Mandel experiments. The controllable external phase difference between the arms of the interferometer can be applied by a variety of methods, such as the application of a red- or blue-detuned dipole potential, or possibly a magnetic field gradient. An appealing aspect of this proposed method is that the measurement of cross correlations is not limited by detection efficiency, making this experiment suitable for our metastable helium apparatus despite the relatively low quantum efficiency of our detectors which prevents us from implementing other procedures subject to the fair sampling loophole [313].

Several other pathways towards testing Bell's theorem with ultracold gases have been proposed which may also be suitable for our apparatus. Entanglement can be generated by four-wave mixing [323, 324] or other short-range state-dependent interactions [325] in a periodic potential, or by superradiant scattering [326]. Theoretical studies have also investigated the possibility of detecting continuous-variable entanglement without the need for a coherent local oscillator [327], which can be a severe limitation for atomic experiments as a coherent BEC would inevitably subject to interactions and consequently a relatively short dephasing time. Another class of experiments which may allow entanglement to be investigated with ultracold gases is ghost imaging [328, 329], where images can be extracted from one arm of an interferometer, despite the object to be imaged being present in a different arm. Ghost imaging is intricately linked to the Hanbury-Brown Twiss effect [330], where correlations between the signal and idler arms of the interferometer are used to extract an image of the object, and entanglement between particles in the two arms can be probed by an EPR condition on the spread in position and momentum for the image produced [331]. Interestingly, higher-order correlations for incoherent sources can also improve the visibility of ghost imaging [84].

Ghost imaging is also possible for ultracold atoms, however the trap geometry, atomic spin state, number and correlation length of atoms in the cloud and outcoupling procedure must be carefully controlled to optimise the imaging resolution. Also, some form of magnetic or optical lensing must be implemented to create images in either real or momentum space without introducing distortion or aberrations. Ghost imaging with momentum-entangled atoms created via four-wave mixing in a Bose-Einstein condensate has been explored theoretically in Ref. [332], which shows that a test of entanglement is possible for such a procedure despite challenges such as pair identification and limited detector resolution. However, each of these experiments appear to be more technically difficult to implement and more dependent on detector performance than the Rarity and Tapster method, which suggests that the latter may be most suitable for our experimental setup.

Aside from investigations of quantum entanglement, a considerable range of other topics may possibly be investigated with ultracold metastable helium. Our dual-beam dipole trap may be suitable for forming a controllable two-dimensional potential, and gases of such dimensionality display a rich variety of novel behaviour, such as the proliferation [138] and pairing [333] of vortices. The onset of the Berezinskii–Kosterlitz–Thouless (BKT) transition [136, 137] can also be identified with a change in the correlation length of a 2D gas. Other phenomena such as quantum turbulence and vortex tangling [334], the transfer of energy between different length scales via the Kolmogorov spectrum [335], and probing analogues of Hawking radiation by nonlocal

density correlations in a BEC [336] could be investigated with ultracold gases.

The formation of a condensate from a thermal gas could also be probed, where a direct comparison of the portion of the cloud with suppressed density fluctuations (that is, the (quasi)condensate fraction) with a measurement of Hanbury Brown-Twiss bunching could be made. This would also shed light on the nature of this phase transition, as to whether the growth of the condensate occurs by nucleation or the coalescence of multiple quasicondensates via the Kibble-Zurek mechanism to establish long-range order. Initial experimental studies of this with our system described in Ref. [270] were not able to accurately map the change in coherence across the phase transition, due to imperfect trap stability which distorted the correlation functions measured, while computational modelling by a stochastic projected GPE *c*-field method [337] did not expect a delay between the suppression of density fluctuations and the onset of long-range order to be observed. However, inducing a phase transition for a small number of atoms in a highly stable and symmetric dual-beam dipole trap may be able to test this conclusively, by slowing the condensate growth rate and eliminating the effect of an elongated trap geometry. Similarly, investigating the critical behaviour of this phase transition by probing the length scale over which fluctuations occur could also allow the real-time formation of long-range order to be observed [132].

By developing techniques to create, manipulate and characterise ultracold gases in a variety of trapping geometries which display macroscopic wave interference, the work described in this thesis will hopefully enable the aforementioned experiments to be undertaken, in addition to other novel experiments which broaden the horizons of quantum atom optics. In particular, the use of metastable helium will be especially advantageous for the measurement of high-contrast quantum correlation functions which are key to several of the proposed investigations. These studies are important to not only confirm that ultracold gases behaves according to our understanding of quantum mechanics, but to also strive towards the realisation of quantum simulators and the development of exciting new technologies such as atomtronics.

Appendix

A.1 Wick's theorem

A derivation of the generalised Wick's theorem for boson operators [338] will be given here, as a precursor to the decomposition of higher-order correlation functions in terms of first-order functions. Wick's theorem [77] was originally derived to simplify the calculation of transition probabilities using the S-matrices developed by Feynman [339] and Dyson [340] to describe the scattering of positrons. This theorem essentially amounts to the ability to simplify $2n$-point correlation functions as a sum of all possible products of irreducible two-point moments of the distribution. It was later found to be useful for a wide range of applications in quantum field theory, where it can be applied to simplify either path integrals of Gaussian functions, or products of boson or fermion operators [341]. As such, it can be arrived at by a number of different approaches, including the successive differentiation of integrals of Gaussian probability distributions [342]. However, here we will summarise the approach of Gaudin [338, 343] to simplify higher-order correlation functions for thermal averages of boson operators, which is of particular relevance to the experiments described in Chapter 4 of this thesis.

If we have bosonic creation or annihilation operators $\hat{\Psi}_1, \hat{\Psi}_2, \ldots$ which correspond to the states of a harmonic oscillator with a Hamiltonian $H_0 = \sum_j \hbar\omega_j \hat{a}_j^\dagger \hat{a}_j$, the density operator for a Boltzmann distribution at thermal equilibrium at temperature T is

$$\hat{\rho} = \frac{\mathrm{e}^{-H_0/k_B T}}{\mathrm{tr}\left\{\mathrm{e}^{-H_0/k_B T}\right\}}, \tag{A.1}$$

where $\mathrm{tr}\left\{\hat{O}\right\}$ denotes the trace of the operator $\hat{O}$. We will use the following theorem (Thm. 9, §3.3 [343]) which states that for a thermal average $\langle \ldots \rangle_0$ of any function $f\left(\hat{a}, \hat{a}^\dagger\right)$ of creation and annihilation operators $\hat{a}^\dagger$ and $\hat{a}$, we can write

$$\left\langle f\left(\hat{a}, \hat{a}^\dagger\right)\right\rangle_0 \equiv \left(1 - \mathrm{e}^{-\lambda}\right) \mathrm{tr}\left\{f\left(\hat{a}, \hat{a}^\dagger\right) \mathrm{e}^{-\lambda \hat{a}^\dagger \hat{a}}\right\}, \tag{A.2}$$

where λ is a parameter and the average number of bosons is $\bar{n} = \left(\mathrm{e}^{\lambda} - 1\right)^{-1}$. Applying this to Eq. A.1 gives

$$\langle \hat{\rho} \rangle_0 = \prod_j \left(1 - \mathrm{e}^{-\lambda_j}\right) \mathrm{e}^{-\lambda_j \hat{a}_j^\dagger \hat{a}_j}, \qquad \lambda_j = \frac{\hbar\omega_j}{k_B T}. \tag{A.3}$$

To simplify the thermal average of a product of boson operators, we first note that

$$\left\langle \hat{\Psi}_1 \hat{\Psi}_2 \ldots \hat{\Psi}_{2n} \right\rangle_0 \equiv \frac{\mathrm{tr}\left\{\hat{\Psi}_1 \hat{\Psi}_2 \ldots \hat{\Psi}_{2n} \mathrm{e}^{-H_0/k_B T}\right\}}{\mathrm{tr}\left\{\mathrm{e}^{-H_0/k_B T}\right\}}. \tag{A.4}$$

where we recall that $\left\langle \hat{O} \right\rangle = \mathrm{tr}\left\{\hat{\rho}\hat{O}\right\}$ and that the trace of a trace is equivalent to a trace.

For the $n=1$ case, we first want to show that

$$\left\langle \hat{\Psi}_1 \hat{\Psi}_2 \right\rangle_0 \equiv \frac{\mathrm{tr}\left\{\hat{\Psi}_1 \hat{\Psi}_2 \mathrm{e}^{-H_0/k_B T}\right\}}{\mathrm{tr}\left\{\mathrm{e}^{-H_0/k_B T}\right\}} = \frac{\left[\hat{\Psi}_1, \hat{\Psi}_2\right]}{1-\mathrm{e}^{\pm\lambda_j}}. \tag{A.5}$$

For bosonic operators with $[\hat{a}_i, \hat{a}_j^\dagger] = \delta_{ij}$, the only non-zero combinations for the terms in Eq. A.5 will be if $\hat{\Psi}_1 = \hat{a}_j$ and $\hat{\Psi}_2 = \hat{a}_j^\dagger$, or $\hat{\Psi}_1 = \hat{a}_j^\dagger$ and $\hat{\Psi}_2 = \hat{a}_j$, as $\left\langle \hat{\Psi}_1 \hat{\Psi}_2 \right\rangle_0 = 0$ if $\hat{\Psi}_1$ and $\hat{\Psi}_2$ are both annihilation or creation operators, or if they are for different modes in the field.

If we take $\hat{\Psi}_1 = \hat{a}_j^\dagger$ and $\hat{\Psi}_2 = \hat{a}_j$, then

$$\left\langle \hat{a}_j^\dagger \hat{a}_j \right\rangle_0 = \bar{n} = \frac{1}{\mathrm{e}^{\lambda_j} - 1} = \frac{\left[\hat{a}_j^\dagger, \hat{a}_j\right]}{1-\mathrm{e}^{\lambda_j}}. \tag{A.6}$$

Otherwise, if $\hat{\Psi}_1 = \hat{a}_j$ and $\hat{\Psi}_2 = \hat{a}_j^\dagger$, then

$$\left\langle \hat{a}_j \hat{a}_j^\dagger \right\rangle_0 = 1 + \left\langle \hat{a}_j^\dagger \hat{a}_j \right\rangle_0 = \frac{\mathrm{e}^{\lambda_j} - 1 + 1}{\mathrm{e}^{\lambda_j} - 1} = \frac{1}{1-\mathrm{e}^{-\lambda_j}} = \frac{\left[\hat{a}_j, \hat{a}_j^\dagger\right]}{1-\mathrm{e}^{-\lambda_j}}. \tag{A.7}$$

So, in general we can write this in the compact form

$$\left\langle \hat{\Psi}_1 \hat{\Psi}_2 \right\rangle_0 = \frac{\left[\hat{\Psi}_1, \hat{\Psi}_2\right]}{1-\mathrm{e}^{\pm\lambda_j}}, \qquad \begin{cases} +\lambda_j \text{ for } \hat{\Psi}_1 = \hat{a}_j^\dagger \\ -\lambda_j \text{ for } \hat{\Psi}_1 = \hat{a}_j \end{cases}. \tag{A.8}$$

Moving on to the $n = 2$ case, and recalling that for non-commuting operators $[u, vw] = [u, v]\, w + v\, [u, w]$ and thus

$$\left[\hat{\Psi}_1, \hat{\Psi}_2 \hat{\Psi}_3 \hat{\Psi}_4\right] = \hat{\Psi}_1 \hat{\Psi}_2 \hat{\Psi}_3 \hat{\Psi}_4 - \hat{\Psi}_2 \hat{\Psi}_3 \hat{\Psi}_4 \hat{\Psi}_1, \tag{A.9}$$

we want to evaluate

$$\begin{aligned} \left\langle \hat{\Psi}_2 \hat{\Psi}_3 \hat{\Psi}_4 \hat{\Psi}_1 \right\rangle_0 &= \frac{\mathrm{tr}\left\{\hat{\Psi}_2 \hat{\Psi}_3 \hat{\Psi}_4 \hat{\Psi}_1 \mathrm{e}^{-H_0/k_B T}\right\}}{\mathrm{tr}\left\{\mathrm{e}^{-H_0/k_B T}\right\}}, \\ &= \frac{\mathrm{tr}\left\{\hat{\Psi}_2 \hat{\Psi}_3 \hat{\Psi}_4 \mathrm{e}^{-H_0/k_B T} \mathrm{e}^{H_0/k_B T} \hat{\Psi}_1 \mathrm{e}^{-H_0/k_B T}\right\}}{\mathrm{tr}\left\{\mathrm{e}^{-H_0/k_B T}\right\}}. \end{aligned} \tag{A.10}$$

Using Thm. 5 from §3.3 of Ref. [343], we have

$$\mathrm{e}^{\lambda \hat{a}^\dagger \hat{a}} \hat{a}^\dagger \mathrm{e}^{-\lambda \hat{a}^\dagger \hat{a}} = \mathrm{e}^{\lambda} \hat{a}^\dagger, \tag{A.11}$$

$$\mathrm{e}^{-\lambda \hat{a}^\dagger \hat{a}} \hat{a} \mathrm{e}^{-\lambda \hat{a}^\dagger \hat{a}} = \mathrm{e}^{-\lambda} \hat{a}, \tag{A.12}$$

and thus

$$\mathrm{e}^{H_0/k_B T} \hat{\Psi}_1 \mathrm{e}^{-H_0/k_B T} = \hat{\Psi}_1 \mathrm{e}^{\pm\lambda_j}, \qquad \begin{cases} +\lambda_j \text{ for } \hat{\Psi}_1 = \hat{a}_j^\dagger \\ -\lambda_j \text{ for } \hat{\Psi}_1 = \hat{a}_j \end{cases}. \tag{A.13}$$

Applying Eq. A.13 to Eq. A.10 gives

$$\begin{aligned}\left\langle \hat{\Psi}_2\hat{\Psi}_3\hat{\Psi}_4\hat{\Psi}_1\right\rangle_0 &= \frac{\mathrm{tr}\left\{\hat{\Psi}_2\hat{\Psi}_3\hat{\Psi}_4 e^{-H_0/k_BT}\hat{\Psi}_1\right\} e^{\pm\lambda_j}}{\mathrm{tr}\left\{e^{-H_0/k_BT}\right\}},\\ &= \frac{\mathrm{tr}\left\{\hat{\Psi}_1\hat{\Psi}_2\hat{\Psi}_3\hat{\Psi}_4 e^{-H_0/k_BT}\right\} e^{\pm\lambda_j}}{\mathrm{tr}\left\{e^{-H_0/k_BT}\right\}}, \qquad \text{(cyclic trace)}\\ &= e^{\pm\lambda_j}\left\langle \hat{\Psi}_1\hat{\Psi}_2\hat{\Psi}_3\hat{\Psi}_4\right\rangle_0. \end{aligned} \tag{A.14}$$

Finding the thermal average of Eq. A.9 given the result of Eq. A.14 allows us to simplify the $n=2$ case to

$$\begin{aligned}\left\langle\left[\hat{\Psi}_1,\hat{\Psi}_2\hat{\Psi}_3\hat{\Psi}_4\right]\right\rangle_0 &= \left\langle\hat{\Psi}_1\hat{\Psi}_2\hat{\Psi}_3\hat{\Psi}_4\right\rangle_0 - \left\langle\hat{\Psi}_2\hat{\Psi}_3\hat{\Psi}_4\hat{\Psi}_1\right\rangle_0,\\ \therefore \left(1-e^{\pm\lambda_j}\right)\left\langle\hat{\Psi}_1\hat{\Psi}_2\hat{\Psi}_3\hat{\Psi}_4\right\rangle_0 &= \left\langle\left[\hat{\Psi}_1,\hat{\Psi}_2\right]\hat{\Psi}_3\hat{\Psi}_4 + \left[\hat{\Psi}_1,\hat{\Psi}_3\right]\hat{\Psi}_2\hat{\Psi}_4 + \left[\hat{\Psi}_1,\hat{\Psi}_4\right]\hat{\Psi}_2\hat{\Psi}_3\right\rangle_0,\\ \therefore \left\langle\hat{\Psi}_1\hat{\Psi}_2\hat{\Psi}_3\hat{\Psi}_4\right\rangle_0 &= \frac{1}{1-e^{\pm\lambda_j}}\Big\{\left[\hat{\Psi}_1,\hat{\Psi}_2\right]\left\langle\hat{\Psi}_3\hat{\Psi}_4\right\rangle_0\\ &\quad + \left[\hat{\Psi}_1,\hat{\Psi}_3\right]\left\langle\hat{\Psi}_2\hat{\Psi}_4\right\rangle_0 + \left[\hat{\Psi}_1,\hat{\Psi}_4\right]\left\langle\hat{\Psi}_2\hat{\Psi}_3\right\rangle_0\Big\}. \end{aligned} \tag{A.15}$$

Plugging in the result of Eq. A.8 then simplifies this to the desired form

$$\left\langle\hat{\Psi}_1\hat{\Psi}_2\hat{\Psi}_3\hat{\Psi}_4\right\rangle_0 = \left\langle\hat{\Psi}_1\hat{\Psi}_2\right\rangle_0\left\langle\hat{\Psi}_3\hat{\Psi}_4\right\rangle_0 + \left\langle\hat{\Psi}_1\hat{\Psi}_3\right\rangle_0\left\langle\hat{\Psi}_2\hat{\Psi}_4\right\rangle_0 + \left\langle\hat{\Psi}_1\hat{\Psi}_4\right\rangle_0\left\langle\hat{\Psi}_2\hat{\Psi}_3\right\rangle_0. \tag{A.16}$$

This process can be reapplied repeatedly to decompose higher-order correlation functions, which take the general form

$$\left\langle\hat{\Psi}_1\ldots\hat{\Psi}_{2n}\right\rangle_0 = \left\langle\hat{\Psi}_1\hat{\Psi}_2\right\rangle_0\left\langle\hat{\Psi}_3\hat{\Psi}_4\right\rangle_0\ldots\left\langle\hat{\Psi}_{2n-1}\hat{\Psi}_{2n}\right\rangle_0 + \text{permutations}. \tag{A.17}$$

A.2 Decomposition of higher-order correlation functions using Wick's theorem

We can now apply Wick's theorem to the quantum correlation functions defined by Glauber which were discussed in §2.1.1. Following from the theory for Bose gases in Ref. [186], we can consider operators of the form

$$\hat{\Psi}^\dagger(\mathbf{r}) = \sum_j \psi_j^*(\mathbf{r})\hat{a}_j^\dagger, \tag{A.18}$$

where $\hat{a}_j^\dagger$ creates particle in state $|\psi_j\rangle$, and thus $\hat{\Psi}^\dagger(\mathbf{r})$ creates a particle at position $\mathbf{r}$. The Hermitian conjugates of these quantities correspond to annihilation operations. We wish to decompose correlation functions related to the type defined in Eq. 2.17, which for first- through third-orders are

$$G^{(1)}(\mathbf{r}_1,\mathbf{r}_2) = \left\langle\hat{\Psi}^\dagger(\mathbf{r}_1)\hat{\Psi}(\mathbf{r}_2)\right\rangle, \tag{A.19}$$

$$G^{(2)}_{\mathrm{dens}}(\mathbf{r}_1,\mathbf{r}_2) = \left\langle\hat{\Psi}^\dagger(\mathbf{r}_1)\hat{\Psi}(\mathbf{r}_1)\hat{\Psi}^\dagger(\mathbf{r}_2)\hat{\Psi}(\mathbf{r}_2)\right\rangle, \tag{A.20}$$

$$G^{(3)}_{\mathrm{dens}}(\mathbf{r}_1,\mathbf{r}_2,\mathbf{r}_3) = \left\langle\hat{\Psi}^\dagger(\mathbf{r}_1)\hat{\Psi}(\mathbf{r}_1)\hat{\Psi}^\dagger(\mathbf{r}_2)\hat{\Psi}(\mathbf{r}_2)\hat{\Psi}^\dagger(\mathbf{r}_3)\hat{\Psi}(\mathbf{r}_3)\right\rangle, \tag{A.21}$$

and so on for higher orders. The density of the atomic cloud is given by $\rho(\mathbf{r}) = \left\langle \hat{\Psi}^\dagger(\mathbf{r})\hat{\Psi}(\mathbf{r})\right\rangle$. Note, however, that these are not strictly equivalent to Glauber's definition in Eq. 2.17, as the operators are not normally ordered[2], but represent the density correlations for $n \geq 2$ which are explicitly measured in our experimental data, as is demonstrated in Eq. 2.22.

A.2.1 Second-order density correlation function

First, we will consider how the second-order density correlation function can be expressed in terms of $G^{(1)}(\mathbf{r}_1, \mathbf{r}_2)$. Writing the first two functions out in full, we have

$$\begin{aligned} G^{(1)}(\mathbf{r}_1, \mathbf{r}_2) &= \left\langle \left(\sum_j \psi_j^*(\mathbf{r}_1)\hat{a}_j^\dagger\right)\left(\sum_k \psi_k(\mathbf{r}_2)\hat{a}_k\right)\right\rangle, \\ &= \sum_{j,k} \psi_j^*(\mathbf{r}_1)\psi_k(\mathbf{r}_2)\left\langle \hat{a}_j^\dagger\hat{a}_k\right\rangle, \qquad \text{(A.22)} \\ G^{(2)}_{\text{dens}}(\mathbf{r}_1, \mathbf{r}_2) &= \sum_{i,j,k,l} \psi_i^*(\mathbf{r}_1)\psi_j(\mathbf{r}_2)\psi_k^*(\mathbf{r}_1)\psi_l(\mathbf{r}_2)\left\langle \hat{a}_i^\dagger\hat{a}_j\hat{a}_k^\dagger\hat{a}_l\right\rangle. \qquad \text{(A.23)} \end{aligned}$$

As the wavefunctions $\psi_j(\mathbf{r})$ are simply scalar functions, we will concentrate on the boson operators $\hat{a}_j$ and $\hat{a}_j^\dagger$, which obey the usual commutation relationships $[\hat{a}_i^\dagger, \hat{a}_j^\dagger] = [\hat{a}_i, \hat{a}_j] = 0$ and $[\hat{a}_i, \hat{a}_j^\dagger] = \delta_{ij}$. Applying Wick's theorem (Eq. A.16) to the correlation function of the boson operators results in

$$\begin{aligned} \left\langle \hat{a}_i^\dagger\hat{a}_j\hat{a}_k^\dagger\hat{a}_l\right\rangle &= \left\langle \hat{a}_i^\dagger\left(\hat{a}_k^\dagger\hat{a}_j + \delta_{jk}\right)\hat{a}_l\right\rangle, \\ &= \left\langle \hat{a}_i^\dagger\hat{a}_k^\dagger\hat{a}_j\hat{a}_l\right\rangle + \delta_{jk}\left\langle \hat{a}_i^\dagger\hat{a}_l\right\rangle, \\ \text{(using Wick's theorem)} &= \cancelto{0}{\left\langle \hat{a}_i^\dagger\hat{a}_k^\dagger\right\rangle\left\langle \hat{a}_j\hat{a}_l\right\rangle} + \left\langle \hat{a}_i^\dagger\hat{a}_j\right\rangle\left\langle \hat{a}_k^\dagger\hat{a}_l\right\rangle + \left\langle \hat{a}_i^\dagger\hat{a}_l\right\rangle\left\langle \hat{a}_k^\dagger\hat{a}_j\right\rangle + \delta_{jk}\left\langle \hat{a}_i^\dagger\hat{a}_l\right\rangle, \\ \text{(keep pairs with same index)} &= \delta_{ij}\left\langle \hat{a}_i^\dagger\hat{a}_j\right\rangle\delta_{kl}\left\langle \hat{a}_k^\dagger\hat{a}_l\right\rangle + \delta_{il}\left\langle \hat{a}_i^\dagger\hat{a}_l\right\rangle\delta_{kj}\left\langle \hat{a}_k^\dagger\hat{a}_j\right\rangle + \delta_{jk}\left\langle \hat{a}_i^\dagger\hat{a}_l\right\rangle, \\ &= \left\langle \hat{a}_i^\dagger\hat{a}_i\right\rangle\left\langle \hat{a}_k^\dagger\hat{a}_k\right\rangle\left(\delta_{ij}\delta_{kl} + \delta_{il}\delta_{kj}\right) + \delta_{jk}\delta_{il}\left\langle \hat{a}_i^\dagger\hat{a}_i\right\rangle. \qquad \text{(A.24)} \end{aligned}$$

Thus, the full form for the second-order density correlation function is

$$\begin{aligned} G^{(2)}_{\text{dens}}(\mathbf{r}_1, \mathbf{r}_2) &= \sum_{i,j,k,l} \psi_i^*(\mathbf{r}_1)\psi_j(\mathbf{r}_2)\psi_k^*(\mathbf{r}_1)\psi_{ml}(\mathbf{r}_2)\left(\left\langle \hat{a}_i^\dagger\hat{a}_i\right\rangle\left\langle \hat{a}_k^\dagger\hat{a}_k\right\rangle\left(\delta_{ij}\delta_{kl} + \delta_{il}\delta_{kj}\right) + \delta_{jk}\delta_{il}\left\langle \hat{a}_i^\dagger\hat{a}_i\right\rangle\right), \\ &= \sum_{i,k} \psi_i^*(\mathbf{r}_1)\,\psi_k^*(\mathbf{r}_2)\left\langle \hat{a}_i^\dagger\hat{a}_i\right\rangle\left[\psi_i(\mathbf{r}_1)\,\psi_k(\mathbf{r}_2)\left\langle \hat{a}_k^\dagger\hat{a}_k\right\rangle + \psi_k(\mathbf{r}_1)\,\psi_i(\mathbf{r}_2)\left\langle \hat{a}_k^\dagger\hat{a}_k\right\rangle + \psi_k(\mathbf{r}_1)\,\psi_i(\mathbf{r}_2)\right], \\ &= G^{(1)}(\mathbf{r}_1, \mathbf{r}_1)G^{(1)}(\mathbf{r}_2, \mathbf{r}_2) + G^{(1)}(\mathbf{r}_1, \mathbf{r}_2)G^{(1)}(\mathbf{r}_2, \mathbf{r}_1) + G^{(1)}(\mathbf{r}_1, \mathbf{r}_2)\sum_k \psi_k^*(\mathbf{r}_2)\psi_k(\mathbf{r}_1), \\ &= \rho(\mathbf{r}_1)\,\rho(\mathbf{r}_2) + \left|G^{(1)}(\mathbf{r}_1, \mathbf{r}_2)\right|^2 + \cancelto{0}{\rho(\mathbf{r}_1)\,\delta(\mathbf{r}_1 - \mathbf{r}_2)}, \qquad \text{(A.25)} \end{aligned}$$

where we use the fact that $G^{(1)}(\mathbf{r}_1, \mathbf{r}_2) = G^{(1)}(\mathbf{r}_2, \mathbf{r}_1)^*$. Also, the last 'shot noise' term is insignificant compared to the other terms for a high temperature thermal distribution [186], and consequently $G^{(2)}_{\text{dens}}(\mathbf{r}_1, \mathbf{r}_2) = G^{(2)}(\mathbf{r}_1, \mathbf{r}_2)$ in this limit. This can then be

[2]This requires all the creation operators to be ordered to the left of all the annihilation operators.

normalised to

$$g^{(2)}(\mathbf{r}_1,\mathbf{r}_2)=\frac{G^{(2)}(\mathbf{r}_1,\mathbf{r}_2)}{\rho\left(\mathbf{r}_1\right)\rho\left(\mathbf{r}_2\right)}=1+\frac{\left|G^{(1)}(\mathbf{r}_1,\mathbf{r}_2)\right|^2}{\rho\left(\mathbf{r}_1\right)\rho\left(\mathbf{r}_2\right)}, \tag{A.26}$$

which is the form quoted in Eq. 2.23.

It can be shown, however, that the 'shot noise' term does become important if $T\sim T_c$, where a significant occupation of the ground state such that $\rho\left(\mathbf{r}\right)\rightarrow\rho_0\left(\mathbf{r}\right)$ leads to [186]

$$\begin{aligned}G^{(2)}(\mathbf{r}_1,\mathbf{r}_2)&=\rho\left(\mathbf{r}_1\right)\rho\left(\mathbf{r}_2\right)+\left|G^{(1)}(\mathbf{r}_1,\mathbf{r}_2)\right|^2-\rho_0\left(\mathbf{r}_1\right)\rho_0\left(\mathbf{r}_2\right),\\ g^{(2)}(\mathbf{r}_1,\mathbf{r}_2)&=1+\frac{\left|G^{(1)}(\mathbf{r}_1,\mathbf{r}_2)\right|^2}{\rho_0\left(\mathbf{r}_1\right)\rho_0\left(\mathbf{r}_2\right)}-\frac{\rho_0\left(\mathbf{r}_1\right)\rho_0\left(\mathbf{r}_2\right)}{\rho_0\left(\mathbf{r}_1\right)\rho_0\left(\mathbf{r}_2\right)}=1.\end{aligned} \tag{A.27}$$

This is the familiar result for Bose-Einstein condensates that $g^{(n)}(\mathbf{r}_1,\ldots,\mathbf{r}_n)=1$ for a coherent state.

A.2.2 Third-order density correlation function

We can now extend this to the third-order correlation function

$$G^{(3)}_{\text{dens}}(\mathbf{r}_1,\mathbf{r}_2,\mathbf{r}_3)=\sum_{i,j,k,l,m,p}\psi_i^*(\mathbf{r}_1)\psi_j(\mathbf{r}_1)\psi_k^*(\mathbf{r}_2)\psi_l(\mathbf{r}_2)\psi_m^*(\mathbf{r}_3)\psi_p(\mathbf{r}_3)\left\langle\hat{a}_i^\dagger\hat{a}_j\hat{a}_k^\dagger\hat{a}_l\hat{a}_m^\dagger\hat{a}_p\right\rangle. \tag{A.28}$$

As before, we can rearrange the bosonic operators

$$\begin{aligned}\left\langle\hat{a}_i^\dagger\hat{a}_j\hat{a}_k^\dagger\hat{a}_l\hat{a}_m^\dagger\hat{a}_p\right\rangle&=\left\langle\hat{a}_i^\dagger\left(\hat{a}_k^\dagger\hat{a}_j+\delta_{jk}\right)\left(\hat{a}_m^\dagger\hat{a}_l+\delta_{ml}\right)\hat{a}_p\right\rangle,\\ &=\left\langle\hat{a}_i^\dagger\hat{a}_k^\dagger\left(\hat{a}_m^\dagger\hat{a}_j+\delta_{jm}\right)\hat{a}_l\hat{a}_p\right\rangle+\delta_{lm}\left\langle\hat{a}_i^\dagger\hat{a}_k^\dagger\hat{a}_j\hat{a}_p\right\rangle+\delta_{jk}\left\langle\hat{a}_i^\dagger\hat{a}_m^\dagger\hat{a}_l\hat{a}_p\right\rangle+\delta_{jk}\delta_{lm}\left\langle\hat{a}_i^\dagger\hat{a}_p\right\rangle,\\ &=\left\langle\hat{a}_i^\dagger\hat{a}_k^\dagger\hat{a}_m^\dagger\hat{a}_j\hat{a}_l\hat{a}_p\right\rangle+\delta_{jm}\left\langle\hat{a}_i^\dagger\hat{a}_k^\dagger\hat{a}_l\hat{a}_p\right\rangle+\delta_{lm}\left\langle\hat{a}_i^\dagger\hat{a}_k^\dagger\hat{a}_j\hat{a}_p\right\rangle\\ &\quad+\delta_{jk}\left\langle\hat{a}_i^\dagger\hat{a}_m^\dagger\hat{a}_l\hat{a}_p\right\rangle+\delta_{jk}\delta_{lm}\left\langle\hat{a}_i^\dagger\hat{a}_p\right\rangle.\end{aligned} \tag{A.29}$$

Applying Wick's theorem,

$$\begin{aligned}&\left\langle\hat{a}_i^\dagger\hat{a}_j\hat{a}_k^\dagger\hat{a}_l\hat{a}_m^\dagger\hat{a}_p\right\rangle=\left\langle\hat{a}_i^\dagger\hat{a}_j\right\rangle\left(\left\langle\hat{a}_k^\dagger\hat{a}_l\right\rangle\left\langle\hat{a}_m^\dagger\hat{a}_p\right\rangle+\left\langle\hat{a}_k^\dagger\hat{a}_p\right\rangle\left\langle\hat{a}_m^\dagger\hat{a}_l\right\rangle\right)\\ &+\left\langle\hat{a}_i^\dagger\hat{a}_l\right\rangle\left(\left\langle\hat{a}_k^\dagger\hat{a}_j\right\rangle\left\langle\hat{a}_m^\dagger\hat{a}_p\right\rangle+\left\langle\hat{a}_k^\dagger\hat{a}_p\right\rangle\left\langle\hat{a}_m^\dagger\hat{a}_j\right\rangle\right)+\left\langle\hat{a}_i^\dagger\hat{a}_p\right\rangle\left(\left\langle\hat{a}_k^\dagger\hat{a}_j\right\rangle\left\langle\hat{a}_m^\dagger\hat{a}_l\right\rangle+\left\langle\hat{a}_k^\dagger\hat{a}_l\right\rangle\left\langle\hat{a}_m^\dagger\hat{a}_j\right\rangle\right)\\ &+\delta_{jm}\left(\left\langle\hat{a}_i^\dagger\hat{a}_l\right\rangle\left\langle\hat{a}_k^\dagger\hat{a}_p\right\rangle+\left\langle\hat{a}_i^\dagger\hat{a}_p\right\rangle\left\langle\hat{a}_k^\dagger\hat{a}_l\right\rangle\right)+\delta_{lm}\left(\left\langle\hat{a}_i^\dagger\hat{a}_j\right\rangle\left\langle\hat{a}_k^\dagger\hat{a}_p\right\rangle+\left\langle\hat{a}_i^\dagger\hat{a}_p\right\rangle\left\langle\hat{a}_k^\dagger\hat{a}_l\right\rangle\right)\\ &+\delta_{jk}\left(\left\langle\hat{a}_i^\dagger\hat{a}_l\right\rangle\left\langle\hat{a}_m^\dagger\hat{a}_p\right\rangle+\left\langle\hat{a}_i^\dagger\hat{a}_p\right\rangle\left\langle\hat{a}_m^\dagger\hat{a}_l\right\rangle\right)+\delta_{jk}\delta_{lm}\left\langle\hat{a}_i^\dagger\hat{a}_p\right\rangle,\end{aligned} \tag{A.30}$$

From here, we can recognise that terms of the form $\left\langle\hat{a}_i^\dagger\hat{a}_j\right\rangle=\delta_{ij}\left\langle\hat{a}_i^\dagger\hat{a}_i\right\rangle$, and we can throw away any terms which do not contain the product of three first-order moments (i.e. retain only the first two lines of Eq. A.30) which is again equivalent to equating

$\left\langle \hat{a}_i^\dagger \hat{a}_j \hat{a}_k^\dagger \hat{a}_l \hat{a}_m^\dagger \hat{a}_p \right\rangle = \left\langle \hat{a}_i^\dagger \hat{a}_k^\dagger \hat{a}_m^\dagger \hat{a}_j \hat{a}_l \hat{a}_p \right\rangle$, to arrive at

$$\begin{aligned} G^{(3)}(\mathbf{r}_1,\mathbf{r}_2,\mathbf{r}_3) &= G^{(1)}(\mathbf{r}_1,\mathbf{r}_1)\,G^{(1)}(\mathbf{r}_2,\mathbf{r}_2)\,G^{(1)}(\mathbf{r}_3,\mathbf{r}_3) + G^{(1)}(\mathbf{r}_1,\mathbf{r}_1)\,G^{(1)}(\mathbf{r}_2,\mathbf{r}_3)\,G^{(1)}(\mathbf{r}_3,\mathbf{r}_2) \\ &\quad + G^{(1)}(\mathbf{r}_1,\mathbf{r}_2)\,G^{(1)}(\mathbf{r}_2,\mathbf{r}_1)\,G^{(1)}(\mathbf{r}_3,\mathbf{r}_3) + G^{(1)}(\mathbf{r}_2,\mathbf{r}_1)\,G^{(1)}(\mathbf{r}_2,\mathbf{r}_3)\,G^{(1)}(\mathbf{r}_3,\mathbf{r}_1) \\ &\quad + G^{(1)}(\mathbf{r}_1,\mathbf{r}_3)\,G^{(1)}(\mathbf{r}_2,\mathbf{r}_1)\,G^{(1)}(\mathbf{r}_3,\mathbf{r}_2) + G^{(1)}(\mathbf{r}_1,\mathbf{r}_3)\,G^{(1)}(\mathbf{r}_2,\mathbf{r}_2)\,G^{(1)}(\mathbf{r}_3,\mathbf{r}_1)\,, \\ &= \rho(\mathbf{r}_1)\,\rho(\mathbf{r}_2)\,\rho(\mathbf{r}_3) + \rho(\mathbf{r}_1)\left|G^{(1)}(\mathbf{r}_2,\mathbf{r}_3)\right|^2 + \rho(\mathbf{r}_3)\left|G^{(1)}(\mathbf{r}_1,\mathbf{r}_2)\right|^2 + \rho(\mathbf{r}_2)\left|G^{(1)}(\mathbf{r}_1,\mathbf{r}_3)\right|^2 \\ &\quad + G^{(1)}(\mathbf{r}_1,\mathbf{r}_3)\,G^{(1)}(\mathbf{r}_2,\mathbf{r}_1)\,G^{(1)}(\mathbf{r}_3,\mathbf{r}_2) + G^{(1)}(\mathbf{r}_2,\mathbf{r}_1)\,G^{(1)}(\mathbf{r}_2,\mathbf{r}_3)\,G^{(1)}(\mathbf{r}_3,\mathbf{r}_1)\,. \end{aligned} \tag{A.31}$$

This normalises to the form given in Eq. 2.24, which is

$$\begin{aligned} g^{(3)}(\mathbf{r}_1,\mathbf{r}_2,\mathbf{r}_3) = 1 &+ \frac{\left|G^{(1)}(\mathbf{r}_2,\mathbf{r}_3)\right|^2}{\rho(\mathbf{r}_2)\,\rho(\mathbf{r}_3)} + \frac{\left|G^{(1)}(\mathbf{r}_1,\mathbf{r}_3)\right|^2}{\rho(\mathbf{r}_1)\,\rho(\mathbf{r}_3)} + \frac{\left|G^{(1)}(\mathbf{r}_1,\mathbf{r}_2)\right|^2}{\rho(\mathbf{r}_1)\,\rho(\mathbf{r}_2)} \\ &+ \frac{2\Re\left\{G^{(1)}(\mathbf{r}_1,\mathbf{r}_3)\,G^{(1)}(\mathbf{r}_2,\mathbf{r}_1)\,G^{(1)}(\mathbf{r}_3,\mathbf{r}_2)\right\}}{\rho(\mathbf{r}_1)\,\rho(\mathbf{r}_2)\,\rho(\mathbf{r}_3)}. \end{aligned} \tag{A.32}$$

The maximum value of this function is $g^{(3)}(\mathbf{0},\mathbf{0},\mathbf{0}) = 6$, which is consistent with $g^{(n)}(\mathbf{0},\ldots,\mathbf{0}) = n!$ as expected. Finally, we can write this in terms of second- and third-order terms only, as is investigated in §4.4, which results in

$$\begin{aligned} g^{(3)}(\mathbf{r}_1,\mathbf{r}_2,\mathbf{r}_3) = &\frac{2\Re\left\{G^{(1)}(\mathbf{r}_1,\mathbf{r}_3)\,G^{(1)}(\mathbf{r}_2,\mathbf{r}_1)\,G^{(1)}(\mathbf{r}_3,\mathbf{r}_2)\right\}}{\rho(\mathbf{r}_1)\,\rho(\mathbf{r}_2)\,\rho(\mathbf{r}_3)} \\ &+ g^{(2)}(\mathbf{r}_1,\mathbf{r}_2) + g^{(2)}(\mathbf{r}_1,\mathbf{r}_3) + g^{(2)}(\mathbf{r}_2,\mathbf{r}_3) - 2. \end{aligned} \tag{A.33}$$

A.2.3 Fourth-order density correlation function

Applying this same procedure to the fourth-order correlation function gives

$$\begin{aligned} g^{(4)}(\mathbf{r}_1,\mathbf{r}_2,\mathbf{r}_3,\mathbf{r}_4) = 1 &\\ &+ \sum_{i<j}^{6\text{ terms}} \frac{\left|G^{(1)}(\mathbf{r}_i,\mathbf{r}_j)\right|^2}{\rho(\mathbf{r}_i)\,\rho(\mathbf{r}_j)}, \\ &+ \sum_{i<j,l<m}^{3\text{ terms}} \frac{\left|G^{(1)}(\mathbf{r}_i,\mathbf{r}_j)\,G^{(1)}(\mathbf{r}_l,\mathbf{r}_m)\right|^2}{\rho(\mathbf{r}_i)\,\rho(\mathbf{r}_j)\,\rho(\mathbf{r}_l)\,\rho(\mathbf{r}_m)}, \\ &+ \sum_{i\neq j\neq l}^{4\text{ terms}} \frac{2\Re\left\{G^{(1)}(\mathbf{r}_i,\mathbf{r}_j)\,G^{(1)}(\mathbf{r}_j,\mathbf{r}_l)\,G^{(1)}(\mathbf{r}_l,\mathbf{r}_i)\right\}}{\rho(\mathbf{r}_i)\,\rho(\mathbf{r}_j)\,\rho(\mathbf{r}_l)}, \\ &+ \sum_{i\neq j\neq l\neq m}^{6\text{ terms}} \frac{G^{(1)}(\mathbf{r}_i,\mathbf{r}_j)\,G^{(1)}(\mathbf{r}_j,\mathbf{r}_l)\,G^{(1)}(\mathbf{r}_l,\mathbf{r}_m)\,G^{(1)}(\mathbf{r}_m,\mathbf{r}_i)}{\rho(\mathbf{r}_i)\,\rho(\mathbf{r}_j)\,\rho(\mathbf{r}_l)\,\rho(\mathbf{r}_m)}. \end{aligned} \tag{A.34}$$

Note that $g^{(4)}(\mathbf{0},\mathbf{0},\mathbf{0},\mathbf{0}) = 24 = 4!$ is again satisfied. This can be rewritten in a form suitable for density correlation measurements as

$$\begin{aligned} g^{(4)}(\mathbf{r}_1,\mathbf{r}_2,\mathbf{r}_3,\mathbf{r}_4) = & \sum_{i\neq j\neq l\neq m}^{6\text{ terms}} \frac{G^{(1)}(\mathbf{r}_i,\mathbf{r}_j)\,G^{(1)}(\mathbf{r}_j,\mathbf{r}_l)\,G^{(1)}(\mathbf{r}_l,\mathbf{r}_m)\,G^{(1)}(\mathbf{r}_m,\mathbf{r}_i)}{\rho(\mathbf{r}_i)\,\rho(\mathbf{r}_j)\,\rho(\mathbf{r}_l)\,\rho(\mathbf{r}_m)} \\ & + \sum_{i<j,l<m}^{3\text{ terms}} \frac{\left|G^{(1)}(\mathbf{r}_i,\mathbf{r}_j)\,G^{(1)}(\mathbf{r}_l,\mathbf{r}_m)\right|^2}{\rho(\mathbf{r}_i)\,\rho(\mathbf{r}_j)\,\rho(\mathbf{r}_l)\,\rho(\mathbf{r}_m)} \\ & + \sum_{i<j<l}^{4\text{ terms}} g^{(3)}(\mathbf{r}_i,\mathbf{r}_j,\mathbf{r}_l) \\ & - \sum_{i<j}^{6\text{ terms}} g^{(2)}(\mathbf{r}_i,\mathbf{r}_j) \\ & - 3. \end{aligned} \tag{A.35}$$

Functions for order $n \geq 5$ will follow in a similar fashion, each with $n!$ terms.

Bibliography

[1] Feynman, R. P. *The Character of Physical Law* (Random House, New York, 1965). [cited on pages 1 and 3].

[2] Schlosshauer, M., Kofler, J. & Zeilinger, A. A snapshot of foundational attitudes toward quantum mechanics. *Studies in History and Philosophy of Science Part B: Studies in History and Philosophy of Modern Physics* **44**, 222–230 (2013). doi:10.1016/j.shpsb.2013.04.004. [cited on pages 1 and 22].

[3] Sommer, C. Another Survey of Foundational Attitudes Towards Quantum Mechanics. *ArXiv e-prints* (2013). `http://arxiv.org/abs/1303.2719`. [cited on page 1].

[4] Norsen, T. & Nelson, S. Yet Another Snapshot of Foundational Attitudes Toward Quantum Mechanics. *ArXiv e-prints* (2013). `http://arxiv.org/abs/1306.4646`. [cited on page 1].

[5] Whitaker, A. *Einstein, Bohr and the Quantum Dilemma (2nd edition)* (Cambridge University Press, Cambridge, 2006). [cited on pages 1, 2, and 3].

[6] Hecht, E. *Optics (4th Ed.)* (Addison Wesley, San Francisco, 2002). [cited on page 2].

[7] Planck, M. Ueber das Gesetz der Energieverteilung im Normalspectrum. *Annalen der Physik* **309**, 553–563 (1901). doi:10.1002/andp.19013090310. [cited on page 2].

[8] Einstein, A. Über einen die Erzeugung und Verwandlung des Lichtes betreffenden heuristischen Gesichtspunkt. *Annalen der Physik* **322**, 132–148 (1905). doi:10.1002/andp.19053220607. [cited on page 2].

[9] Compton, A. H. A Quantum Theory of the Scattering of X-rays by Light Elements. *Phys. Rev.* **21**, 483–502 (1923). doi:10.1103/PhysRev.21.483. [cited on page 2].

[10] de Broglie, L. *Recherches sur la théorie des quanta*. Ph.D. thesis, Université Paris (1924). [cited on page 2].

[11] Davisson, C. & Germer, L. H. Diffraction of Electrons by a Crystal of Nickel. *Phys. Rev.* **30**, 705–740 (1927). doi:10.1103/PhysRev.30.705. [cited on page 2].

[12] Arndt, M. *et al.* Wave-particle duality of C_{60} molecules. *Nature* **401**, 680–682 (1999). doi:10.1038/44348. [cited on page 2].

[13] Bachor, H. A. & Ralph, T. C. *A Guide to Experiments in Quantum Optics* (Wiley, Weinheim, 2004). [cited on pages 2, 12, and 13].

[14] Dirac, P. A. Quantum theory of emission and absorption of radiation. *Proc. Roy. Soc. Lond.* **A114**, 243 (1927). doi:10.1098/rspa.1927.0039. [cited on page 2].

[15] Fermi, E. Quantum Theory of Radiation. *Rev. Mod. Phys.* **4**, 87–132 (1932). doi:10.1103/RevModPhys.4.87. [cited on page 2].

[16] Bohr, N. The Quantum Postulate and the Recent Development of Atomic Theory. *Nature* **121**, 580–590 (1928). doi:10.1038/121580a0. [cited on pages 3 and 23].

[17] Einstein, A., Podolsky, B. & Rosen, N. Can Quantum-Mechanical Description of Physical Reality Be Considered Complete? *Phys. Rev.* **47**, 777–780 (1935). doi:10.1103/PhysRev.47.777. [cited on pages 3 and 22].

[18] Bell, J. S. *Speakable and Unspeakable in Quantum Mechanics* (Cambridge University Press, Cambridge, 2004). [cited on pages 3 and 23].

[19] Aspect, A., Grangier, P. & Roger, G. Experimental Tests of Realistic Local Theories via Bell's Theorem. *Phys. Rev. Lett.* **47**, 460–463 (1981). doi:10.1103/PhysRevLett.47.460. [cited on pages 3 and 131].

[20] Aspect, A., Dalibard, J. & Roger, G. Experimental Test of Bell's Inequalities Using Time- Varying Analyzers. *Phys. Rev. Lett.* **49**, 1804–1807 (1982). doi:10.1103/PhysRevLett.49.1804. [cited on pages 3, 23, and 96].

[21] Jacques, V. *et al.* Experimental Realization of Wheeler's Delayed-Choice Gedanken Experiment. *Science* **315**, 966–968 (2007). doi:10.1126/science.1136303. [cited on pages 4, 26, and 127].

[22] Scully, M. O., Englert, B.-G. & Walther, H. Quantum optical tests of complementarity. *Nature* **351**, 111–116 (1991). doi:10.1038/351111a0. [cited on page 4].

[23] Englert, B.-G. Fringe Visibility and Which-Way Information: An Inequality. *Phys. Rev. Lett.* **77**, 2154–2157 (1996). doi:10.1103/PhysRevLett.77.2154. [cited on page 4].

[24] Ionicioiu, R. & Terno, D. R. Proposal for a Quantum Delayed-Choice Experiment. *Phys. Rev. Lett.* **107**, 230406 (2011). doi:10.1103/PhysRevLett.107.230406. [cited on pages 4 and 26].

[25] Peruzzo, A., Shadbolt, P., Brunner, N., Popescu, S. & O'Brien, J. L. A Quantum Delayed-Choice Experiment. *Science* **338**, 634–637 (2012). doi:10.1126/science.1226719. [cited on pages 4 and 26].

[26] Kaiser, F., Coudreau, T., Milman, P., Ostrowsky, D. B. & Tanzilli, S. Entanglement-Enabled Delayed-Choice Experiment. *Science* **338**, 637–640 (2012). doi:10.1126/science.1226755. [cited on pages 4 and 26].

[27] Tang, J.-S. *et al.* Realization of quantum Wheeler's delayed-choice experiment. *Nature Photon.* 600–604 (2012). doi:10.1038/nphoton.2012.179. [cited on pages 4 and 26].

[28] Pauli, W. Über den Zusammenhang des Abschlusses der Elektronengruppen im Atom mit der Komplexstruktur der Spektren. *Zeitschrift für Physik* **31**, 765–783 (1925). doi:10.1007/BF02980631. [cited on page 4].

[29] Bose, S. N. Plancks Gesetz und Lichtquantenhypothese. *Zeitschrift für Physik* **26**, 178–181 (1924). doi:10.1007/BF01327326. [cited on pages 4 and 31].

[30] Einstein, A. Quantentheorie des einatomigen idealen Gases. *Sitz. Preuss. Akad. Wissen.* 261–267 (1924). doi:10.1002/3527608958.ch27. [cited on pages 4 and 31].

[31] Hanbury Brown, R. & Twiss, R. Q. A Test of a New Type of Stellar Interferometer on Sirius. *Nature* **178**, 1046–1048 (1956). doi:10.1038/1781046a0. [cited on pages 5 and 15].

[32] Glauber, R. J. The Quantum Theory of Optical Coherence. *Phys. Rev.* **130**, 2529–2539 (1963). doi:10.1103/PhysRev.130.2529. [cited on pages 5 and 16].

[33] Hong, C. K., Ou, Z. Y. & Mandel, L. Measurement of subpicosecond time intervals between two photons by interference. *Phys. Rev. Lett.* **59**, 2044–2046 (1987). doi:10.1103/PhysRevLett.59.2044. [cited on pages 5, 21, and 153].

[34] Naraschewski, M. & Glauber, R. J. Spatial coherence and density correlations of trapped Bose gases. *Phys. Rev. A* **59**, 4595–4607 (1999). doi:10.1103/PhysRevA.59.4595. [cited on pages 5, 20, 66, 80, 103, and 114].

[35] Meystre, P. *Atom Optics* (Springer, New York, 2001). [cited on page 6].

[36] Pitaevskii, L. & Stringari, S. *Bose-Einstein Condensation* (Oxford University Press, Oxford, 2003). [cited on pages 6, 30, and 32].

[37] Allen, J. F. & Misener, A. D. Flow of Liquid Helium II. *Nature* **141**, 75 (1938). doi:10.1038/141075a0. [cited on page 6].

[38] Kapitza, P. Viscosity of Liquid Helium below the λ-Point. *Nature* **141**, 74 (1938). doi:10.1038/141074a0. [cited on page 6].

[39] London, F. The λ-Phenomenon of Liquid Helium and the Bose-Einstein Degeneracy. *Nature* **141**, 643–644 (1938). doi:10.1038/141643a0. [cited on page 6].

[40] Bogoliubov, N. On the theory of superfluidity. *J. Phys. USSR* **11** (1947). [cited on page 6].

[41] Landau, L. & Lifshitz, E. *Statisticheskai Fizika* (Fizmatgiz, Moscow, 1951). [cited on page 6].

[42] Penrose, O. CXXXVI. On the quantum mechanics of helium II. *Philosophical Magazine Series 7* **42**, 1373–1377 (1951). doi:10.1080/14786445108560954. [cited on page 6].

[43] Penrose, O. & Onsager, L. Bose-Einstein Condensation and Liquid Helium. *Phys. Rev.* **104**, 576–584 (1956). doi:10.1103/PhysRev.104.576. [cited on page 6].

[44] Anderson, M. H., Ensher, J. R., Matthews, M. R., Wieman, C. E. & Cornell, E. A. Observation of Bose-Einstein Condensation in a Dilute Atomic Vapor. *Science* **269**, 198–201 (1995). doi:10.1126/science.269.5221.198. [cited on page 6].

[45] Davis, K. B. *et al.* Bose-Einstein Condensation in a Gas of Sodium Atoms. *Phys. Rev. Lett.* **75**, 3969–3973 (1995). doi:10.1103/PhysRevLett.75.3969. [cited on page 6].

[46] Bradley, C. C., Sackett, C. A., Tollett, J. J. & Hulet, R. G. Evidence of Bose-Einstein Condensation in an Atomic Gas with Attractive Interactions. *Phys. Rev. Lett.* **75**, 1687–1690 (1995). doi:10.1103/PhysRevLett.75.1687. [cited on page 6].

[47] Robert, A. *et al.* A Bose-Einstein Condensate of Metastable Atoms. *Science* **292**, 461–464 (2001). doi:10.1126/science.1060622. [cited on pages 6 and 39].

[48] Pereira Dos Santos, F. *et al.* Bose-Einstein Condensation of Metastable Helium. *Phys. Rev. Lett.* **86**, 3459–3462 (2001). doi:10.1103/PhysRevLett.86.3459. [cited on pages 6 and 39].

[49] Kasprzak, J. *et al.* Bose-Einstein condensation of exciton polaritons. *Nature* **443**, 409–414 (2006). doi:10.1038/nature05131. [cited on page 6].

[50] Plumhof, J. D., Stöferle, T., Mai, L., Scherf, U. & Mahrt, R. F. Room-temperature Bose–Einstein condensation of cavity exciton–polaritons in a polymer. *Nature Materials* (2013). doi:10.1038/nmat3825. [cited on page 6].

[51] Klaers, J., Schmitt, J., Vewinger, F. & Weitz, M. Bose-Einstein condensation of photons in an optical microcavity. *Nature* **468**, 545–548 (2010). doi:10.1038/nature09567. [cited on page 6].

[52] Deng, L. *et al.* Four-wave mixing with matter waves. *Nature* **398**, 218–220 (1999). doi:10.1038/18395. [cited on page 6].

[53] RuGway, W., Hodgman, S. S., Dall, R. G., Johnsson, M. T. & Truscott, A. G. Correlations in Amplified Four-Wave Mixing of Matter Waves. *Phys. Rev. Lett.* **107**, 075301 (2011). doi:10.1103/PhysRevLett.107.075301. [cited on pages 6 and 21].

[54] Yasuda, M. & Shimizu, F. Observation of Two-Atom Correlation of an Ultracold Neon Atomic Beam. *Phys. Rev. Lett.* **77**, 3090–3093 (1996). doi:10.1103/PhysRevLett.77.3090. [cited on pages 7, 21, 72, and 139].

[55] Schellekens, M. *et al.* Hanbury Brown Twiss Effect for Ultracold Quantum Gases. *Science* **310**, 648–651 (2005). doi:10.1126/science.1118024. [cited on pages 7, 21, 73, 75, and 78].

[56] Jeltes, T. *et al.* Comparison of the Hanbury Brown-Twiss effect for bosons and fermions. *Nature* **445**, 402–405 (2007). doi:10.1038/nature05513. [cited on pages 7, 21, 73, and 78].

[57] Greiner, M., Mandel, O., Esslinger, T., Hänsch, T. & Bloch, I. Quantum phase transition from a superfluid to a Mott insulator in a gas of ultracold atoms. *Nature* 39–44 (2002). doi:10.1038/415039a. [cited on pages 7 and 131].

[58] Braun, S. *et al.* Negative absolute temperature for motional degrees of freedom. *Science* **339**, 52–55 (2013). doi:10.1126/science.1227831. [cited on page 7].

[59] Manning, A. G., Hodgman, S. S., Dall, R. G., Johnsson, M. T. & Truscott, A. G. The Hanbury Brown-Twiss effect in a pulsed atom laser. *Opt. Express* **18**, 18712–18719 (2010). doi:10.1364/OE.18.018712. [cited on pages 8 and 78].

[60] Hodgman, S. S., Dall, R. G., Manning, A. G., Baldwin, K. G. H. & Truscott, A. G. Direct Measurement of Long-Range Third-Order Coherence in Bose-Einstein Condensates. *Science* **331**, 1046–1049 (2011). doi:10.1126/science.1198481. [cited on page 9].

[61] Dall, R. G., Hodgman, S. S., Manning, A. G. & Truscott, A. G. Observation of the first excited transverse mode in guided matter waves. *Opt. Lett.* **36**, 1131–1133 (2011). doi:10.1364/OL.36.001131. [cited on page 9].

[62] Dall, R. G. *et al.* Observation of atomic speckle and Hanbury Brown–Twiss correlations in guided matter waves. *Nat. Commun.* **2**, 291 (2011). doi:10.1038/ncomms1292. [cited on page 9].

[63] Manning, A. G. *et al.* Third-order spatial correlations for ultracold atoms. *New J. Phys.* **15**, 013042 (2013). doi:10.1088/1367-2630/15/1/013042. [cited on page 9].

[64] Dall, R. G. *et al.* Ideal n-body correlations with massive particles. *Nature Phys.* **9**, 341–344 (2013). doi:10.1038/nphys2632. [cited on page 9].

[65] RuGway, W. *et al.* Observation of Transverse Bose-Einstein Condensation via Hanbury Brown-Twiss Correlations. *Phys. Rev. Lett.* **111**, 093601 (2013). doi:10.1103/PhysRevLett.111.093601. [cited on page 9].

[66] Manning, A. G., Khakimov, R., Dall, R. G. & Truscott, A. G. Single-Atom Source in the Picokelvin Regime. *Phys. Rev. Lett.* **113**, 130403 (2014). doi:10.1103/PhysRevLett.113.130403. [cited on pages 9 and 135].

[67] Michelson, A. A. & Morley, E. W. On the Relative Motion of the Earth and the Luminiferous Ether. *AJS* **34**, 333–345 (1887). [cited on page 12].

[68] Scully, M. O. & Zubairy, M. S. *Quantum Optics* (Cambridge University Press, Cambridge, 1997). [cited on pages 13 and 14].

[69] Hanbury Brown, R. & Twiss, R. Q. Correlation between Photons in two Coherent Beams of Light. *Nature* **177**, 27–29 (1956). doi:10.1038/177027a0. [cited on page 15].

[70] Hanbury Brown, R. *The Intensity Interferometer: its Application to Astronomy* (Taylor & Francis Ltd, London, 1974). [cited on page 15].

[71] Dirac, P. A. M. *The principles of quantum mechanics* (Oxford University Press, Oxford, 1930). [cited on page 15].

[72] Brannen, E. & Ferguson, H. I. S. The Question of Correlation between Photons in Coherent Light Rays. *Nature* **178**, 481–482 (1956). doi:10.1038/178481a0. [cited on page 15].

[73] Purcell, E. M. The Question of Correlation between Photons in Coherent Light Rays. *Nature* **178**, 1449–1450 (1956). doi:10.1038/1781449a0. [cited on page 15].

[74] Maygar, G. & Mandel, L. Interference Fringes Produced by Superposition of Two Independent Maser Light Beams. *Nature* **198**, 255–256 (1963). doi:10.1038/198255a0. [cited on page 15].

[75] Pfleegor, R. L. & Mandel, L. Interference of Independent Photon Beams. *Phys. Rev.* **159**, 1084–1088 (1967). doi:10.1103/PhysRev.159.1084. [cited on page 15].

[76] Fano, U. Quantum Theory of Interference Effects in the Mixing of Light from Phase-Independent Sources. *Am. J. Phys.* **29**, 539–545 (1961). doi:10.1119/1.1937827. [cited on page 15].

[77] Wick, G. C. The Evaluation of the Collision Matrix. *Phys. Rev.* **80**, 268–272 (1950). doi:10.1103/PhysRev.80.268. [cited on pages 19 and 157].

[78] Carmichael, H. J. & Walls, D. F. A quantum-mechanical master equation treatment of the dynamical Stark effect. *J. Phys. B* **9**, 1199 (1976). doi:10.1088/0022-3700/9/8/007. [cited on page 21].

[79] Kimble, H. J., Dagenais, M. & Mandel, L. Photon Antibunching in Resonance Fluorescence. *Phys. Rev. Lett.* **39**, 691–695 (1977). doi:10.1103/PhysRevLett.39.691. [cited on pages 21 and 130].

[80] U'Ren, A. B., Silberhorn, C., Ball, J. L., Banaszek, K. & Walmsley, I. A. Characterization of the nonclassical nature of conditionally prepared single photons. *Phys. Rev. A* **72**, 021802 (2005). doi:10.1103/PhysRevA.72.021802. [cited on page 21].

[81] Ivanova, O. A., Iskhakov, T. S., Penin, A. N. & Chekhova, M. V. Multiphoton correlations in parametric down-conversion and their measurement in the pulsed regime. *Quantum Electronics* **36**, 951 (2006). doi:10.1070/QE2006v036n10ABEH013300. [cited on page 21].

[82] Fearn, H. & Loudon, R. Quantum theory of the lossless beam splitter. *Opt. Commun.* **64**, 485–490 (1987). doi:10.1016/0030-4018(87)90275-6. [cited on page 21].

[83] Rarity, J. G. & Tapster, P. R. Experimental violation of Bell's inequality based on phase and momentum. *Phys. Rev. Lett.* **64**, 2495–2498 (1990). doi:10.1103/PhysRevLett.64.2495. [cited on pages 21, 96, and 153].

[84] Chan, K. W. C., O'Sullivan, M. N. & Boyd, R. W. High-order thermal ghost imaging. *Opt. Lett.* **34**, 3343–3345 (2009). doi:10.1364/OL.34.003343. [cited on pages 21 and 154].

[85] Zhou, Y., Simon, J., Liu, J. & Shih, Y. Third-order correlation function and ghost imaging of chaotic thermal light in the photon counting regime. *Phys. Rev. A* **81**, 043831 (2010). doi:10.1103/PhysRevA.81.043831. [cited on pages 21 and 85].

[86] Baym, G. The Physics of Hanbury Brown–Twiss Intensity Interferometry: from Stars to Nuclear Collisions. *Acta Physica Polonica B* **29**, 1839 (1998). `http://arxiv.org/abs/nucl-th/9804026`. [cited on page 21].

[87] Kiesel, H., Renz, A. & Hasselbach, F. Observation of Hanbury Brown-Twiss anticorrelations for free electrons. *Nature* **418**, 392–394 (2002). doi:10.1038/nature00911. [cited on page 21].

[88] Iannuzzi, M., Orecchini, A., Sacchetti, F., Facchi, P. & Pascazio, S. Direct Experimental Evidence of Free-Fermion Antibunching. *Phys. Rev. Lett.* **96**, 080402 (2006). doi:10.1103/PhysRevLett.96.080402. [cited on page 21].

[89] Rom, T. *et al.* Free fermion antibunching in a degenerate atomic Fermi gas released from an optical lattice. *Nature* **444**, 733–736 (2006). doi:10.1038/nature05319. [cited on pages 21 and 74].

[90] Greiner, M., Regal, C. A., Stewart, J. T. & Jin, D. S. Probing Pair-Correlated Fermionic Atoms through Correlations in Atom Shot Noise. *Phys. Rev. Lett.* **94**, 110401 (2005). doi:10.1103/PhysRevLett.94.110401. [cited on pages 21 and 74].

[91] Perrin, A. *et al.* Observation of Atom Pairs in Spontaneous Four-Wave Mixing of Two Colliding Bose-Einstein Condensates. *Phys. Rev. Lett.* **99**, 150405 (2007). doi:10.1103/PhysRevLett.99.150405. [cited on page 21].

[92] Kheruntsyan, K. V. *et al.* Violation of the Cauchy-Schwarz Inequality with Matter Waves. *Phys. Rev. Lett.* **108**, 260401 (2012). doi:10.1103/PhysRevLett.108.260401. [cited on pages 21 and 139].

[93] Korbicz, J. K., Cirac, J. I. & Lewenstein, M. Spin Squeezing Inequalities and Entanglement of N Qubit States. *Phys. Rev. Lett.* **95**, 120502 (2005). doi:10.1103/PhysRevLett.95.120502. [cited on page 21].

[94] Korbicz, J. K. *et al.* Generalized spin-squeezing inequalities in N-qubit systems: Theory and experiment. *Phys. Rev. A* **74**, 052319 (2006). doi:10.1103/PhysRevA.74.052319. [cited on page 21].

[95] Trotzky, S., Chen, Y.-A., Schnorrberger, U., Cheinet, P. & Bloch, I. Controlling and Detecting Spin Correlations of Ultracold Atoms in Optical Lattices. *Phys. Rev. Lett.* **105**, 265303 (2010). doi:10.1103/PhysRevLett.105.265303. [cited on page 21].

[96] Eckert, K., Zawitkowski, L., Sanpera, A., Lewenstein, M. & Polzik, E. S. Quantum Polarization Spectroscopy of Ultracold Spinor Gases. *Phys. Rev. Lett.* **98**, 100404 (2007). doi:10.1103/PhysRevLett.98.100404. [cited on page 21].

[97] Eckert, K. *et al.* Quantum non-demolition detection of strongly correlated systems. *Nature Phys.* **4**, 50–54 (2008). doi:10.1038/nphys776. [cited on page 21].

[98] Horikiri, T. *et al.* Higher order coherence of exciton-polariton condensates. *Phys. Rev. B* **81**, 033307 (2010). doi:10.1103/PhysRevB.81.033307. [cited on page 22].

[99] Aßmann, M., Veit, F., Bayer, M., van der Poel, M. & Hvam, J. M. Higher-Order Photon Bunching in a Semiconductor Microcavity. *Science* **325**, 297–300 (2009). doi:10.1126/science.1174488. [cited on page 22].

[100] Stevens, M. J. *et al.* High-order temporal coherences of chaotic and laser light. *Opt. Express* **18**, 1430–1437 (2010). doi:10.1364/OE.18.001430. [cited on page 22].

[101] Avenhaus, M., Laiho, K., Chekhova, M. V. & Silberhorn, C. Accessing Higher Order Correlations in Quantum Optical States by Time Multiplexing. *Phys. Rev. Lett.* **104**, 063602 (2010). doi:10.1103/PhysRevLett.104.063602. [cited on page 22].

[102] Kraemer, T. *et al.* Evidence for Efimov quantum states in an ultracold gas of caesium atoms. *Nature* **440**, 315–318 (2006). doi:10.1038/nature04626. [cited on pages 22 and 85].

[103] Giraud, A. & Serreau, J. Decoherence and Thermalization of a Pure Quantum State in Quantum Field Theory. *Phys. Rev. Lett.* **104**, 230405 (2010). doi:10.1103/PhysRevLett.104.230405. [cited on page 22].

[104] Schilling, U., von Zanthier, J. & Agarwal, G. S. Measuring arbitrary-order coherences: Tomography of single-mode multiphoton polarization-entangled states. *Phys. Rev. A* **81**, 013826 (2010). doi:10.1103/PhysRevA.81.013826. [cited on pages 22, 96, and 115].

[105] Bohr, N. Can Quantum-Mechanical Description of Physical Reality be Considered Complete? *Phys. Rev.* **48**, 696–702 (1935). doi:10.1103/PhysRev.48.696. [cited on page 23].

[106] Saunders, S. Complementarity and Scientific Rationality. *Foundations of Physics* **35**, 417–447 (2005). doi:10.1007/s10701-004-1982-x. [cited on page 23].

[107] Zeilinger, A., Weihs, G., Jennewein, T. & Aspelmeyer, M. Happy centenary, photon. *Nature* **433**, 230–238 (2005). doi:10.1038/nature03280. [cited on page 23].

[108] Wheeler, J. A. *Mathematical Foundations of Quantum Theory*, 9–48 (Academic Press, New York, 1978). [cited on pages 23, 25, and 127].

[109] Bohr, N. *The Philosophical Writings of Niels Bohr, Vol. 2* (Ox Bow Press, Woodbridge, 1949). [cited on page 23].

[110] Wheeler, J. A. *Quantum Theory and Measurement*, 182–213 (Princeton University Press, Princeton, 1983). [cited on page 25].

[111] Grangier, P., Roger, G. & Aspect, A. Experimental Evidence for a Photon Anticorrelation Effect on a Beam Splitter: A New Light on Single-Photon Interferences. *Europhys. Lett.* **1**, 173 (1986). doi:10.1209/0295-5075/1/4/004. [cited on pages 25 and 131].

[112] Alley, C. O., Jacubowicz, O. G. & Wickes, W. C. *Proceedings of the Second International Symposium on the Foundations of Quantum Mechanics* 36–47 (1987). [cited on page 25].

[113] Hellmuth, T., Walther, H., Zajonc, A. & Schleich, W. Delayed-choice experiments in quantum interference. *Phys. Rev. A* **35**, 2532–2541 (1987). doi:10.1103/PhysRevA.35.2532. [cited on page 25].

[114] Baldzuhn, J., Mohler, E. & Martienssen, W. A wave-particle delayed-choice experiment with a single-photon state. *Zeitschrift für Physik B Condensed Matter* **77**, 347–352 (1989). doi:10.1007/BF01313681. [cited on page 25].

[115] Lawson-Daku, B. J. *et al.* Delayed choices in atom Stern-Gerlach interferometry. *Phys. Rev. A* **54**, 5042–5047 (1996). doi:10.1103/PhysRevA.54.5042. [cited on page 25].

[116] Kawai, T. *et al.* Realization of a delayed choice experiment using a multilayer cold neutron pulser. *Nuclear Instruments and Methods in Physics Research Section A: Accelerators, Spectrometers, Detectors and Associated Equipment* **410**, 259–263 (1998). doi:10.1016/S0168-9002(98)00263-0. [cited on page 25].

[117] Scully, M. O. & Drühl, K. Quantum eraser: A proposed photon correlation experiment concerning observation and "delayed choice" in quantum mechanics. *Phys. Rev. A* **25**, 2208–2213 (1982). doi:10.1103/PhysRevA.25.2208. [cited on page 26].

[118] Kim, Y.-H., Yu, R., Kulik, S. P., Shih, Y. & Scully, M. O. Delayed "Choice" Quantum Eraser. *Phys. Rev. Lett.* **84**, 1–5 (2000). doi:10.1103/PhysRevLett.84.1. [cited on page 26].

[119] Metcalf, H. J. & van der Straten, P. *Laser Cooling and Trapping* (Springer, New York, 1999). [cited on pages 26, 39, and 142].

[120] Foot, C. J. *Atomic Physics* (Oxford University Press, Oxford, 2005). [cited on pages 26, 49, 136, and 137].

[121] Helmerson, K. & Phillips, W. D. Cooling, Trapping and Manipulation of Neutral Atoms and Bose-Einstein Condensates by Electromagnetic Fields. *Modern Physics Letters B* **14**, 231–280 (2000). doi:10.1142/S0217984900001567. [cited on page 26].

[122] Prodan, J. V., Phillips, W. D. & Metcalf, H. Laser Production of a Very Slow Monoenergetic Atomic Beam. *Phys. Rev. Lett.* **49**, 1149–1153 (1982). doi:10.1103/PhysRevLett.49.1149. [cited on page 27].

[123] Raab, E. L., Prentiss, M., Cable, A., Chu, S. & Pritchard, D. E. Trapping of Neutral Sodium Atoms with Radiation Pressure. *Phys. Rev. Lett.* **59**, 2631–2634 (1987). doi:10.1103/PhysRevLett.59.2631. [cited on page 28].

[124] Migdall, A. L., Prodan, J. V., Phillips, W. D., Bergeman, T. H. & Metcalf, H. J. First Observation of Magnetically Trapped Neutral Atoms. *Phys. Rev. Lett.* **54**, 2596–2599 (1985). doi:10.1103/PhysRevLett.54.2596. [cited on page 29].

[125] Chu, S., Bjorkholm, J. E., Ashkin, A. & Cable, A. Experimental Observation of Optically Trapped Atoms. *Phys. Rev. Lett.* **57**, 314–317 (1986). doi:10.1103/PhysRevLett.57.314. [cited on page 30].

[126] Ketterle, W., Durfee, D. S. & Stamper-Kurn, D. M. Making, probing and understanding Bose-Einstein condensates. *ArXiv e-prints* (1999). `http://arxiv.org/abs/cond-mat/9904034v2`. [cited on pages 30, 32, and 55].

[127] Pethick, C. J. & Smith, H. *Bose-Einstein Condensation in Dilute Gases* (Cambridge University Press, Cambridge, 2002). [cited on pages 30 and 34].

[128] Castin, Y. & Dum, R. Bose-Einstein Condensates in Time Dependent Traps. *Phys. Rev. Lett.* **77**, 5315–5319 (1996). doi:10.1103/PhysRevLett.77.5315. [cited on page 33].

[129] Schroeder, D. V. *An Introduction to Thermal Physics* (Addison Wesley, San Francisco, 2000). [cited on page 33].

[130] Mermin, N. D. & Wagner, H. Absence of Ferromagnetism or Antiferromagnetism in One- or Two-Dimensional Isotropic Heisenberg Models. *Phys. Rev. Lett.* **17**, 1133–1136 (1966). doi:10.1103/PhysRevLett.17.1133. [cited on pages 34 and 35].

[131] Hohenberg, P. C. Existence of Long-Range Order in One and Two Dimensions. *Phys. Rev.* **158**, 383–386 (1967). doi:10.1103/PhysRev.158.383. [cited on pages 34 and 35].

[132] Donner, U. T. *Critical Behavior of a Trapped Interacting Bose Gas*. Ph.D. thesis, ETH Zürich (2008). [cited on pages 34 and 155].

[133] Ketterle, W. & van Druten, N. J. Bose-Einstein condensation of a finite number of particles trapped in one or three dimensions. *Phys. Rev. A* **54**, 656–660 (1996). doi:10.1103/PhysRevA.54.656. [cited on pages 34, 35, and 110].

[134] Mullin, W. Bose-Einstein condensation in a harmonic potential. *Journal of Low Temperature Physics* **106**, 615–641 (1997). doi:10.1007/BF02395928. [cited on page 34].

[135] Donner, T. *et al.* Critical Behavior of a Trapped Interacting Bose Gas. *Science* **315**, 1556–1558 (2007). doi:10.1126/science.1138807. [cited on page 35].

[136] Hadzibabic, Z., Krüger, P., Cheneau, M., Battelier, B. & Dalibard, J. Berezinskii-Kosterlitz-Thouless crossover in a trapped atomic gas. *Nature* **441**, 1118–1121 (2006). doi:10.1038/nature04851. [cited on pages 35, 102, and 154].

[137] Cladé, P., Ryu, C., Ramanathan, A., Helmerson, K. & Phillips, W. D. Observation of a 2D Bose Gas: From Thermal to Quasicondensate to Superfluid. *Phys. Rev. Lett.* **102**, 170401 (2009). doi:10.1103/PhysRevLett.102.170401. [cited on pages 35, 102, and 154].

[138] Schweikhard, V., Tung, S. & Cornell, E. A. Vortex Proliferation in the Berezinskii-Kosterlitz-Thouless Regime on a Two-Dimensional Lattice of Bose-Einstein Condensates. *Phys. Rev. Lett.* **99**, 030401 (2007). doi:10.1103/PhysRevLett.99.030401. [cited on pages 35 and 154].

[139] Imambekov, A., Schmidt, T. L. & Glazman, L. I. One-dimensional quantum liquids: Beyond the Luttinger liquid paradigm. *Rev. Mod. Phys.* **84**, 1253–1306 (2012). doi:10.1103/RevModPhys.84.1253. [cited on page 35].

[140] Girardeau, M. Relationship between Systems of Impenetrable Bosons and Fermions in One Dimension. *Journal of Mathematical Physics* **1**, 516–523 (1960). doi:10.1063/1.1703687. [cited on page 35].

[141] Girardeau, M. D. Permutation Symmetry of Many-Particle Wave Functions. *Phys. Rev.* **139**, B500–B508 (1965). doi:10.1103/PhysRev.139.B500. [cited on page 35].

[142] Gangardt, D. M. & Shlyapnikov, G. V. Stability and Phase Coherence of Trapped 1D Bose Gases. *Phys. Rev. Lett.* **90**, 010401 (2003). doi:10.1103/PhysRevLett.90.010401. [cited on page 35].

[143] Kinoshita, T., Wenger, T. & Weiss, D. S. Local Pair Correlations in One-Dimensional Bose Gases. *Phys. Rev. Lett.* **95**, 190406 (2005). doi:10.1103/PhysRevLett.95.190406. [cited on pages 35 and 102].

[144] Kormos, M., Chou, Y.-Z. & Imambekov, A. Exact Three-Body Local Correlations for Excited States of the 1D Bose Gas. *Phys. Rev. Lett.* **107**, 230405 (2011). doi:10.1103/PhysRevLett.107.230405. [cited on page 35].

[145] Kheruntsyan, K. V., Gangardt, D. M., Drummond, P. D. & Shlyapnikov, G. V. Pair Correlations in a Finite-Temperature 1D Bose Gas. *Phys. Rev. Lett.* **91**, 040403 (2003). doi:10.1103/PhysRevLett.91.040403. [cited on pages 35, 36, and 102].

[146] Bouchoule, I., Arzamasovs, M., Kheruntsyan, K. V. & Gangardt, D. M. Two-body momentum correlations in a weakly interacting one-dimensional Bose gas. *Phys. Rev. A* **86**, 033626 (2012). doi:10.1103/PhysRevA.86.033626. [cited on pages 35, 36, 96, 102, and 109].

[147] Deuar, P. P. *First-principles Quantum Simulations of Many-mode Open Interacting Bose Gases Using Stochastic Gauge Methods*. Ph.D. thesis, University of Queensland (2004). [cited on page 35].

[148] van Amerongen, A. H. *One-dimensional Bose gas on an atom chip*. Ph.D. thesis, University of Amsterdam (2008). [cited on page 36].

[149] Deuar, P. *et al.* Nonlocal pair correlations in the one-dimensional Bose gas at finite temperature. *Phys. Rev. A* **79**, 043619 (2009). doi:10.1103/PhysRevA.79.043619. [cited on pages 36 and 96].

[150] Kheruntsyan, K. V., Gangardt, D. M., Drummond, P. D. & Shlyapnikov, G. V. Finite-temperature correlations and density profiles of an inhomogeneous interacting one-dimensional Bose gas. *Phys. Rev. A* **71**, 053615 (2005). doi:10.1103/PhysRevA.71.053615. [cited on pages 36 and 96].

[151] van Druten, N. J. & Ketterle, W. Two-Step Condensation of the Ideal Bose Gas in Highly Anisotropic Traps. *Phys. Rev. Lett.* **79**, 549–552 (1997). doi:10.1103/PhysRevLett.79.549. [cited on pages 37, 90, 93, and 102].

[152] Vassen, W. *et al.* Cold and trapped metastable noble gases. *Rev. Mod. Phys.* **84**, 175–210 (2012). doi:10.1103/RevModPhys.84.175. [cited on pages 38, 44, 55, 57, 72, 139, and 142].

[153] Hodgman, S. S. *et al.* Metastable Helium: A New Determination of the Longest Atomic Excited-State Lifetime. *Phys. Rev. Lett.* **103**, 053002 (2009). doi:10.1103/PhysRevLett.103.053002. [cited on pages 39 and 132].

[154] Jeltes, T. *Bose-Einstein Condensation of Metastable Helium Atoms*. Ph.D. thesis, Vrije Universiteit (2008). [cited on page 40].

[155] Dall, R. & Truscott, A. Bose–Einstein condensation of metastable helium in a bi-planar quadrupole Ioffe configuration trap. *Opt. Commun.* **270**, 255–261 (2007). doi:10.1016/j.optcom.2006.09.031. [cited on pages 40, 43, 46, and 75].

[156] Doret, S. C., Connolly, C. B., Ketterle, W. & Doyle, J. M. Buffer-Gas Cooled Bose-Einstein Condensate. *Phys. Rev. Lett.* **103**, 103005 (2009). doi:10.1103/PhysRevLett.103.103005. [cited on page 40].

[157] Ebner, M. *Development of a metastable helium BEC as a platform for experiments with EPR-entangled matter waves*. Ph.D. thesis, Universität Wien (2012). [cited on page 40].

[158] Kaufman, V. & Minnhagen, L. Accurate ground-term combinations in ne i. *J. Opt. Soc. Am.* **62**, 92–95 (1972). doi:10.1364/JOSA.62.000092. [cited on page 40].

[159] Dall, R. G. *Optical guiding with bright sources of cold 2^3S_1 metastable helium*. Ph.D. thesis, Australian National University (2004). [cited on page 40].

[160] Browaeys, A. *et al.* Two body loss rate in a magneto-optical trap of metastable He. *The European Physical Journal D* **8**, 199–203 (2000). doi:10.1007/s100530050027. [cited on page 40].

[161] Julienne, P. S. & Mies, F. H. Collisions of ultracold trapped atoms. *J. Opt. Soc. Am. B* **6**, 2257–2269 (1989). doi:10.1364/JOSAB.6.002257. [cited on page 40].

[162] Fedichev, P. O., Reynolds, M. W., Rahmanov, U. M. & Shlyapnikov, G. V. Inelastic decay processes in a gas of spin-polarized triplet helium. *Phys. Rev. A* **53**, 1447–1453 (1996). doi:10.1103/PhysRevA.53.1447. [cited on page 40].

[163] Venturi, V., Whittingham, I. B., Leo, P. J. & Peach, G. Close-coupled calculation of collisions of magnetostatically trapped metastable helium atoms. *Phys. Rev. A* **60**, 4635–4646 (1999). doi:10.1103/PhysRevA.60.4635. [cited on pages 40, 41, and 132].

[164] Shlyapnikov, G. V., Walraven, J. T. M., Rahmanov, U. M. & Reynolds, M. W. Decay Kinetics and Bose Condensation in a Gas of Spin-Polarized Triplet Helium. *Phys. Rev. Lett.* **73**, 3247–3250 (1994). doi:10.1103/PhysRevLett.73.3247. [cited on pages 40, 41, and 132].

[165] Partridge, G. B., Jaskula, J.-C., Bonneau, M., Boiron, D. & Westbrook, C. I. Bose-Einstein condensation and spin mixtures of optically trapped metastable helium. *Phys. Rev. A* **81**, 053631 (2010). doi:10.1103/PhysRevA.81.053631. [cited on pages 41, 132, and 134].

[166] Venturi, V. & Whittingham, I. B. Close-coupled calculation of field-free collisions of cold metastable helium atoms. *Phys. Rev. A* **61**, 060703 (2000). doi:10.1103/PhysRevA.61.060703. [cited on pages 41 and 132].

[167] Fedichev, P. O., Reynolds, M. W. & Shlyapnikov, G. V. Three-Body Recombination of Ultracold Atoms to a Weakly Bound *s* Level. *Phys. Rev. Lett.* **77**, 2921–2924 (1996). doi:10.1103/PhysRevLett.77.2921. [cited on page 41].

[168] Bedaque, P. F., Braaten, E. & Hammer, H.-W. Three-body Recombination in Bose Gases with Large Scattering Length. *Phys. Rev. Lett.* **85**, 908–911 (2000). doi:10.1103/PhysRevLett.85.908. [cited on page 41].

[169] Sirjean, O. *et al.* Ionization Rates in a Bose-Einstein Condensate of Metastable Helium. *Phys. Rev. Lett.* **89**, 220406 (2002). doi:10.1103/PhysRevLett.89.220406. [cited on page 41].

[170] Jagutzki, O. *et al.* Fast position and time-resolved read-out of micro-channelplates with the delay-line technique for single-particle and photon-detection. In Descour, M. R. & Shen, S. S. (eds.) *Society of Photo-Optical Instrumentation Engineers (SPIE) Conference Series*, vol. 3438 of *Society of Photo-Optical Instrumentation Engineers (SPIE) Conference Series*, 322–333 (1998). doi:10.1117/12.328113. [cited on pages 41 and 61].

[171] Swansson, J., Baldwin, K., Hoogerland, M., Truscott, A. & Buckman, S. A high flux, liquid-helium cooled source of metastable rare gas atoms. *Applied Physics B* **79**, 485–489 (2004). doi:10.1007/s00340-004-1600-9. [cited on page 45].

[172] Swansson, J. A., Dall, R. G. & Truscott, A. Efficient loading of a He* magneto-optic trap using a liquid He cooled source. *Review of Scientific Instruments* **77**, 046103–046103–4 (2006). doi:10.1063/1.2190307. [cited on page 45].

[173] Dedman, C. J. *et al.* Optimum design and construction of a Zeeman slower for use with a magneto-optic trap. *Review of Scientific Instruments* **75**, 5136–5142 (2004). doi:10.1063/1.1820524. [cited on page 45].

[174] Lu, Z. T. *et al.* Low-Velocity Intense Source of Atoms from a Magneto-optical Trap. *Phys. Rev. Lett.* **77**, 3331–3334 (1996). doi:10.1103/PhysRevLett.77.3331. [cited on page 45].

[175] Dedman, C. J., Dall, R. G., Byron, L. J. & Truscott, A. G. Active cancellation of stray magnetic fields in a Bose-Einstein condensation experiment. *Review of Scientific Instruments* **78**, 024703 (2007). doi:10.1063/1.2472600. [cited on page 47].

[176] Grimm, R., Weidemüller, M. & Ovchinnikov, Y. B. Optical dipole traps for neutral atoms. *Advances In Atomic, Molecular, and Optical Physics* **42**, 95–170 (2000). doi:10.1016/S1049-250X(08)60186-X. [cited on pages 49 and 132].

[177] Stamper-Kurn, D. M. *et al.* Optical Confinement of a Bose-Einstein Condensate. *Phys. Rev. Lett.* **80**, 2027–2030 (1998). doi:10.1103/PhysRevLett.80.2027. [cited on page 52].

[178] Garrett, M. C. *et al.* Growth dynamics of a Bose-Einstein condensate in a dimple trap without cooling. *Phys. Rev. A* **83**, 013630 (2011). doi:10.1103/PhysRevA.83.013630. [cited on page 52].

[179] Robins, N., Altin, P., Debs, J. & Close, J. Atom lasers: Production, properties and prospects for precision inertial measurement. *Physics Reports* **529**, 265–296 (2013). doi:10.1016/j.physrep.2013.03.006. [cited on pages 52, 116, and 117].

[180] Dall, R. G. *et al.* Observation of transverse interference fringes on an atom laser beam. *Opt. Express* **15**, 17673–17680 (2007). doi:10.1364/OE.15.017673. [cited on pages 54, 78, and 116].

[181] Münstermann, P., Fischer, T., Pinkse, P. & Rempe, G. Single slow atoms from an atomic fountain observed in a high-finesse optical cavity. *Opt. Commun.* **159**, 63–67 (1999). doi:10.1016/S0030-4018(98)00596-3. [cited on pages 55 and 131].

[182] Öttl, A., Ritter, S., Köhl, M. & Esslinger, T. Correlations and Counting Statistics of an Atom Laser. *Phys. Rev. Lett.* **95**, 090404 (2005). doi:10.1103/PhysRevLett.95.090404. [cited on pages 55, 73, and 78].

[183] Bücker, R. *et al.* Single-particle-sensitive imaging of freely propagating ultracold atoms. *New J. Phys.* **11**, 103039 (2009). doi:10.1088/1367-2630/11/10/103039. [cited on page 55].

[184] Hoendervanger, A. L. *et al.* Influence of gold coating and interplate voltage on the performance of chevron micro-channel plates for temporally and spatially resolved single particle detection. *Review of Scientific Instruments* **84**, 023307 (2013). doi:10.1063/1.4793402. [cited on page 57].

[185] Jaskula, J.-C. *et al.* Sub-Poissonian Number Differences in Four-Wave Mixing of Matter Waves. *Phys. Rev. Lett.* **105**, 190402 (2010). doi:10.1103/PhysRevLett.105.190402. [cited on pages 62, 71, and 139].

[186] Gomes, J. V. *et al.* Theory for a Hanbury Brown Twiss experiment with a ballistically expanding cloud of cold atoms. *Phys. Rev. A* **74**, 053607 (2006). doi:10.1103/PhysRevA.74.053607. [cited on pages 66, 78, 103, 159, 160, and 161].

[187] Andrews, M. R. *et al.* Observation of Interference Between Two Bose Condensates. *Science* **275**, 637–641 (1997). doi:10.1126/science.275.5300.637. [cited on pages 72 and 112].

[188] Stenger, J. *et al.* Bragg Spectroscopy of a Bose-Einstein Condensate. *Phys. Rev. Lett.* **82**, 4569–4573 (1999). doi:10.1103/PhysRevLett.82.4569. [cited on page 72].

[189] Hagley, E. W. *et al.* Measurement of the Coherence of a Bose-Einstein Condensate. *Phys. Rev. Lett.* **83**, 3112–3115 (1999). doi:10.1103/PhysRevLett.83.3112. [cited on page 72].

[190] Dall, R. G., Hodgman, S. S., Johnsson, M. T., Baldwin, K. G. H. & Truscott, A. G. Transverse mode imaging of guided matter waves. *Phys. Rev. A* **81**, 011602 (2010). doi:10.1103/PhysRevA.81.011602. [cited on pages 72, 112, 115, 116, 117, and 122].

[191] Hellweg, D. *et al.* Measurement of the Spatial Correlation Function of Phase Fluctuating Bose-Einstein Condensates. *Phys. Rev. Lett.* **91**, 010406 (2003). doi:10.1103/PhysRevLett.91.010406. [cited on page 73].

[192] Fölling, S. *et al.* Spatial quantum noise interferometry in expanding ultracold atom clouds. *Nature* 481–484 (2005). doi:10.1038/nature03500. [cited on page 74].

[193] Bloch, I., Hänsch, T. W. & Esslinger, T. Measurement of the spatial coherence of a trapped Bose gas at the phase transition. *Nature* 166–170 (2000). doi:10.1038/35003132. [cited on page 74].

[194] Perrin, A. *et al.* Hanbury Brown and Twiss correlations across the Bose-Einstein condensation threshold. *Nature Phys.* **8**, 195–198 (2012). doi:10.1038/nphys2212. [cited on page 74].

[195] Schellekens, M. *L'Effet Hanbury Brown et Twiss pour les Atomes Froids*. Ph.D. thesis, Université Paris XI (2007). [cited on page 77].

[196] Yavin, I., Weel, M., Andreyuk, A. & Kumarakrishnan, A. A calculation of the time-of-flight distribution of trapped atoms. *Am. J. Phys.* **70**, 149–152 (2002). doi:10.1119/1.1424266. [cited on page 78].

[197] Mewes, M.-O. *et al.* Output Coupler for Bose-Einstein Condensed Atoms. *Phys. Rev. Lett.* **78**, 582–585 (1997). doi:10.1103/PhysRevLett.78.582. [cited on page 78].

[198] Burt, E. A. *et al.* Coherence, Correlations, and Collisions: What One Learns about Bose-Einstein Condensates from Their Decay. *Phys. Rev. Lett.* **79**, 337–340 (1997). doi:10.1103/PhysRevLett.79.337. [cited on pages 80, 85, and 101].

[199] Tolra, B. L. *et al.* Observation of Reduced Three-Body Recombination in a Correlated 1D Degenerate Bose Gas. *Phys. Rev. Lett.* **92**, 190401 (2004). doi:10.1103/PhysRevLett.92.190401. [cited on pages 80, 85, and 102].

[200] Zień, P., Trippenbach, M. & Gajda, M. Pair-correlation function of a metastable helium Bose-Einstein condensate. *Phys. Rev. A* **69**, 023614 (2004). doi:10.1103/PhysRevA.69.023614. [cited on page 80].

[201] Moal, S. *et al.* Accurate Determination of the Scattering Length of Metastable Helium Atoms Using Dark Resonances between Atoms and Exotic Molecules. *Phys. Rev. Lett.* **96**, 023203 (2006). doi:10.1103/PhysRevLett.96.023203. [cited on pages 80 and 104].

[202] Manz, S. *et al.* Two-point density correlations of quasicondensates in free expansion. *Phys. Rev. A* **81**, 031610 (2010). doi:10.1103/PhysRevA.81.031610. [cited on pages 80, 85, and 101].

[203] Armijo, J., Jacqmin, T., Kheruntsyan, K. V. & Bouchoule, I. Probing Three-Body Correlations in a Quantum Gas Using the Measurement of the Third Moment of Density Fluctuations. *Phys. Rev. Lett.* **105**, 230402 (2010). doi:10.1103/PhysRevLett.105.230402. [cited on pages 85 and 105].

[204] Haller, E. *et al.* Three-Body Correlation Functions and Recombination Rates for Bosons in Three Dimensions and One Dimension. *Phys. Rev. Lett.* **107**, 230404 (2011). doi:10.1103/PhysRevLett.107.230404. [cited on pages 85 and 102].

[205] Knoop, S. *et al.* Observation of an Efimov-like trimer resonance in ultracold atom-dimer scattering. *Nature Phys.* **5**, 227–230 (2009). doi:10.1038/nphys1203. [cited on page 85].

[206] Zaccanti, M. *et al.* Observation of an Efimov spectrum in an atomic system. *Nature Phys.* **5**, 586–591 (2009). doi:10.1038/nphys1334. [cited on page 85].

[207] Jack, B. *et al.* Holographic Ghost Imaging and the Violation of a Bell Inequality. *Phys. Rev. Lett.* **103**, 083602 (2009). doi:10.1103/PhysRevLett.103.083602. [cited on page 90].

[208] Bouchoule, I., Kheruntsyan, K. V. & Shlyapnikov, G. V. Interaction-induced crossover versus finite-size condensation in a weakly interacting trapped one-dimensional Bose gas. *Phys. Rev. A* **75**, 031606 (2007). doi:10.1103/PhysRevA.75.031606. [cited on pages 91, 103, and 104].

[209] Guarrera, V. *et al.* Observation of Local Temporal Correlations in Trapped Quantum Gases. *Phys. Rev. Lett.* **107**, 160403 (2011). doi:10.1103/PhysRevLett.107.160403. [cited on page 91].

[210] Stamper-Kurn, D. M. *et al.* Reversible Formation of a Bose-Einstein Condensate. *Phys. Rev. Lett.* **81**, 2194–2197 (1998). doi:10.1103/PhysRevLett.81.2194. [cited on page 91].

[211] Stenger, J. *et al.* Optically Confined Bose–Einstein Condensates. *Journal of Low Temperature Physics* **113**, 167–188 (1998). doi:10.1023/A:1022565725910. [cited on page 91].

[212] Inouye, S. *et al.* Superradiant Rayleigh Scattering from a Bose-Einstein Condensate. *Science* **285**, 571–574 (1999). doi:10.1126/science.285.5427.571. [cited on page 91].

[213] Ou, Z. Y., Pereira, S. F., Kimble, H. J. & Peng, K. C. Realization of the Einstein-Podolsky-Rosen paradox for continuous variables. *Phys. Rev. Lett.* **68**, 3663–3666 (1992). doi:10.1103/PhysRevLett.68.3663. [cited on page 96].

[214] Kitagawa, T., Aspect, A., Greiner, M. & Demler, E. Phase-Sensitive Measurements of Order Parameters for Ultracold Atoms through Two-Particle Interferometry. *Phys. Rev. Lett.* **106**, 115302 (2011). doi:10.1103/PhysRevLett.106.115302. [cited on pages 96 and 154].

[215] Petrov, D., Gangardt, D. & Shlyapnikov, G. Low-dimensional trapped gases. *J. Phys. IV France* **116**, 5–44 (2004). doi:10.1051/jp4:2004116001. [cited on page 100].

[216] Petrov, D. S., Shlyapnikov, G. V. & Walraven, J. T. M. Regimes of Quantum Degeneracy in Trapped 1D Gases. *Phys. Rev. Lett.* **85**, 3745–3749 (2000). doi:10.1103/PhysRevLett.85.3745. [cited on page 101].

[217] Petrov, D. S., Shlyapnikov, G. V. & Walraven, J. T. M. Phase-Fluctuating 3D Bose-Einstein Condensates in Elongated Traps. *Phys. Rev. Lett.* **87**, 050404 (2001). doi:10.1103/PhysRevLett.87.050404. [cited on page 101].

[218] Imambekov, A. *et al.* Density ripples in expanding low-dimensional gases as a probe of correlations. *Phys. Rev. A* **80**, 033604 (2009). doi:10.1103/PhysRevA.80.033604. [cited on page 101].

[219] Dettmer, S. *et al.* Observation of Phase Fluctuations in Elongated Bose-Einstein Condensates. *Phys. Rev. Lett.* **87**, 160406 (2001). doi:10.1103/PhysRevLett.87.160406. [cited on page 101].

[220] Kinoshita, T., Wenger, T. & Weiss, D. S. Observation of a One-Dimensional Tonks-Girardeau Gas. *Science* **305**, 1125–1128 (2004). doi:10.1126/science.1100700. [cited on page 101].

[221] Paredes, B. *et al.* Tonks-Girardeau gas of ultracold atoms in an optical lattice. *Nature* **429**, 277–281 (2004). doi:10.1038/nature02530. [cited on page 101].

[222] Stöferle, T., Moritz, H., Schori, C., Köhl, M. & Esslinger, T. Transition from a Strongly Interacting 1D Superfluid to a Mott Insulator. *Phys. Rev. Lett.* **92**, 130403 (2004). doi:10.1103/PhysRevLett.92.130403. [cited on page 101].

[223] Yang, C. N. & Yang, C. P. Thermodynamics of a One-Dimensional System of Bosons with Repulsive Delta-Function Interaction. *Journal of Mathematical Physics* **10**, 1115–1122 (1969). doi:10.1063/1.1664947. [cited on page 102].

[224] van Amerongen, A. H., van Es, J. J. P., Wicke, P., Kheruntsyan, K. V. & van Druten, N. J. Yang-Yang Thermodynamics on an Atom Chip. *Phys. Rev. Lett.* **100**, 090402 (2008). doi:10.1103/PhysRevLett.100.090402. [cited on page 102].

[225] Jacqmin, T., Armijo, J., Berrada, T., Kheruntsyan, K. V. & Bouchoule, I. Sub-Poissonian Fluctuations in a 1D Bose Gas: From the Quantum Quasicondensate to the Strongly Interacting Regime. *Phys. Rev. Lett.* **106**, 230405 (2011). doi:10.1103/PhysRevLett.106.230405. [cited on pages 102 and 153].

[226] Krüger, P., Hadzibabic, Z. & Dalibard, J. Critical Point of an Interacting Two-Dimensional Atomic Bose Gas. *Phys. Rev. Lett.* **99**, 040402 (2007). doi:10.1103/PhysRevLett.99.040402. [cited on page 102].

[227] Armijo, J., Jacqmin, T., Kheruntsyan, K. & Bouchoule, I. Mapping out the quasicondensate transition through the dimensional crossover from one to three dimensions. *Phys. Rev. A* **83**, 021605 (2011). doi:10.1103/PhysRevA.83.021605. [cited on page 104].

[228] Huang, D. *et al.* Optical coherence tomography. *Science* **254**, 1178–1181 (1991). doi:10.1126/science.1957169. [cited on page 110].

[229] Hillery, M., O'Connell, R., Scully, M. & Wigner, E. Distribution functions in physics: Fundamentals. *Physics Reports* **106**, 121–167 (1984). doi:10.1016/0370-1573(84)90160-1. [cited on page 114].

[230] Case, W. B. Wigner functions and Weyl transforms for pedestrians. *Am. J. Phys.* **76**, 937–946 (2008). doi:10.1119/1.2957889. [cited on page 114].

[231] Wigner, E. On the Quantum Correction For Thermodynamic Equilibrium. *Phys. Rev.* **40**, 749–759 (1932). doi:10.1103/PhysRev.40.749. [cited on page 114].

[232] Kurtsiefer, C., Pfau, T. & Mlynek, J. Measurement of the Wigner function of an ensemble of helium atoms. *Nature* **386**, 150–153 (1997). doi:10.1038/386150a0. [cited on page 114].

[233] Bertrand, J. & Bertrand, P. A tomographic approach to Wigner's function. *Foundations of Physics* **17**, 397–405 (1987). doi:10.1007/BF00733376. [cited on page 114].

[234] Vogel, K. & Risken, H. Determination of quasiprobability distributions in terms of probability distributions for the rotated quadrature phase. *Phys. Rev. A* **40**, 2847–2849 (1989). doi:10.1103/PhysRevA.40.2847. [cited on page 114].

[235] Riedel, M. F. *et al.* Atom-chip-based generation of entanglement for quantum metrology. *Nature* 1170–1173 (2010). doi:10.1038/nature08988. [cited on page 115].

[236] Schmied, R. & Treutlein, P. Tomographic reconstruction of the Wigner function on the Bloch sphere. *New J. Phys.* **13**, 065019 (2011). doi:10.1088/1367-2630/13/6/065019. [cited on page 115].

[237] Steel, M. J. *et al.* Dynamical quantum noise in trapped Bose-Einstein condensates. *Phys. Rev. A* **58**, 4824–4835 (1998). doi:10.1103/PhysRevA.58.4824. [cited on page 115].

[238] Opanchuk, B. & Drummond, P. D. Functional Wigner representation of quantum dynamics of Bose-Einstein condensate. *Journal of Mathematical Physics* **54**, 042107 (2013). doi:10.1063/1.4801781. [cited on page 115].

[239] Jeunhomme, L. & Pocholle, J. P. Selective mode excitation of graded index optical fibers. *Appl. Opt.* **17**, 463–468 (1978). doi:10.1364/AO.17.000463. [cited on pages 115 and 119].

[240] Sukhorukov, A. A., Handmer, C. J., de Sterke, C. M. & Steel, M. J. Slow light with flat or offset band edges in few-mode fiber with two gratings. *Opt. Express* **15**, 17954–17959 (2007). doi:10.1364/OE.15.017954. [cited on page 115].

[241] Kumar, A., Goel, N. K. & Varshney, R. K. Studies on a Few-Mode Fiber-Optic Strain Sensor Based on LP01-LP 02 Mode Interference. *J. Lightwave Technol.* **19**, 358 (2001). doi:10.1109/50.918888. [cited on page 115].

[242] Carbone, L., Bogan, C., Fulda, P., Freise, A. & Willke, B. Generation of High-Purity Higher-Order Laguerre-Gauss Beams at High Laser Power. *Phys. Rev. Lett.* **110**, 251101 (2013). doi:10.1103/PhysRevLett.110.251101. [cited on page 115].

[243] Janousek, J. *et al.* Optical entanglement of co-propagating modes. *Nature Photon.* **3**, 399–402 (2009). doi:10.1038/nphoton.2009.97. [cited on page 115].

[244] Dowling, J. P. & Gea-Banacloche, J. Evanescent light-wave atom mirrors, resonators, waveguides, and traps. *Advances In Atomic, Molecular, and Optical Physics* **37**, 1–94 (1996). doi:10.1016/S1049-250X(08)60098-1. [cited on page 115].

[245] Renn, M. J. *et al.* Laser-Guided Atoms in Hollow-Core Optical Fibers. *Phys. Rev. Lett.* **75**, 3253–3256 (1995). doi:10.1103/PhysRevLett.75.3253. [cited on pages 115 and 116].

[246] Dall, R. G., Hoogerland, M. D., Baldwin, K. G. H. & Buckman, S. J. Guiding of metastable helium atoms through hollow optical fibres. *Journal of Optics B: Quantum and Semiclassical Optics* **1**, 396 (1999). doi:10.1088/1464-4266/1/4/307. [cited on pages 115 and 116].

[247] Takekoshi, T. & Knize, R. J. Optical Guiding of Atoms through a Hollow-Core Photonic Band-Gap Fiber. *Phys. Rev. Lett.* **98**, 210404 (2007). doi:10.1103/PhysRevLett.98.210404. [cited on page 115].

[248] Christensen, C. A. *et al.* Trapping of ultracold atoms in a hollow-core photonic crystal fiber. *Phys. Rev. A* **78**, 033429 (2008). doi:10.1103/PhysRevA.78.033429. [cited on page 115].

[249] Fortagh, J., Grossmann, A., Zimmermann, C. & Hänsch, T. W. Miniaturized Wire Trap for Neutral Atoms. *Phys. Rev. Lett.* **81**, 5310–5313 (1998). doi:10.1103/PhysRevLett.81.5310. [cited on page 115].

[250] Denschlag, J., Cassettari, D. & Schmiedmayer, J. Guiding Neutral Atoms with a Wire. *Phys. Rev. Lett.* **82**, 2014–2017 (1999). doi:10.1103/PhysRevLett.82.2014. [cited on pages 115 and 116].

[251] Guerin, W. *et al.* Guided Quasicontinuous Atom Laser. *Phys. Rev. Lett.* **97**, 200402 (2006). doi:10.1103/PhysRevLett.97.200402. [cited on pages 115 and 116].

[252] Couvert, A. *et al.* A quasi-monomode guided atom laser from an all-optical Bose-Einstein condensate. *Europhys. Lett.* **83**, 50001 (2008). doi:10.1209/0295-5075/83/50001. [cited on pages 115, 116, and 122].

[253] Gattobigio, G. L., Couvert, A., Jeppesen, M., Mathevet, R. & Guéry-Odelin, D. Multimode-to-monomode guided-atom lasers: An entropic analysis. *Phys. Rev. A* **80**, 041605 (2009). doi:10.1103/PhysRevA.80.041605. [cited on pages 115 and 116].

[254] Günther, A. *et al.* Combined chips for atom optics. *Phys. Rev. A* **71**, 063619 (2005). doi:10.1103/PhysRevA.71.063619. [cited on page 115].

[255] Okamoto, K. *Fundamentals of Optical Waveguides (2nd Edition)* (Academic Press, Burlington, Massachusetts, 2005). [cited on page 116].

[256] Ito, H. *et al.* Laser Spectroscopy of Atoms Guided by Evanescent Waves in Micron-Sized Hollow Optical Fibers. *Phys. Rev. Lett.* **76**, 4500–4503 (1996). doi:10.1103/PhysRevLett.76.4500. [cited on page 116].

[257] Xu, X., Kim, K., Jhe, W. & Kwon, N. Efficient optical guiding of trapped cold atoms by a hollow laser beam. *Phys. Rev. A* **63**, 063401 (2001). doi:10.1103/PhysRevA.63.063401. [cited on page 116].

[258] Cennini, G., Ritt, G., Geckeler, C. & Weitz, M. Bose–Einstein condensation in a CO2-laser optical dipole trap. *Applied Physics B* **77**, 773–779 (2003). doi:10.1007/s00340-003-1333-1. [cited on pages 116 and 117].

[259] Altin, P. A. *The role of interactions in atom interferometry with Bose-condensed atoms*. Ph.D. thesis, Australian National University (2012). [cited on page 116].

[260] Busch, T., Köhl, M., Esslinger, T. & Mølmer, K. Transverse mode of an atom laser. *Phys. Rev. A* **65**, 043615 (2002). doi:10.1103/PhysRevA.65.043615. [cited on page 116].

[261] Riou, J.-F. *et al.* Beam Quality of a Nonideal Atom Laser. *Phys. Rev. Lett.* **96**, 070404 (2006). doi:10.1103/PhysRevLett.96.070404. [cited on page 116].

[262] Bongs, K. & Sengstock, K. Physics with coherent matter waves. *Reports on Progress in Physics* **67**, 907 (2004). doi:10.1088/0034-4885/67/6/R03. [cited on pages 116 and 117].

[263] Cronin, A. D., Schmiedmayer, J. & Pritchard, D. E. Optics and interferometry with atoms and molecules. *Rev. Mod. Phys.* **81**, 1051–1129 (2009). doi:10.1103/RevModPhys.81.1051. [cited on pages 116 and 136].

[264] Wang, Y.-J. *et al.* Atom Michelson Interferometer on a Chip Using a Bose-Einstein Condensate. *Phys. Rev. Lett.* **94**, 090405 (2005). doi:10.1103/PhysRevLett.94.090405. [cited on page 116].

[265] Fabre, C. M. *et al.* Realization of a Distributed Bragg Reflector for Propagating Guided Matter Waves. *Phys. Rev. Lett.* **107**, 230401 (2011). doi:10.1103/PhysRevLett.107.230401. [cited on page 116].

[266] Gattobigio, G. L., Couvert, A., Reinaudi, G., Georgeot, B. & Guéry-Odelin, D. Optically Guided Beam Splitter for Propagating Matter Waves. *Phys. Rev. Lett.* **109**, 030403 (2012). doi:10.1103/PhysRevLett.109.030403. [cited on page 116].

[267] Vorrath, S., Möller, S. A., Windpassinger, P., Bongs, K. & Sengstock, K. Efficient guiding of cold atoms through a photonic band gap fiber. *New J. Phys.* **12**, 123015 (2010). doi:10.1088/1367-2630/12/12/123015. [cited on page 116].

[268] Vermersch, F. *et al.* Guided-atom laser: Transverse mode quality and longitudinal momentum distribution. *Phys. Rev. A* **84**, 043618 (2011). doi:10.1103/PhysRevA.84.043618. [cited on page 116].

[269] Gattobigio, G. L., Couvert, A., Georgeot, B. & Guéry-Odelin, D. Interaction of a propagating guided matter wave with a localized potential. *New J. Phys.* **12**, 085013 (2010). doi:10.1088/1367-2630/12/8/085013. [cited on page 116].

[270] Hodgman, S. S. *Transition Lifetime Measurements and Correlation Experiments with Ultra-cold Metastable Helium*. Ph.D. thesis, Australian National University (2011). [cited on pages 116, 122, and 155].

[271] Choi, S., Japha, Y. & Burnett, K. Adiabatic output coupling of a Bose gas at finite temperatures. *Phys. Rev. A* **61**, 063606 (2000). doi:10.1103/PhysRevA.61.063606. [cited on page 117].

[272] Griffiths, D. J. *Introduction to Quantum Mechanics (2nd Edition)* (Pearson Prentice Hall, New Jersey, 2004). [cited on page 120].

[273] Beijersbergen, M., Allen, L., van der Veen, H. & Woerdman, J. Astigmatic laser mode converters and transfer of orbital angular momentum. *Opt. Commun.* **96**, 123–132 (1993). doi:10.1016/0030-4018(93)90535-D. [cited on page 120].

[274] Meschede, D. *Optics, Light and Lasers* (Wiley, Weinheim, 2007). [cited on page 122].

[275] Westbrook, C. I. & Boiron, D. The Hanbury Brown Twiss effect for atomic matter waves. *ArXiv e-prints* (2010). `http://arxiv.org/abs/1004.2384`. [cited on page 122].

[276] Feynman, R. Simulating physics with computers. *International Journal of Theoretical Physics* **21**, 467–488 (1982). doi:10.1007/BF02650179. [cited on page 130].

[277] Taylor, G. I. Interference fringes with feeble light. *Proc. Camb. Phil. Soc.* **15**, 91–92 (1909). [cited on page 130].

[278] Clauser, J. F. Experimental distinction between the quantum and classical field-theoretic predictions for the photoelectric effect. *Phys. Rev. D* **9**, 853–860 (1974). doi:10.1103/PhysRevD.9.853. [cited on page 130].

[279] İmamoğlu, A. & Yamamoto, Y. Turnstile device for heralded single photons: Coulomb blockade of electron and hole tunneling in quantum confined *p-i-n* heterojunctions. *Phys. Rev. Lett.* **72**, 210–213 (1994). doi:10.1103/PhysRevLett.72.210. [cited on page 130].

[280] Lounis, B. & Moerner, W. E. Single photons on demand from a single molecule at room temperature. *Nature* **407**, 491–493 (2000). doi:10.1038/35035032. [cited on page 130].

[281] Eisaman, M. D., Fan, J., Migdall, A. & Polyakov, S. V. Invited Review Article: Single-photon sources and detectors. *Review of Scientific Instruments* **82**, 071101 (2011). doi:10.1063/1.3610677. [cited on page 130].

[282] Oxborrow, M. & Sinclair, A. G. Single-photon sources. *Contemporary Physics* **46**, 173–206 (2005). doi:10.1080/00107510512331337936. [cited on page 130].

[283] Lounis, B. & Orrit, M. Single-photon sources. *Reports on Progress in Physics* **68**, 1129 (2005). doi:10.1088/0034-4885/68/5/R04. [cited on page 130].

[284] Clauser, J. F. & Shimony, A. Bell's theorem. Experimental tests and implications. *Reports on Progress in Physics* **41**, 1881 (1978). doi:10.1088/0034-4885/41/12/002. [cited on page 131].

[285] Mabuchi, H., Turchette, Q. A., Chapman, M. S. & Kimble, H. J. Real-time detection of individual atoms falling through a high-finesse optical cavity. *Opt. Lett.* **21**, 1393–1395 (1996). doi:10.1364/OL.21.001393. [cited on page 131].

[286] Schlosser, N., Reymond, G., Protsenko, I. & Grangier, P. Sub-poissonian loading of single atoms in a microscopic dipole trap. *Nature* **411**, 1024–1027 (2001). doi:10.1038/35082512. [cited on page 131].

[287] Kuhr, S. *et al.* Deterministic Delivery of a Single Atom. *Science* **293**, 278–280 (2001). doi:10.1126/science.1062725. [cited on page 131].

[288] Dumke, R. *et al.* Micro-optical Realization of Arrays of Selectively Addressable Dipole Traps: A Scalable Configuration for Quantum Computation with Atomic Qubits. *Phys. Rev. Lett.* **89**, 097903 (2002). doi:10.1103/PhysRevLett.89.097903. [cited on page 131].

[289] Schrader, D. *et al.* Neutral Atom Quantum Register. *Phys. Rev. Lett.* **93**, 150501 (2004). doi:10.1103/PhysRevLett.93.150501. [cited on page 131].

[290] Nelson, K. D., Li, X. & Weiss, D. S. Imaging single atoms in a three-dimensional array. *Nature Phys.* **3**, 556–560 (2007). doi:10.1038/nphys645. [cited on page 131].

[291] Karski, M. *et al.* Nearest-Neighbor Detection of Atoms in a 1D Optical Lattice by Fluorescence Imaging. *Phys. Rev. Lett.* **102**, 053001 (2009). doi:10.1103/PhysRevLett.102.053001. [cited on page 131].

[292] Bakr, W. S. *et al.* Probing the Superfluid–to–Mott Insulator Transition at the Single-Atom Level. *Science* **329**, 547–550 (2010). doi:10.1126/science.1192368. [cited on page 131].

[293] DePue, M. T., McCormick, C., Winoto, S. L., Oliver, S. & Weiss, D. S. Unity Occupation of Sites in a 3D Optical Lattice. *Phys. Rev. Lett.* **82**, 2262–2265 (1999). doi:10.1103/PhysRevLett.82.2262. [cited on page 131].

[294] Gruenzweig, T., Hilliard, A., McGovern, M. & Andersen, M. F. Near-deterministic preparation of a single atom in an optical microtrap. *Nature Phys.* **6**, 951–954 (2010). doi:10.1038/nphys1778. [cited on page 131].

[295] Kaufman, A. M., Lester, B. J. & Regal, C. A. Cooling a Single Atom in an Optical Tweezer to Its Quantum Ground State. *Phys. Rev. X* **2**, 041014 (2012). doi:10.1103/PhysRevX.2.041014. [cited on page 131].

[296] Reiserer, A., Nölleke, C., Ritter, S. & Rempe, G. Ground-State Cooling of a Single Atom at the Center of an Optical Cavity. *Phys. Rev. Lett.* **110**, 223003 (2013). doi:10.1103/PhysRevLett.110.223003. [cited on page 131].

[297] Yi, Z., ju Gu, W. & xiang Li, G. Ground-state cooling for a trapped atom using cavity-induced double electromagnetically induced transparency. *Opt. Express* **21**, 3445–3462 (2013). doi:10.1364/OE.21.003445. [cited on page 131].

[298] Wilk, T., Webster, S. C., Kuhn, A. & Rempe, G. Single-Atom Single-Photon Quantum Interface. *Science* **317**, 488–490 (2007). doi:10.1126/science.1143835. [cited on page 131].

[299] Ourjoumtsev, A. *et al.* Observation of squeezed light from one atom excited with two photons. *Nature* 623–626 (2011). doi:10.1038/nature10170. [cited on page 131].

[300] Thompson, J. D. *et al.* Coupling a Single Trapped Atom to a Nanoscale Optical Cavity. *Science* **340**, 1202–1205 (2013). doi:10.1126/science.1237125. [cited on page 131].

[301] Berman, P. R. (ed.). *Atom Interferometry* (Academic Press, San Diego, 1997). [cited on pages 137, 138, and 139].

[302] McGuirk, J. M., Snadden, M. J. & Kasevich, M. A. Large Area Light-Pulse Atom Interferometry. *Phys. Rev. Lett.* **85**, 4498–4501 (2000). doi:10.1103/PhysRevLett.85.4498. [cited on page 137].

[303] Szigeti, S. S., Debs, J. E., Hope, J. J., Robins, N. P. & Close, J. D. Why momentum width matters for atom interferometry with Bragg pulses. *New J. Phys.* **14**, 023009 (2012). doi:10.1088/1367-2630/14/2/023009. [cited on pages 137, 144, and 146].

[304] Shimizu, F., Shimizu, K. & Takuma, H. Double-slit interference with ultracold metastable neon atoms. *Phys. Rev. A* **46**, R17–R20 (1992). doi:10.1103/PhysRevA.46.R17. [cited on page 139].

[305] Fujita, J. *et al.* Manipulation of an atomic beam by a computer-generated hologram. *Nature* **380**, 691–694 (1996). doi:10.1038/380691a0. [cited on page 139].

[306] Morinaga, M. *et al.* Holographic Manipulation of a Cold Atomic Beam. *Phys. Rev. Lett.* **77**, 802–805 (1996). doi:10.1103/PhysRevLett.77.802. [cited on page 139].

[307] Fujita, J., Mitake, S. & Shimizu, F. Interferometric Modulation of an Atomic Beam by an Electric Field: A Phase Hologram for Atoms. *Phys. Rev. Lett.* **84**, 4027–4030 (2000). doi:10.1103/PhysRevLett.84.4027. [cited on page 139].

[308] Shimizu, F. & Fujita, J.-i. Reflection-Type Hologram for Atoms. *Phys. Rev. Lett.* **88**, 123201 (2002). doi:10.1103/PhysRevLett.88.123201. [cited on page 139].

[309] Krachmalnicoff, V. *Deux experiences de correlations quantiques sur des gaz de helium metastable: degroupement de fermions et etude de paires de bosons correles par collision de condensats*. Ph.D. thesis, Université Paris XI (2009). [cited on pages 139 and 142].

[310] Perrin, A. *et al.* Atomic four-wave mixing via condensate collisions. *New J. Phys.* **10**, 045021 (2008). doi:10.1088/1367-2630/10/4/045021. [cited on page 139].

[311] Krachmalnicoff, V. *et al.* Spontaneous Four-Wave Mixing of de Broglie Waves: Beyond Optics. *Phys. Rev. Lett.* **104**, 150402 (2010). doi:10.1103/PhysRevLett.104.150402. [cited on page 139].

[312] Altin, P. A. *et al.* Precision atomic gravimeter based on Bragg diffraction. *New J. Phys.* **15**, 023009 (2013). doi:10.1088/1367-2630/15/2/023009. [cited on page 149].

[313] Lewis-Swann, R. & Kheruntsyan, K. V. private communication (2013). [cited on pages 153 and 154].

[314] Giustina, M. *et al.* Bell violation using entangled photons without the fair-sampling assumption. *Nature* **497**, 227–230 (2013). doi:10.1038/nature12012. [cited on page 153].

[315] Estève, J., Gross, C., Weller, A., Giovanazzi, S. & Oberthaler, M. K. Squeezing and entanglement in a Bose-Einstein condensate. *Nature* **455**, 1216–1219 (2008). doi:10.1038/nature07332. [cited on page 153].

[316] Gross, C. *et al.* Atomic homodyne detection of continuous-variable entangled twin-atom states. *Nature* **480**, 219–223 (2011). doi:10.1038/nature10654. [cited on page 153].

[317] Reid, M. D. Demonstration of the Einstein-Podolsky-Rosen paradox using nondegenerate parametric amplification. *Phys. Rev. A* **40**, 913–923 (1989). doi:10.1103/PhysRevA.40.913. [cited on page 153].

[318] Leggett, A. J. & Garg, A. Quantum mechanics versus macroscopic realism: Is the flux there when nobody looks? *Phys. Rev. Lett.* **54**, 857–860 (1985). doi:10.1103/PhysRevLett.54.857. [cited on page 153].

[319] Aharonov, Y. & Vaidman, L. Properties of a quantum system during the time interval between two measurements. *Phys. Rev. A* **41**, 11–20 (1990). doi:10.1103/PhysRevA.41.11. [cited on page 153].

[320] Tamir, B. & Cohen, E. Introduction to weak measurements and weak values. *Quanta* **2** (2013). doi:10.12743/quanta.v2i1.14. [cited on page 153].

[321] Ou, Z. Y. & Mandel, L. Violation of Bell's Inequality and Classical Probability in a Two-Photon Correlation Experiment. *Phys. Rev. Lett.* **61**, 50–53 (1988). doi:10.1103/PhysRevLett.61.50. [cited on page 153].

[322] Clauser, J. F., Horne, M. A., Shimony, A. & Holt, R. A. Proposed Experiment to Test Local Hidden-Variable Theories. *Phys. Rev. Lett.* **23**, 880–884 (1969). doi:10.1103/PhysRevLett.23.880. [cited on page 153].

[323] Olsen, M. K. & Davis, M. J. Entanglement properties of degenerate four-wave mixing of matter waves in a periodic potential. *Phys. Rev. A* **73**, 063618 (2006). doi:10.1103/PhysRevA.73.063618. [cited on page 154].

[324] Ferris, A. J., Olsen, M. K. & Davis, M. J. Atomic entanglement generation and detection via degenerate four-wave mixing of a Bose-Einstein condensate in an optical lattice. *Phys. Rev. A* **79**, 043634 (2009). doi:10.1103/PhysRevA.79.043634. [cited on page 154].

[325] Bloch, I. Quantum coherence and entanglement with ultracold atoms in optical lattices. *Nature* **453**, 1016–1022 (2008). doi:10.1038/nature07126. [cited on page 154].

[326] Taşgın, M., Oktel, M. Ö., You, L. & Müstecaplıoğlu, Ö. E. Quantum entanglement via superradiance of a Bose-Einstein condensate. *Laser Physics* **20**, 700–708 (2010). doi:10.1134/S1054660X10050191. [cited on page 154].

[327] Ferris, A. J., Olsen, M. K., Cavalcanti, E. G. & Davis, M. J. Detection of continuous variable entanglement without coherent local oscillators. *Phys. Rev. A* **78**, 060104 (2008). doi:10.1103/PhysRevA.78.060104. [cited on page 154].

[328] Strekalov, D. V., Sergienko, A. V., Klyshko, D. N. & Shih, Y. H. Observation of Two-Photon "Ghost" Interference and Diffraction. *Phys. Rev. Lett.* **74**, 3600–3603 (1995). doi:10.1103/PhysRevLett.74.3600. [cited on page 154].

[329] Pittman, T. B., Shih, Y. H., Strekalov, D. V. & Sergienko, A. V. Optical imaging by means of two-photon quantum entanglement. *Phys. Rev. A* **52**, R3429–R3432 (1995). doi:10.1103/PhysRevA.52.R3429. [cited on page 154].

[330] Wang, L.-G., Qamar, S., Zhu, S.-Y. & Zubairy, M. S. Hanbury Brown–Twiss effect and thermal light ghost imaging: A unified approach. *Phys. Rev. A* **79**, 033835 (2009). doi:10.1103/PhysRevA.79.033835. [cited on page 154].

[331] D'Angelo, M., Kim, Y.-H., Kulik, S. P. & Shih, Y. Identifying Entanglement Using Quantum Ghost Interference and Imaging. *Phys. Rev. Lett.* **92**, 233601 (2004). doi:10.1103/PhysRevLett.92.233601. [cited on page 154].

[332] Kofler, J. *et al.* Einstein-Podolsky-Rosen correlations from colliding Bose-Einstein condensates. *Phys. Rev. A* **86**, 032115 (2012). doi:10.1103/PhysRevA.86.032115. [cited on page 154].

[333] Foster, C. J., Blakie, P. B. & Davis, M. J. Vortex pairing in two-dimensional Bose gases. *Phys. Rev. A* **81**, 023623 (2010). doi:10.1103/PhysRevA.81.023623. [cited on page 154].

[334] Neely, T. W. *Formation, Dynamics, and Decay of Quantized Vortices in Bose-Einstein Condensates: Elements of Quantum Turbulence*. Ph.D. thesis, University of Arizona (2010). [cited on page 154].

[335] Paret, J. & Tabeling, P. Experimental Observation of the Two-Dimensional Inverse Energy Cascade. *Phys. Rev. Lett.* **79**, 4162–4165 (1997). doi:10.1103/PhysRevLett.79.4162. [cited on page 154].

[336] Balbinot, R., Fabbri, A., Fagnocchi, S., Recati, A. & Carusotto, I. Nonlocal density correlations as a signature of Hawking radiation from acoustic black holes. *Phys. Rev. A* **78**, 021603 (2008). doi:10.1103/PhysRevA.78.021603. [cited on page 155].

[337] Garrett, M. C. *Formation dynamics and phase coherence of Bose-Einstein condensates*. Ph.D. thesis, University of Queensland (2012). [cited on page 155].

[338] Gaudin, M. Une démonstration simplifiée du théorème de wick en mécanique statistique. *Nuclear Physics* **15**, 89–91 (1960). doi:10.1016/0029-5582(60)90285-6. [cited on page 157].

[339] Feynman, R. P. The Theory of Positrons. *Phys. Rev.* **76**, 749–759 (1949). doi:10.1103/PhysRev.76.749. [cited on page 157].

[340] Dyson, F. J. The Radiation Theories of Tomonaga, Schwinger, and Feynman. *Phys. Rev.* **75**, 486–502 (1949). doi:10.1103/PhysRev.75.486. [cited on page 157].

[341] Tsvelik, A. M. *Quantum Field Theory in Condensed Matter Physics*, chap. 3 (Cambridge University Press, Cambridge, 2003). [cited on page 157].

[342] le Bellac, M. *Quantum and Statistical Field Theory*, chap. 5.1, 154 (Oxford University Press, New York, New York, 1991). [cited on page 157].

[343] Louisell, W. H. *Quantum statistical properties of radiation*, chap. 3.7, 182 (John Wiley & Sons, New York, New York, 1973). [cited on pages 157 and 158].